

UNIVERSITY OF COPENHAGEN



PhD Thesis

Murillo Longo Martins

FACULTY OF SCIENCE - NIELS BOHR INSTITUTE

Synthesis and characterization of a bio-nanocomposite for cancer treatment

PhD thesis

Synthesis and characterization of a bio-nanocomposite for cancer
treatment

Submitted to: The Graduate School of Science

Faculty of Science

Niels Bohr Institute

University of Copenhagen

Denmark

by

Murillo Longo Martins

Niels Bohr Institute
University of Copenhagen
Universitetsparken 5
2100 Copenhagen
Denmark

Instituto de Biociências
Universidade Estadual Paulista
(UNESP)
Distrito de Rubião Júnior,
S/N CEP: 18618-970 - Botucatu /
SP, Brasil

October 2014

Supervisor: Heloisa Nunes Bordallo

Co-Supervisor: Margarida Juri Saeki

Abstract

Cancer is one of the biggest public health problems in the whole world. In 2014, about 585,720 Americans are expected to die of cancer, almost 1,600 people per day. Cancer is the second most common cause of death in the US, exceeded only by heart disease, accounting for nearly 1 of every 4 deaths. Anyone can develop cancer. Since the risk of being diagnosed with cancer increases with age, most cases occur in adults who are middle aged or older. The disease is caused by both external factors (tobacco, infectious organisms, chemicals, and radiation) and internal factors (inherited mutations, hormones, immune conditions, and mutations that occur from metabolism). These causal factors may act together or in sequence to initiate or promote the development of cancer. Cancer is treated with surgery, radiation, chemotherapy, hormone therapy, immune therapy, and targeted therapy. In the case of chemotherapy, Paclitaxel is one of the most effective anti-cancer drugs currently available, however it causes a number of undesirable side effects.

The main goal of this work was to develop a new drug carrier that will help reducing these side effects. To achieve such objective the synthesis methodology of a bio-nanocomposite (bio-NCP) that combines the magnetic properties of Mn-Zn ferrite nanoparticles to the biocompatibility of chitosan and hydroxyapatite was developed and the drug was encapsulated. Subsequently, characterization of the drug delivery system was carried out using state-of-the-art solid-state tools, such as synchrotron and neutron diffraction, Near Edge X-Ray Absorption Fine Structure (NEXAFS) and neutron scattering spectroscopies. From the images obtained using Scanning Transmission X-ray Microscopy (STXM), we were then able to show that the drug carrier has a core-shell like structure and a study comparing the vibrational spectra of the pure drug to the one obtained for the encapsulated and released ones was performed. Using density functional theory (DFT) we were able to get initial information on the interactions between the encapsulation and the drug, which will allow, in the future, for designing drug carriers with reduced influence in the drug dynamics. Finally, results of *in-vitro* tests performed with macrophages indicate the low toxicity of the bio-NCP, since no immune response was detected.

Resumé

Kræft er et af de største problemer for folkesundheden i hele verden. I 2014 forventes ca. 585.720 amerikanere at dø af kræft, dette betyder at næsten 1600 mennesker om dagen. Kræft er den næst hyppigste dødsårsag i USA, kun overgået af hjertesygdomme, svarende til næsten 1 ud af hver 4 dødsfald. Alle kan udvikle kræft. Da risikoen for at blive diagnosticeret med kræft stiger med alderen, opstår de fleste tilfælde hos voksne, midaldrende eller ældre. Sygdommen er forårsaget af både eksterne faktorer (tobak, smitsomme organismer, kemikalier og stråling) og interne faktorer (arvelige mutationer, hormoner, immune betingelser og mutationer, der opstår fra stofskifte). Disse faktorer kan i sammenspil eller efter hinanden aktivere eller fremme udviklingen af kræft. Kræft behandles med kirurgi, stråling, kemoterapi, hormonterapi, immunterapi og målrettet terapi. I tilfælde af behandlingsformen kemoterapi, er Paclitaxel et af de mest effektive tilgængelige anti-cancerlægemidler, men det forårsager en række uønskede bivirkninger.

Det primære mål med dette arbejde var at udvikle et nyt "*drug carrier*", der vil medvirke til at reducere disse bivirkninger. For at opnå dette resultat, blev syntese metodologi af en "*bio-nanocomposite (bio-NCP)*", der kombinerer de magnetiske egenskaber af Mn-Zn ferrit nanopartikler til biokompatibilitet chitosan og hydroxyapatite udviklet, og lægemidlet indkapslet. Efterfølgende blev karakterisering af medikamentafgivelsesenhedens uføret ved anvendelse af state-of-the-art solid-state værktøjer, såsom synkrotron og neutrodiffraction, "*Near Edge X-Ray Absorption Fine Structure*" (NEXAFS) og neutronsprengning spektroskopi. Fra de billeder, der er opnået ved hjælp af "*Scanning Transmission X-ray Microscopy (STXM)*" Vi var derefter i stand til at vise, at "drug carrier" har en kerne-skal lignende struktur. En undersøgelse, der sammenligner den vibrationelle spektre af henholdsvis det rene stof, stoffet der forekommer når det indkapslede og det frigivet stof blev udført. Ved hjælp af "*density functional theory (DFT)*" var vi i stand til at få de første oplysninger om samspillet mellem indkapslingen og lægemidlet, som vil gøre det muligt i fremtiden, at designe medikamentbærere med reduceret indflydelse i "*drug dynamics*". Endelig resultater af *in-vitro* tests udført med makrofager indikere lave toksicitet for bio-NCP, da ingen immunrespons blev opdaget.

List of symbols and abbreviations

$G_d(\vec{r}, t)$ – Distinct van Hove function

$G_s(\vec{r}, t)$ – Sel van Hove function

\vec{k} – Wave vector

\vec{p} – Momentum

\vec{Q} – Momentum transfer

\vec{v} – Neutron velocity

AR – Aromatic ring

b_{coh} – Coherent scattering length

b_{inc} – Incoherent scattering length

bio-NCP – Bio-nanocomposite

bio-NCP + PTX – Paclitaxel encapsulated into the bio-nanocomposite

DFT – Density functional theory

$F(\vec{G})$ – Form factor

f_j – Scattering factor for an atom j

FTIR – Fourier Transformed Infrared Spectroscopy

HAP - Hydroxyapatite

$I(\vec{G})$ – Diffracted intensity

ICSD – Inorganic Crystal Structure Database

ILL – Institute Laue Langevin

INS – Inelastic neutron scattering

MD – Molecular dynamics

MNP – Magnetic nanoparticle

NEXAFS – Near Edge X-ray Absorption Fine Structure

PSI – Paul Scherrer Institute

PTX - Paclitaxel

QENS – Quasielastic neutron scattering

$S(\vec{Q}, \omega)$ – Scattering function

STXM - Scanning Transmission X ray Microscopy

TEM – Transmission electron microscopy

XPD – X-ray powder diffraction

λ – Wavelength

μ_b – Bohr magneton

σ – Cross section

Φ – Neutron flux

Publications

1. Publications on which this thesis is based

Paper I

Martins, M. L.; Gates, W. P.; Michot, L.; Ferrage, E.; Marry, V.; Bordallo, H.N.. **Neutron scattering, a powerful tool to study clay minerals.** Appl. Clay Sci., 96, 22-35, 2014.

Description: This work was developed as an introduction to the PhD student on neutron scattering concepts. Studying those concepts on clays was particularly valuable since these systems have been used as drug delivery matrixes and the water motion in clays is highly dependent on the cations concentration, such as in cellular membranes. As the first author, the student was directly involved in the theory, development and design of the paper.

Paper II

Martins, M. L.; Saeki, M. J.; Telling, M. T. F.; Parra, J. P. R. L. L.; Landsgesell, S.; Smith, R. I.; Bordallo, H. N. **Development and characterization of a new bio-nanocomposite (bio-NCP) for diagnosis and treatment of breast cancer.** J. alloys compd, 584, 514–519, 2014.

Description: This work presents the synthesis of the bio-nanocomposite which will be used to encapsulate the drug paclitaxel. The PhD student was directly involved in the collection of all data presented in the work as well as on their interpretation and discussion.

Paper III

Murillo L. Martins, Andrea Orecchini, Luis Aguilera, Juergen Eckert, Jan Embs, Aleksander Matic, Margarida J. Saeki, Heloisa N. Bordallo. **Encapsulation of paclitaxel into a bio-nanocomposite. A study combining Inelastic Neutron Scattering to Thermal Analysis and Infrared Spectroscopy.** Accepted by European Physical Journal Web of Conferences.

Description: This work presents the first insights on the paclitaxel molecule

encapsulated into the bio-nanocomposite. As in Paper II, the PhD student was directly involved in the collection of the data presented in the work as well as on their interpretation and discussion. For the DFT calculations we had the invaluable collaboration of Dr. Juergen Eckert (University of South Florida).

Paper IV

Murillo L. Martins, Rosanna Ignazzi, Juergen Eckert, Benjamin Watts, Ramon Kaneno, Margarida J. Saeki and Heloisa N. Bordallo. **Study on the antitumor drug paclitaxel encapsulated into a magnetic chitosan/hydroxyapatite bio-nanocomposite and first insights on the released drug.** In elaboration.

Description: In this work we present additional insights on the paclitaxel molecule encapsulated into the bio-nanocomposite as well as the first insights on the released drug. Moreover, we present the first biological tests on the bio-NCP. The PhD student is also directly involved in the data collection as well as on their interpretation and discussion. We have also the collaboration of Dr. Juergen Eckert for the DFT calculations and Dr. Ramon Kaneno (Universidade Estadual Paulista) for the biological trials.

2. Other publications

Paper V

Murillo L. Martins, Marcos F. Calabresi, Caio Quini, Juliana F. Matos, José R. A. Miranda, Margarida J. Saeki, Heloisa N. Bordallo. **Enhancing the versatility of Alternate Current Biosusceptometry (ACB) through the synthesis of a dextrose-modified tracer and a magnetic muco-adhesive cellulose gel.** Submitted to “Materials Science and Engineering C”.

Paper VI

Murillo L. Martins, Ariovaldo O. Florentino, Alberto A. Cavaleiro, Rafael I.V. Silva, Dayse I. Dos Santos, Margarida J. Saeki. **Mechanisms of phase formation along the synthesis of Mn–Zn ferrites by the polymeric precursor method.** Ceramics International 40, 16023 – 16031, 2014.

Acknowledgements

This work could not be developed without the help and support of many people in personal and professional points of view.

First I would like to thank my supervisor Heloisa Bordallo for her support, friendship, patience and especially courage for accepting develop this project with me. I can surely say that her enthusiasm has been one of the greatest fuels for the progress of this thesis. I would also like to thank my co-supervisor Margarida Saeki whose invaluable efforts and friendship will never be forgotten.

I would also like to thank everyone who provided me technical and experimental support at LNLS, ISIS, PSI, ILL, HZB and LANSCE. Special thanks must be done for Dr. Juergen Eckert and Dr. Ramon Kaneno for the great support on DFT calculations and biological tests, respectively. I could never forget all my colleagues at the University of Copenhagen and UNESP, with a special acknowledgment for Julio Tedesco, Ana Benetti, Nikolaos Tsapatsaris, Rosanna Ignazzi, João Luiz Parra and Rafael Innocenti. I would also like to thank the staff of the University of Copenhagen, specially Gitte Michelsen, Dorthe Djergskov, Ulla Lindberg and Professor Kell Mortensen, and the financial support from CAPES, CNPQ, DanScatt and FAPESP. I also thank the Professors Lise Arleth and Tommy Nylander and Dr. Henrique Faneca for accepting evaluate this work.

There are no words to properly describe the support and positivity from my parents, Luiz and Janet, as well as from my brother Felipe and my sister Kamila. They, together with my godchildren Luis Felipe and Tomás, have shown to me how powerful the love and family can be in challenging situations.

Finally, I would like to thank my better half Isabela for her friendship, comprehension and, most importantly, love and complicity. The certainty of having her always by my side for any obstacle was my strength during the last years.

Contents

CHAPTER 1: INTRODUCTION	1
CHAPTER 2: RELEVANT CONCEPTS.....	5
2.1. BASIC PRINCIPLES OF NEUTRON SCATTERING.....	5
2.1.1. <i>Concepts of scattering length and cross section.....</i>	<i>6</i>
2.1.2. <i>Diffraction experiments and the complementarity of X-rays and neutron....</i>	<i>8</i>
2.1.3. <i>Inelastic (INS) and quasielastic (QENS) neutron scattering.....</i>	<i>11</i>
2.2. BASIC PRINCIPLES OF NEAR-EDGE X-RAY ABSORPTION FINE STRUCTURE (NEXAFS) AND SCANNING TRANSMISSION X-RAY MICROSCOPY (STXM).....	17
CHAPTER 3: SYNTHESIS OF MN-ZN FERRITE MAGNETIC NANOPARTICLES (MNPS) AND SURFACE MODIFICATION FOR OBTAINING THE BIO-NANOCOMPOSITE (BIO- NCP) – PAPER II.....	20
3.1. INTRODUCTION TO PAPER II	20
3.2. EXPERIMENTAL DETAILS.....	21
3.2.1. <i>Synthesis of the Mn-Zn ferrite nanoparticles: the co-precipitation method </i>	<i>21</i>
3.2.2. <i>Coating the magnetic nanoparticles with the polymer chitosan: reverse micelle technique.....</i>	<i>22</i>
3.2.3. <i>Modification of the polymeric chitosan surface with hydroxyapatite nanoparticles: mimetization method.....</i>	<i>23</i>
3.2.4. <i>Details on the characterization techniques.....</i>	<i>25</i>
3.3. RESULTS AND DISCUSSION: A BIO-NCP WITH HIGH MAGNETIC RESPONSE AT ROOM TEMPERATURE.....	26
3.3.1. <i>Structural characterization of the MNPs.....</i>	<i>26</i>
3.3.2. <i>Verifying the success of chitosan coating and surface modification with hydroxyapatite nanoparticles.....</i>	<i>27</i>
3.4. CONCLUSIONS AND OUTLINE.....	29
CHAPTER 4: ENCAPSULATION OF THE ANTI-TUMOR DRUG PACLITAXEL (PTX) INTO THE BIO-NANOCOMPOSITE (BIO-NCP) – PAPERS III AND IV.....	30
4.1. DOES ENCAPSULATION MODIFY THE DYNAMICS OF A DRUG?	30
4.2. THE PACLITAXEL (PTX) MOLECULE.....	32
4.3. EXPERIMENTAL DETAILS.....	33

4.3.1. Encapsulation of PTX into the bio-NCP.....	33
4.3.2. Details on the characterization techniques.....	34
4.4. RESULTS AND DISCUSSION	37
4.5. CONCLUSIONS AND OUTLINE.....	43
CHAPTER 5: FURTHER IDEAS, CONSIDERATIONS AND PERSPECTIVES	45
BIBLIOGRAPHY	48
APPENDIX: PUBLICATIONS.....	55
PUBLICATION I	56
PUBLICATION II.....	70
PUBLICATION III.....	83
PUBLICATION IV	77
PUBLICATION V.....	104
PUBLICATION VI	123

Chapter 1

Introduction

Cancer is one of the biggest worldwide public health concerns. Specifically in Europe, the incidence of this disease has increased from 3.2 million new cases in 2008 to 3.45 million in 2012, with a death rate around 50% (Ferlay, Parkin and Steliarova-Foucher, 2010 and Ferlay et al., 2013). Certainly, new approaches for early diagnosis and treatment are still an arduous challenge, which calls for interactions between scientists from different areas, such as medicine, biology, chemistry, physics and mathematics.

Currently, the most common cancer treatment approaches are radio and chemotherapy, or a combination of both. The latter has, in fact, provided the best results in most types of cancer (Beijer et al., 2013). Radiotherapy is based on the application of a well-calculated radiation dose into the tumor tissue, while chemotherapy is based on drugs that are able to disrupt or interrupt the cancer cell life cycle. However, both techniques present drawbacks, for example the low efficiency of radiotherapy in multiple metastasis cases and the serious damage to life quality caused by chemotherapy (Nakazaki et al., 2013; Monsuez et al., 2010).

Paclitaxel (PTX) is one of the most effective currently available anti-cancer drugs in the treatment of breast, lung and ovarian cancer treatments (Halder, Chintapalli and Croce, 1996; Miller et al., 2007; Zhou et al., 2013; Vilos et al., 2013). Its peculiar mechanism of action, based on the stabilization of cell microtubules, explains such a success. However, considerable limitations still exist, especially PTX low water solubility ($\sim 0.4 \mu\text{g/mL}$) and its toxicity in healthy cells. To increase

solubility, a drug is often formulated in organic solvents, such as dehydrated ethanol and polyoxyethylated castor oil. However, this approach causes many side effects, such as hypersensitivity reactions and hyperlipidaemia (Ma and Mumper, 2013). As an alternative, a promising approach is the development of new encapsulation systems for drug delivery. A common methodology is the use of soluble polymeric nano-carriers that allows for controlling the pharmacokinetic and biodistribution of the drug. Under these lines, the biopolymer chitosan has attracted great interest in biomedical applications due to its biocompatibility and biodegradability. This path has also been used as a PTX encapsulation matrix with satisfactory results (Yu and Pishko, 2010; Lv et al., 2011).

On the other hand, toxicity of a drug to healthy cells can be attenuated by encapsulating the substance into a nanocomposite with the surface modified by compounds with low toxicity. Additionally, this procedure may further improve the drug adhesion to the cancer cells (Pathi et al., 2011). In this case, hydroxyapatite [$\text{Ca}_{10}(\text{PO}_4)_6(\text{OH})_2$] (HAP), which is the main inorganic constituent of human bones and teeth, is the candidate of choice. In the nano-scale, HAP presents special biocompatibility, non-immunogenicity, non-inflammatory behavior and high osteoconductivity and, most importantly, good adhesion to cancer cells, for example, from the breast (Huang et al., 2007; Pathi et al., 2011). Nanocomposites loaded with HAP nanoparticles have already shown anti-tumor properties in colon, prostate, liver, breast and other cancers (Andronescu et al., 2010; Yuan et al., 2010; Liang et al., 2011; Venkatesen et al., 2011; Meena et al., 2012; Jin et al., 2014).

Additionally to the features provided by the polymer and HAP modification, the inclusion of a drug into nano-carriers with magnetic properties, provided for example by Mn-Zn ferrites nanoparticles, offers remarkable possibilities. For instance, by using an external magnetic field it is possible to guide the drug along the body and attach it in the tissue of interest (Alexiou et al., 2007). Moreover, the position of the material can be easily monitored by either low cost gradiometric systems or by magnetic resonance imaging apparatus. Finally, an additional cancer treatment approach is possible by magnetic hyperthermia, which represents a cheap and promising technique to be used in combination to radio and chemotherapy (Americo et al., 2010; Mikhaylov et al., 2011; Corato et al., 2014). With this in mind, a new form of PTX encapsulation into a bio-nanocomposite (bio-NCP) formed by a magnetic nanoparticles core, covered with chitosan whose and HAP nanocrystals, as

presented in the scheme in Figure 1.1, was developed during this thesis.

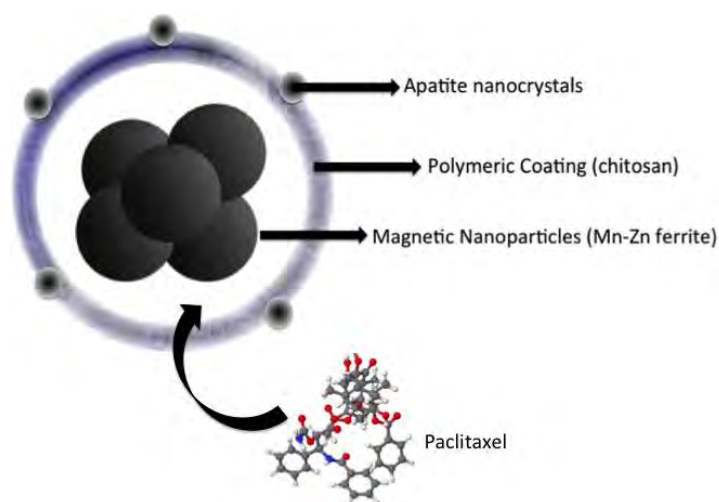


Figure 1.1. Sketch of the bio-nanocomposite (bio-NCP) synthesized for paclitaxel encapsulation. The nanocomposite is formed by a magnetic nanoparticles core, encapsulated with chitosan whose surface is modified with HAP nanocrystals.

Once the synthesis aspects for the bio-NCP + PTX were proven effective, it was necessary to focus on the possible interactions between the encapsulation media and the encapsulated drug molecule. It is well known that the molecular flexibility of a drug is closely related to its activity and that different substrates and environment may drastically change the drug conformation, which might not be recovered after the releasing process (Kuntz, 1992). Therefore, comparing the dynamics of encapsulated drug to its pure form was a key step.

Given the limitations of spectroscopic investigations of the bio-NCP, interesting challenge could be overcome by combining different state-of-the-art techniques, such as NEXAFS, STXM, INS and DFT. Our results show that the drug is distributed along the polymeric part of the bio-NCP and some vibrations, mainly from phenyl (AR1, A2 and AR3, highlighted in red in Figure 1.2), acetyl groups (bonded to C4 and C10 highlighted as blue) and methyl groups (highlighted as green) are constrained by the encapsulation, but they are most likely recovered after the PTX release. Moreover, we present extremely encouraging in-vitro toxicity tests for the bio-NCP performed in macrophages. Finally, in preliminary assays, colon and lung cancer cells present great morphological changes after being in contact with the bio-NCP.

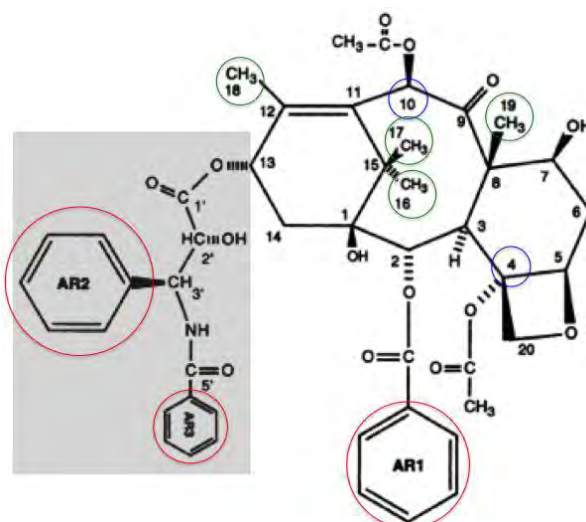


Figure 1.2. Schematic of the PTX molecule adapted from Matropaolo et al., (1995). Circles highlight C-atoms cited along the text. Phenyl (AR1, A2 and AR3) are highlighted in red, methyl groups in green and carbons bonded to acetyl groups in blue.

Chapter 2

Relevant concepts

2.1. Basic principles of neutron scattering

In this section we provide the most relevant concepts of x-rays and neutron scattering necessary for the comprehension of our work. For deeper details we refer the reader to Paper I (Martins et al., 2014a)

Neutrons are subatomic particles, firstly postulated by Rutherford in 1920 and later observed by J. Chadwick in 1932, which present very unique properties on interaction with matter. Since they are non-charged, neutrons can penetrate deeply into matter, which allows studying the structure and dynamics of materials under very precise environmental conditions such as pH, extreme pressure, controlled temperature, hydration conditions and under application of magnetic or electric field. Neutrons are found in all atomic nuclei with exception of the hydrogen atom (^1H) and have a comparable mass to protons, so they can be described either as particle using a classical mechanics with momentum $\vec{p} = m\vec{v}$, where m is the neutron mass ($1.675 \cdot 10^{-27}$ kg) and \vec{v} is its velocity, or as a wave with momentum $\vec{p} = \hbar\vec{k}$, where $|\vec{k}| = \frac{2\pi}{\lambda}|k|$ is the wave vector of the neutron and λ is the associated wavelength. Moreover, neutrons have a magnetic moment of $-1.913\mu_B$ and a nuclear spin of $\frac{1}{2}$, which allow for this particle to interact with unpaired electrons in magnetic atoms.

Neutron scattering techniques are based on the analysis of momentum and

energy transfer, which may occur due to interactions between neutrons and matter.

The corresponding neutron energy E can be described as:

$$E = \frac{p^2}{2m} = \frac{1}{2}mv^2 = \frac{h^2}{2m\lambda^2} = \frac{\hbar^2 k^2}{2m} \quad (2.1)$$

where $h = 2\pi\hbar = 6.626 \cdot 10^{-34} \text{J}\cdot\text{s}$ is the Planck's constant. Thus, the energy and momentum transfer, \vec{Q} , measured in a neutron scattering experiment are given by:

$$\Delta E = E_i - E_f = \frac{\hbar^2}{2m}(k_i^2 - k_f^2) \quad (2.2)$$

for energy, and

$$\vec{Q} = \vec{k}_i - \vec{k}_f \quad (2.3)$$

for momentum transfer.

2.1.1. Concepts of scattering length and cross section

After interacting with a nucleus of a single fixed atom, the scattered neutron wave is isotropic, and can be described as:

$$\psi = \frac{b}{r} e^{(ik_1 r)} \quad (2.4)$$

where r is the distance between the atom and a given detector and b is the scattering length, which can then be defined, for each element j , as a coherent scattering length b_{coh} (2.5) plus an incoherent scattering length b_{inc} (2.6) as:

$$b_{coh} = \bar{b}_j \quad (2.5)$$

$$b_{inc} = \sqrt{\bar{b}_j^2 - \bar{b}_j^2} \quad (2.6)$$

where \bar{b} denotes the average value of b .

While coherent scattering length describes a system in which all the isotopes and spin fluctuations for a single element are smeared out, the incoherent scattering length is exactly composed of such fluctuations. Therefore, in very broad terms, b denotes the scattering “ability” of the atomic nucleus, in which the coherent part describes a collective behavior of an ensemble of atoms and the incoherent part describes individual behaviors. The scattering length b is related to the cross section (σ), which describes the probability of interactions between neutrons and a given atom, as:

$$\sigma = 4\pi b^2 \quad (2.7)$$

As presented in Table 2.1, for each isotope, characteristic values of coherent and incoherent cross sections (σ_{coh} and σ_{inc}) exist, for different elements. It is worth noting the different σ_{coh} values for Fe, Mn and Zn, which allowed for spinel site occupancy determination in diffraction experiments on Mn-Zn ferrites. This is of extremely relevance for this work given influence of cation distribution into the spinel structure in the magnetic nanoparticles properties. On the other hand, the highest σ_{inc} value of ^1H in comparison to the other elements allowed using the incoherent approximation on the analysis of the inelastic scattering investigations of PTX.

Table 2.1. Coherent (σ_{coh}) and incoherent (σ_{inc}) cross-sections in 10^{-24} cm^2 for selected elements and isotopes (Dianoux and Lander, 2003).

	^1H	^2D	C	O	Fe	Mn	Zn
σ_{coh}	1.76	5.59	5.55	4.23	9.45	-3.73	5.68
σ_{inc}	80.27	2.05	<0.01	<0.01	<0.01	1.79	<0.01

In a neutron experiment we obtain the partial differential cross-section, $d^2\sigma/dEd\Omega$, given by (Squires, 1978):

$$\frac{d^2\sigma}{d\Omega dE_f} = \frac{k_f}{k_i} \frac{1}{\hbar} [b_{coh}^2 S_{coh}(\vec{Q}, \omega) + b_{inc}^2 S_{inc}(\vec{Q}, \omega)] \quad (2.8)$$

where $S_{coh}(\vec{Q}, \omega)$ and $S_{inc}(\vec{Q}, \omega)$ are the so-called coherent and incoherent scattering

functions. These functions are Fourier transformations of the van Hove correlation functions $G(\vec{r}, t)$, which can be described as the probability for an atom at the origin at time 0, to also be found within the unit volume at a position \vec{r} at a time t . The van Hove correlation functions can be divided as a distinct part, $G_d(\vec{r}, t)$, and a self part, $G_s(\vec{r}, t)$. The first deals with situations where the atom located at the origin at time 0 is different from the one found at position \vec{r} at time t . The self part deals with situations where the same atom located at the origin at time 0 is found at position \vec{r} at time t . Therefore, the Fourier transformation of $G_d(\vec{r}, t)$ lead to $S_{coh}(\vec{Q}, \omega)$ and the transformation of $G_s(\vec{r}, t)$ leads to $S_{inc}(\vec{Q}, \omega)$ (Bee, 1998).

2.1.2. Diffraction experiments and the complementarity of X-rays and neutron

In diffraction experiments the coherent scattering takes place and, since elastic scattering events are considered, we have:

$$|\vec{k}_i| = |\vec{k}_f| = \frac{2\pi}{\lambda} \quad (2.9)$$

and

$$|\vec{Q}| = \frac{4\pi}{\lambda} \sin\theta \quad (2.10)$$

Moreover, an integral over all energy values is measured and the partial differential cross-section in Eq. (2.8) takes the form of the differential cross section, defined as:

$$\frac{d\sigma}{d\Omega} = \frac{(\text{neutrons} \cdot \text{s}^{-1} \text{ scattered into } d\Omega)}{\Phi d\Omega} \quad (2.11)$$

where σ is the previously defined cross section and Φ is the neutron flux (number of neutrons $\text{cm}^{-2} \cdot \text{s}^{-1}$).

Describing diffraction can be done with the Bragg's equation independently of the radiation used in the experiment. In this description, an incoming wave with the wavelength λ is reflected by atomic planes and if the Bragg-condition

$$2d\sin\theta = n\lambda \quad (2.12)$$

is satisfied, the waves reflected by atomic planes separated by a distance d interfere constructively. The angle θ in Eq. (6) is defined as the angle between the incoming ray and the diffracting atomic plane and by measuring the angles that obey the Bragg-condition it is possible to gain information on atomic distances and therefore to determine structural parameters such as the lattice constants.

The diffracted intensity $I(\vec{G})$ is then proportional to the square of the so-called form factor $F(\vec{G})$, which contains information of atomic coordinates, site occupations and thermal vibrations and brings the dependence on the type of radiation used in the experiment (neutrons or X rays) (Rietveld, 1969):

$$I(\vec{G}) \sim |F(\vec{G})|^2 \quad (2.13)$$

where \vec{G} is the reciprocal lattice vector.

At this point, it is necessary to take into account the differences between the interactions of neutrons and X-rays with matter. Neutrons interact with the nuclei of the atoms by potential scattering as well as with the magnetic moment of unpaired electrons in the electron shells of the atoms, while for X-rays, the interaction occurs with their electron cloud. Considering the nuclear scattering for the neutrons, which is particularly useful for structure determination, the atom can be considered as a point scatter. The main implication of such a feature is that the phase difference of waves scattered from different parts of the nucleus is essentially zero, leading to constant form factor with θ (or Q) while the form factor in an X-ray experiment decreases with θ , as presented in Figure 2.1. As in a magnetic structure determination experiment the interaction between the neutrons and the unpaired electrons has to be taken into account, the form-factor in this case also falls with the Q evolution.

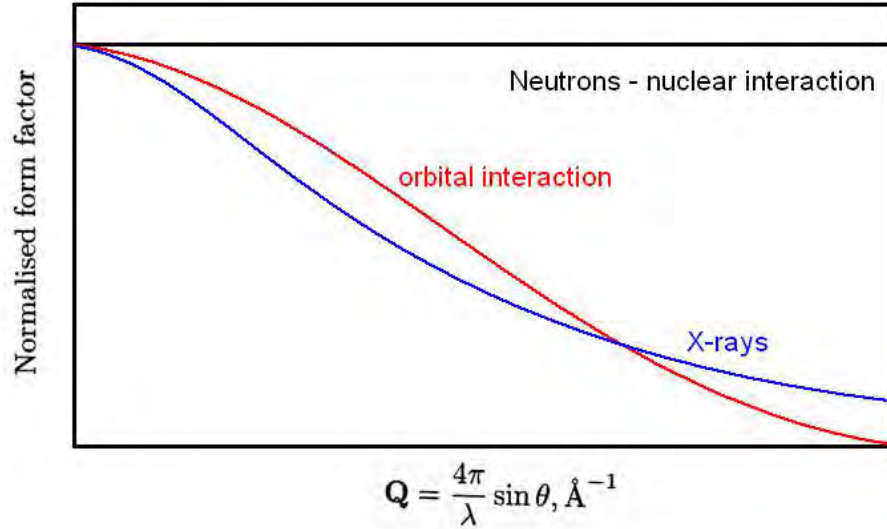


Figure 2.1. Evolution of form-factors for different diffraction experiments.

In an X-ray experiment:

$$F(\vec{G}) = \sum_j f_j e^{(2\pi i(\vec{G} \cdot \vec{r}))} T_j(\vec{G}) \quad (2.14)$$

where \vec{r} represents the atomic coordinates and f_j is the scattering factor for an atom j that linearly increases with the atomic number (Z) of a given atom j . Then, it is expected that the scattered intensity in an X-ray experiment is higher for heavy atoms and the distinction of neighbor elements is not straightforward. $T_j(\vec{G})$ is the Debye-Waller factor, which depicts dynamical and static displacements (usually due to thermal effects) of an atom around its equilibrium position.

In a neutron diffraction experiment,

$$F(\vec{G}) = \sum_j b_{j_{coh}} e^{(2\pi i(\vec{G} \cdot \vec{r}))} T_j(\vec{G}) \quad (2.15)$$

Here, $b_{j_{coh}}$ is the coherent scattering length for an atom j , which will be described in details in the next section. Note, however, that the variation of $b_{j_{coh}}$ is not linear with Z and, in this case, the distinction of neighbor atoms, such as Mn and Fe, is highly favored in a neutron diffraction experiment, as highlighted in Figure 2.2. Another important feature provided by this kind of experiment is the detection of light atoms even with the presence of much heavier atoms in a sample, which is often not possible

with X-rays. On the other hand, in X-ray experiments the probability of interactions between the sample and the radiation is increased by a factor of 10 in comparison to neutrons and, summed to the very high intensity provided available synchrotron facilities, one has a great gain in intensity. Finally, focusing X-rays is considerably easier than focusing a neutron beam, which leads to very higher resolutions for the first.

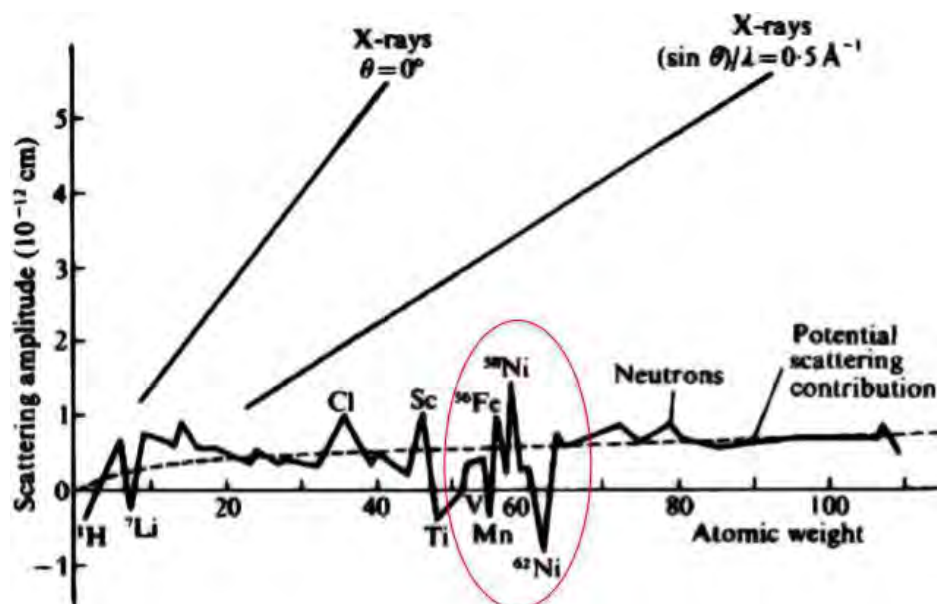


Figure 2.2. Variation in the scattering amplitude of neutrons and X-rays with atomic number. This figure was adapted from JCNS (2012).

2.1.3. Inelastic (INS) and quasielastic (QENS) neutron scattering

If one is interested in the analysis of individual contributions from each atom, then the incoherent part of the neutron scattering is considered and INS data are collected. In such cases only the second part of Eq.(2.8), $b_{inc}^2 S_{inc}(\vec{Q}, \omega)$, as well as the self part of the van Hove correlation function, $G_s(\vec{r}, t)$, are considered. The latter can be divided in two parts (Bee, 1998):

$$G_s(\vec{r}, t) = G_s(\vec{r}, \infty) + G'_s(\vec{r}, t) \quad (2.16)$$

where the first term denotes the correlation for very long times. The Fourier transformation in both space and time domains lead to the incoherent scattering

function, which is separated into elastic and inelastic components whose sum is constant for a same sample analyzed in a same instrument.

$$S_{inc}(\vec{Q}, \omega) = S_{inc}^{elas}(\vec{Q}, \omega)\delta(\omega) + S_{inc}^{in}(\vec{Q}, \omega) \quad (2.17)$$

One should be careful at this point since periodical arrangement of atoms can also lead to elastic contributions, but those are essentially coherent, as discussed in the previous section, while the incoherent part basically denotes individual immobile atoms. Usually, the coherent elastic contribution is avoided in INS data analysis by disconsidering Bragg peaks of the data set. Regarding the inelastic part, it can be also further divided into a purely inelastic scattering (INS) part, formed by vibrational motions, and a quasielastic (QENS), which is formed by atomic translational and rotational motions, mainly from hydrogen in both cases. Therefore, a complete incoherent spectrum can be describe as in Figure 2.3, with the QENS signal comprising a region of small energy exchanges between neutrons and the sample, on either side of the elastic line, where the energy exchange is 0. At higher values of energy transfer there is the INS part of the spectrum, formed by molecular vibrations.

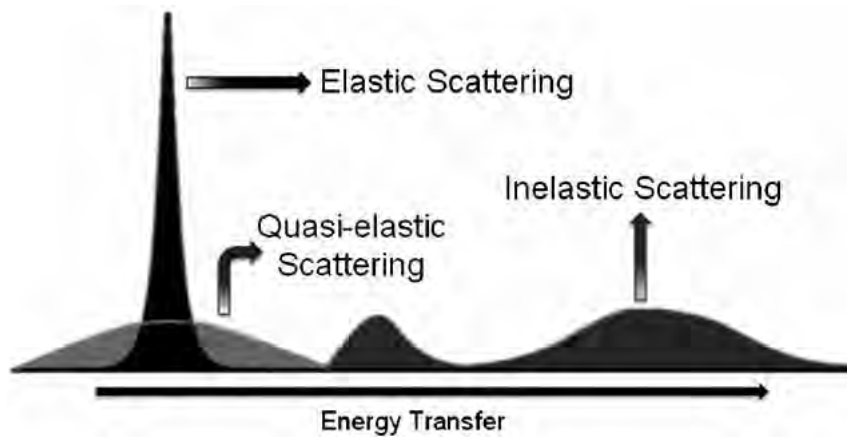


Figure 2.3. Elastic and quasi-elastic scattering are both centered at $\omega = 0$. For positive ω the sample gains energy from the neutron by entering an excited state and creating a phonon and for negative ω the sample loses energy to the neutron, which absorbs a phonon (Martins et al, 2014a).

Quasielastic neutron scattering (QENS)

The QENS signal is formed by hydrogen translational, $S_{inc}^{trans}(\vec{Q}, \omega)$, and rotational, $S_{inc}^{rot}(\vec{Q}, \omega)$, motions, whose time scales are around, respectively, 10^{-9} to 10^{-10} s and 10^{-11} to 10^{-12} s. Vibrational modes, $S_{inc}^{vib}(\vec{Q}, \omega)$, with a timescale of 10^{-14} s to 10^{-15} s will mainly contribute to the background and can be just substituted with an attenuation term, such as the Debye–Waller factor (BÉE, 1988). Then, the incoherent scattering function for the QENS data can be described as:

$$S_{inc}(\vec{Q}, \omega) = [S_{inc}^{trans}(\vec{Q}, \omega) \otimes S_{inc}^{rot}(\vec{Q}, \omega)] e^{\frac{-(u(T)^2)Q^2}{3}} \quad (2.18)$$

The most interesting application for QENS is the possibility of extracting translational and rotational coefficients, which are of great interest in many subjects. These values are related to the width of Lorentzian functions observed in the reciprocal space in Figure 2.4. The translational contribution, which is not truly relevant in this work but highly important for dispersed molecules, for example, can be described by an isotropic continuous translation diffusion model, where S_{inc}^{trans} assumes the Lorentzian form:

$$S_{inc}^{trans}(\vec{Q}, \omega) = \frac{1}{\pi} \frac{\Gamma_{trans}}{(\Gamma_{trans})^2 + \omega^2} \quad (2.19)$$

$\Gamma_{trans} = D_{trans} \vec{Q}^2$ is the half-width at half-maximum (HWHM) of the Lorentzian curve, where D_{trans} is the translational diffusion coefficient.

Regarding the form of the rotational contribution, the simplest assumption is the model of isotropic rotational motion on a sphere, developed by Sears (1967), which considers reorientations of atoms in a molecule by small random angle changes. The corresponding scattering function is an infinite sum over Lorentzians weighted by spherical Bessel functions j_l with increasing l , plus an elastic part due to the spatial restriction to the sphere:

$$S_{inc}^{rot}(\vec{Q}, \omega) = A_0(\vec{Q}_a) \cdot \delta(\omega) + \sum_{l=1}^{\infty} A_l(\vec{Q}_a) \frac{1}{\pi} \cdot \frac{\tau_l}{1 + \omega^2 \tau^2} \quad (2.20)$$

where $A_0(\vec{Q}_a)$ is the elastic structure factor, $A_l(\vec{Q}_a)$ is the quasi-elastic structure factor and a is the radius of the sphere on which the molecule rotates. The relaxation time τ_l describes the half-width half-maximum (HWHM) of the Lorentzians. Note, however, that even though the Bessel series is an infinite sum of Lorentzians, only a finite series contribute to the Q-range accessed by one instrument. Therefore, in practice the collected data can be described by one or two Lorentzians.

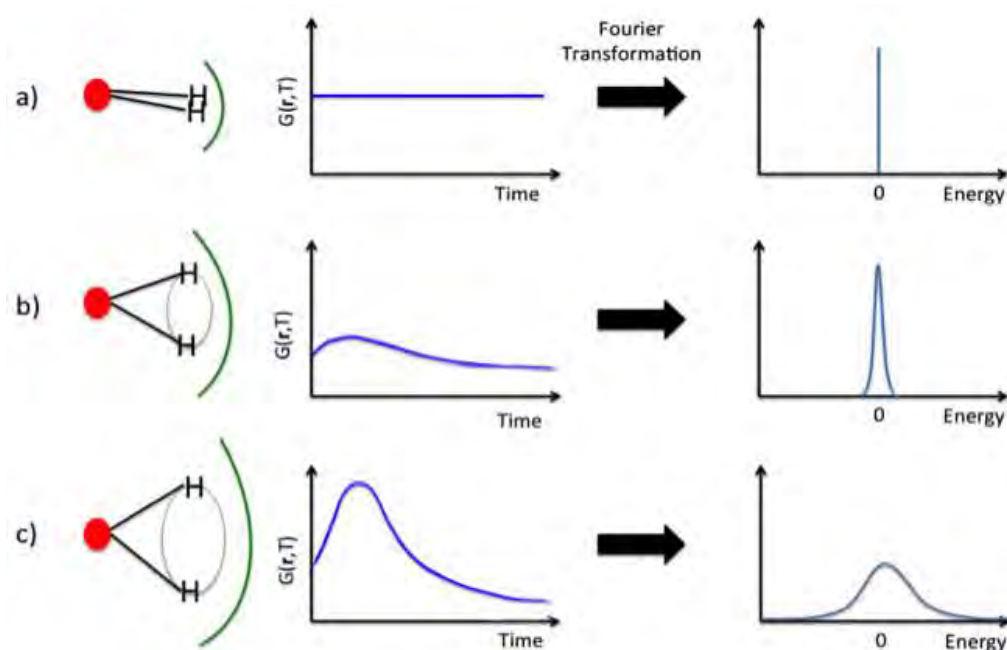


Figure 2.4. Probability distributions in real and reciprocal space for a molecular group with different confinement degrees. An infinitely confined group (a) leads to a Dirac function in reciprocal space less confined situations (b) leads to Lorentzian functions that become broader as the confinement is relaxed (c).

However, one should keep in mind that since the energy and time are connected through the Heisenberg uncertainty relation, the timescale of the motions that can be effectively detected as part of the QENS signal, and not as a component of the elastic line, depends on the experimental (energy) resolution as well as on the space available to the motion. Slower motions, whose energy exchange between the sample and the neutron beam is smaller, require higher resolutions to be detected. However, higher resolutions can be achieved by reducing the spread in energy in the neutron beam and by using higher values of λ for the neutrons, which leads to flux reduction and a limit

in the Q-range in which the analysis can be performed, respectively.

By considering these concepts, it is possible to extend the ideas discussed so far to the paclitaxel encapsulated into the bio-NCP by recalling the concept of the van Hove self-correlation function, $G_s(\vec{r}, t)$, previously described as the probability of finding an atom at the origin at time 0 and at position \vec{r} at time t . As shown in Figure 2.4, for a infinitely confined group (a) the probability distribution remains constant with time and in the reciprocal space, in which the neutron data is collected, leads to a Dirac function since the second term in Eq.(2.16) becomes 0. In less confined situations (b) a molecule is free to move and the variation of the probability distribution with time leads to a Lorentzian function in the reciprocal space and the reduction on the confinement leads to gradually broader Lorentzians (c). The same concept can be applied to different temperatures in the experiment, were low temperatures lead to a “frozen” while higher temperatures lead to “flexible” ones.

Inelastic neutron scattering (INS) and Density functional theory (DFT) calculations

Inelastic neutron scattering (INS) is often called as neutron spectroscopy and is mainly, which can be formed by fast hydrogen vibrational motions. The vibrations of molecules can be divided in internal molecular vibrations (periodical stretching and bending motions), external librations (slight rotations) and external translational vibrations.

Neutron spectroscopy presents some features that allows for the users to have insights of a molecule that cannot be achieved by other spectroscopic techniques. For example, there are no selection rules due to it neutron–nucleus interaction and neutrons can be produced with wavelengths of the order of interatomic spacings thus providing information not only about the dynamics of a molecule, but also of its structure. As well as in other spectroscopic techniques, an INS investigation consists of the determination of characteristic frequencies of motion of a given material and the results are basically spectra with several peaks, which broaden with increasing temperature due to the Debye-Waller factor. However, it is necessary to understand the origin of each of the observed peaks, which can be done with the support of Molecular dynamics (MD) calculations.

MD are based on the numerical integration of the classical equations of motion of a collection of particles and can provide theoretical INS spectra of a molecule. Most importantly, the main contributions for each peak in such a spectra can be assigned. The INS turns out to be the a perfect match for MD since both methods cover the same time and space domains (from 0.1 fs to 10 ns, and 1 – 100 Å), and neutrons probe the atomic nuclei, which are the basic objects in MD simulations (Tsapatsaris et al., 2014). In this work we have used Density Functional Theory (DFT) method, based on an iterative process briefly described in Figure 2.5. Although INS and DFT calculations were proven to be extremely important in the final steps of this work, their deep understanding is part of my post-doctoral research.

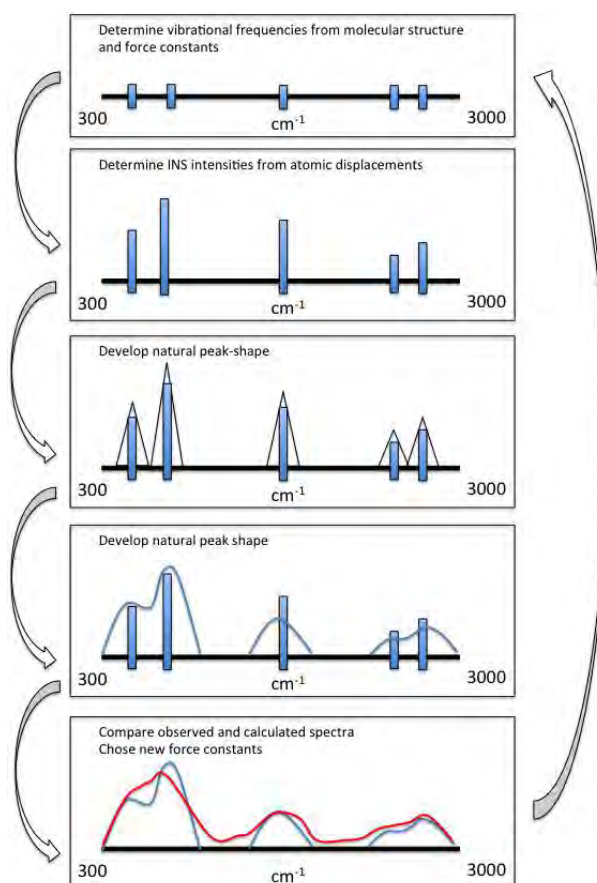


Figure 2.5. Brief description of the DFT method used in this thesis as a support for the INS data interpretation. Adapted from (Kearley, 1992).

2.2. Basic principles of Near-Edge X-Ray Absorption Fine Structure (NEXAFS) and Scanning Transmission X-ray Microscopy (STXM)

The technique of NEXAFS can be considered as a recent application of X-ray scattering whose development has been accelerated with the advent of several synchrotron facilities. NEXAFS uses soft X-rays in the range between 250 eV – 2000 eV and is very suitable to investigate surface scattering molecules and their orbitals. As the name of the technique suggests, it deals with the absorption of X-rays at energies close to the edge of the ionization of an inner orbital shell (K and L shells) of the components in a given sample. Due to the absorption of the X-ray photons, an electron in this shell is excited, and by following the subsequent relaxation of this state, the atomic fine structure can be determined.

This technique is often used to analyze materials constituted by low-Z atoms, since the electrons in the K-shell are easily excited (K-edge measurement). This fits perfectly to the investigation of the encapsulated drugs, used in this work in Chapter 4, or polymeric blends (Collins et al., 2010). However, NEXAFS can also be very useful in studies involving heavier atoms, for example Fe, Mn and Zn, where the L-shell can be excited instead of the K-shell.

In a typical NEXAFS experiment, the sample is hit by X-ray photons, which are absorbed and cause an electron from an inner orbital shell either to be excited and released from the atom (photoelectron) or to be excited to an unoccupied orbital. This last excited state comes to relaxation by different ways: an electron jumps from a higher orbital shell to fill the hole either by emitting a fluorescent photon or by emitting a so-called Auger electron. A fluorescent photon is a photon that has lower energy (and higher λ) than the absorbed photon (due to conservation of energy), while an Auger electron is an electron from an outer orbital shell, which is freed from the atom by absorbing the energy liberated by the relaxation jump of the electron (Stör, 2003). The transition from excited state to relaxed state can be seen in Figure 2.6.

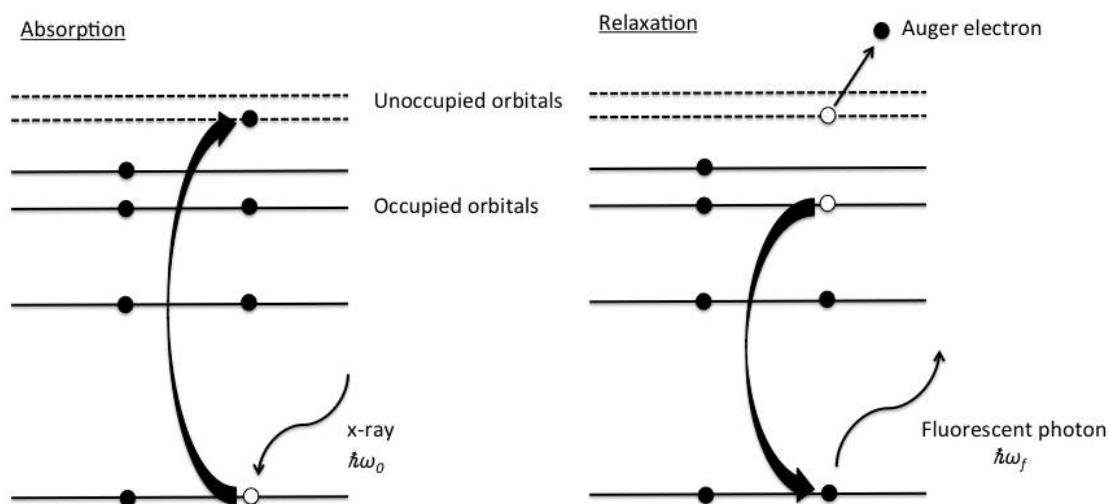


Figure 2.6. The mechanism behind NEXAFS, with the absorption of a photon, which results in the emission of a fluorescent photon or an Auger electron adapted from Watts, Thomsen and Dastoor (2006).

A NEXAFS spectrum is obtained by measuring the intensity of transmitted photons in comparison to the intensity of those sent to the sample, by monitoring the photoelectrons, the Auger electrons or the emitted fluorescent photons. However, considering the low probability for low Z atoms to produce fluorescent photons, the need for energy discrimination in a small range, typical of Auger electrons (whose probability of emission is inherently higher for low Z atoms) and the high background usually generated by the detection of all the photoelectrons, a good alternative for NEXAFS experiments is to use an energy threshold in order to detect only a part of the emitted electrons. This method is called Partial Electron Yield (PEY) and is a midway between the detection of Auger and photoelectrons (Watts, 2005).

Regarding the analysis of NEXAFS spectra itself, the first step to be performed is the data normalization by measuring a background signal from the sample holder, which will be subtracted from the sample signal. After the normalization, the spectra are ready to be interpreted however this task can be rather challenging. For instance, when large molecules, such as the PTX used in this work, are investigated, different bonds (double C bonds or C-H bonds) can be excited at the same time. As a consequence, some of the resonance peaks are shifted and a convolution of peaks from different orbitals is obtained. Therefore, even if NEXAFS is considered a powerful tool to describe the presence and orientation of different groups into a molecule, the resulting data might be very intricate and only a few conclusions can

be made.

By using the same experimental apparatus one can also obtain information from the Scanning Transmission X-Ray Micro-spectroscopy (STXM). In such a technique, the transmission of photons through a surface at a certain fixed energy is measured and an image is created with the optical density being shown by a gray scale where black denotes total absorption and white denotes total transmission (Watts, Mcneill and Raabe, 2012). After measuring the NEXAFS spectra for each component of the analyzed sample, several x-rays transmission images are taken using selected energies, which have typically the values of the absorption peaks in the NEXAFS spectra. Therefore, each one of these images is able to highlight a specific component in the sample. This approach is represented in Figure 2.7.

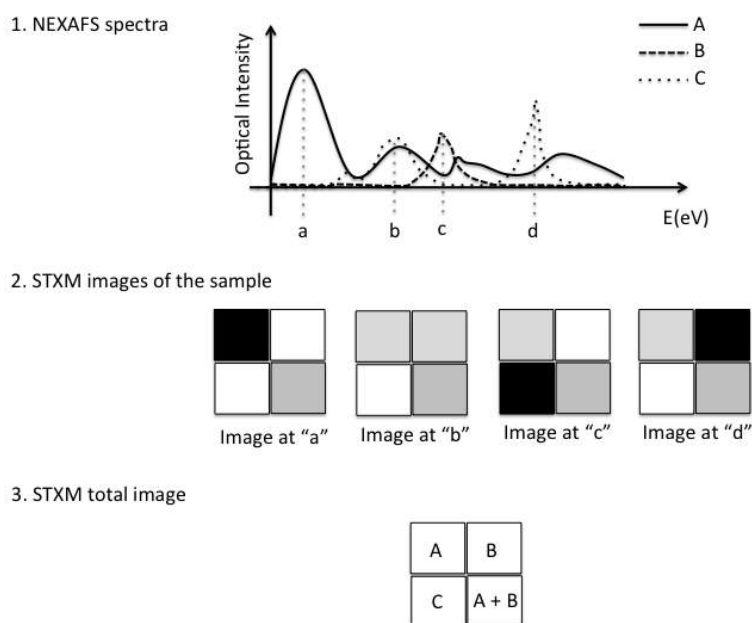


Figure 2.7. Schematic procedure of a STXM experiment. The top part shows the spectra collected with NEXAFS, the middle part shows the creation of images at different energies while the bottom part shows the map of the sample created from the different images.

Chapter 3

Synthesis of Mn-Zn ferrite magnetic nanoparticles (MNPs) and surface modification for obtaining the bio-nanocomposite (bio-NCP) – Paper II

3.1. Introduction to Paper II

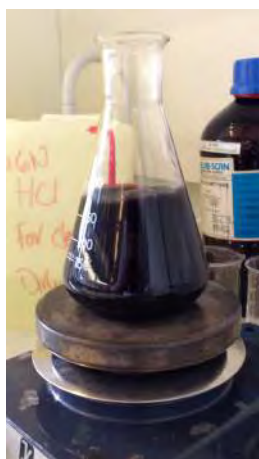
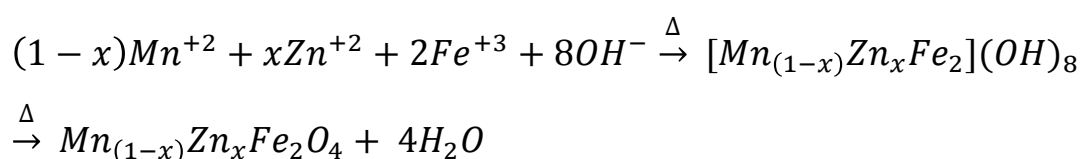
In this chapter we detail the scientific concepts that were used in the development of Paper II (Martins et al., 2014b). The Mn-Zn ferrite magnetic nanoparticles ($\text{Mn}_{(1.30-x)}\text{Zn}_x\text{Fe}_{1.70}\text{O}_4$), MNPs, were synthesized by the co-precipitation method and the influence of different synthesis parameters on the nanoparticles properties were evaluated. Following these steps the nanoparticles were coated with the bio-polymer chitosan, which has then been modified with hydroxyapatite nanocrystals leading to a final material referred as bio-nanocomposite (bio-NCP). The characterization of the materials was performed combining medium infrared spectroscopy, x-rays and neutron (diffraction) scattering.

3.2. Experimental details

In this section, details of the synthesis procedures used to achieve the bio-NCP are described. The synthesis details provided here are also relevant for a better understanding of Chapter 4. A brief description of the experimental methods used in the materials characterization is also given.

3.2.1. Synthesis of the Mn-Zn ferrite nanoparticles: the co-precipitation method

The co-precipitation method is based on the addition of metal salts in alkaline solution (NaOH solutions in this work) at $\sim 100^\circ\text{C}$ and further precipitation of such metals in the form of hydroxides. As denoted by the reaction shown below, the hydroxides are subjected to dehydration processes leading to a black suspension of magnetic nanoparticles, Figure 3.1(a), which can be collected with a magnet, Figure 3.1(b), and washed to be suspended in aqueous dispersions with neutral pH (Zhao et al., 2009).



(a)



(b)

Figure 3.1. After the co-precipitation reaction a black suspension of magnetic nanoparticles is obtained (a). The nanoparticles are collected with a magnet (b), and washed to be suspended in aqueous dispersions with neutral pH.

This method can be, in principle, considered simple and suited for nanoparticle preparation. However, due to the different solubilities of each metal hydroxide ($\text{Mn(OH)}_2 > \text{Zn(OH)}_2 > \text{Fe(OH)}_3$) (Brauer, 1965), and also to the distinct thermodynamical behavior of each element, which leads to different rates of incorporation into the spinel structure ($\text{Fe} > \text{Mn} > \text{Zn}$) occurs (Kovtunenکو, 1997). Therefore, the properties of the obtained material can be deeply affected by synthesis parameters, such as reaction time and $[\text{OH}^-]$ concentration into the alkaline solution.

In Paper II we have assumed Mn-Zn ferrites with nominal composition $\text{Mn}_{(1.30-x)}\text{Zn}_x\text{Fe}_{1.70}\text{O}_4$. For the co-precipitation synthesis $\text{Mn(NO}_2)_2$, $\text{Zn(NO}_2)_2$ and FeCl_3 (Sigma-Aldrich) were used as starting salts. The “x” value, or the Zn content, was taken as 0.15, 0.20, 0.25 and 0.30 and the ferrite nanoparticles were obtained after 120 min of reaction in 300mL of 0.1 mol L⁻¹ NaOH boiling solutions. Moreover, the influence of the NaOH concentration was also investigated by synthesizing Mn-Zn ferrites with $x = 0.25$ in 300mL of boiling NaOH solutions for with the following concentrations: 0.10 mol L⁻¹, 0.5 mol L⁻¹ and 1.0 mol L⁻¹. The reaction time was 120 min in all cases. Finally, the influence of the reaction time on the nanoparticles was evaluated by synthesizing Mn-Zn ferrites in 300mL of boiling 0.10 mol L⁻¹ NaOH solutions for 0, 30 and 120 min.

3.2.2. Coating the magnetic nanoparticles with the polymer chitosan: reverse micelle technique.

The reverse micelle technique is based on the formation of a water-in-oil micelle, in which a polymeric shell traps the magnetic nanoparticles. To this procedure the chitosan molecules are first protonated after being dissolved in acetic solution and an aqueous suspension of ferrite nanoparticles in neutral pH is added to this solution and subjected to stirring. Since the MNPs present negative surface charge at neutral pH, as discussed in Paper V, they can readily interact with the protonated chitosan and a first encapsulation step takes place. The chitosan + MNPs suspension is then added to an organic solution of paraffin oil and oleic acid and, by means of a vigorous stirring, a water-in-oil micelle is formed with MNPs in a core surrounded by chitosan. The final step of the encapsulation is the so-called crosslinking reaction, which is performed in order to provide mechanical and

chemical stability to the polymeric capsule. The crosslinking agent used in this work is glutaraldehyde, whose reaction with chitosan is shown in Figure 3.2.

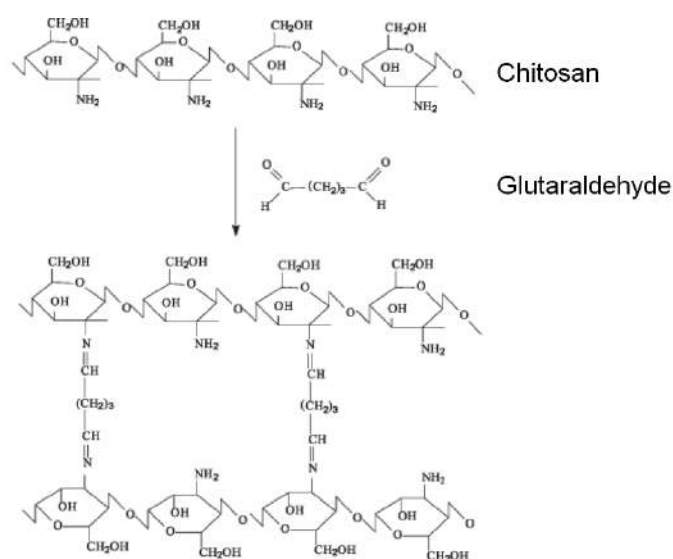


Figure 3.2. Crosslinking reaction of chitosan with glutaraldehyde, adapted from Gonçalves et al. (2005).

In a standard procedure, 20 mg of chitosan were dissolved in acetic solution (4%) and, to this solution, 40mg of ferrite was added (ferrite/chitosan mass ratio 2:1). This mixture was stirred for 30 minutes and it was added to the solution constituted by 50 mL of paraffin oil (Sigma-Aldrich) and 3.12 mL of oleic acid (Sigma-Aldrich). The mixture was vigorously stirred until a emulsion was formed. To promote the crosslinking reaction, 0.1 mL of a 25% glutaraldehyde solution was added to the emulsion and stirred for 2 h. The coated nanoparticles were then washed with chloroform, ethanol and acetone and dried at room temperature for 48h.

3.2.3. Modification of the polymeric chitosan surface with hydroxyapatite nanoparticles: mimetization method

After coating the magnetic nanoparticles, the next step for the bio-NCP preparation was the surface modification with hydroxyapatite by a mimetization method. To do so, the OH and NH₂ groups of the polymer should not be strongly associated to water molecules, since their free electrons are preferred sites to adsorb Ca²⁺ that will further combine to PO₄³⁻ and promote the hydroxyapatite nanocrystals growth. As presented in the scheme of Figure 3.3, the coated nanoparticles are

dispersed in a CaCl_2 solution whose high ionic concentration promote a diffusive motion of water molecules from the nanoparticle surface to the solution and allows for Ca^{2+} adsorption on the groups with free electron pairs (OH and NH_2). The period necessary for the combination of Ca^{2+} with the chitosan surface is referred as the “aging period”. Sequentially, PO_4^{3-} ions are added to the reaction and tend to combine with the Ca^{2+} ions adsorbed onto the chitosan surface in order to form the hydroxyapatite nanocrystals (Martins et al., 2014b).

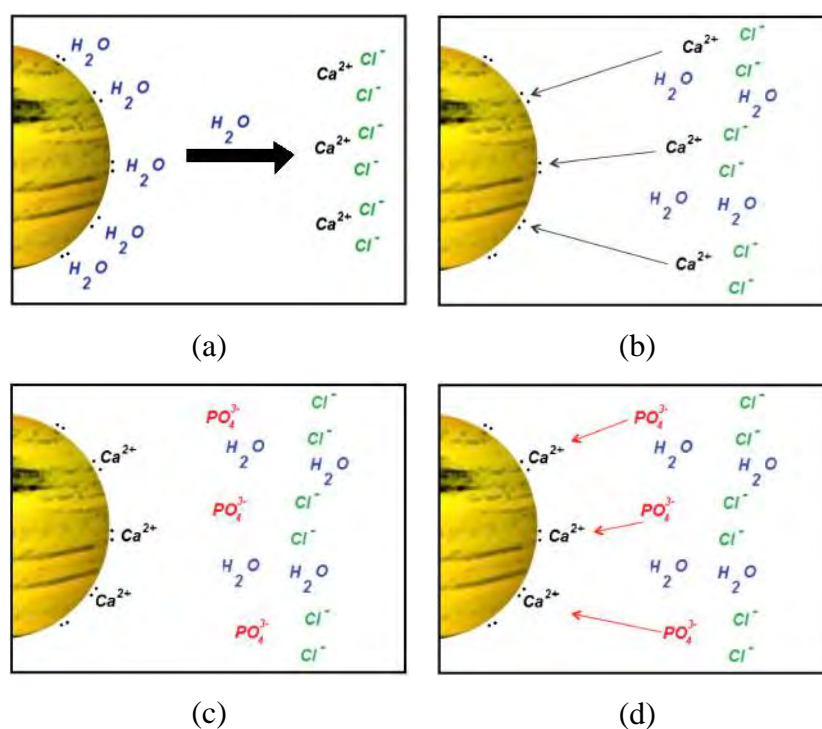


Figure 3.3. Representative scheme of mimetization technique used to modify the coated nanoparticle surface with hydroxyapatite nanocrystals. The coated nanoparticles are dispersed in a CaCl_2 solution whose high ionic concentration causes a diffusive motion of water molecules from the nanoparticles to the solution (a). Then, the free electrons groups (OH and NH_2) are released for the Ca^{2+} adsorption (b and c). Sequentially, PO_4^{3-} groups are added to the reaction and interact with the Ca^{2+} leading to the hydroxyapatite nanostructures (d).

In Paper II, 60mg of the coated nanoparticles were subjected to the hydroxyapatite modification and the influence of both, aging and mimetization times, were studied for Ca/P molar ratios equal to 1.50 and 1.67 and using a fixed value of 2 for chitosan:hydroxyapatite mass ratio. The aging periods (Ca^{2+} adsorption) were

varied as 1h, 2h, 4h, 12h and 24h, with the further mimetization time (PO_4^{3-} reaction) fixed as 4h. To study mimetization time, the aging time was fixed as 1h the mimetization was carried out for 1h, 2h, 4h, 12h and 24 h. Finally, the influence of chitosan:hydroxyapatite mass ratio was studied under aging and mimetization times of 1h and 4h, respectively. The tested chitosan:hydroxyapatite mass ratios were 1, 2 and 4.

3.2.4. Details on the characterization techniques

The crystalline phases of the ferrite nanoparticles as well as the bio-NCP were investigated by X-ray powder diffraction (XPD) using 10KeV ($\lambda = 1.24\text{\AA}$) synchrotron radiation in the D10B-XPD beamline at the Brazilian Synchrotron Light Laboratory (LNLS, Brazil), Figure 3.4(a). The samples were placed in flat aluminum holder, Figure 3.4(b), and a MYTHEN X ray detector was used. The structure refinements were performed using the GSAS software package (Larson and Von Dreele, 2004) and input parameter data were those from the Inorganic Crystal Structure Database (ICSD).

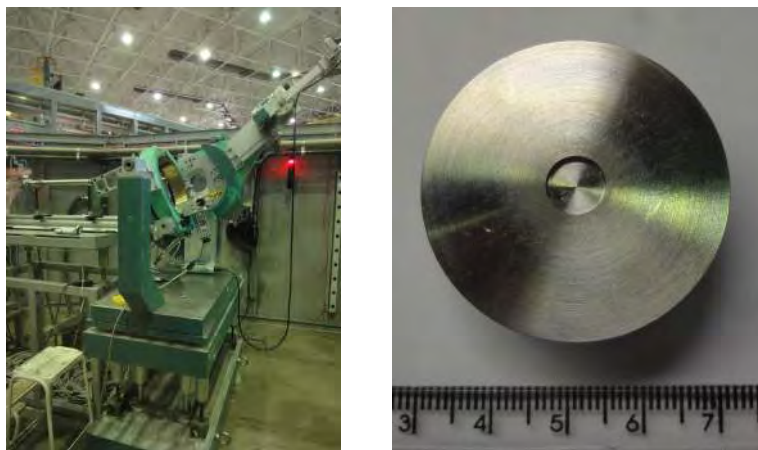


Figure 3.4. D10B-XPD beamline at the Brazilian Synchrotron Light Laboratory (LNLS, Brazil) (a) and aluminum holder used for powder samples (b).

The presence of organic groups in the bio-NCP, as well as their hydration level, were further characterized by Fourier Transformed Infrared Spectroscopy (FTIR) using a Nicolet spectrometer, Nexus 670, using DRIFT accessory, in the Chemistry Department – IBB (UNESP).

Morphological analysis was performed by Scanning Electron Microscopy (SEM) using a FEI microscope, Quanta 200 of the Microscopy Center – IBB (UNESP) and finally the magnetic response (M x H curve) of the selected nanocomposite was studied at room temperature using a Quantum Design Magnetometer (VSM) available in the LaMMB – MagLab (HZB – Germany).

3.3. Results and discussion: a bio-NCP with high magnetic response at room temperature

3.3.1. Structural characterization of the MNPs

The final aim of this part of the work was to investigate the influence of the synthesis parameters in the production of MNPs with nominal composition $Mn_{(1.30-x)}Zn_xFe_{1.70}O_4$ in order to obtain a final bio-NCP with high magnetic response. Initially, samples with different compositions ($x = 0.15, 0.20, 0.25$ and 0.30) were obtained and investigated by XPD whose data allow for two main observations:

- i) for $x = 0.30$ a considerable amount of contaminant phases are noted and;
- ii) increasing “x” from 0.15 to 0.25 lead to a reduction of both cell parameter and crystallite size on the nanoparticles.

The composition of the MNPs was then fixed as $Mn_{1.05}Zn_{0.25}Fe_{1.70}O_4$ (i.e $x = 0.25$) and the influence of the NaOH concentration into the precipitant alkaline solution in the nanoparticles structures was evaluated. The materials were precipitated in 1 mol L^{-1} , 0.5 mol L^{-1} and 0.1 mol L^{-1} NaOH solutions and the XPD data indicated that the increase of NaOH concentration to 1 mol L^{-1} leads to serious damage to the crystalline structure. This result was explained based on the high ionic strength into the 1 mol L^{-1} solution, which reduces the nanoparticles surface energy by cations adsorption and prevents their coalescence and growth (Vayssieres et al., 1998). Meanwhile, nanoparticles with a satisfactory crystallization degree were obtained after precipitation on 0.5 mol L^{-1} and 0.1 mol L^{-1} NaOH solutions.

As a next step, the influence of the reaction time in the synthesis of $Mn_{1.05}Zn_{0.25}Fe_{1.70}O_4$ nanoparticles in 0.1 mol L^{-1} NaOH solutions was evaluated. The samples were allowed to react for 0, 30 and 120 min, and the crystallite size and cell parameter, as expected, increase from 0 to 30 min but only slight changes in the XPD patterns are noted between 30 min and 120 min. The sample with nominal composition $Mn_{0.75}Zn_{0.25}Fe_2O_4$ obtained after 120 min reaction into a 0.1 mol L^{-1}

NaOH solution has been chosen as the standard sample for the following tests. This sample was then investigated by means of neutron powder diffraction and the composition into the spinel structure of the ferrite was determined by structure refinement and is in good agreement to the nominal composition. A representative scheme of the spinel structure, characteristic of Mn-Zn ferrites is shown in Figure 3.5.

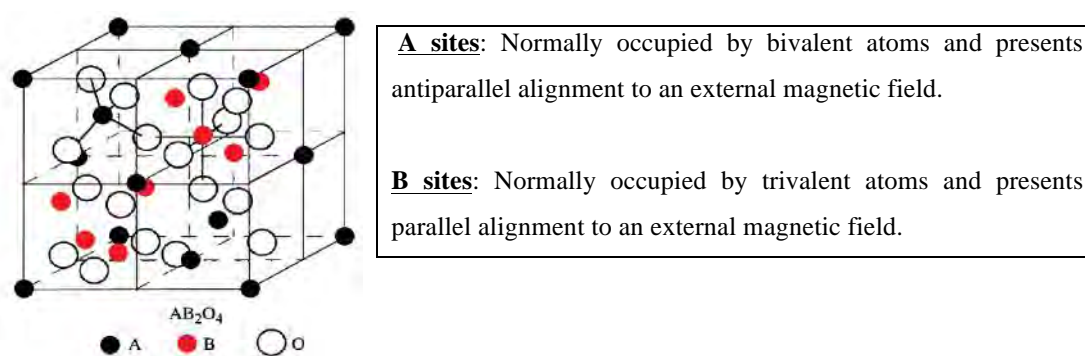


Figure 3.5. Representative scheme of the spinel structure, characteristic of Mn-Zn ferrites

3.3.2. Verifying the success of chitosan coating and surface modification with hydroxyapatite nanoparticles

Subsequently, the selected MNPs were coated with chitosan whose presence into the sample was confirmed by FTIR. Additionally, XPD data showed that the encapsulation causes no changes to the ferrite structure.

After coating the magnetic nanoparticles, the next step for the bio-NCP preparation was the surface modification with hydroxyapatite by aging and mimetization procedures. The effectiveness of this method was monitored by FTIR analyses, in which one can observe shifts on OH stretch bands between 3750 and 3250cm^{-1} where the blue shifts indicate a reduction in the amount of water (Madejova, 2003). Besides, the evolution on PO_4^{3-} bands between 1100 and 800cm^{-1} , which are a good indicative of hydroxyapatite presence in the samples. As presented in Figure 3.6(a), we have shown that by using a molar ratio $\text{Ca/P} = 1.67$ and a mass ratio $\text{chitosan/hydroxyapatite} = 4$ the signals from the hydroxyapatite as well as the sample dehydration increase with aging time, while no significant changes are noted when only the mimetization time is increased.

Controlling the hydroxyapatite modification degree onto the composite surface, and consequently the final bio-NCP size, was also successfully done by increasing the chitosan/hydroxyapatite mass ratio from 1 to 4 into the synthesis process, which allowed obtaining the bio-NCP in considerable shorter reaction times (1h of aging and 4h of mimetization) with different size distributions. Finally, the transmission electron microscopy (TEM) image presented in Figure 3.6(b) was taken for the bio-NCP obtained with chitosan/hydroxyapatite = 4 and 1h of aging and 4h of mimetization, which was selected as our standard condition. Note that the d-spacing of the particle in the surface, highlighted in the inset, is $5.5(5)\text{\AA}$, which is in agreement with the (101) hydroxyapatite plane according to the ICSD-26204 file.

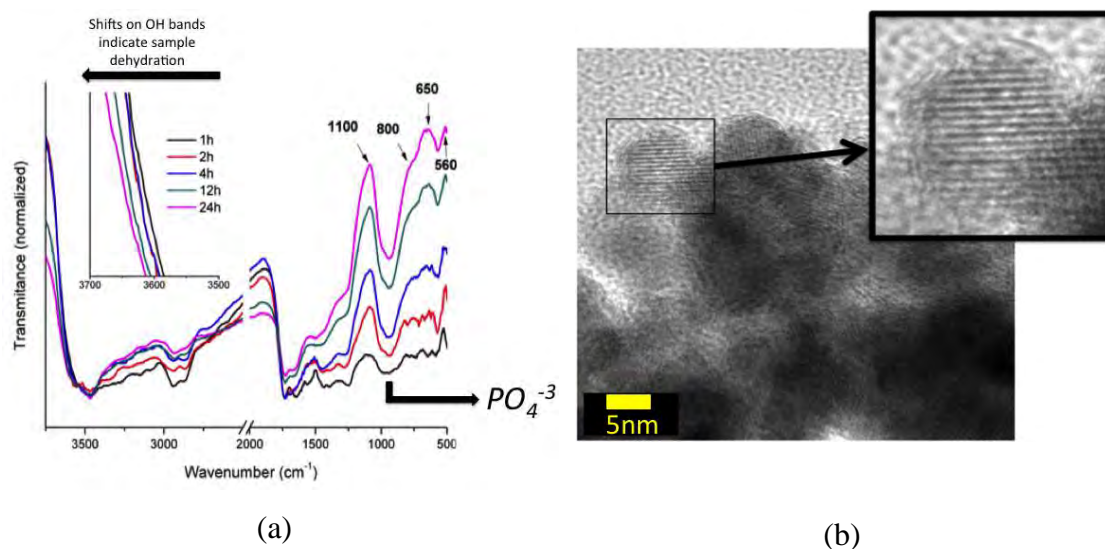


Figure 3.6. (a) FTIR spectra for the bio-NCP prepared with different aging times for the hydroxyapatite nanocrystals growth. The PO_4^{-3} band increases with the aging time and the shifts on OH bands indicate the importance of hydration degree in the sample for the hydroxyapatite nanocrystals growth. In (b), a TEM image of the surface of a bio-NCP prepared with molar ratio Ca/P = 1.67, mass ratio chitosan/hydroxyapatite = 1 and aging and mimetization times of 1h and 4h respectively. The d-spacing of the particle in the surface is in agreement with the (101) hydroxyapatite plane.

3.4. Conclusions and outline

Paper II described the synthesis of a magnetic bio-NCP to be used in target treatment of tumors and possibly on their diagnosis. That work defined the methodological approach to be used for obtaining this bio-NCP, which is based on magnetic nanoparticles of Mn and Zn ferrite coated with the polymer chitosan and surface modified by hydroxyapatite nanocrystals. The magnetic nanoparticles were obtained by a co-precipitation method and the influence of various parameters of this reaction in the nanoparticles structural properties were investigated allowing for establishing the optimum synthesis condition. When coated with a biocompatible polymer and modified with hydroxyapatite nanocrystals, the structure of the Mn-Zn ferrite is not affected by the polymeric encapsulation, highlighting the great stability of such a compound in comparison to Fe_3O_4 . The latter, is often used in biomedical applications however its properties are highly affected by polymeric coatings, as show in the XPD of Figure 3.7 for such a compound coated with chitosan where the arrows indicate the formation of secondary phases into the sample.

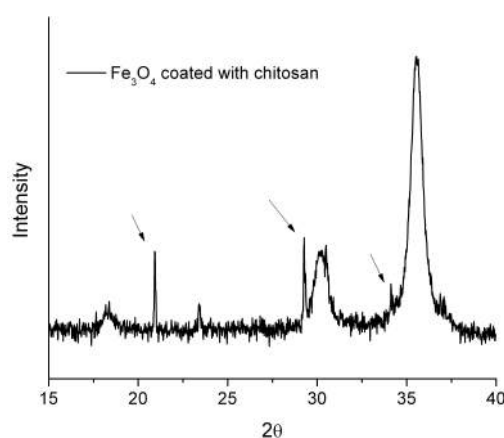


Figure 3.7. XPD pattern for Fe_3O_4 coated with chitosan. The arrows indicate the formation of secondary phases into the sample due to the presence of the polymer.

We have also presented in this paper the modification of the polymer with hydroxyapatite nanoparticles and discussed on the important role played by the hydration degree onto the particle surface. These results are key for to the success of the nanocrystals growth as well as the reaction with Ca^{+2} ions rather than with PO_4^{3-} .

Chapter 4

Encapsulation of the anti-tumor drug paclitaxel (PTX) into the bio-nanocomposite (bio-NCP) – Papers III and IV.

In this chapter we discuss on the results of Papers III (Martins et al., 2014c) and IV, which are focused on the characterization of paclitaxel (PTX) encapsulated into the bio-NCP as well as spectroscopic and thermal analysis of the pure drug (as purchased). These papers are related to the development of a methodology to study encapsulated drugs, consisting of a combination of thermal analysis, imaging, scattering techniques (light, X-rays and neutrons) and DFT calculations. Furthermore, Paper IV presents the first biological characterization of the bio-NCP, which consists of in-vitro tests with defense (macrophages) and cancer cells (colon and lung). Some of the results presented in Paper IV were obtained during the bachelor work of the student Rosanna Ignazzi (Ignazzi, 2014).

4.1. Does encapsulation modify the dynamics of a drug?

Drug encapsulation is currently the most used approach by pharmacology and biophysics as an attempt to reduce pharmacological side effects, such as low water solubility and toxicity in healthy cells. However, questions regarding how the encapsulation system can change the molecular dynamics of the encapsulated drug as

well as its mechanism of action and effectiveness are often raised. Considering the PTX molecule and its malleability depending on chemical environment, several research groups have reported in the last decades considerable differences in conformation and biological activity depending on dispersion media, ligands and humidity level of the drug. For example, Mastropaolo et. al (1995) investigated PTX single crystals prepared by dispersion in dioxane, water and xylene solutions. Their results showed that the crystals presented similar crystalline arrangements, with a $P2_1$ space group, but distinct molecular conformations. The differences were mainly related to the C13 side chain, considered the active part of the molecule. Harper et. al (2005) described a PTX powder sample, free of any organic solvents, arranged in a $P2_12_12_1$ space group. Therefore, it is clear that the PTX may acquire different molecular conformations or even crystallographic arrangements by simply changing its chemical environment. In the case of encapsulated drugs, such changes can be even more severe considering the various possible drug-encapsulation interactions. Therefore, a careful investigation in order to allow for designing carrier systems with reduced effects in the drug molecule is crucial.

Investigating encapsulated drugs is not be an easy challenge, especially considering a complex encapsulation system such as the bio-NCP. For example, infrared spectroscopy is not able to deeply penetrate into the encapsulation shell, composed by the polymer and the by ceramic hydroxyapatite crystals. Dielectric relaxation spectroscopy does not provide information about methyl groups re-orientation, which play a great role in the PTX dynamics. Additionally, the presence of MNPs into the composite limits the applications of Raman spectroscopy, since the sample becomes black (as shown in Figure 4.1), while nuclear magnetic resonance might be subjected to depolarization effects. Another aggravating factor, both Raman and infrared spectroscopies are subjected to selection rules that often lead to spectral information loss.

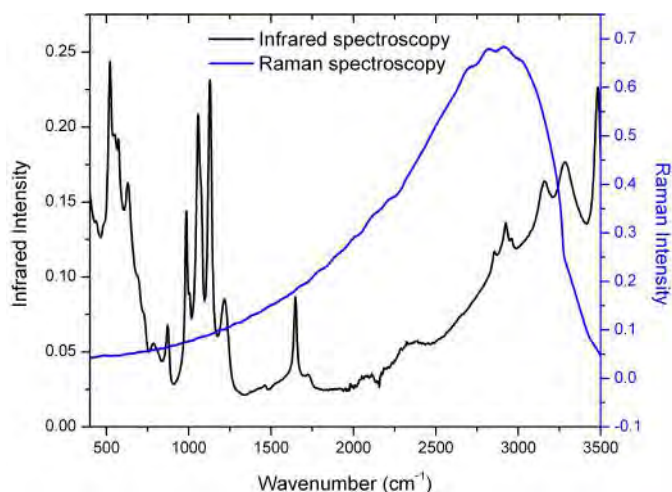


Figure 4.1. Comparison of Raman and infrared spectroscopy data for a same sample of the bio-NCP. No information is provided by the Raman data since the sample is black.

Considering these issues, inelastic neutron scattering (INS) is a virtuous approach since the relative simplicity of the neutron–nucleus interaction implies that no selection rules exist in neutron scattering and, in principle, all modes can be observed. Moreover, due to the exceptionally high incoherent scattering cross-section of hydrogen compared to any other elements, displacements involving hydrogen atoms dominate the vibrational density of available neutron states (Tsapatsaris et al., 2013). Furthermore, the INS data interpretation, can be obtained by combining such experimental results with theoretical data obtained by molecular dynamics simulations (MD). MD subject atoms to Newton’s equation of motion and their interactions are obtained from a force field, which is a parameterization of the potential energy surface of the system (Marry et al., 2011). Neutron scattering methods are the most relevant experimental reference for MD since both methods cover the same time and space domains (from 0.1 fs to 10 ns, and 1 – 100 Å), and neutrons probe the atomic nuclei, which are the basic objects in MD simulations.

4.2. The Paclitaxel (PTX) molecule

PTX is a diterpene, whose properties against several kinds of tumors have been extensively reported (Wang, Ho and Lim, 2010; Yu and Pishko, 2010; Camirand et al., 2013). The action of such a drug against cancer cells is given by the molecule

bonding to the cell microtubules, which leads to the stabilization and inhibition of cell development and replication (Mastropaolo, et. al 1995).

The PTX molecule presented in Figure 4.2 is formed by 11 asymmetric centers and a rigid conformation with three cycles A, B and C, and an oxetane cycle, often called as the D cycle. Among the asymmetric centers, a flexible side chain bonded to the C13 of the terpene system is, according to several works, essential to the biological activity of the drug (Williams, Moyna and Scott, 1996).

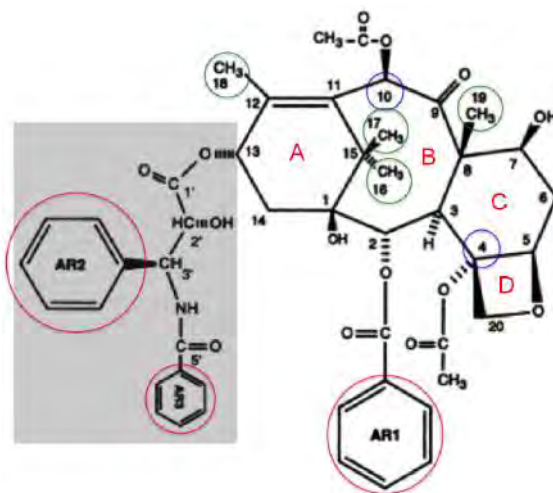


Figure 4.2. Skeletal formula of Paclitaxel. The highlighted area shows the side chain bonded to C13 and the circles highlight C-atoms cited along the text. Phenyl (AR1, A2 and AR3) are highlighted in red, methyl groups in green and carbons bonded to acetyl groups in blue. Adapted from Mastropaolo et al., 1995.

4.3. Experimental details

4.3.1. Encapsulation of PTX into the bio-NCP

To encapsulate PTX into the bio-NCP the double micelle method was used (Lv et al., 2011). Basically, one can consider such a method as an adaptation of the reverse micelle procedure used to coat the ferrite magnetic nanoparticles (MNPs) with chitosan. To include the PTX into the composite, a dichloromethane solution containing the drug was added to the chitosan + MNPs dispersion together with a surfactant, Tween 80, allowed to stir for 30 min and oil-in-water micelles have been formed. Then, similarly to the procedure described in Section 3.2.2, the dispersion was added to an organic solution, vigorously stirred resulting in a water-in-oil micelle formed with MNPs together with the PTX in a core surrounded by chitosan. A

crosslinking reaction was performed and the sample was then kept at 70⁰C for 12h to ensure the dichloromethane elimination. The resulting material was washed, dried and subjected to the surface modification with hydroxyapatite using the conditions set as standard in Chapter 3. The sample containing the encapsulated PTX is hereafter referred as bio-NCP + PTX. The bio-NCP studied in Papers III and IV were prepared by following the steps describe above, including the addition of the dichloromethane solution.

4.3.2. Details on the characterization techniques

a) Paper III

The crystalline phases of PTX (as purchased) were investigated by X-ray powder diffraction (XPD) using synchrotron radiation ($\lambda=1.24\text{\AA}$) at the D10B-XPD beamline of LNLS - Brazil.

TGA and DSC analyses were performed in air using a TG209 F1 Iris ASC, NETZSCH and a DSC (Q100)-TA instrument, respectively, available at the Physics Department of the Chalmers University of Technology. The measurements were carried out between 120K and 473K to evaluate the solid-state properties of PTX, bio-NCP, bio-NCP + PTX and a pure chitosan (as purchased).

PTX, bio-NCP + PTX and the bio-NCP were further studied by Fourier transformed infrared spectroscopy (FTIR) in a Bruker Spectrometer at room temperature between 400 and 4000 cm^{-1} using an Attenuated Total Reflectance (ATR) accessory also in the Chalmers University of Technology.

QENS and INS data were obtained with an incident wavelength $\lambda=5\text{\AA}$ ($\Delta E=100\mu\text{eV}$) using the FOCUS spectrometer (PSI -Switzerland), shown in Figure 4.3(a). INS data were collected at IN4 (ILL-France) at 10K with incident wavelengths of $\lambda=2.2\text{\AA}$ and 1.1\AA . In both cases, the samples were mounted using the slab geometry inside of aluminum containers, Figure 4.3(b), with a calculated normal beam transmission 0.75. At FOCUS, PTX was analyzed at 100K, 150K, 200K, 250K and 300K, while the bio-NCP and bio-NCP + PTX were analyzed at 100K, 200K and 300K. In both experiments, a vanadium run was used to determine the resolution function and to calibrate the detectors efficiency. To analyze the QENS data, the Bragg reflections were removed and the spectra were fitted using the 1D PAN:Peak

Analysis software (Azuah et al., 2009). The temperature dependence of the elastic intensity in the PTX data was also analyzed to identify relevant dynamical transitions. The INS data were transformed into the generalized density of vibrational states using the software LAMP (Richard et al., 1996).

Density Functional Theory (DFT) calculations for the PTX were performed to support the neutron scattering data analysis in collaboration with Dr. Juergen Eckert at the University of South Florida.

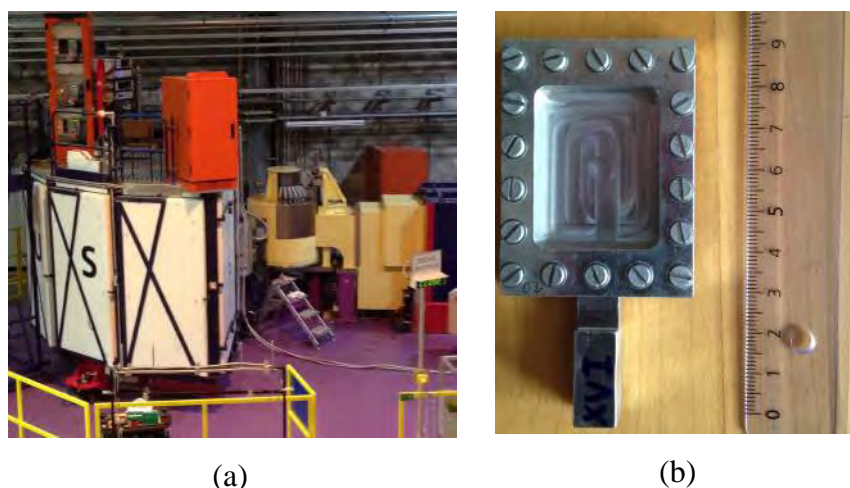


Figure 4.3. FOCUS spectrometer at PSI –Switzerland (a) and aluminum containers with slab geometry

b) Paper IV

Near Edge X-ray Absorption Fine Structure (NEXAFS) data were collected at the PolLux beamline (PSI –Switzerland) whose scheme is presented in Figure 4.4 (a). The data were collected in the C K-edge energy range (250 to 350eV) for PTX, bio-NCP, bio-NCP + PTX and pure chitosan mounted in silicon nitride membranes, as shown in Figure 4.4(b).

Scanning Transmission X ray Microscopy (STXM) images were also collected at PolLux using X-rays with energies where each of the bio-NCP + PTX components presented maximum absorption in the NEXAFS spectra as: 283eV, 286eV, 300eV, 320eV and 347eV. One image was also collected with X-rays with 275eV to be used as a background image, since no absorption is detected in this spectral region. The

images were uploaded together with the NEXAFS spectra to the software axis2000, aligned and superposed in order to create a composition map.

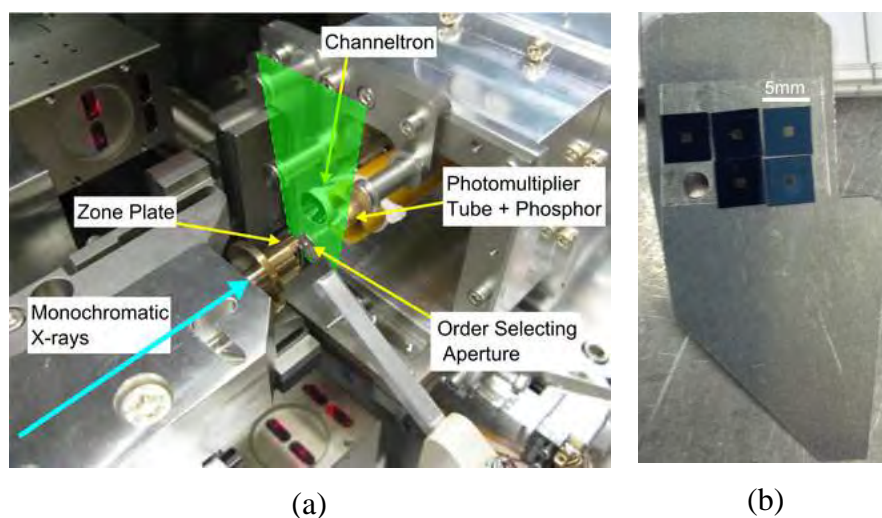


Figure 4.4. Schematic view of the PoLux beamline at PSI (a) and samples mounted in silicon membranes in order to perform both NEXAFS and STXM analyses.

INS data were collected using the FDS spectrometer at the Los Alamos Neutron Science Institute (USA). In this case, PTX, bio-NCP and bio-NCP + PTX were investigated at 10K to minimize the Debye-Waller factor (i.e. the contribution from temperature to the vibrations).

In order to get insight from the drug after being released in water, 20mg of the bio-NCP+PTX sample was dispersed in aqueous media for 7 days to allow the PTX release and then analyzed by infrared spectroscopy (FTIR) using a Nicolet spectrometer, Nexus 670. The peaks in the INS and FTIR spectra were indexed based on the DFT calculations.

For the in vitro assays with Human monocytes and HCT116 (colon cancer) and 3LL (lung cancer) human monocytes were isolated from 40 mL of peripheral blood of healthy donors collected with heparin. Blood sample was diluted with equal volume of phosphate buffered salt solution (PBS) and mononuclear cells were obtained by centrifugation on a gradient of Ficoll-Isopaque solution ($d=1,077$ g/mL) for 30 min at $900 \times g$. Mononuclear cell suspension was washed three times with fresh RPMI 1640 culture medium, and suspended with PBS containing 5% of fetal bovine serum (FBS) and centrifuged on a Percoll 51% gradient in order to separate most of monocyte (interface) from lymphocytes (pellet).

This monocyte-rich suspension as well as HCT116 3LL cells were washed three times with RPMI 1640, supplemented with 10% FBS, 1% nonessential aminoacids, 1% sodium pyruvate, 25 mM HEPES, 2mM L-glutamine, and 1% antibiotic/antimytotic solution (complete culture medium). Cells were set to 2×10^5 cells/mL and dispensed on a rounded glass slide ($\varnothing 13$ mm), previously coated with poly-L-lysine. Cultures were kept for 2h at 37°C under 5% CO₂, in order to promote cell attachment on slides.

Glass slides were washed three times with warm complete medium (1 mL each time) and challenged with 50 μ g of different preparations of nanoparticles. Cell cultures were kept for 2 h at 37°C under 5% CO₂ to allow straight contact between cell surface and nanoparticles. Then, slides were washed with fresh PBS at room temperature, cell monolayer were fixed with 2.5% glutaraldehyde and routinely processed.

After fixation of monocyte monolayer on glass slides, cells were dehydrated with ethanol solutions at 7.5, 15, 30, 50, 70, 90 and 100% (2 times for 10 min each alcohol concentration), and submitted to supercritical drying (over the critical point) in a CO₂ atmosphere, for further metallization. Samples were then analyzed by electronic scanning microscopy (SEM) (FEI, Quanta 200) equipped with Oxford, Inca, 250P20 EDS to detect the internalization of the materials by mapping Fe over cells.

4.4. Results and discussion

a) Paper III: a promising new drug delivery system

We have first performed a XPD analysis for the pure PTX that indicated the presence of at least two distinct crystalline phases attributed to dehydrated and hydrated forms of the drug (Neto et al., 2005). Such an observation was then confirmed by the DSC analysis of PTX, in which an extended phase transition was detected between 287 and 367K and attributed to partial dehydration and structural arrangement of the drug. A second transition was also observed at 433K most likely due to a solid-solid transition (Liggins et al., 1997). A pure chitosan sample, as purchased, was also investigated by thermal analyses and an extended endothermic

event related to water loss is detected between 370 and 470K (Neto et al., 2005). Interestingly, due to the changes caused by the crosslinking reactions into the polymer, the bio-NCP and bio-NCP + PTX present this water loss separated into two distinct steps. The first step was observed between 340 and 435K and 310K and 430K for the bio-NCP and bio-NCP + PTX, respectively. The second one, which occurs in higher temperatures, shows that massive higher amount of energy is involved in such a process for the bio-NCP in comparison to the bio-NCP + PTX. In the latter the dehydration is facilitated by the presence of the drug that may compete with water molecules for interacting with NH and OH groups from the polymer. This observation was further confirmed by FTIR analyses, in which vibrations of NH and OH from the primary alcohol groups of chitosan were detected for bio-NCP + PTX but not for the bio-NCP sample, as show in Figure 4.5.

Additionally, FTIR data for bio-NCP + PTX also showed a reduction of the prominent peak related to the C-N bonds formed during the cross-linking reaction involving NH groups from the polymer.

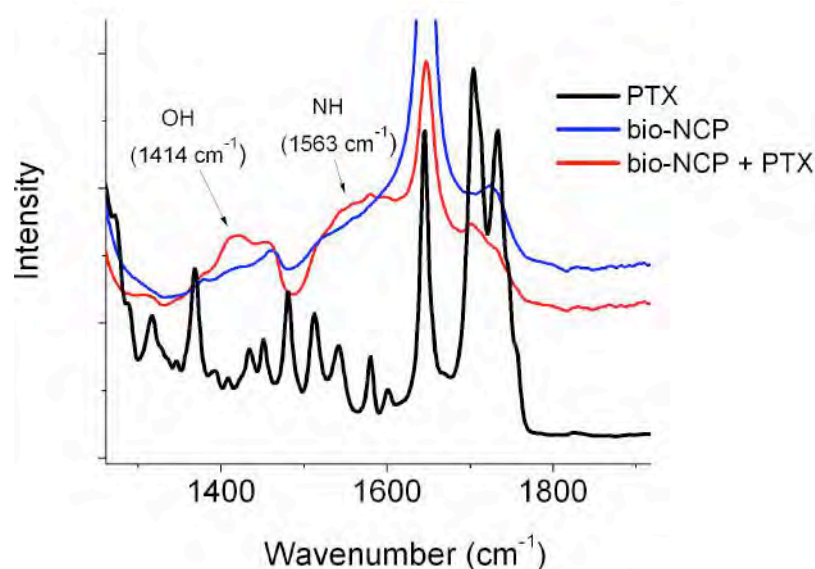


Figure 4.5. FTIR analyses of the PTX, bio-NCP and bio-NCP + PTX. The vibrations from NH and OH from the primary alcohol groups of chitosan are highlighted in the bio-NCP + PTX spectrum.

Sequentially, in Paper III we discussed on the temperature dependence of low frequency INS and QENS data collected at FOCUS (PSI) for the pure drug. The INS part of the spectra presents four main broad bands below 200K centered at 80, 150,

103 and 250 cm^{-1} , which can be attributed to lattice vibration. Above this temperature clear changes in the vibrational spectra as well as a QENS signal are noted, as shown in Figure 4.6(a). To get insight on the activation energy, E_a , of the processes related to the QENS signal the data was fitted using a Dirac function and, a sum of Lorentzians and a flat background function. A single Lorentzian (hereinafter called as the first Lorentzian) was necessary to fit the 100K data and an additional function (second Lorentzian) was included to the model to fit the data collected in higher temperatures. Then, the temperature dependence of the elastic line intensity, where an intensity decrease denotes the activation of hydrogen motions, and the Lorentzians width were evaluated (the latter in the form of Arrhenius plots).

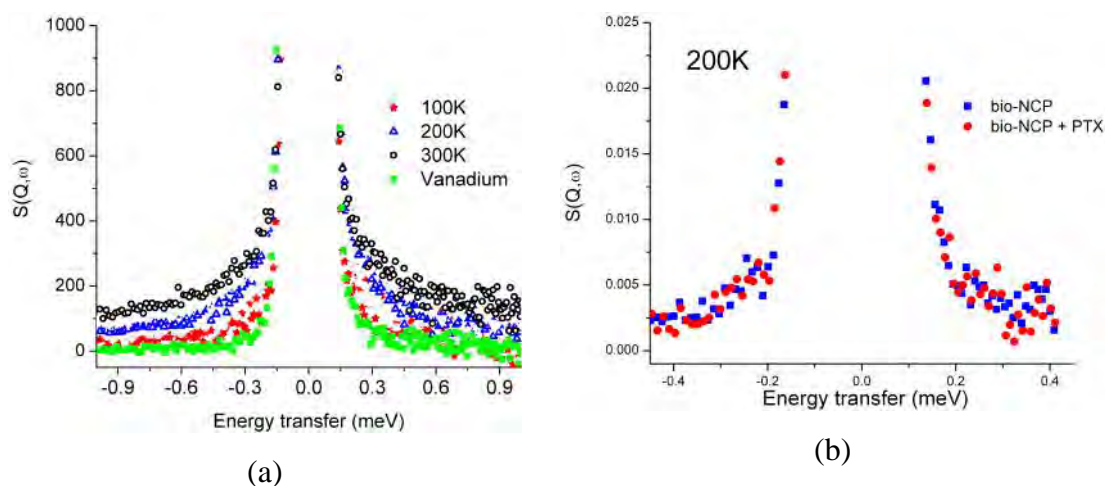


Figure 4.6. Evolution with temperature of the QENS signal for the pur PTX (a) and a comparison of the QENS signals of the bio-NCP and bio-NCP + PTX at 200K (b)

The temperature dependence of the integrated intensity under the elastic line indicates the activation of ~ 10 H in the PTX molecule, or at least three CH_3 groups, assuming that the time scale of our QENS experiments probes mainly the dynamics of such groups. Meanwhile, by using the Arrhenius law, activation energies of 1.16 and 3.6 kJ/mol were obtained for the first Lorentzian, and 6.11 kJ/mol, for the second one. If the assumption that only the dynamics of CH_3 groups is observed is right, then we would expect librational peaks in the INS spectra around 64, 96 and 144 cm^{-1} . The DFT calculations show that the two lower vibrations are mainly attributed to the acetyl groups bonded to C4 and C10 and the methyl group in C12, marked as blue and green in Figure 4.2., respectively. These vibrations were, calculated respectively at 66 and 96 cm^{-1} . Indeed, the DFT results can readily explain the differences between the

theoretical and experimental values as well as the broadening in the observed peaks by denoting the contributions from the side chain in C13 and the oxetane ring to the data.

We have also presented in Paper III QENS spectra for the bio-NCP and bio-NCP + PTX, which showed no significant differences in the data collected at 100K and 200K, presented in Figure 4.6(b), suggesting the strong confinement of the PTX inside the bio-NCP. A slight difference between these samples can be observed at 300K, when the Lorentzian function used to fit the bio-NCP + PTX was 0.72 meV broader than the function used to fit the pure bio-NCP data.

Additional insight in the dynamics of PTX, bio-NCP + PTX and bio-NCP were obtained by analyzing the INS spectra obtained at IN4 (ILL) once more with the support of the DFT calculations. The first relevant observation in those data lies on the PTX band centered at 48 cm^{-1} , mainly attributed to phenyl rings and acetyl groups of the drug, which is damped in the bio-NCP + PTX spectra, indicating the constraining of such groups after the encapsulation. On the other hand, it was possible to detect peaks in the bio-NCP + PTX spectra that first indicated that, even after the encapsulation, the drug could preserve some of its molecular vibrations.

b) Paper IV: additional investigation on the bio-NCP and the encapsulated drug with first insights on the released molecule

This paper was initially devoted to the results of immunologic response generated in macrophages after being in contact with pure MNPs as well as the bio-NCP. The macrophages are defense cells whose function is to phagocyte foreign particles or molecules that may be a threat to the human body. In the case of drug-carriers, a high macrophage response could mean that the material would not easily reach the tissue where the drug is supposed to be delivered. Then we have investigated by EDS the Fe concentration into the cells after 2h in contact with the samples since this metal is the main component of the magnetic nanoparticles used in the bio-NCP synthesis. Our results in presented Paper IV show a considerable internalization of the pure ferrite nanoparticles, which becomes more critical when they are coated with chitosan, as presented in Figure 4.7. The green color highlights the areas with high Fe concentration. After the hydroxyapatite modification in the

polymeric surface and achievement of the bio-NCP, no Fe concentration was detected into the macrophages.

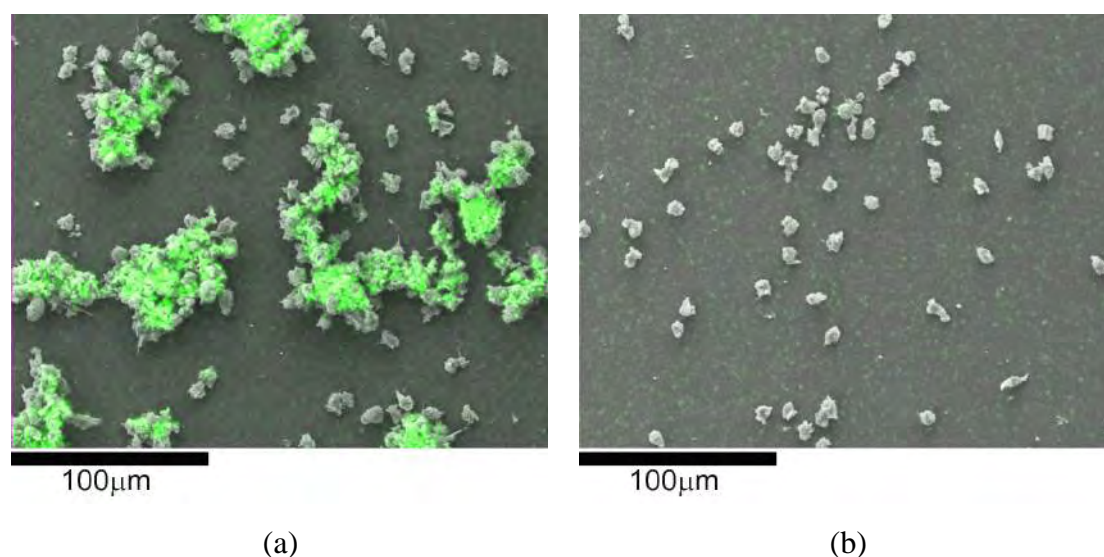


Figure 4.7. Immunologic response generated by macrophages in the control group (a) Mn-Zn ferrite nanoparticles coated with chitosan and (b) the bio-NCP. High Fe concentrations into the cells were determined by EDS and are depicted by the green color and highlighted by arrows in selected positions.

The initial in-vitro tests on colon and lung cancer cells are also shown in Paper IV. The bio-NCP seems to generate a considerable higher uptake effect on the colon cells rather than on the lung ones. Considering the complex composition of the composite, efforts in attempt to understand the drug/encapsulation interactions as well as the dynamical behavior of the encapsulated drug in comparison to its pure form were also made.

First, NEXAFS spectra for PTX, bio-NCP, bio-NCP + PTX and also for pure chitosan (as purchased) were obtained. Although the PTX data showed a convolution of excitations it was still possible to detect a fingerprint for the drug. Interestingly, this characteristic peak was lost in the bio-NCP + PTX spectrum, where new characteristic peaks were observed indicating a strong confinement in the drug. The information obtained by the NEXAFS spectra was then used to obtain compositional maps of the bio-NCP + PTX by means of STXM, which showed that the drug is distributed along the polymeric shell with the magnetic nanoparticles forming the core

of the composite. Figure 4.8 presents a comparison of the theoretical conformation of the bio-NCP + PTX to the STXM image.

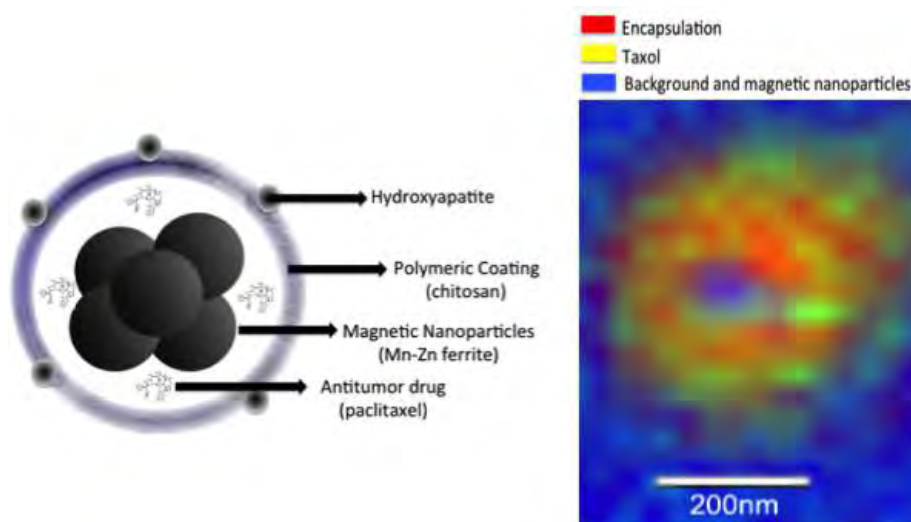


Figure 4.8. Comparison of the theoretical conformation of the bio-NCP + PTX to the STXM image.

After obtaining indicatives of the confinement of the drug into the bio-NCP as well as its distribution along the composite, the next question to be answered in Paper IV was the possibility of recovering the original PTX conformation after the release. To answer this question, the bio-NCP was irradiated and the encapsulation was melted forcing the drug to be released. From the new NEXAFS spectrum of the melted sample we could observe that the original PTX fingerprint was restored, as presented in Figure 4.9.

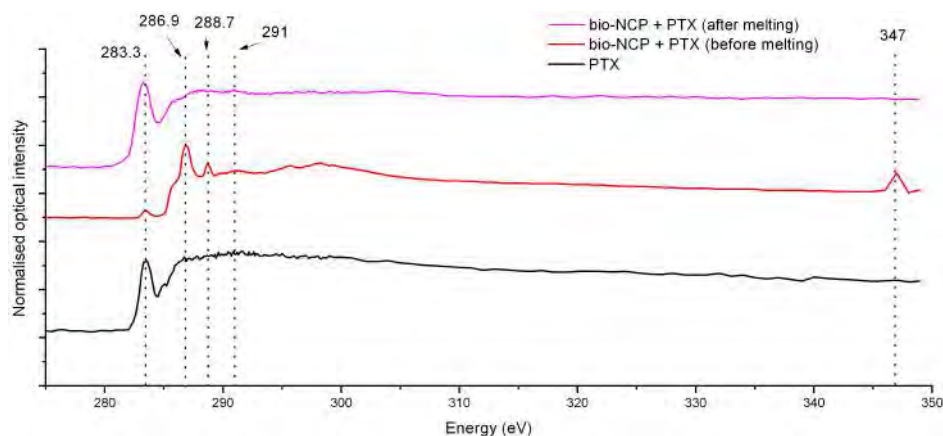


Figure 4.9. NEXAFS spectra for the pure PTX as well as for the bio-NCP + PTX before and after being melted. The PTX fingerprint is recovered in the latter.

Further assessment on the analysis of the encapsulation/drug interactions was provided by a combination of INS data and DFT calculations that showed that the modes assigned to methyl, acetyl and phenyl groups of the drug were damped in the encapsulated PTX. Based on these results we can argue that the encapsulated PTX is in an inactive form, since the groups that are more relevant to its biological activity were constrained. These results are in good agreement to the ones presented in Paper III, which have already indicated the constraining on these groups. Of more interest, some of the vibrations from these groups are observed in the FTIR spectrum after allowing the drug to be released in water dispersion indicating a possible reactivation of PTX after the release, even after being under strong confinement into the bio-NCP.

4.5. Conclusions and outline

Paper III represents our first approaches in the characterization of the encapsulated PTX into the bio-NCP. This work highlights the importance of combining the features of several experimental techniques as well as the insights provided by theoretical calculations.

A general behavior of the samples was obtained by thermal analyses, widely considered as a standard approach for the evaluation of a successful encapsulation procedure. The FTIR data provided interesting insights on the effects on the bio-NCP caused by the presence of PTX, indicating interactions with the OH and NH groups of the polymer. In a very complementary way, the neutron scattering data gave invaluable information on the effects of the encapsulation media. Here, DFT calculations fully supported the clearly showing that encapsulation affects particular vibrational modes of the PTX. The methyl, acetyl and phenyl groups are the most affected ones. These findings were further confirmed in Paper IV.

In Paper IV encouraging initial in-vitro tests results were shown. The low toxicity of the bio-NCP in macrophages was confirmed while great morphological changes were observed in cancer cells after being in contact the composite. A compositional map obtained by NEXAFS + STX confirmed that the drug is

distributed along the polymeric shell in a likely inactive form, as already indicated by the INS + DFT results. Most importantly, we have strong indicatives that it can be released in an active form by either irradiation or dispersion in water.

Chapter 5

Further ideas, considerations and perspectives

Nowadays, there is an increasingly perspective for magnetic nanoparticles application in medicine either in diagnosis or in treatment of diseases. This perspective can be attributed not only to the wide range of properties achieved by the nanoparticles themselves, but also to the possibility of surface modifications with inorganic or organic compounds. The main goal of this PhD thesis was the development of a potential carrier for Paclitaxel (PTX), an anti-cancer drug, by modifying the surface of Mn-Zn ferrite nanoparticles with chitosan and hydroxyapatite nanocrystals. In addition, these materials can be further modified with different compounds leading to a wide range of possible applications, which are presented in Paper V.

Namely, the preparation of a magnetic tracer for gastric emptying exams and an easily traceable magnetic muco-adhesive gel are presented. The first, obtained by a dextrose modification onto the magnetic nanoparticles, is an attempt for carrying out physiological examinations without ionizing radiation and provide relevant information on the diagnosis of diseases related to the gastro intestinal tract, such as Chagas Disease (Oliveira et al., 1998), Parkinson's (Greene et al., 2009) or Diabetes Mellitus (Bharucha et al., 2009). Regarding the muco-adhesive gel, it was obtained by a cellulose modification onto the magnetic nanoparticles and is a potential system to delivery complex molecules while retaining a dosage form at the gastro intestinal tract

and magnetic hyperthermia treatments. Indeed, there is still a lot to be done, for example extended biological trials (i.e toxicity and bio-distribution tests), although the initial in-vivo assays confirm with the Alternate current biosusceptometry technique the potential of both materials.

Regarding the bio-NCP itself, there is also a long way to be crossed. We have first shown in Paper II the great influence of the synthesis parameters in the properties of Mn-Zn ferrite nanoparticles. Certainly, a complete investigation on such influences is relevant, mainly on the structure and magnetic properties of the nanoparticles. We have started such investigations and initial results are presented in Rosanna Ignazzi's bachelor work (Ignazzi, 2014).

We have also shown that the encapsulation of the magnetic nanoparticles into chitosan polymeric capsules can be easily performed by a reverse micelle technique. Ongoing experiments have shown that it is possible to obtain such coatings with distinct sizes and shapes, as presented in Figure 5.1. Further investigations will be also carried out to correlate possible biological properties of each of the bio-NCP shapes.

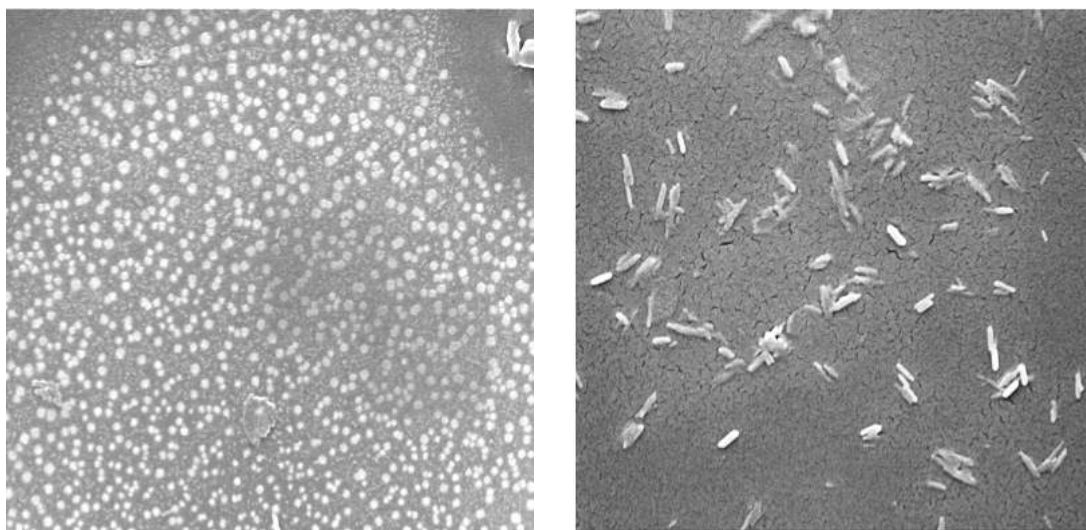


Figure 5.1. Bio-NCPs synthesized with different shapes, which may lead to different biological properties

Our data also have shown that the chitosan coating can be efficiently modified with hydroxyapatite nanocrystals and that such modification provides for interesting properties to the biomaterial, specially the ones related to the low macrophages uptake. Further in-vitro assays are being currently performed to better understand the

influence of the hydroxyapatite crystals in tumor and healthy cells. As a next step, in-vivo tests should be also performed for evaluation of bio-distribution, toxicity and cell viability.

Regarding the PTX encapsulation we have presented the characterization of the bio-NCP+PTX mainly with physical techniques. A pharmacological characterization focused on drug release profile and encapsulation efficiency is our next goal.

Bibliography

Americo, M. F.; Marques, R. G.; Randona, E. A.; Andreis, U. ; Stelzer, M. ; Cora, L. A.; Oliveira, R. B. and Miranda, J. R. A. Validation of ACB in vitro and in vivo as a biomagnetic method for measuring stomach contraction. *Neurogastroenterol Motil*, 22, 1340 – e374, 2010.

Alexiou, C.; Jurgons, R.; Seliger, C.; Brunke, O.; Irom, H. and Odenbach, S.. Delivery of Superparamagnetic Nanoparticles for Local Chemotherapy after Intraarterial Infusion and Magnetic Drug Targeting. *Anticancer Res.*, 27, 2019 - 2022, 2007.

Andronescu, E.; Fikai, M.; Voicu, G.; Fikai, D.; Maganu, M. and Fikai, A. Synthesis and characterization of collagen/hydroxyapatite: magnetite composite material for bone cancer treatment. *J. Mater. Sci. Materials in Medicine*, 21, 7, 2237-2242, 2010.

Azuah, R. T.; Kneller, L. R.; Qiu, Y.; Brown, C. M.; Copley, J. R. D.; Dimeo, R. M.; Tregenna-piggott, P. L. W.; DAVE: A Comprehensive Software Suite for the Reduction, Visualization, and Analysis of Low Energy Neutron Spectroscopic Data. *J. Res. Natl. Inst. Stand. Technol.*, 114, 341 - 358, 2009.

Bharucha, A. E.; Camilleri, M.; Forstrom, L. A. and Zinsmeister, A. R. Relationship between clinical features and gastric emptying disturbances in diabetes mellitus. *Clin. Endocrinol.*, 70, 415–420, 2009.

Bée, M. Quasielastic Neutron Scattering, Principles and Applications in Solid State Chemistry, Biology and Materials Science, CRC Press, 1988.

Beijer, Y. J.; Koopman, M.; Terhaard, C. H. J.; Braunius, W. W.; van Es R. J. J. and de Graeff A. Outcome and toxicity of radiotherapy combined with chemotherapy or cetuximab for head and neck cancer: Our experience in one hundred and twenty-five patients. *Clin. Otolaryngology*, 38, 1, 69-74, 2013.

Brauer, G. Handbook of Preparative Inorganic Chemistry, Volume 2. Academic Press, London, 1965.

Camirand, A.; Fadhil, I.; Luco, A.; Ochiatti, B. and Kremer, R. B. Enhancement of taxol, doxorubicin and zoledronate anti-proliferation action on triple-negative breast cancer cells by a PTHrP blocking monoclonal antibody. *Am. J. Cancer. Res.*, 3, 5, 500 – 508, 2013.

Collins, B. A.; Gann, E.; Guignard, L.; He, X.; McNeill, C. R. and Ade, H. Molecular Miscibility of Polymer–Fullerene Blends. *J. Phys. Chem. Lett.*, 1, 21, 3160–3166, 2010.

Di Corato, R.; Espinosa, A.; Lartigue, L.; Tharaud, M.; Chat, S.; Pellegrino, T.; Ménager, C.; Gazeau, F. and Wilhelm, C. Magnetic hyperthermia efficiency in the cellular environment for different nanoparticle designs. *Biomater.*, 35, 6400 – 6411, 2014.

Dianoux, A. J. and Lander, G. (Eds.). Neutron data booklet. ISBN: 0-9704143-7-4.

Ferlay, J.; Parkin, D. M. and Steliarova-Foucher, E. Estimates of cancer incidence and mortality in Europe in 2008. *Eur. J. Cancer*, 46, 4, 764-781, 2010.

Ferlay, J.; Steliarova-Foucher, E.; Lortet-Tieulent, J.; Rosso, S.; Coebergh, J.W.W.; Comber, H.; Forman, D. and Bray, F. Cancer incidence and mortality patterns in Europe: Estimates for 40 countries in 2012. *Eur. J. Cancer*, 49, 6, 1374-1403, 2013.

Gonçalves, V. L.; Laranjeira, M. C. M.; Fávere, V. T.; Pedrosa, R. C. Effect of crosslinking agents on chitosan microspheres in controlled release of diclofenac sodium. *Polímeros*, 15, 1, 2005.

Greene, J. G.; Noorian, A. R. and Srinivasan, S. Delayed gastric emptying and enteric nervous system dysfunction in the rotenone model of Parkinson's disease. *Exp. Neurol.*, 218, 154–161, 2009.

Haldar, S.; Chintapalli, J. and Croce, C. M. Taxol Induces *bcl-2* Phosphorylation and Death of Prostate Cancer Cells. *Cancer res.*, 56, 1253, 1996.

Harper, J. K.; Barich, D. H.; Heider, E. M.; Grant, D. M.A. Combined Solid state NMR and X-ray Powder Diffraction Study of a Stable Polymorph of Paclitaxel. *Cryst. Growth Des.*, 5, 5, 1737 – 1742, 2005.

Huang, J.; Lin, Y. W.; Fu, X. W.; Best, S. M.; Brooks, R. A.; Rushton, N.; Bonfield, W. Development of nano-sized hydroxyapatite reinforced composites for tissue engineering scaffolds. *J. Mater. Sci.: Materials in Medicine*, 18, 11, 2151-2157, 2007.

Ignazzi, R. Characterization of a new bio-nanocomposite (bio-NCP) for diagnosis and treatment of breast cancer, Bachelor work, University of Copenhagen, Denmark, 2014.

JCNS, 2012. In: Brückel, T.; Heger, G.; Richter, D.; Roth, G.; Zorn, R. (Eds.), Neutron Scattering Lectures of the JCNS Laboratory Course held at Forschungszentrum Jülich and the Research Reactor FRM II of TU Munich in Cooperation with RWTH Aachen and University of Münster.

Jin, J.; Zuo, G.; Xiong, G.; Luo, H.; Li, Q.; Ma, C.; Li, D.; Gu, F.; Ma, Y. and Wan, Y. The inhibition of lamellar hydroxyapatite and lamellar magnetic hydroxyapatite on the migration and adhesion of breast cancer cells. *J Mater Sci: Mater Med.*, 25, 1025 – 1031, 2014.

Kerley, G. J. The application of normal coordinate analysis to INS spectra. *Spectrochimica Acta*, 48A, 3 349 – 362, 1992.

Kovtunenکو, P. V. Defect formation in spinels in oxygen nonstoichiometry. *Glass Ceram.*, 54, 1997.

Kuntz, I. Structure-Based Strategies for Drug Design and Discovery. *Science*, 257, 21, 1992.

Larson, A. C. and Von Dreele, R. B. General Structure Analysis System (GSAS). Los Alamos National Laboratory Report, LAUR 86 – 748, 2004.

Liang, Z.; Guo B.; Li, Y.; Li, X.; Li, X.; Zhao, L.; Gao, L.; Yu, H.; Zhao, X.; Zhang L. and Yang, B. Plasmid-based Stat3 siRNA delivered by hydroxyapatite

nanoparticles suppresses mouse prostate tumour growth in vivo. *Asian J. Andrology*, 13, 481 – 486, 2011.

Liggins, R. T.; Hunter, W. L. and Burt, H. M. Solid-state characterization of paclitaxel. *J Pharm Sci*, 86, 1458, 1997.

Lv, P.; Wei, W.; Yue, H.; Yang, T.; Wang, L. and Ma G. Porous Quaternized Chitosan Nanoparticles Containing Paclitaxel Nanocrystals Improved Therapeutic Efficacy in Non-Small-Cell Lung Cancer after Oral Administration. *Biomacromol.*, 12, 4230 – 4239, 2011.

Ma, P. and Mumper, R. J. Paclitaxel Nano-Delivery Systems: A Comprehensive Review. *J Nanomed Nanotechnol.* 4(2), 1000164, 2013.

Madejová, J. FTIR techniques in clay mineral studies. *Vib. Spectrosc.*, 31, 1–10, 2003.

Marry, V.; Dubois, E.; Malikova, N.; Durand-Vidal, S.; Longeville, S. and Brey, J. Water Dynamics in Hectorite Clays: Influence of Temperature Studied by Coupling Neutron Spin Echo and Molecular Dynamics. *Environ. Sci. Technol.*, 45, 7, 2850 – 2855, 2011.

Martins, M. L.; Gates, W. P.; Michot, L.; Ferrage, E.; Marry, V.; Bordallo, H.N.. Neutron scattering, a powerful tool to study clay minerals. *Appl. Clay Sci.*, 96, 22-35, 2014.

Martins, M. L.; Saeki, M. J.; Telling, M. T. F.; Parra, J. P. R. L. L.; Landsgesell, S.; Smith, R. I.; Bordallo, H. N. Development and characterization of a new bio-nanocomposite (bio-NCP) for diagnosis and treatment of breast cancer. *J. alloys compd*, 584, 514–519, 2014.

Martins, M. L.; Orecchini, A.; Aguilera, L.; Eckert, J.; Embs, J.; Matic, A.; Saeki, M. J. and Bordallo, H. N. Encapsulation of paclitaxel into a bio-nanocomposite. A study combining Inelastic Neutron Scattering to Thermal Analysis and Infrared Spectroscopy. Accepted by *Eur. J. Phys.*

Mastropaolo, D.; Camerman, A.; Luo, Y.; Brayer, G. D. and Camerman, N. Crystal and molecular structure of paclitaxel (taxol). *Proc. Natl. Acad. Sci. USA*, 92, 6920 - 6924, 1995.

Meena, R.; Kesari, K. K.; Rani, M. and Paulraj, R. Effects of hydroxyapatite nanoparticles on proliferation and apoptosis of human breast cancer cells (MCF-7). *J. Nanopart. Res.*, 14, 712, 2012.

Mikhaylov, G.; Mikac, U.; Magaeva, A. A.; Itin, V. I.; Naiden, E. P.; Psakhye, I.; Babes, L.; Reinheckel, T.; Peters, C.; Zeiser, R.; Bogyo, M.; Turk, V.; Psakhye, S. G.; Turk, B. and Vasiljeva, O. Ferri-liposomes as an MRI-visible drug-delivery system for targeting tumours and their microenvironment. *Nat. nanotech.*, 6, 2011.

Miller, K.; Wang, M.; Gralow, J.; Dickler, M.; Cobleigh, M.; Perez, E. A.; Shenkier, T.; Cella, D. and Davidson, N. E. Paclitaxel plus Bevacizumab versus Paclitaxel Alone for Metastatic Breast Cancer. *NEJM*, 357, 2666 – 2676, 2007.

Monsuez, J.; Charniot, J.; Vignat, N. and Artigou, J. Cardiac side-effects of cancer chemotherapy. *Intern. J. Cardiol.*, 144, 1, 3-15, 2010.

Nakazaki, K.; Higuchi, Y.; Nagano, O. and Serizawa, T. Efficacy and limitations of salvage gamma knife radiosurgery for brain metastases of small-cell lung cancer after whole-brain radiotherapy. *Acta Neurochir.* 155, 107–114, 2013.

Neto, C. G. T.; Giacometti, J. A.; Job, A. E.; Ferreira, F. C.; Fonseca, J. L. C. and Pereira, M. R. Thermal Analysis of Chitosan Based Networks. *Carb. Polymers*, 62, 97, 2005.

Oliveira, R. B.; Troncon, L. E.; Dantas, R. O. and Meneghelli, U.G.. *Am. J. Gastroenterol.*, 93, 884 – 889, 1998.

Pathi, S. P.; Lin, D. D. W.; Dorvee, J. R.; Estroff, L. A. and Fischbach C. Hydroxyapatite nanoparticle-containing scaffolds for the study of breast cancer bone metastasis. *Biomater.*, 32, 5112–5122, 2011.

Richard, D.; Ferrand, M.; Kearley, G.J. Analysis and Visualisation of Neutron-Scattering Data. *J. Neutron Res.*, 4, 33, 1996.

Rietveld, H. M. J. *Apl. Cryst.* 10, 65-71, 1969.

Sears, V. F. Cold neutron scattering by molecular liquids: III. Methane. *Can. J. Phys.* 45, 237–254, 1967.

Squires, G. L. *Introduction to the Theory of Thermal Neutron Scattering*. Cambridge University Press, New York, 1978.

Squires, G. L. *Introduction to the Theory of Thermal Neutron Scattering*. Cambridge University Press, New York, 1978.

Stöhr, J. *NEXAFS Spectroscopy*, Second Printing Springer, 2003

Tsapatsaris, N.; Kolesov, B. A.; Fischer, J.; Boldyreva, E. V.; Daemen, L.; Eckert, J. and Bordallo, H. N. Polymorphism of Paracetamol: A New Understanding of Molecular Flexibility through Local Methyl Dynamics. *Mol. Pharmaceutics*, 11, 1032 - 1041, 2014.

Tsapatsaris, N.; Landsgesell, S.; Koza, M. M.; Frick, B.; Boldyreva, E. and Bordallo, H. N. Polymorphic drugs examined with neutron spectroscopy: Is making more stable forms really that simple? *Chem. Phys.*, 427, 124 - 128, 2013.

Vayssières, L.; Chanéac, C.; Tronc, E.; Jolivet, J. Size Tailoring of Magnetite Particles Formed by Aqueous Precipitation: An Example of Thermodynamic Stability of Nanometric Oxide Particles. *J. Colloid Interface Sci.*, 205, 2, 205 – 212, 1998.

Venkatesan, P.; Puvvada, N.; Dash, R.; Kumar, B. N. P.; Sarkar, D.; Azab, B.; Pathak, A.; Kundu, S. C.; Fisher, P. B. and Mandal, M. The potential of celecoxib-loaded hydroxyapatite-chitosan nanocomposite for the treatment of colon cancer. *Biomater.*, 32, 3794 – 3806, 2011.

Vilos, C.; Morales, F. A.; Solar, P. A.; Herrera, N. S.; Gonzalez-Nilo, F. D.; Aguayo, D. A., Mendoza, H. L.; Comer, J.; Bravo, M. L.; Gonzalez, P. A.; Kato, S.; Cuello, M. A.; Alonso, C.; Bravo, E. J.; Bustamante, E. I.; Owen, G. I. and Velasquez, L. A. Paclitaxel-PHBV nanoparticles and their toxicity to endometrial and primary ovarian cancer cells. *Biomater.*, 34, 15, 4098 - 4108, 2013.

Wang, C.; Ho, P. C. and Lim, L. Y. Wheat germ agglutinin-conjugated PLGA nanoparticles for enhanced intracellular delivery of paclitaxel to colon cancer cells. *Int. J. Pharm.*, 400, 201–210, 2010.

Watts, B. The Orientational Dynamics of γ -APS on Zinc Oxide Surfaces, Phd thesis, The University of Newcastle, Australia, 2005.

Watts, B.; McNeill, C.R.; Raabe, J. Imaging Nanostructures in Organic Semiconductor Films with Scanning Transmission X-ray Spectro-microscopy. *Synth. Met.*, 161, 2516 – 2520, 2012.

Watts, B.; Thomsen, L. and Dastoor, P. C. Methods in carbon K-edge NEXAFS: Experiment and analysis. *J. Electron Spectro. Relat. Phenom.*, 151, 105–120, 2006.

Williams, H. J.; Moyna, G.; Scott, A. I. NMR and Molecular Modeling Study of the Conformations of Taxol 2'-Acetate in Chloroform and Aqueous Dimethyl Sulfoxide Solutions. *J. Med. Chem.*, 39, 1555-1559, 1996.

Yu, X. and Pishko, M. V. Nanoparticle-Based Biocompatible and Targeted Drug Delivery: Characterization and in Vitro Studies. *Biomacromol.*, 12, 3205–3212, 2010

Yuan, Y.; Liu, C.; Qian, J.; Wang, J. and Zhang, Y. Size-mediated cytotoxicity and apoptosis of hydroxyapatite nanoparticles in human hepatoma HepG2 cells. *Biomater.* 31, 730 – 740, 2011.

Zhao D, Wang X, Zeng X, Xia Q, Tang J. Preparation and inductive heating property of Fe₃O₄-chitosan composite nanoparticles in an AC magnetic field for localized hyperthermia. *J. Alloys Compd*, 477, 739 – 743, 2009.

Zhou, J.; Zhao, W.; Ma, X.; Ju, R.; Li, X.; Li, N.; Sun, M.; Shi, J.; Zhang, C. and Lu, W. The anticancer efficacy of paclitaxel liposomes modified with mitochondrial targeting conjugate in resistant lung cancer. *Biomaterials*, 34, 14, 3626 - 3638, 2013.

Appendix

Publications

Publication I

Martins, M. L.; Gates, W. P.; Michot, L.; Ferrage, E.; Marry, V.; Bordallo, H.N.
Neutron scattering, a powerful tool to study clay minerals. Appl. Clay Sci., 96, 22-35, 2014.



Review article

Neutron scattering, a powerful tool to study clay minerals

Murillo L. Martins ^a, Will P. Gates ^{b,c}, Laurent Michot ^d, Eric Ferrage ^e, Virginie Marry ^d, Heloisa N. Bordallo ^{a,*}^a The Niels Bohr Institute, University of Copenhagen, DK-2100 Copenhagen, Denmark^b SmecTech Research Consulting, 9 Purtell Street, Bentleigh East, VIC 3165, Australia^c Department of Civil Engineering, Monash University, Clayton, VIC 3800, Australia^d Laboratoire Phenix Sorbonne Universités, UPMC Univ Paris 06, CNRS, UMR 8234, Paris F-75005, France^e Université de Poitiers, CNRS IC2MP-HydrASA UMR 7285, Poitiers cedex F-86022, France

ARTICLE INFO

Article history:

Received 19 March 2014

Received in revised form 8 May 2014

Accepted 9 May 2014

Available online 28 May 2014

Keywords:

Clay minerals

Cross-section

Neutron diffraction

Quasi-elastic neutron scattering

Hydrogen dynamics

ABSTRACT

Of the techniques used to study clay minerals, neutron scattering has become more familiar to clay scientists over the past decade. A brief account of neutron scattering theory is given in this review, followed by a description of measurements that can be made using neutron diffraction and neutron scattering spectroscopy, and especially quasi-elastic neutron scattering. Then recent examples of the application of neutron scattering methods to the study of clay minerals are presented, and finally the potential advantages of such experimental results when combined to molecular dynamics are discussed. To conclude, the potential perspectives that the European Spallation Source brings to this subject are pointed out.

© 2014 Elsevier B.V. All rights reserved.

1. Introduction

The usefulness of smectites in many industries stems from their ability to take up and retain large amounts of water due largely to their high interlayer surface area and presence of hydrated cations (Bérend et al., 1995; Cases et al., 1992, 1997; Ormerod and Newman, 1983). Neutron scattering spectroscopy has been used to probe water mobility dynamics in clay minerals for more than 4 decades (Adams et al., 1979; Cebula et al., 1981; Hunter et al., 1971; Olejnik and White, 1972; Olejnik et al., 1970; Poinsignon et al., 1987; Ross and Hall, 1978; Tuck et al., 1984, 1985), but interest in this methodology has increased markedly since the mid 1990s (Bordallo et al., 2008; Chakrabarty et al., 2006; Gates et al., 2012; Kamitakahara and Wada, 2008; Malikova et al., 2006; Michot et al., 2007; Nair et al., 2005; Powell et al., 1997, 1998; Swenson et al., 2000, 2001a; Williams et al., 1998) in conjunction with developments in molecular dynamic simulations (Skipper et al., 1991, 1994, 1995; de Siqueira et al., 1999; Greathouse et al., 2000; Skipper et al., 2000; de Carvalho and Skipper, 2001; Sutton and Sposito, 2001; Marry et al., 2002; Marry and Turq, 2003; Marry et al., 2008; Wang et al., 2004, 2006; Malikova et al., 2006).

Water mobility in smectites is largely controlled by the type of interlayer cation (Bordallo et al., 2008; Cases et al., 1992; Gates et al. 2012). The interactions of water (solutes) with the different surfaces of

smectites often have diffusion or exchange times on the order of 10 ps to 100 ms that correspond in part to the time scale probed by neutron spectroscopy. Other methods, such as nuclear magnetic resonance (e.g., Bowers et al., 2011), are also highly successful at probing these interactions, but will not be discussed here.

Neutron scattering has several features that make it a powerful technique to study the structure and dynamics of heterogeneous systems such as smectite–water dynamics. The wavelength of thermal neutrons is suitable for probing the structure of a clay at the molecular level (neutron powder diffraction, NPD), as well as their long range order in colloidal dispersions and the macroscopic structure of the particles themselves (small-angle neutron scattering, SANS) (Cebula and Thomas, 1978). When compared to X-ray diffraction, neutron diffraction offers the advantage of a smaller attenuation coefficient, thus making surface effects negligible. Moreover in the study of sol or gel states the wavelength of the neutrons can be adjusted, so that Bragg diffraction reflections resulting from the clay mineral structure can be avoided. Additionally, by varying the hydrogen–deuterium ratio of the fluid, or possibly even the clay mineral itself, the contrast between the mineral particles and their surrounding water molecules can be better identified. On the other hand, although water dynamics can be investigated by many experimental techniques, such as infrared and Raman spectroscopies (Brubach et al., 2001) and nuclear magnetic resonance (NMR) (Kyakuno et al., 2011), neutron scattering spectroscopy offers a number of advantages presented in this work (Bordallo et al., 2008; Cebula et al., 1979; Cole et al., 2006; Malikova et al., 2008). Due to the exceptionally large scattering cross-section of the H-atoms, incoherent

* Corresponding author at: Niels Bohr Institute, University of Copenhagen, Universitetsparken 5, 2100 Copenhagen, Denmark. Tel.: +45 213 088 29.
E-mail address: bordallo@nbi.ku.dk (H.N. Bordallo).

inelastic neutron scattering (IINS) enables probing of diffusive proton motions over a broad time-scale (from few nano to a few hundred ps) as well as the observation of quite high vibrational frequencies (up to 2000 cm⁻¹).

To date, neutron flux has been a key challenge in the study of many interesting problems in clay science, where understanding of kinetic effects is of the foremost importance. The unprecedented neutron flux offered by the European Spallation Source (operational in 2020) will, however, open up new opportunities for enquiry. For example, ESS will enable detailed dynamic analysis of real-time hydration and dehydration processes in clays. In order to better take advantage of this experimental technique, the most important theoretical points that must be known by novices, as well as examples of successful experiments, are described in this review.

2. Neutron scattering: an overview

Neutrons are non-charged subatomic particles, first postulated by Rutherford in 1920 and later observed by J. Chadwick in 1932. They are found in all atomic nuclei with exception of the hydrogen atom (¹H) and have a comparable mass to protons, a magnetic moment of -1.913 μ_B and a nuclear spin of 1/2.

Neutron scattering techniques are based on the analysis of momentum and energy transfer, which may occur following interactions between neutrons and matter. Note that during such interaction the wave-particle duality must be considered for neutrons, so they can be described either as a classical particle with momentum $\vec{p} = m\vec{v}$, where m is the neutron mass (1.675.10⁻²⁷ kg) and \vec{v} is its velocity, or as a wave with momentum $\vec{p} = \hbar\vec{k}$, where $|k| = (2\pi)/\lambda$ is the wave vector of the neutron and λ is the associated wavelength. Therefore, the corresponding neutron energy E can be described as:

$$E = \frac{p^2}{2m} = \frac{1}{2}mv^2 = \frac{\hbar^2}{2m\lambda^2} = \frac{\hbar^2 k^2}{2m} \quad (1)$$

where $\hbar = 2\pi\hbar = 6.626.10^{-34}$ J·s is the Planck's constant.

Thus, the energy and momentum transfer, \vec{Q} , measured in a neutron scattering experiment, are given by:

$$\Delta E = E_i - E_f = \frac{\hbar^2}{2m} (k_i^2 - k_f^2) \quad (2)$$

for energy, and

$$\vec{Q} = \vec{k}_i - \vec{k}_f \quad (3)$$

for momentum transfer. Eqs. (2) and (3) can be then graphically described as in Fig. 1.

Since their first observation, neutrons have been used as a powerful probe to study a wide range of materials due to their very unique

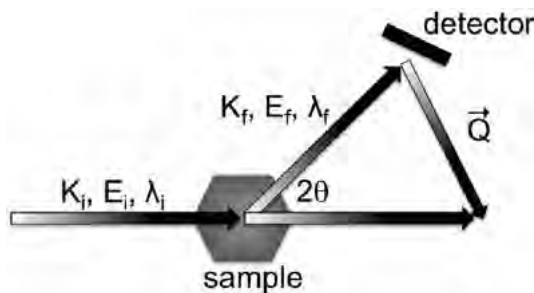


Fig. 1. In a scattering experiment, incoming neutrons with incident wavelength λ_i, energy E_i and wave vector k_i interact with the sample and are detected at an angle 2θ with final λ_f, E_f and k_f. The scattering vector \vec{Q} is defined as the change in wave vector $\vec{Q} = \vec{k}_i - \vec{k}_f$.

properties on interaction with matter. First, as will be seen in more detail in the following sections, the scattering cross section, which describes the probability of interactions between neutrons and atoms, follows a complex relation with the atomic number of elements, whereas for X-rays, for example, the relation is generally predictable. Therefore, neutrons turn out to be a perfect probe for studies involving hydrogen, specially considering their isotope sensitivity. For example, while hydrogen presents the highest cross section for interactions with neutrons among all atoms, the probability of such interactions with deuterium is considerably lower. Therefore, one can use this feature in order to generate contrast in a given molecule or a specific portion or region of a material. Additionally, neutrons penetrate deeply into matter, which allows for the study of structure and dynamics of materials under very precise environmental conditions such as pH, pressure, temperature, hydration and others, providing information not easily accessed by NMR, optical microscopy, light scattering, X-ray diffraction or X-ray absorption spectroscopy.

2.1. Production of neutrons

The half-life of a free neutron is about 900 s. Such a short lifetime makes necessary the production of neutrons concurrent with the experiment. Free neutrons for scientific purposes can be obtained by means of nuclear reactions in fission reactors or from spallation sources. In both cases large scale facilities are required in order to operate the sources and provide adequate instrumentation for the users.

In the case of nuclear fission reactors, free neutrons are obtained after a slow neutron is captured by an ²³⁵U nucleus, which splits and liberates 2 or 3 additional neutrons with an energy of 1.29 MeV together with fission fragments. Each of these neutrons can hit other ²³⁵U nuclei giving rise to 2 or 3 additional neutrons. From those, 1 neutron is used to continue the chain reactions, which can be either accelerated if the fissile materials mass is above the so-called critical mass M_c leading to an uncontrollable reaction or it can stop if the fissile material mass remains below M_c. Research reactors operate below M_c to control the nuclear reaction, but delayed neutrons together with secondary neutrons originating from the highly excited fission fragments allow the reaction to continue practically indefinitely.

The wavelength of neutrons being in thermal equilibrium with the moderator has a Maxwellian distribution (Fig. 2), and one can further describe the neutrons based on their energy as

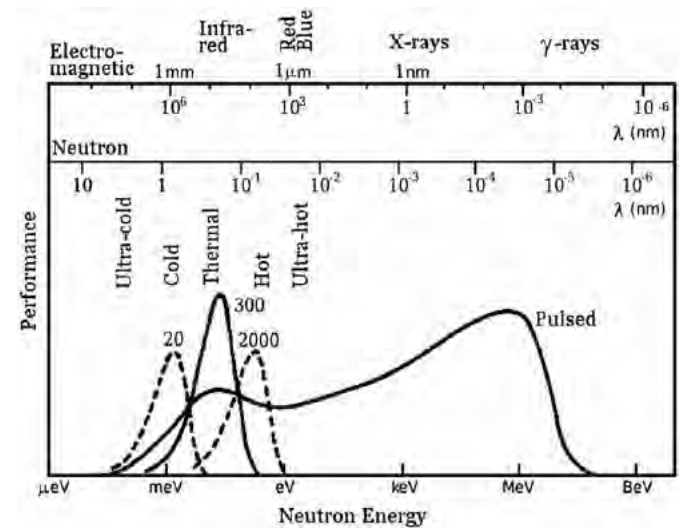


Fig. 2. A reactor's performance depends on the neutron flux at each energy. The solid curve labeled thermal shows the Maxwellian distribution of neutrons from an ambient moderator, which can be shifted by using a cold ≈ 20 K or a hot moderator ≈ 200 K. A pulsed spallation source performance depends on the flux and pulse width. The curve shows the flux per unit fractional energy.

hot ($T \approx 2300$ K, $E \approx 200$ meV), thermal ($T \approx 300$ K, $E \approx 26$ meV) or cold neutrons ($T \approx 25$ K, $E \approx 2.5$ meV). If the moderator has a temperature of 300 K, the most probable wavelength is 1.45 Å matching interatomic spacings. Therefore, experiments like single crystal, powder diffraction and stress analysis are carried out with thermal neutrons. On the other hand, neutrons that have been further slowed in a cold source, typically an aluminum tank filled with liquid deuterium kept at a temperature of 25 K, allow shifting of the peak flux to higher wavelengths. Those neutrons have wavelengths between 3 and 6 Å and a corresponding energy of the order of phonon excitations and internal vibrational modes of molecules. Thus, experiments on dynamics (time-of-flight, backscattering and spin echo), reflectometry, tomography and small angle neutron scattering are performed using cold neutrons. Therefore, a spatial and energetic (temporal) match can be found between the wavelength and energy of neutrons and the characteristic length and time-scale of atomic motions and distances in condensed and soft matter (Squires, 1978), Fig. 3.

The neutron flux in research reactors rapidly increased in the 1960s, but it has also been hampered by environmental and political pressures due to critical problems associated with heat and the potential for radiation damage. The most powerful research reactor presently is at the Institute Laue–Langevin (ILL) – France, which became critical for the first time in 1974. The FRMII reactor, at the Heinz Maier-Leibnitz Zentrum – Germany, provides half of the thermal neutron flux in comparison to ILL, but uses only one third of the reactor power.

In the case of the spallation sources, which are inherently safe because less energy is needed and the thermal dissipation is lower, free neutrons are obtained with high energy proton pulses being accelerated onto a target made of a neutron rich material. Corresponding neutron pulses are freed by the target and after being moderated are guided to the instruments. The neutron yield from spallation is typically between 20 and 50 per event; however it depends ultimately on the target material used. Since the spallation reaction is not possible without the operation of an accelerator, production of neutrons by spallation can be inherently safer than reactors, where a chain reaction must be continuously ongoing to obtain neutrons. Regarding the neutron flux, the most powerful existing spallation source is SNS, at Oak Ridge – USA, with a power of 1.2 MW ramping up to 1.4 MW. The ISIS source at the Rutherford Appleton Laboratory – UK (160 kW) and J-Parc – Japan (expected to reach 2 MW) are other examples of highly productive facilities.

Nowadays, reactor sources still provide a higher average flux than the spallation sources. However, the time structure of the latter can provide higher monochromatic intensities and consequently unprecedented gains in flux. After the advent of the European Spallation Source (ESS) – Sweden, whose operation is expected to start in 2020, the 5 MW power will enable a similar average flux as currently available from the reactors.

2.2. X-rays and neutron scattering: complementarity due to different interactions with matter

Describing diffraction can be done in an elegant way with the Bragg-equation. In this description an incoming wave with the wavelength λ is reflected by atomic planes and if the Bragg-condition

$$2d \sin\theta = n\lambda \quad (4)$$

is satisfied, the waves reflected by atomic planes having distance d interfere constructively. Specifically for a Bragg reflection, the maximum intensity detected is at 2θ . The angle θ in Eq. (4) is defined as the angle between the incoming ray and the diffracting atomic plane. By measuring the angle-positions of Bragg-reflections it is possible to gain information on atomic distances and therefore to calculate structural parameters such as the lattice constants.

To obtain additional information regarding the unit cell, it is necessary to analyze Bragg reflection intensities, which are related to the atomic positions via the structure factor and can be derived by Fourier analysis (Bacon, 1975; Rietveld, 1969).

Just as perfect crystals have a periodic structure the scattering function $\rho(\vec{r})$ has a periodic nature as well. In other words, $\rho(\vec{r})$ is invariant against translation $\vec{T} = m_1 \vec{a} + m_2 \vec{b} + m_3 \vec{c}$ and satisfies $\rho(\vec{r}) = \rho(\vec{r} + \vec{T})$. Thus, $\rho(\vec{r})$ can be expanded in a Fourier series:

$$\rho(\vec{r}) = \sum_{\vec{G}} \rho_{\vec{G}} e^{i\vec{G} \cdot \vec{r}} \quad (5)$$

where $\rho_{\vec{G}} = V_c^{-1} \int_{\text{cell}} dV \rho(\vec{r}) e^{-i\vec{G} \cdot \vec{r}}$ is the Fourier components and $\vec{G} = h\vec{a}^* + k\vec{b}^* + l\vec{c}^*$ is the reciprocal lattice vector. If the reciprocal axes $\vec{a}^*, \vec{b}^*, \vec{c}^*$ are defined, $\rho(\vec{r})$ in Eq. (5) is indeed invariant

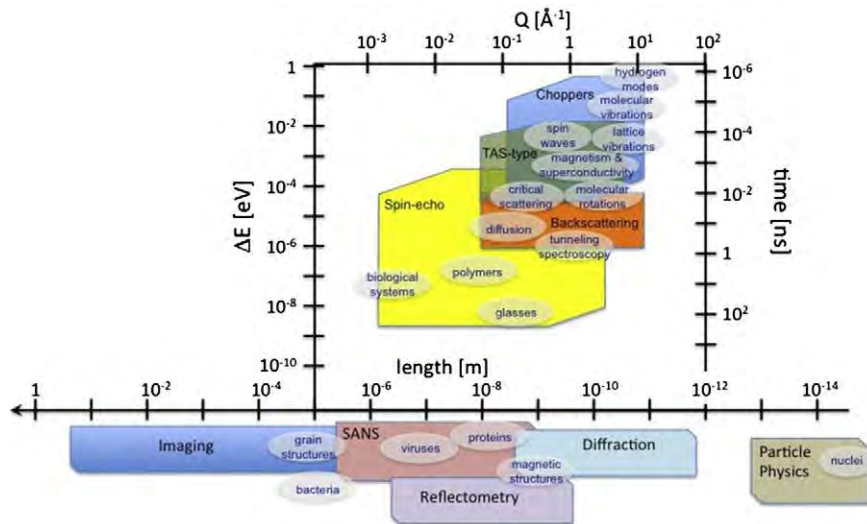


Fig. 3. Using neutrons and complementary techniques to explore different length and time scales. The horizontal axes indicate real and reciprocal length scales, while the vertical axes refer to time and energy scales. Scientific areas falling within different length and time scales are indicated along the edges. The experimentally accessible areas of the various neutron-based techniques are shown as polygons in strong colors. Those techniques that are sensitive to both time and length scales are represented above the main horizontal axis; those that measure only length-scales below. In addition to the neutron-based techniques, the analogous areas for a selection of complementary experimental techniques are shown in grey.

against a translation \vec{T} . Generally, the scattering amplitude A of the scattered beam can be expressed as follows (Kittel, 1996):

$$A = \sum_{\vec{G}} A_{\vec{G}} = \int dV \rho(\vec{r}) e^{(-i\Delta\vec{k}\cdot\vec{r})} \quad (6)$$

$$A = \sum_{\vec{G}} \int dV \rho_{\vec{G}} e^{[i(\vec{G}-\Delta\vec{k})\cdot\vec{r}]} \quad (7)$$

where $\Delta\vec{k} = \vec{k}_1 - \vec{k}_0$ is the difference between the outgoing and incoming wave vectors, and the phase factor $e^{[i(\vec{k}-\vec{k}')\cdot\vec{r}]}$ arises from the beam scattered by different volume elements dV . From Eq. (7) it can be seen that Bragg reflections can be observed only if $\vec{G} = \Delta\vec{k}$, the Laue-condition. Then the scattering amplitude A for a crystal with N unit cells of the volume V_c can be rewritten as:

$$A_{\vec{G}} = N \int_{\text{cell}} dV \rho(\vec{r}) e^{(-i\vec{G}\cdot\vec{r})} = N F_{\vec{G}}. \quad (8)$$

In this expression, $F_{\vec{G}}$ is the structure factor that contains information about the distribution of the atoms and is connected to the intensity via:

$$I = A_{\vec{G}}^* \cdot A_{\vec{G}} = N^2 F_{\vec{G}}^* \cdot F_{\vec{G}} \quad (9)$$

Recall that X-rays are scattered by the electronic shell of the atoms and the scattering function is equal to the electron density $n(\vec{r})$. On the other hand, because neutrons are scattered directly by the nucleus, $\rho(\vec{r})$ describes the nuclear potential $V(\vec{r})$ and the structure factor can be then rewritten as (JCMS, 2012):

$$\text{neutrons :} \quad F_{\vec{G}} = \int_{\text{cell}} dV b_i e^{(-i\vec{G}\cdot\vec{r}_i)} \quad (10)$$

$$\text{X-rays :} \quad F_{\vec{G}} = \int_{\text{cell}} dV f_i e^{(-i\vec{G}\cdot\vec{r}_i)} \quad (11)$$

with the position \vec{r}_i of the i -th atom. In the case of neutrons, b_i is the scattering length, obtained experimentally and tabulated (Bacon, 1975), whose value depends on the atom type, and, most importantly, on the isotope and the spin-state of the neutron–nucleus system. The corresponding factor for X-ray scattering is the atomic scattering factor f_i and is defined as:

$$f_i = \int dV n_i(\vec{r}-\vec{r}_i) e^{[-i\vec{G}\cdot(\vec{r}-\vec{r}_i)]} \quad (12)$$

Consequently, the atomic scattering factor f_i increases with increasing atomic number Z , so that heavy atoms give more intense Bragg reflections in X-ray diffraction patterns. On the other hand b_i does not vary monotonously with Z and the real interaction is rather complex. This difference in scattering behavior makes X-ray and neutron scattering two complementary tools for crystal structure investigation.

Thermal motions of the atoms around their average position \vec{r}_i also affect the scattered intensity. Therefore, the so called Debye–Waller factor $\exp(-W_i)$ has to be taken into account. In the harmonic, isotropic approximation (JCMS, 2012), W_i is defined as follows:

$$W_i = 8\pi^2 \frac{\sin^2\theta}{\lambda^2} \cdot \langle u^2 \rangle \quad (13)$$

with the mean square displacement $\langle u^2 \rangle$ of the atom around its equilibrium position. Thus, at high temperatures the scattered intensity decreases substantially for light atoms and at high diffraction angles. Other factors, like absorption, experimental geometry and extinction affect the intensities and have to be considered when analyzing diffraction patterns (Klug and Alexander, 1974).

2.3. Neutron scattering: the concepts of scattering length and cross section

After interacting with a nucleus of a single fixed atom, the scattered neutron wave is isotropic, and described as:

$$\psi = \frac{b}{r} e^{(ik_1 r)} \quad (14)$$

where r is the distance between the atom and a given detector. Here, considering that the real part of the scattering length, b , dominates, the complex part representing the absorption coefficient is not discussed. Thus, the scattering length can then be defined, for each element j , as a coherent scattering length plus an incoherent scattering length:

$$b_{\text{coh}} = \bar{b}_j \quad (15)$$

for coherent scattering, and

$$b_{\text{inc}} = \sqrt{\overline{b_j^2} - \bar{b}_j^2} \quad (16)$$

for incoherent scattering.

In Eqs. (15) and (16), the notation \bar{b} denotes the average value of the quantity b . Note that while the coherent scattering length describes a system in which all the isotopes and spin fluctuations for a single element are smeared out, the incoherent scattering length is composed of exactly such fluctuations. In broad terms, b denotes the scattering ability of the atomic nucleus, where the coherent part describes a collective behavior of an ensemble of atoms and the incoherent part describes individual behaviors.

In a typical neutron scattering experiment, the number of neutrons scattered in a particular direction is determined. In the simplest case such as in diffraction experiments where neutron momentum is considered constant, if the distance between the detector and the nucleus is large enough to define the solid angle $d\Omega$ subtended by the detector, then the measured quantity is the differential cross section, defined as:

$$\frac{d\sigma}{d\Omega} = \frac{(\text{neutrons} \cdot \text{s}^{-1} \text{ scattered into } d\Omega)}{\Phi d\Omega} \quad (17)$$

where Φ is the neutron flux (number of neutrons $\text{cm}^{-2} \cdot \text{s}^{-1}$). The total scattering cross-section is defined as the total number of neutrons scattered per second, normalized to the flux:

$$\sigma = \int \frac{d\sigma}{d\Omega} d\Omega \quad (18)$$

and is related to b as:

$$\sigma = 4\pi b^2 \quad (19)$$

As a result, the cross-section, previously defined as the probability of interactions between neutrons and atoms can also be adequately defined as the effective area that the target nucleus presents to the incident beam of neutrons.

Therefore, for each isotope, characteristic values of coherent and incoherent cross sections (σ_{coh} and σ_{inc}) exist. In practice, one always measures a combination of both and the relative weight between such values depends on the sample composition. Such weight balance provides the great possibility of contrast variation in neutron experiments

Table 1

Coherent (σ_{coh}) and incoherent (σ_{inc}) cross-sections in 10^{-24} cm² for selected elements and isotopes present in clay samples (Dianoux and Lander, 2003).

	¹ H	² D	C	O	²³ Na	S
σ_{coh}	1.76	5.59	5.55	4.23	1.66	1.02
σ_{inc}	80.27	2.05	<0.01	<0.01	1.62	<0.01

specifically by selective deuteration of samples. However, care should be taken as isotopic substitutions might cause structural change and, consequently, modifications in the relaxational phenomena can occur. In Table 1 are presented a few values of σ_{coh} and σ_{inc} for different elements and isotopes.

It is further worth noting the difference between the values of σ_{inc} for ¹H and ²D. The extraordinary role that hydrogen plays in neutron scattering is explained by its large incoherent cross-section compared to its coherent cross-section. Moreover, σ_{inc} (H) is also much larger than any other element, making incoherent neutron scattering a unique tool for investigating hydrogenous compounds. Because, deuterium is mainly a coherent scatterer, it is highly useful for contrast-matching, for hiding parts of organic molecules or for diffraction experiments. Isotopic incoherence can be avoided by using isotopically pure samples.

2.4. Neutron scattering: the concept of double differential cross-section

In more general terms, in a scattering experiment all neutrons with an energy dE scattered into a certain solid angle $d\Omega$, in a given direction defined by two angles with respect to the incident beam direction and normalized to the unit, are counted by the detector. During the measurements, what is obtained is in reality the partial differential cross-section, $d^2\sigma/dE d\Omega$. Considering a mono-atomic crystal and applying the Born-approximation, this quantity is given by (Squires, 1978):

$$\frac{d^2\sigma}{d\Omega dE} = \frac{k_f}{k_i} \frac{1}{2\pi\hbar N} \sum_{jj'} \overline{b_j b_{j'}} \int_{-\infty}^{+\infty} \langle e^{i\vec{Q}\cdot\vec{R}_j(t)} e^{-i\vec{Q}\cdot\vec{R}_j(0)} \rangle e^{-i\omega t} dt \quad (20)$$

where N is the number of scattering nuclei in the sample, $R_j(t)$ and $R_j(0)$ are the positions of the scatters, t is time and other quantities are defined as before. The double differential cross-section can be divided into one part concerning coherent scattering, which arises from pair correlations between positions of nucleus j at time 0 and different nuclei (including nucleus j) at time t :

$$\frac{d^2\sigma}{d\Omega dE} = \frac{k_f}{k_i} \frac{1}{2\pi\hbar N} b_{coh}^2 \sum_{jj'} \int_{-\infty}^{+\infty} \langle e^{i\vec{Q}\cdot\vec{R}_j(t)} e^{-i\vec{Q}\cdot\vec{R}_j(0)} \rangle e^{-i\omega t} dt. \quad (21)$$

The other part corresponding to incoherent scattering arises from position correlation of the same nucleus at different times. Therefore, incoherent neutron scattering exclusively looks at the dynamics of the molecules themselves. In this case, the double differential cross-section is written as:

$$\frac{d^2\sigma}{d\Omega dE} = \frac{k_f}{k_i} \frac{1}{2\pi\hbar N} b_{inc}^2 \sum_j \int_{-\infty}^{+\infty} \langle e^{i\vec{Q}\cdot\vec{R}_j(t)} e^{-i\vec{Q}\cdot\vec{R}_j(0)} \rangle e^{-i\omega t} dt. \quad (22)$$

Each time correlation described in Eqs. (21) and (22) is a corresponding intermediate scattering function:

$$I_{coh}(\vec{Q}, t) = \frac{1}{N} \sum_{jj'} \langle e^{i\vec{Q}\cdot\vec{R}_j(t)} e^{-i\vec{Q}\cdot\vec{R}_j(0)} \rangle \quad (23)$$

$$I_{inc}(\vec{Q}, t) = \frac{1}{N} \sum_j \langle e^{i\vec{Q}\cdot\vec{R}_j(t)} e^{-i\vec{Q}\cdot\vec{R}_j(0)} \rangle. \quad (24)$$

By factoring the contributions from the translational, rotational and vibrational motions, the expression of the incoherent intermediate scattering function (Eq. (24)) can then be re-written as:

$$I_{inc}(\vec{Q}, t) = \frac{1}{N} \sum_j \langle e^{i\vec{Q}\cdot\vec{R}_j^{trans}(t)} e^{-i\vec{Q}\cdot\vec{R}_j^{trans}(0)} \rangle \langle e^{i\vec{Q}\cdot\vec{R}_j^{rot}(t)} e^{-i\vec{Q}\cdot\vec{R}_j^{rot}(0)} \rangle \langle e^{i\vec{Q}\cdot\vec{R}_j^{vib}(t)} e^{-i\vec{Q}\cdot\vec{R}_j^{vib}(0)} \rangle \quad (25)$$

or simply

$$I_{inc}(\vec{Q}, t) = I_{inc}^{trans}(\vec{Q}, t) I_{inc}^{rot}(\vec{Q}, t) I_{inc}^{vib}(\vec{Q}, t). \quad (26)$$

Performing the temporal Fourier transformation in the intermediate scattering functions, $I(\vec{Q}, t)$ one obtains the so-called scattering functions, described as:

$$S(\vec{Q}, \omega) = \frac{1}{2\pi} \int_{-\infty}^{+\infty} I(\vec{Q}, t) e^{-i\omega t} dt. \quad (27)$$

Therefore, the double differential cross-section can be rewritten as:

$$\frac{d^2\sigma}{d\Omega dE} = \frac{k_f}{k_i} \frac{1}{\hbar} [b_{coh}^2 S_{coh}(\vec{Q}, \omega) + b_{inc}^2 S_{inc}(\vec{Q}, \omega)]. \quad (28)$$

Considering the contributions from the translational, rotational and vibrational modes described in Eq. (26), the incoherent scattering function can be also written as:

$$S_{inc}(\vec{Q}, t) = S_{inc}^{trans}(\vec{Q}, t) \otimes S_{inc}^{rot}(\vec{Q}, t) \otimes S_{inc}^{vib}(\vec{Q}, t) \quad (29)$$

because the Fourier transform of a product of functions is the convolution of Fourier transforms of the individual functions.

Considering scattering from atoms in a crystal, the coherent scattering function can be described in the general form:

$$S_{coh} = |F(\vec{Q})|^2 \delta(\omega) \sum_{\vec{G}/2\pi} \delta(\vec{Q} - \vec{G}) + \sum_{s, \vec{q}} |F_{s, \vec{q}}|^2 \frac{\langle n(\omega) + \frac{1}{2} \pm \frac{1}{2} \rangle}{\omega} \delta(\omega \mp \omega_{s, \vec{q}}) \sum_{\vec{G}/2\pi} \delta(\vec{Q} + \vec{q} - \vec{G}). \quad (30)$$

Here, the first term represents Bragg-scattering. The delta function gives the Laue-condition and $F(\vec{Q})$ is the structure factor defined in Eq. (10). The second term describes inelastic coherent scattering that is due to single excitations (de-excitations) of collective atomic motions with frequencies $\omega_s(\vec{q})$, where \vec{q} is the wave vector of the collective atomic motion and s an index that specifies the various modes of such collective motions. Energy conservation is expressed with the first δ -function:

$$\pm \hbar\omega = E_0 - E_1 = \hbar\omega_s(\vec{q}). \quad (31)$$

The second δ -function implies the inelastic interference condition: neutrons are scattered by the density waves with wave vector \vec{q} originating from collective atomic motions which propagate in phase through the crystal. The expression $\langle n(\omega) + \frac{1}{2} \pm \frac{1}{2} \rangle$ is the thermal population of the initial state and $F_{s, \vec{q}}$ is the dynamical structure factor that is defined as:

$$F_{s, \vec{q}} = \frac{1}{V^{1/2}} \sum_i b_i \left(\frac{\hbar}{M_i} \right)^{1/2} \exp[i(\vec{G} + \vec{q}) \cdot \vec{r}_i] \exp[-W_i(\vec{Q})] (\vec{Q} \cdot \vec{e}_{i, s, \vec{q}}) \quad (32)$$

with the mass of the i -th atom and the unit vector $\vec{e}_{i,s,\vec{q}}$ in the direction of the displacement of atom i being in mode s with a wave vector \vec{q} . Such collective motions manifest themselves in the low energy range of a few meV. However, this signal in a spectrum is generally quite small, especially in hydrogenous compounds, so that the measured spectra are mainly due to incoherent inelastic neutron scattering.

Now, in the next sections a general overview on how the understanding of the spatial and temporal information on the atoms can be achieved using the above equations will be presented.

3. Neutron diffraction in clay minerals

3.1. Smectite swelling at ambient conditions

As already mentioned (Table 1), neutron scattering lengths are isotope-dependent. For instance, neutron scattering lengths for H, D, Si, and Al are -3.74 , 6.67 , 4.15 , and 3.45 fm, respectively. As a consequence, structural studies of water in clay minerals are possible and largely benefit from the isotopic dependence on scattering length. Using $\text{H}_2\text{O}/\text{D}_2\text{O}$ exchange yields additional information that is helpful on getting the precise location of hydrated species. The use of neutron diffraction to study smectite swelling dates back to the end of the 1970s. Cebula et al. (1979) undertook a complete experimental diffraction study on a series of monovalent exchanged montmorillonites (Mt) by combining (i) experiments in classical diffraction conditions to follow the evolution of the (001) reflections as a function of relative humidity, (ii) mosaic spread evaluation by measuring the intensity of (001) Bragg reflections for different positions of samples relative to the neutron beam to obtain the degree of ordering of layers, and (iii) small-angle scattering measurements.

When D_2O was used instead of H_2O (Hawkins and Egelstaff, 1980), it was possible to carry out a one-dimensional (1D) Fourier transform of intensity to obtain scattering density profiles. In the case of Na^+ -Mt this revealed a low degree of structure of the interlayer water, a conclusion in line with numerous subsequent experimental and simulation studies (e.g. Ferrage et al., 2005 and references within). Numerous neutron diffraction studies on Mt took further advantage of isotopic sensitivity to study cation environment in interlayer spaces. For instance, Powell et al. (1997, 1998) used H/D and $6\text{Li}/\text{natLi}$ or $58\text{Ni}/\text{natNi}$ isotopic substitutions to describe two-layer hydrates in Li^+ -Mt- and Ni^{2+} -Mt whereas a similar approach was used for hazardous cations such as Sm or Hg by Sobolev et al. (2007, 2011). In that case, pair radial distribution functions describing the interlayer molecules could be evaluated via Fourier transform of difference functions calculated by subtracting the intensities recorded in the same conditions with two isotopes. Such an approach allows a detailed description of the hydration shell of the cation for various relative humidities. A description of the method and its implications for various environmental issues can be found in the work of Cuello et al. (2008).

Clay minerals with less disorder such as vermiculites or saponites were also studied with regard to their hydration properties. In contrast with Mt both types of samples present much more well-defined hydration steps along the water adsorption isotherms (De la Calle et al., 1978; Michot et al., 2005; Rinnert et al., 2005). Experimentally, it is then easier to control the hydration states that are studied. In the case of vermiculite, Skipper et al. (1991, 1994, 1995) undertook a complete description of the interlayer space, with either monovalent (Li^+ , Na^+), or divalent (Ca^{2+} , Ni^{2+}) counter cations. The method used to derive the interlayer distribution of cations and water molecules was based on an inverse Monte Carlo (MC) technique. Diffraction patterns were recorded after equilibrating the samples with either H_2O or D_2O . The experiments carried out on Li-, Ca-, and Ni-vermiculites (Skipper et al., 1991, 1994, 1995) revealed that in the 2-layer hydrated state, these cations were solvated by six water molecules forming octahedral hydration complexes, giving

rise to more ordered interlayers than for sodium-vermiculite (Skipper et al., 1994).

3.2. Clay structure at non-ambient conditions

Swelling clays, and in particular Mt, are used as barrier materials in the context of hazardous waste disposal (including nuclear waste repositories), where compacted clay (bentonite) barriers are used to inhibit pollutants and contaminants migration (Push, 2006). In this regard, being able to describe bentonite, and specifically smectite hydration behavior in conditions where clay minerals are compacted and confined, often at elevated temperatures, is of prime importance. Neutron diffraction techniques are particularly relevant for studying such phenomena due to the ability of neutron beams to penetrate the walls of sample holders. This is illustrated by a recent work where compacted bentonite samples were equilibrated at various humidities under isochoric conditions (Devineau et al., 2006). The influence of confinement was only observable for the most hydrated bentonite pellets ($p/p_0 = 0.98$). Further studies by small angle neutron scattering on the same systems can be found in the work of Bihannic et al. (2008). A similar system based on compacted vermiculite was recently investigated by neutron diffraction to analyze particle orientation distribution in thick samples (Hubert et al., 2013).

Along similar lines, neutrons can also be used for investigating samples in conditions mimicking deep environments as illustrated in experiments by Skipper et al. (2000), where the swelling of vermiculites was followed under fluid pressures of up to 150 MPa and temperatures of up to 300 °C. The authors took advantage of the low absorption of neutrons by some alloys with high mechanical resistance to conduct experiments in temperature and pressure conditions analogous to those encountered in sedimentary basin conditions.

Moreover, numerous industrial applications use clay minerals exchanged with organic cations, which can completely modify their swelling behavior. This can also be studied using neutron diffraction, and here again the H/D isotope labeling can be advantageously exploited. Although such a feature has been relatively rarely exploited (Swenson et al., 2001b; Williams et al., 1998), the successful results demonstrate that neutron scattering studies on organo-clay interactions is a worthwhile pursuit. Finally, as will be discussed in Section 5.3 neutron diffraction data can be used for assessing the validity of force fields in simulation studies.

4. Quasi-elastic neutron scattering (QENS) of clay minerals

The first studies of smectites by means of QENS date back to 1970 (Hunter et al., 1971; Olejnik and White, 1972; Olejnik et al., 1970) and since then, it has been possible to achieve remarkable results regarding the water dynamics and the variety of diffusion processes in these materials (Bordallo et al., 2008; Chakrabarty et al., 2006; Nair et al., 2005; Gates et al., 2012; Kamitakahara and Wada, 2008; Malikova et al., 2006; Michot et al., 2007; Poinsignon et al., 1987; Swenson et al., 2000; Swenson et al., 2001b).

The QENS signal is formed by atomic translational and rotational motions, mainly from the hydrogens of water, whose time scales are, respectively, 10^{-9} to 10^{-10} s and 10^{-11} to 10^{-12} s. Vibrational modes, with a timescale of 10^{-14} s to 10^{-15} s also play a role, but in the QENS region such signal will mainly contribute to the background (Bée, 1988). Considering a full neutron scattering spectrum, Fig. 4, the QENS signal comprises a region of small energy exchanges between neutrons and the sample, on either side of the elastic line, where the energy exchange is 0. However, one should keep in mind that since the energy and time are connected through the Heisenberg uncertainty relation, the timescale of the motions that can be effectively detected as part of the QENS signal, and not as a component of the elastic line, depends on experimental (energy) resolution. Slower motions, whose energy exchange between the sample and the neutron beam is smaller, require

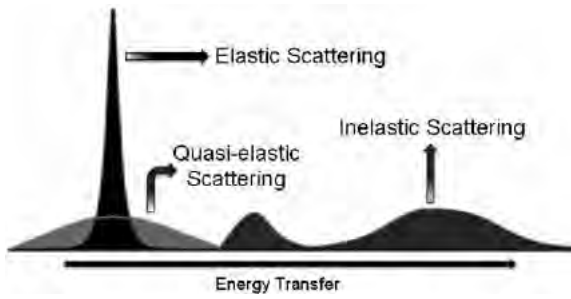


Fig. 4. Elastic and quasi-elastic scattering are both centered at $\omega = 0$. For positive ω the sample gains energy from the neutron by entering an excited state and creating a phonon, this is the Stokes side of the spectrum. For negative ω the sample loses energy to the neutron, which absorbs a phonon, this is the anti-Stokes side of the spectrum.

higher resolutions to be detected. However, higher resolutions can be achieved by reducing the spread in energy in the neutron beam and by using higher values of λ for the neutrons, which leads to flux reduction and a limit in the Q-range in which the analysis can be performed, respectively.

Motions in a timescale of ps can be well accessed by time-of-flight spectrometers, such as IN5 (ILL) or TOF-TOF (FRM2), while slower water diffusion in the ns scale can be studied by means of backscattering spectrometers, such as IN16 (ILL), SPHERES (FRM2), IRIS (ISIS) and BASIS (SNS). Even slower motions, on the order of μ s can be still accessed by the neutron spin-echo technique, for instance in IN15 (ILL), RESEDA (FRM2) and NSE (SNS) (Fig. 5). However, one should note that there is an overlap between the energy resolutions (i.e. time-scales) of time-of-flight (TOF) and backscattering spectrometers, and also between the latter and neutron spin-echo instruments.

Finally, the last part of the neutron scattering spectrum refers to the inelastic neutron scattering (INS). In this region it is possible to observe well defined peaks of fast hydrogen vibrational motions, while at a continuous low energy region ($5 < E < 200$ meV), the study of phonons, librions or librations, mostly related to hydrogen can be made.

4.1. Extracting vibrational, translational and rotational motions from the Quasi-elastic scattering

As pointed out above, in the QENS region, the contributions from lattice vibrations are mainly contained in the background. Therefore, $S_{inc}^{vib}(\vec{Q}, t)$ in Eq. (29) can be substituted with an attenuation term, such as the Debye–Waller factor, $u(T)^2$:

$$S_{inc}(\vec{Q}, t) = [S^{trans}(\vec{Q}, t) \otimes S^{rot}(\vec{Q}, t)] e^{-\frac{(u(T)^2)Q^2}{3}}. \quad (33)$$

In order to describe the translational contribution, the simplest model to be attributed to such motion is an isotropic continuous translation diffusion. Considering the macroscopic diffusion equation:

$$D\nabla^2 G_s(\vec{r}, t) = \frac{\partial G_s(\vec{r}, t)}{\partial t} \quad (34)$$

any model of long-range translational diffusion has to satisfy such an expression, where D is the diffusion coefficient and $G_s(\vec{r}, t)$ is the time-dependent self-correlation function or, more generally, a probability density function. $G_s(\vec{r}, t)$ will then give the probability of finding an atom, which was at the origin at time 0, at position r at a later time t , and can be described by a Gaussian form as:

$$G_s(\vec{r}, t) = \frac{1}{(4\pi Dt)^{3/2}} e^{-r^2/4Dt} \quad (35)$$

which is transformed into a Lorentzian in the (\vec{Q}, ω) domain:

$$S^{trans}(\vec{Q}, \omega) = \frac{1}{\pi} \frac{\Gamma_{trans}}{(\Gamma_{trans})^2 + \omega^2}. \quad (36)$$

Note that $\Gamma_{trans} = D_t \bar{Q}^2$ is the half-width at half-maximum (HWHM) of the Lorentzian curve, where D_t is the translational diffusion

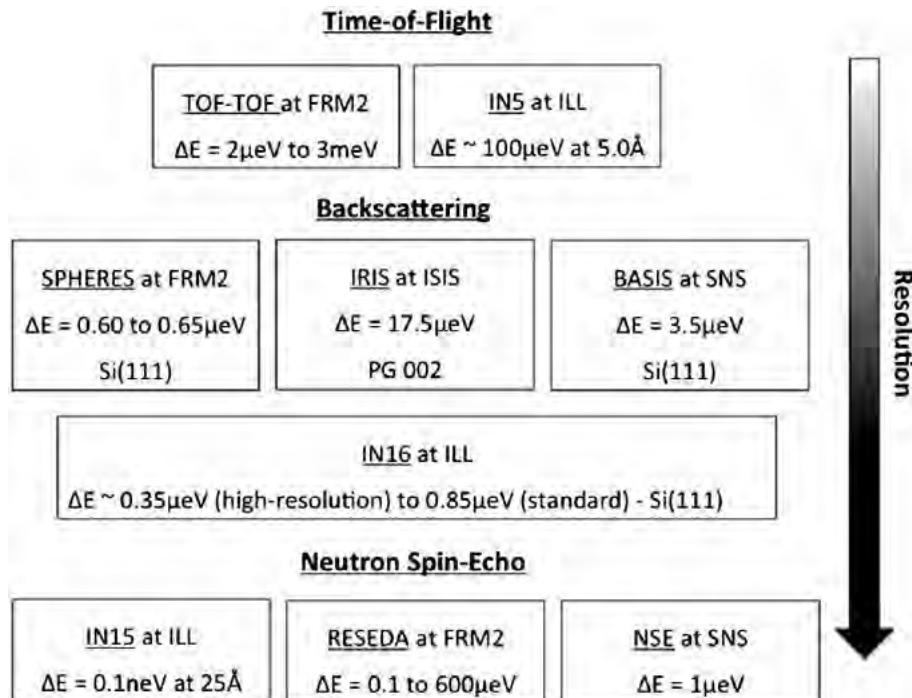


Fig. 5. Values of energy resolution of different instruments of several facilities. TOF spectrometers provide insight about fast water motions while slow water diffusion can be studied by means of backscattering spectrometers as well as by using the neutron spin-echo technique (data available on FRM2, ILL, ISIS and SNS webpages).

coefficient. Finally, in the (\vec{Q}, t) domain, the translational contribution assumes the exponential form:

$$I^{trans}(\vec{Q}, t) = A(\vec{Q})e^{-t/\tau} + B \quad (37)$$

$A(\vec{Q})$ contains the fast dynamical processes, for example librational motions of the molecules, taking place at t too small to be seen in the evolution of $I_{inc}(\vec{Q}, t)$. B corresponds to the fraction of non diffusive H atoms, present in hydroxylated clays and τ is the relaxation time. $1/\tau = D_t \vec{Q}^2$ on the isotropic translational diffusion model.

Regarding the form of the rotational contribution, the simplest assumption is the model of isotropic rotational motion on a sphere, developed by Sears (1967), which considers reorientations of atoms in a molecule by small random angle changes. The corresponding scattering function is an infinite sum over Lorentzians weighted by spherical Bessel functions j_l with increasing l , Fig. 6, plus an elastic part due to the spatial restriction to the sphere:

$$S^{rot}(\vec{Q}, \omega) = A_0(\vec{Q}_a) \cdot \delta(\omega) + \sum_{l=1}^{\infty} A_l(\vec{Q}_a) \frac{1}{\pi} \cdot \frac{\tau_l}{1 + \omega^2 \tau_l^2} \quad (38)$$

where $A_0(\vec{Q}_a)$ is the elastic structure factor, $A_l(\vec{Q}_a)$ is the quasi-elastic structure factor and a is the radius of the sphere on which the molecule rotates. The relaxation time τ_l describes the half-width half-maximum (HWHM) of the Lorentzians. Therefore, considering the models described, both the translational and rotational motions give rise to QENS signals that are described adequately by Lorentzian functions. Consequently, as an example in Fig. 7, an experimental QENS data set can be fitted with a model composed with a convolution of such Lorentzian contributions.

It is now relevant to describe the information that can be accessed by means of the elastic scattering $S_{elas}(\vec{Q}, \omega)$. This part of the neutron scattering spectrum arises from neutrons undergoing no energy exchange after interaction with the sample and contains information concerning the thermal fluctuations of the atoms around their equilibrium position. Moreover, by means of the fixed window approach, elastic incoherent neutron scattering (EINS) measurements can be performed and studies of the structure factor, $S_{elas}(\vec{Q}, \omega \approx 0)$, as a function of temperature in a given Q -range, are possible. Such investigations give special insight on the water dynamics in the material. The evolution of the normalized

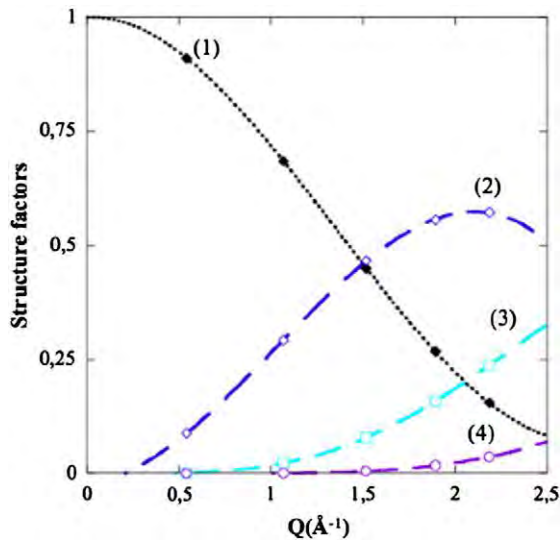


Fig. 6. The spherical Bessel functions included in the first four terms of the Sears expansion. Not all terms contribute to the signal over the entire Q -range and, in practice, no instrument can access all Q s. As a result the Sears expansion can always be approximated to a finite series of Lorentzians.

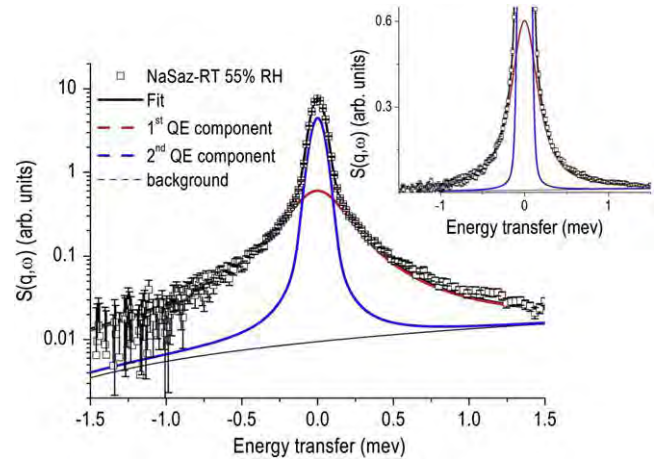


Fig. 7. Example of quasi-elastic experimental spectra (\square) for the Na form of the Arizona Mt (SAZ-1) equilibrated at 55% RH, $Na_{1.03}[Si_{7.98}Al_{0.02}](Al_{2.75}Mg_{1.15}Fe_{0.15})O_{20}(OH)_4 \cdot 6.1 H_2O$, for $Q = 1.1 \text{ \AA}^{-1}$, together with the best fit (solid lines) and the QE component (dotted lines) obtained using NEAT, $DE = 98 \mu\text{eV}$ (Gates et al., 2012). Although in practice a broad range of relaxation times are expected in these smectites giving rise to a sum of many Lorentz functions (Gay-Duchosal et al., 2000), the spectrum is fitted with two Lorentz functions, representing fast and slow motions, respectively. Even if this approach does not provide a more detailed description of the dynamical behavior in such a complex system, it allows a phenomenological analysis of the spectra, where the number of Lorentzian components required within a given energy transfer range is related to the intricacy of the observed dynamics. The inset focus on the larger QE component that can be attributed to faster water (Adapted from Gates et al., 2012).

structure factor with temperature $S_{elas}^{norm}(\vec{Q}, \omega = 0) = S_{elas}(\vec{Q}, \omega = 0) (T)/S_{elas}(T \approx 0)$ can be related to the Debye–Waller factor:

$$S_{elas}^{norm}(\vec{Q}, \omega = 0) = e^{-\frac{\langle u(T)^2 \rangle}{3} Q^2} \quad (39)$$

where $\langle u(T)^2 \rangle$ is the mean square displacement of the atoms and if $\langle u(T)^2 \rangle = 1$, the system follows an harmonic behavior with the normalized elastic signal equal to 1 at low temperatures. At a certain onset, the normalized elastic signal should decrease linearly with increasing temperature if such harmonic behavior remains. However, deviations can be caused by dynamical transitions of the sample, for instance the activation of diffusive motions, Fig. 8. In this case, a sample of Mt was

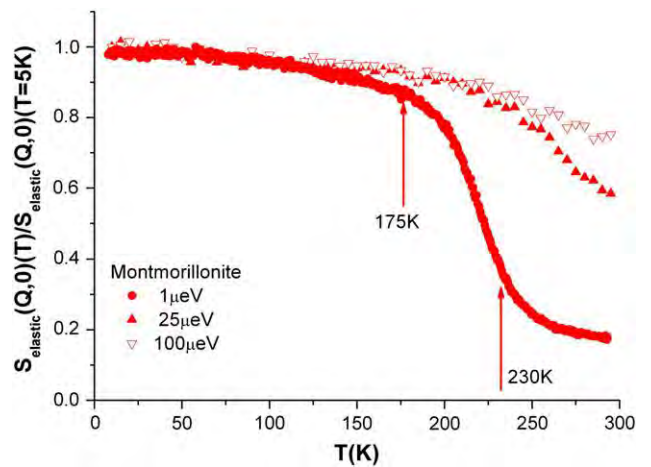


Fig. 8. Example of an elastic incoherent neutron scattering (EINS) measurement performed at IN10 backscattering spectrometer (ILL) and at OSIRIS (ISIS). A sample of Mt was studied and a comparison between the normalized intensity $S_{elas}(\vec{Q}, 0)(T)/S_{elas}(\vec{Q}, 0)(T = 5 \text{ K})$ from three different energy resolutions, 100, 28, and $1 \mu\text{eV}$, as a function of temperature is presented. The arrows indicate the points where $\langle u^2 \rangle$ deviates from the harmonic behavior. Adapted from Bordallo et al. (2008).

studied and a comparison between the normalized intensity $S_{\text{elas}}(\vec{Q}, 0)$ (T)/ $S_{\text{elas}}(\vec{Q}, 0)$ ($T = 5$ K) from three different energy resolutions, 100, 28, and 1 μeV , as a function of temperature, and the Q-range taken between 0.4 and 1 \AA , is presented. The arrows indicate two of the several points where water motions are activated and $\langle u^2 \rangle$ deviates from the harmonic behavior.

4.2. Some QENS studies of clay minerals

As pointed out above, the applications of neutron scattering spectroscopy in studies of clays date back to the 1970s, with investigations on the dynamics of interlamellar water molecules in hydrated Li^+ -vermiculite (Olejnik et al., 1970). In such work, insight on the vibrational motions of the hydrogen in the silicate lattice as well as on diffusional processes in the water layers was obtained. Hunter et al. (1971) also indicated the value of neutron scattering spectroscopy for elucidating the behavior of water molecules very close to the surfaces of Li-vermiculite at different hydration levels. A few years later, Hall and Ross (1978) derived the incoherent scattering function for neutron scattering for an atom or molecule undergoing continuous random walk diffusion in a region bounded by two parallel planes. Therefore a more comprehensive description of molecular diffusion in layered materials was achieved.

The pioneering work of Cebula et al. (1981), using IN5 with an energy resolution of 40 μeV , inferred that for 98% hydrated Li^+ -Mt the water diffusion coefficient was independent of the hydration shell. Later on, Tuck et al. (1984) expanded the analysis to Ca^{2+} -Mt in order to obtain the jump correlation times and found that such value was model-dependent. These findings are related to the fact that the simplest analytical model to describe the diffusion of water in these clays assumed isotropic decoupled translational and rotational motion. After great improvements on the design of neutron spectrometers (Lechner, 1992) provided greater flexibility and improved energy resolution, it rapidly became possible to measure smaller energy transfers and to study slower motions of water in clay minerals with only a few molecular layers of water.

Slight differences in the topology of the surfaces of layer silicates, however, may cause deviations from the isotropic approach, resulting in deviations from the small-angle jump in rotational motion to occur (Ivanov, 1964; Laage and Hynes, 2006), and causing correlations between the translational diffusion and the rotation of the water molecule. Thus to better fit the intermediate scattering functions obtained from QENS experiments, it is generally necessary to add a fitting parameter β to Eq. (37), in order to account for multiple diffusion processes

$$I_{\text{inc}}(\vec{Q}, t) = A(\vec{Q})e^{-(t/\tau)^\beta} + B \quad (40)$$

from which an average relaxation time $\langle \tau \rangle = \frac{1}{\beta} \Gamma\left(\frac{1}{\beta}\right)$ can be estimated. It is essential to bear in mind, however, that this model is expected to be valid only in the low Q-region ($\leq 1 \text{\AA}^{-1}$) and that the time-dependent term describing the rotation of the H atoms around the centers of mass of the water molecules is considered to be sufficiently small.

Another interesting result is the study of the changes caused in the water dynamics under the influence of electrical charge in hectorite, beidellite and vermiculite with Li^+ as the exchangeable cation. Using the features of combining the variable resolution of the time of flight spectrometer IN5 ($\delta E = 20$ and 138 μeV) and the high-resolution offered by the backscattering spectrometer IN10 (1 μeV) different diffusive behaviors attributed to several types of water were reported for the first time (Poinsignon et al., 1989).

The first QENS report for Mt exchanged with alkylammonium (HDTMA) cations in comparison with a Ca^{2+} -Mt showed that the mean jump lengths were quite similar for both samples at equivalent

water contents. However, the residence times were somewhat shorter for HDTMA-clay as compared with Ca^{2+} -Mt (Anderson et al., 1999).

QENS results on the anisotropy of the water mobility in Na^+ -vermiculite at 300 K showed that almost no hydrogen motion occurs perpendicular to the clay layers in the timescale between 2 and 40 ps while an effective diffusion coefficient 2 to 3 times lower than bulk water was reported for the parallel direction. The rotational motion was shown to be directly related to the hydration shells (Swenson et al., 2000).

Differences in the water dynamics related to the presence of cations in clay minerals (Mt and halloysite) were explored as well as the dynamics of their surface water (Bordallo et al., 2008). In this study, by considering that the NSE technique allows reaching the scattering vectors, Q, corresponding to tens of \AA , the authors were able to gather information on the long-range diffusion. On the other hand, by measuring the quasi elastic spectra of reduced charge Mt with or without interlayer water the discrimination of the dynamics of surface water from interlayer water was possible. It was also shown that a quasi-elastic contribution occurs from the magnetic fluctuations caused by the presence of paramagnetic Fe^{3+} ions in the crystalline lattice.

Although the use of NSE to study water dynamics in clay minerals is very recent it has proven to be a worthy technique (Malikova et al., 2005, 2006; Marry et al., 2011).

Meanwhile, works with synthetic fluorinated clay minerals, where OH groups are substituted by F, have also shown interesting results (Kamitakahara and Wada, 2008; Malikova et al., 2008). In such studies one is able to observe quasi-elastic spectra from interlamellar water essentially free of other scattering contributions.

The common picture that has emerged from these studies is that the translational mobility of water in clay minerals is lower than that of bulk water. However, extracting information on local water motions only from neutron scattering experimental data is difficult since, as it has been known for many years, such results are extremely model-dependent. In this sense molecular dynamics simulations have proven to be a valuable tool to interpret such experimental data (Chang et al., 1995; Marry et al., 2008).

5. Molecular dynamics and Monte-Carlo simulations: getting the most of experimental data

Molecular simulations (molecular dynamics and Monte Carlo approaches) offer a description of matter at the atomic level, Fig. 9. Therefore they are useful tools to interpret many experiments covering spatial and time scales matched by neutron scattering in clay minerals.

In molecular dynamics simulations (MD), the atoms are considered as classical objects submitted to the Newton's equation of motion, which is propagated step by step thanks to an algorithm (usually Verlet or Velocity Verlet algorithm (Frenkel and Smit, 2002)). In Monte Carlo simulations (MC), the accessible configurations of the phase space are sampled according to the Metropolis algorithm (Frenkel and Smit, 2002). In both cases, the interactions between the atoms must be calculated using a force-field, which gathers all the atomic parameters necessary for this calculation. Most often, the interaction between two atoms is taken as the sum of an electrostatic interaction, a van der Waals attraction and an interatomic repulsion, which depend on the distance between the atoms. From the trajectories obtained with MD, structural and dynamical quantities like densities, radial distribution functions or diffusion coefficients can be calculated from mean-squared displacements, but also scattering functions, which depend on the relative positions of the atoms according to Eqs. (23) and (24). In MC, dynamical information is not accessible. However, contrary to MD, MC allows simulations using statistical ensembles such as the grand-canonical ensemble, where the number of particles in the system can fluctuate.

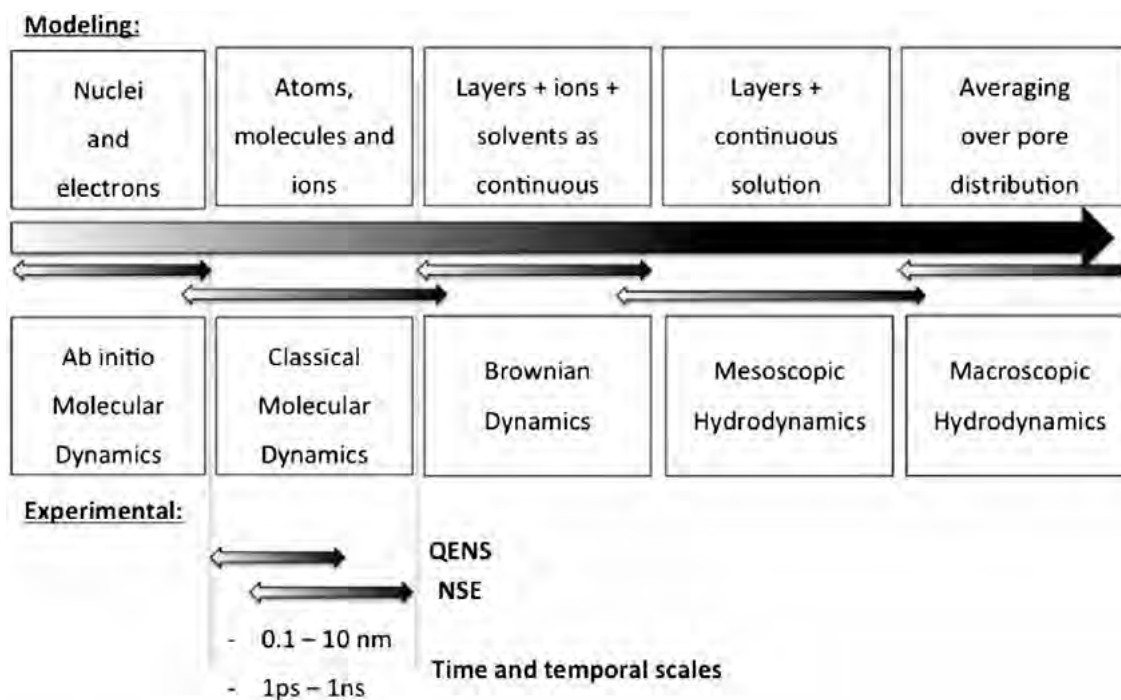


Fig. 9. Spatial and timescales that can be explored by means of molecular simulations as well as a comparison with experimental data.

5.1. Checking and improving the models

First, MD can be used to study the validity of the models chosen to analyze the data. Indeed, once trajectories are obtained, all quantities of interest can be calculated. MD simulations can mimic experimental data, the different components of which can be dissected.

For instance, for a given molecule, the motion of the center of mass and the relative motion of the hydrogen atoms in the referential of the center of mass can be calculated separately, which cannot be done in the real experiment. Thus the global scattering functions of H atoms can be compared to the product/convolution of the translational and rotational components; therefore the assumption that translational and rotational motions are decoupled (Eqs. (26) and (29)) can be checked. It was shown that this assumption is acceptable within a deviation of a few percent (Michot et al., 2007). Moreover, in order to mimic powder samples, the scattering function in the plane parallel or perpendicular to the layers as well as the average over all orientations can be calculated.

An excellent proof of this approach is shown by Marry et al. (2013) where the intermediate scattering functions analyzed from MD trajectories in the plane of the layers are well fitted by the multiple diffusion processes model (Eq. (40)). These results showed that $1/\tau$ as a function of Q^2 is a line over a limited range of Q (from about 0 to approximately 0.7 \AA^{-1}), and that the translational diffusion coefficient (D_t) agrees well with experimental NSE results.

Note that it also corresponds to the value of D obtained independently from the evolution of the mean-squared displacement as a function of t according to:

$$D = \lim_{t \rightarrow \infty} \frac{\langle (r(\vec{t}) - r(\vec{0}))^2 \rangle}{2dt} \quad (41)$$

where d is the dimension of the diffusion process (2 when parallel to clay layers). On the other hand, fitting the $S^{trans}(\vec{Q}, \omega)$ from TOF experiments using the same trajectories by a single Lorentzian function as in Eq. (36) leads to an evolution of the HWHM, Γ_{trans} , which is linear only at small Q_s tending towards a plateau at high Q_s .

The apparent inconsistency between the two analyses at higher Q_s indicates that the physical meaning of the fitting parameters used in the models have to be considered carefully. Indeed, MD simulations show no clear evidence of jump diffusion processes of water molecules in clays, but indicate instead the existence of complex local dynamical phenomena. Nevertheless, traditional fitting procedures remain useful in supporting a comparative goal with other systems.

Now, the interesting question of the orientation of the smectite layers is discussed. Indeed, the system is locally anisotropic and both molecular simulations show that water molecules diffuse differently parallel and perpendicular to the layers. In a powder or a non-perfectly oriented sample, however, these diffusion processes are averaged over all the possible orientations of the particles. If a traditional analysis is always possible (Eqs. (36) and (40)), a more correct approach consists of modeling the scattering functions considering two different diffusion processes (Marry et al., 2013). However, considering different dynamical processes in both directions multiplies the number of fitting parameters, then several sets of parameters can be found to fit the measurements as well. The analysis of the simulated trajectories at least helps to discriminate between realistic and unrealistic sets of parameters.

The same type of analysis can be done for rotational motion, Eq. (38). Michot et al. (2007) showed that the assumption of an isotropic rotational motion on a sphere is acceptable despite the anisotropy of the system and the evidence of preferential orientations of water molecules towards the surfaces. This assumption is not valid for wave vectors higher than 2 \AA^{-1} .

More generally, the complexity of the motions seen in the scattering functions undoubtedly increases with Q . As a consequence, the models used to fit the data at high Q_s need to be more sophisticated, containing more fitting parameters, the meaning of which is not always straightforward. Finally, the limitations of the spectrometers can mask part of the dynamical processes, introducing underestimation of the dynamical quantities during the data fits. For instance, a too coarse resolution in a TOF experiment can mask slow components of the motions, which can be a problem when dealing with complex diffusion processes. This point which has already been addressed in bulk water (Laage, 2009) is very important in clay minerals where dynamical processes are slowed

down due to confinement by the layer structure and the presence of cations in the interlayer space (Malikova et al., 2006). Measurements at multiple energy resolution can be used to address this issue; however, a major limitation remains the neutron flux available. Other types of uncertainties exist with NSE techniques, for instance, the limited range of measured energy transfers leads to a truncation of fast dynamics, and, as a consequence, the factor $A(Q)$ cannot be evaluated and is generally allowed to freely evolve during the experimental data fits (Marry et al., 2008). MD simulations, however, have shown that the water diffusion coefficient was underestimated by about 8% when leaving $A(Q)$ free to evolve (Marry et al., 2013). Thus MD simulations can be used to simulate the experiments at different resolutions and estimate the level of confidence that can be put in the fitting models for a given type of spectrometer.

5.2. Interpreting structural and dynamical features from clay minerals data obtained using neutron scattering

Because simulations allow visualization of the molecules, it is interesting to couple molecular simulations with experiments in order to interpret the data. Such an approach is attractive with neutron scattering, which can offer a description of matter at the same space and time scales.

In this sense, molecular simulations allow evaluation of radial distribution functions and atomic density profiles, especially those perpendicular to the clay layers. These profiles vary according to the hydration level, type of smectite, i.e. the value and the location of its charge and type of compensator cation, which may form either inner or outer sphere complexes. However, as the relative intensities of the (001) Bragg reflections obtained by neutron diffraction depend on these profiles, simulations have first to explain the evolution of the diffraction data with the relative humidity. The simulation works reported by Rinnert et al. (2005) and Ferrage et al. (2005, 2011) provided a degree of confidence in the structural information gained by experiment at the atomic level. For example, they revealed preferential orientations of water molecules towards the surfaces, with the formation of hydrogen bonds with the internal surface oxygen atoms. Thus, they offer a realistic description of the cation hydration, more precise than the picture which can be extracted from the experiments alone, except, perhaps, the polarized infrared studies of adsorbed water molecules in ionic surfaces in Mt, presented by Fripiat et al. (1965). Of course, this type of study can be extended to clays and clay minerals containing other hydrogenated molecules, organic molecules for example (Skipper et al., 2006; Williams et al., 1998).

Moreover, all QENS studies (and molecular simulations) show that water motions in swelling clay minerals slow with decreasing water content. The reasons can be linked to a difficulty for water to move because of the confinement and/or strong interactions with the surface, or to the presence of the interlayer cations, which concentrate a significant part of the water molecules in their hydration shells. Indeed, molecular simulations show that about half of the water molecules are in the first hydration shell of the cations in Ca^{2+} -Mt. This finding was confirmed by the experimental work of Gates et al. (2012).

The evolution of the diffusion coefficients with temperature is also interesting: indeed, assuming that a molecule needs to break its interaction with its environment to be able to move, the diffusion activation energy gives information concerning the strength of bonding between molecules. However few experiments exist detailing this process and those available are not always in agreement. Measurements in natural Mt (Gonzalez-Sanchez et al., 2008; Tuck et al., 1984) showed activation energies lower than in the bulk, although it was found to be higher than in the bulk in synthetic hectorite (Marry et al., 2011, 2013; Soboleva et al., 2010). Because mixtures of different hydrated states can coexist in the natural material, it is possible that the diffusion coefficient at low T is underestimated due to the effect of spectral resolution which is unable to distinguish the slowest water molecules.

MD simulations can also provide interesting information about diffusive processes occurring in clay minerals. Even if the agreement is not always quantitatively equivalent to the QENS experiments, they do show activation energies higher than in the bulk (Marry et al., 2011, 2013; Michot et al., 2012), especially at low temperatures.

In order to explain these results, the relative importance of the interactions with the clay surface and with interlayer cations was studied. It was shown that the presence of the hydrogen bonds formed interlayers at the clay surfaces and can partly explain the slower molecular motions (Marry et al., 2011; Sterpone et al., 2010) but cannot readily explain such an elevation of the activation energy (Marry et al., 2013). On the contrary, the number of hydrogen bonds per water molecule in the interlayer space is rather less than in the bulk, for similar H-bond strength. However, the simulations showed that the water molecules remain within the hydration shell of the interlayer cations for several hundreds of picoseconds (Michot et al., 2012) and that these water molecules were more linked to their environment than in bulk water (Marry et al., 2013). Thus they are linked not just with the cation, but also with the interlayer surfaces of the smectite. Then while the compensator cation is important as indicated by Bordallo, the surfaces may also play a role (Bordallo et al., 2008; Gates et al. 2012).

5.3. How neutron experiments can improve molecular simulations

The previous observations rest on the assumption that molecular simulations give reliable information, i.e. force-fields chosen to simulate the system are accurate. If molecular simulations are helpful for the interpretation of neutron scattering experiments, the latter are useful to check the validity of the former.

In this context, neutron diffraction, especially taking advantage of H/D isotopic sensitivity, represents an extremely stringent test of the structural features obtained by molecular simulations. However, although force fields of water models have been developed since the 80s (Berendsen et al., 1981; Cygan et al., 2004; Smith et al., 2006), only recently after empirical modifications of the ClayFF model (Ferrage et al., 2011) the experimental result could be closely reproduced.

This is shown in recent works on the crystalline swelling of synthetic saponites (Ferrage et al., 2010; Michot et al., 2005, 2007, 2012; Rinnert et al., 2005). The strategy applied for studying such systems, in which the charge can be adjusted, was to measure for various samples' water adsorption isotherms by adsorption gravimetry. From a detailed analysis of the XRD features along the adsorption isotherm, well-defined hydration states were obtained. For each of these states, Grand-Canonical Monte-Carlo simulations were carried out using two widely used force-fields available in the literature, namely Skipper/Smith (Smith et al., 2006) and ClayFF (Cygan et al., 2004), and two water models, SPC and SPC/E (Berendsen et al., 1981). In the SPC, or Simple Point Charge model, the water molecule has three centers of concentrated charge, while the latter represents water as a triatomic molecule with rigid bonds. In parallel, neutron diffraction patterns were recorded for each of these states with both H_2O and D_2O . Simulation results were then used to generate X-ray and neutron diffraction patterns that could be compared with the experimental ones. As an illustration, Fig. 10, the results of applying such a strategy to the case of high-charge saponites with two water layers in the interlayer are presented. It clearly appears that whatever the water model used neither the Skipper/Smith (curves a, b) nor ClayFF (curves c, d) models were able to fully reproduce the experimental neutron diffraction patterns. This is particularly obvious in the patterns obtained with D_2O . On the other hand, it is clear that the slight modification of the ClayFF model (Ferrage et al., 2011) reproduces all the experimental features (Curves d, e in Fig. 10).

This modified ClayFF force field was then used to simulate QENS data and showed quantitative agreement with the experiment (Michot et al., 2012), at least for the synthetic saponite studied.

Progress can still be made in the description of interactions. Indeed, no force-field has yet been able to retrieve quantitatively the structural

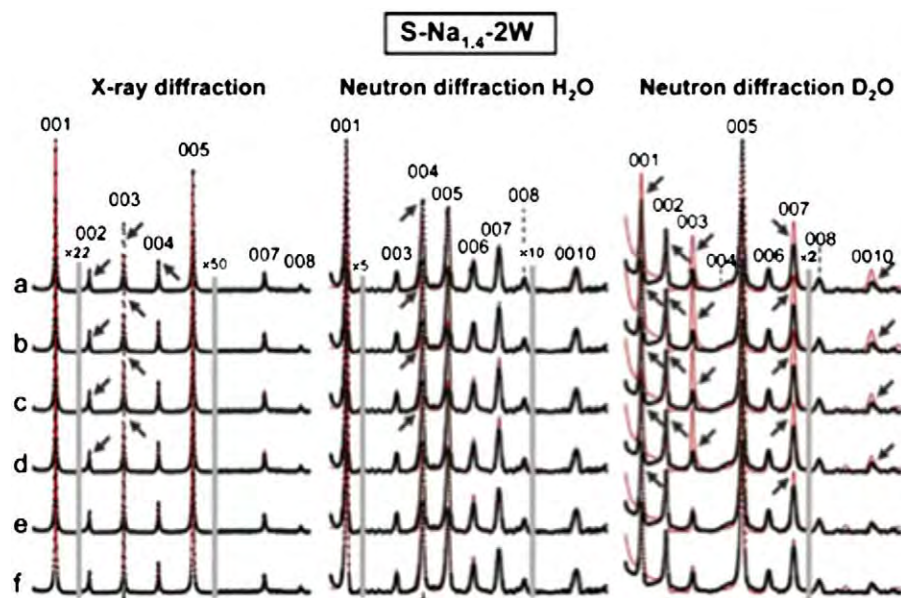


Fig. 10. Experimental (black crosses) and calculated (red lines) intensities of 001 reflections for bihydrated S-Na1.4 and different density profiles of interlayer species. Density profiles were calculated using different force-fields for clay minerals and water: (a) S/SFF + SPC, (b) S/S-FF + SPC/E, (c) ClayFF + SPC, (d) ClayFF + SPC/E, (e) ClayFF-Mod. + SPC, (f) ClayFF-Mod. + SPC/E. The vertical gray bars indicate a modified scale factor for the high-angle regions as compared to the low-angle part of the patterns. Solid arrows indicate a significant misfit between experimental and calculated patterns. 001 reflections are indexed on the top part of the figure (adapted from ref Ferrage et al., 2011).

and dynamical properties of all clay samples. For example, the replacement of hydroxyl groups by fluorine in the synthetic saponite sheets leads to new behaviors of water towards clay mineral surfaces, which are not accurately taken into account by the available force-fields (Marry et al., 2013). As it is known that the presence of an electric field at the surface can polarize water molecules, the creation of polarizable force-fields could help to refine the description of these systems.

Finally, let us underline the importance of sampling in molecular simulations. Calculations made from too short or too few trajectories can lead to biased results (Holmboe and Bourg, 2014), especially when they are compared to experiments which involve times higher than 1 ns. However, this is now rarely a problem, considering the power of current computers.

To conclude, the dialog between neutron experiments and simulations is of prime importance for the understanding of clay minerals, each reinforcing the other one.

6. Final remarks and perspectives

Neutron scattering methods have been applied to problems in the Earth and mineral sciences for many decades and more recently a rebirth of its use has been observed. This current growing interest is partly due to the development of improved neutron sources as well as the development of new methods and instrumentation. With this in mind, and considering that there is a wide range of interesting phenomena of interest to clay scientists that can be studied using neutron scattering, this review article was written not only to describe the versatility of the technique but also to bring attention to the many applications of neutron scattering in clay mineral. Such studies involve engineering issues considered in the construction of clay-based hydraulic barriers, characterization of their internal structure and the study of the associated physico-chemical phenomena. To further contribute to this research field it is necessary to design neutron instrumentation where both flux and variable resolution over a broad Q and dynamic range are available.

Thinking ahead, MIRACLES (Multi-Resolution Analyser Crystal for Life and Energy Science), the proposed European Spallation Source (ESS) backscattering spectrometer (ESS, 2013) will provide access to a unique combination of high energy resolution, intermediate Q , and

large dynamic range. A flexible chopper cascade, matched to the source time structure, will allow a continuous variation of the energy resolution between 2 μeV and 300 μeV together with a variable dynamic range down to about 1 meV. ESS's low repetition rate will provide for an instrument with an un-paralleled dynamic range, perfectly suited for studies of localized relaxational atomic motions with overlapping collective long-range motions. This is expected to revolutionize neutron scattering experimentation of soft materials such as clay minerals.

In addition, at the ESS, neutron spin-echo spectroscopy (ESS, 2013) will reach the longest time scales accessible with neutrons, allowing the measurement of confined liquids in complex structures with fluctuation times of up to 1 μs over many length-scales simultaneously. This type of instrument will accept the full pulse width of ESS, giving rise to a very large improvement in performance compared to the best instruments available today.

Such neutron spectrometers should be combined with new and innovative sample environment. For example, it can mimic the hydration process and allow observation of dynamical information with enough statistics to distinguish how different water populations may be distributed within the complex clay mineral structure in real time. It is, therefore, expected that with the future European Spallation Source such experiments will become standard, and the community will be able to better understand how hydrogen bonds change in a confined space. In addition, from the combination of experiments on these instruments with computer modeling insights, it is then hoped that many challenging questions that are important for our daily life will be finally answered.

Acknowledgments

MLM research is supported through the Brazilian Science without Borders (Process number 246604/2012-3) program. Some travel support was provided to WPG from the Australian Research Council's Discovery Project Scheme DP130102203. HNB thanks the invaluable discussions with Nikolaos Tspatsaris about many issues regarding how to better present the complex theory of neutron scattering to non-experts. We acknowledge the support of the ISIS Facility, ILL and FRM2 for providing the neutron facilities used to perform the

experiments reported by the authors. Financial support was given for travel by the Australian Access to Major Research Facilities Programme and by Danscatt.

References

- Adams, J.M., Breen, C., Riekel, C., 1979. The diffusion of interlamellar water in the 23.3 Å Na-montmorillonite-pyridine/H₂O intercalate by quasielastic neutron scattering. *Clay Clay Miner.* 27, 140–144.
- Anderson, M.A., Trouw, F.R., Tam, C.N., 1999. Properties of water in calcium and hexadecyltrimethylammonium-exchanged bentonite. *Clay Clay Miner.* 47, 28–35.
- Bacon, G.E., 1975. *Neutron Diffraction*. Oxford University Press, Oxford, UK.
- Bée, M., 1988. *Quasielastic Neutron Scattering, Principles and Applications in Solid State Chemistry, Biology and Materials Science*, CRC Press.
- Bérend, I., Cases, J.M., François, M., Uriot, J.P., Michot, L.J., Masion, A., Thomas, F., 1995. Mechanism of adsorption and desorption of water vapour by homoionic montmorillonites: 2. The Li⁺, Na⁺, K⁺, Rb⁺ and the Cs⁺ exchanged form. *Clay Clay Miner.* 43, 324–336.
- Berendsen, H.J.C., Postma, J.P.M., Van Gunsteren, W.F., Hermans, J., 1981. (Chapter 11) In: Reidel, D. (Ed.), *Intermolecular Forces*. Pullman.
- Bihannic, I., Delville, A., Demé, B., Plazanet, M., Villières, F., Michot, L.J., 2008. (Chapter 18) In: Liang, L., Rinaldi, R., Schöber, H. (Eds.), *Neutron Applications in Earth, Energy and Environmental Sciences*. Springer.
- Bordallo, H.N., Aldridge, L.P., Churchman, G.J., Gates, W.P., Telling, M.T.F., Kiefer, K., Fouquet, P., Seydel, T., Kimber, S.A.J., 2008. Quasi-elastic neutron scattering studies on clay interlayer-space highlighting the effect of the cation in confined water dynamics. *J. Phys. Chem. C* 112, 13982–13991.
- Bowers, G.M., Singer, J.W., Bish, D.L., Kirkpatrick, R.J., 2011. Alkali metal and H₂O dynamics at the smectite/water interface. *J. Phys. Chem. C* 115, 23395–23407.
- Brubach, J.B., Mermet, A., Filabozzi, A., Gerschel, V., Lairez, D., Krafft, M.P., Roy, P., 2001. Dependence of water dynamics upon confinement size. *J. Phys. Chem. B* 105, 430–435.
- Cases, J.M., Bérend, I., Besson, G., François, M., Uriot, J.P., Thomas, F., Poirier, J.P., 1992. Mechanism of adsorption and desorption of water vapour by homoionic montmorillonites: 1. The sodium exchanged form. *Langmuir* 8, 2730–2739.
- Cases, J.M., Bérend, I., François, M., Uriot, J.P., Michot, L.J., Tomas, F., 1997. Mechanism of adsorption and desorption of water vapour by homoionic montmorillonite: 3. The Mg²⁺, Ca²⁺, Sr²⁺ and Ba²⁺ exchanged forms. *Clay Clay Miner.* 45, 8–22.
- Cebula, D.J., Thomas, R.K., 1978. Neutron scattering from colloids. *Faraday Discuss. Chem. Soc.* 65, 76–91.
- Cebula, D.J., Thomas, R.K., Middleton, S., Ottewill, R.H., White, J.W., 1979. Neutron diffraction from clay–water systems. *Clay Clay Miner.* 27, 39–52.
- Cebula, D.J., Tomas, R.K., White, J.W., 1981. Diffusion of water in Li–Montmorillonite studied by quasi-elastic neutron scattering. *Clay Clay Miner.* 29, 241–248.
- Chakrabarty, D., Gautam, S., Mitra, S., Gil, A., Vicente, M.A., Mukhopadhyay, R., 2006. Dynamics of adsorbed water in saponite clay: neutron scattering study. *Chem. Phys. Lett.* 426, 296–300.
- Chang, F.C., Skipper, N.T., Sposito, G., 1995. Computer simulation of interlayer molecular structure in sodium montmorillonite hydrates. *Langmuir* 11, 2734–2741.
- Cole, D.R., Herwig, K.W., Mamontov, E., Larese, J.Z., 2006. In: Wenk, H.R. (Ed.), *Reviews in Mineralogy and Geochemistry – Neutron Scattering in Earth Sciences: Neutron Scattering and Diffraction Studies of Fluids and Fluid–Solid Interactions*, pp. 313–362.
- Cuello, G.J., Roman-Ross, G., Fernandez-Martinez, A., Sobolev, O., Charlet, L., Skipper, N.T., 2008. (Chapter 17) In: Liang, L., Rinaldi, R., Schöber, H. (Eds.), *Neutron Applications in Earth, Energy and Environmental Sciences*. Springer.
- Cygan, R.T., Liang, J.J., Kalinichev, A.G., 2004. Molecular models of hydroxide, oxyhydroxide, and clay phases and the development of a general force field. *J. Phys. Chem. B* 108, 1255–1266.
- De Carvalho, R., Skipper, N., 2001. Atomistic computer simulation of the clay–fluid interface in colloidal laponite. *J. Chem. Phys.* 114, 3727–3733.
- De la Calle, C., Suquet, H., Dubernat, J., Pezerat, H., 1978. Mode d'Empilement des feuillets dans les vermiculites hydratées à deux couches. *Clay Miner.* 13, 275–297.
- De Siqueira, A.V., Lobban, C., Skipper, N.T., Williams, G.D., Soper, A.K., Done, R., Dreyer, J.W., Humphreys, R.J., Bones, J.A.R., 1999. The structure of pore fluids in swelling clays at elevated pressures and temperatures. *J. Phys. Condens. Matter* 11, 9179–9188.
- Devineau, K., Bihannic, I., Michot, L.J., Villières, F., Masroui, F., Cuisinier, O., Fragneto, G., Michau, N., 2006. In situ neutron diffraction analysis of the influence of geometric confinement on crystalline swelling of montmorillonite. *Appl. Clay Sci.* 31, 76–84.
- Dianoux, A.-J., Lander, G. (Eds.), 2003. *Neutron data booklet*. ISBN: 0-9704143-7-4. <http://www.ill.eu/top-links/publications/>.
- European Spallation Source (ESS), 2013. In: Peggs, S. (Ed.), *ESS Technical Design Report*.
- Ferrage, E., Lanson, B., Malikova, N., Planon, A., Sakharov, B.A., Drits, V.A., 2005. New insights on the distribution of interlayer water in bi-hydrated smectite from X-ray diffraction profile modeling of 00l reflections. *Chem. Mater.* 17, 3499–3512.
- Ferrage, E., Lanson, B., Michot, L.J., Robert, J.-L., 2010. Hydration properties and interlayer organization of water and ions in synthetic Na-smectite with tetrahedral layer charge. Part 1. Results from X-ray diffraction profile modeling. *J. Phys. Chem. C* 114, 4515–4526.
- Ferrage, E., Sakharov, B.A., Michot, L.J., Delville, A., Bauer, A., Lanson, B., Grangeon, S., Frapper, G., Jimenez-Ruiz, M., Cuello, G.J., 2011. Hydration properties and interlayer organization of water and ions in synthetic Na-smectite with tetrahedral layer charge. Part 2. Toward a precise coupling between molecular simulations and diffraction data. *J. Phys. Chem. C* 115, 1867–1881.
- Frenkel, D., Smit, B., 2002. *Understanding Molecular Simulations, From Algorithms to Applications*. Academic Press.
- Fripiat, J.J., Jelli, A., Poncelet, G., André, J., 1965. Thermodynamic properties of adsorbed water molecules and electrical conduction in montmorillonites and silicas. *J. Phys. Chem.* 69 (7), 2185–2197.
- Gates, W.P., Bordallo, H.N., Aldridge, L.P., Seydel, T., Jacobsen, H., Marry, V., Churchman, G.J., 2012. Neutron time-of-flight quantification of water desorption isotherms of montmorillonite. *J. Phys. Chem. C* 116, 5558–5570.
- Gay-Duchosal, M., Powell, D.H., Lechner, R.E., Rufflé, B., 2000. QINS studies of water diffusion in Na-montmorillonite. *Physica B* 276 (278), 234–235.
- Gonzalez-Sanchez, F., Furanyi, F., Gimmi, T., Van Loon, L., Unruh, T., Diamond, L.W., 2008. Translational diffusion of water and its dependence on temperature in charged and uncharged clays: a neutron scattering study. *J. Chem. Phys.* 129, 174706.
- Greathouse, J.A., Refson, K., Sposito, G., 2000. Molecular dynamics simulation of water mobility in magnesium-smectite hydrates. *J. Am. Chem. Soc.* 122, 11459–11464.
- Hall, P.L., Ross, D.K., 1978. Incoherent neutron scattering function for molecular diffusion in lamellar systems. *Mol. Phys.* 36, 1549–1554.
- Hawkins, R.K., Egelstaff, P.A., 1980. Interfacial water structure in montmorillonite from neutron diffraction experiments. *Clay Clay Miner.* 28, 19–28.
- Holmboe, M., Bourg, I.C., 2014. Molecular dynamics simulations of water and sodium diffusion in smectite interlayer nanopores as a function of pore size and temperature. *J. Phys. Chem. C* 118, 1001–1013.
- Hubert, F., Bihannic, I., Prêt, D., Tertre, E., Nauleau, B., Pelletier, M., Demé, B., Ferrage, E., 2013. Investigating the anisotropic features of particle orientation in synthetic swelling clay porous media. *Clay Clay Miner.* 61, 397–415.
- Hunter, R.J., Stirling, G.C., White, J.W., 1971. Water dynamics in clays by neutron spectroscopy. *Nat. Phys. Sci.* 230, 192–194.
- Ivanov, E.N., 1964. *Sov. Phys.* 18, 1041–1045.
- JCNS, 2012. In: Brückel, Thomas, Heger, Gernot, Richter, Dieter, Roth, Georg, Zorn, Reiner (Eds.), *Neutron Scattering Lectures of the JCNS Laboratory Course held at Forschungszentrum Jülich and the Research Reactor FRM II of TU Munich in Cooperation with RWTH Aachen and University of Münster*.
- Kamitakahara, W.A., Wada, N., 2008. Neutron spectroscopy of water dynamics in NaX and NaA zeolites. *Phys. Rev. E* 77, 041503.1–041503.10.
- Kittel, C., 1996. *Introduction to Solid State Physics*, 7th ed. Wiley.
- Klug, H.P., Alexander, L.E., 1974. *X-Ray Diffraction Procedures: For Polycrystalline and Amorphous Materials*, 2nd ed. John Wiley and Sons, New York.
- Kyakuno, H., Matsuda, K., Yahiro, H., Inami, Y., Fukuoka, T., Miyata, Y., Yanagi, K., Maniwa, Y., Kataura, H., Saito, T., Yumura, M., Iijima, S., 2011. Confined water inside single-walled carbon nanotubes: global phase diagram and effect of finite length. *J. Chem. Phys.* 134 (24), 244501.1–244501.14.
- Laage, D., 2009. Reinterpretation of the liquid water quasi-elastic neutron scattering spectra based on a nondiffusive jump reorientation mechanism. *J. Phys. Chem. B* 113, 2684–2687.
- Laage, D., Hynes, J.T., 2006. Do more strongly hydrogen-bonded water molecules reorient more slowly? *Chem. Phys. Lett.* 433, 80–85.
- Lechner, R.E., 1992. Optimization of the chopper system for the cold-neutron time-of-flight spectrometer NEAT at the HMI, Berlin. *Phys. B: Condens. Matter Phys.* 180, 973–977.
- Malikova, N., Cadène, A., Marry, V., Dubois, E., Turq, P., Zanotti, J.-M., Longeville, S., 2005. Diffusion of water in clays – microscopic simulation and neutron scattering. *Chem. Phys.* 317, 226–235.
- Malikova, N., Cadène, A., Marry, V., Dubois, E., Turq, P., 2006. Diffusion of water in clays on the microscopic scale: modeling and experiment. *J. Phys. Chem. B* 110, 3206–3214.
- Malikova, N., Longeville, S., Zanotti, J.M., Dubois, E., Marry, V., Turq, P., Ollivier, J., 2008. Signature of low-dimensional diffusion in complex systems. *Phys. Rev. Lett.* 101, 265901–265905.
- Marry, V., Turq, P., 2003. Microscopic simulations of interlayer structure and dynamics in bihydrated heteroionic montmorillonites. *J. Phys. Chem. B* 107, 1832–1839.
- Marry, V., Turq, P., Cartailier, T., Levesque, D., 2002. Microscopic simulation of structure and dynamics of water and counterions in a monohydrated montmorillonite. *J. Chem. Phys.* 117, 3454–3463.
- Marry, V., Rotenberg, B., Turq, P., 2008. Structure and dynamics of water at a clay surface from molecular dynamics simulation. *Phys. Chem. Chem. Phys.* 10, 4802–4813.
- Marry, V., Dubois, E., Malikova, N., Durand-Vidal, S., Longeville, S., 2011. Water dynamics in hectorite clays: influence of temperature studied by coupling neutron spin echo and molecular dynamics. *Environ. Sci. Technol.* 45, 2850–2855.
- Marry, V., Dubois, E., Malikova, N., Breu, J., Haussler, W., 2013. Anisotropy of water dynamics in clays: insights from molecular simulations for experimental QENS analysis. *J. Phys. Chem. C* 117, 15106–15115.
- Michot, L.J., Bihannic, I., Pelletier, M., Rinnert, E., Robert, J.-L., 2005. Hydration and swelling of synthetic Na-saponites: influence of layer charge. *Am. Mineral.* 90, 166–172.
- Michot, L.J., Delville, A., Humbert, B., Plazanet, M., Levitz, P., 2007. Diffusion of water in a synthetic clay with tetrahedral charges by combined neutron time-of-flight measurement and molecular dynamic simulations. *J. Phys. Chem. C* 111, 9818–9831.
- Michot, L.J., Ferrage, E., Jimenez-Ruiz, M., Boehm, M., Delville, A., 2012. Anisotropic features of water and ion dynamics in synthetic Na- and Ca-smectites with tetrahedral layer charge. A combined quasi-elastic neutron-scattering and molecular dynamics simulations study. *J. Phys. Chem. C* 116, 16619–16633.
- Nair, S., Chowdhuri, Z., Peral, I., Neuman, D.A., Dickinson, L.C., Tompsett, G., Jeong, H.K., Taspatsis, M., 2005. Translational dynamics of water in a nanoporous layered silicate. *Phys. Rev. B* 71, 104301.1–104301.8.
- Olejnik, S., White, J.W., 1972. The layers of water in vermiculites and montmorillonites – modification of water diffusion. *Nat. Phys. Sci.* 236, 15–16.
- Olejnik, S., Stirling, G.C., White, J.W., 1970. Neutron scattering studies of hydrated layer silicates. *Spec. Discuss. Faraday Soc.* 58, 194–201.

- Ormerod, E.C., Newman, A.C.D., 1983. Water sorption on Ca-saturated clays: II, internal and external surfaces of montmorillonite. *Clay Miner.* 18, 289–299.
- Pitteloud, C., Powell, D.H., Fischer, H.E., 2001. The hydration structure of the Ni²⁺ ion intercalated in montmorillonite clay: a neutron diffraction with isotopic substitution study. *Phys. Chem. Chem. Phys.* 3, 5567–5574.
- Poinsignon, C., Estrade-Swarckopf, J., Conard, J., Dianoux, A., 1987. Proceedings of the International Clay Conference, Denver, pp. 284–291.
- Poinsignon, C., Estrade-Swarckopf, H., Conard, J., Dianoux, A.J., 1989. Structure and dynamics of intercalated water in clay minerals. *Physica B* 156–157, 140–144.
- Powell, D.H., Tongkhao, K., Kennedy, S.J., Slade, P.G., 1997. A neutron diffraction study of interlayer water in sodium Wyoming montmorillonite using a novel difference method. *Clay Clay Miner.* 45, 290–294.
- Powell, D.H., Tongkhao, K., Kennedy, S.J., Slade, P.G., 1998. Interlayer water structure in Na- and Li-montmorillonite clays. *Physica B* 243, 387–389.
- Push, R., 2006. Handbook of Clay Science. In: Bergaya, F., Theng, B.K.G., Lagaly, G. (Eds.), Elsevier, London.
- Rietveld, H.M., 1969. A profile refinement method for nuclear and magnetic structures. *J. Appl. Crystallogr.* 2, 65–71.
- Rinnert, E., Carteret, C., Humbert, B., Fragneto-Cusani, G., Ramsay, J.D.F., Delville, A., Robert, J.-L., Bihannic, I., Pelletier, M., Michot, L.J., 2005. Hydration of a synthetic clay with tetrahedral charges: a multidisciplinary experimental and numerical study. *J. Phys. Chem. B* 109, 23745–23759.
- Ross, K., Hall, P.L., 1978. Incoherent neutron scattering function for molecular diffusion in lamellar systems. *Mol. Phys.* 36, 1549–1554.
- Sears, V.F., 1967. Cold neutron scattering by molecular liquids: III. Methane. *Can. J. Phys.* 45, 237–254.
- Skipper, N.T., Soper, A.K., McConnell, J.D.C., 1991. The structure of interlayer water in vermiculite. *J. Chem. Phys.* 94, 5751–5760.
- Skipper, N.T., Soper, A.K., Smalley, V.M., 1994. *J. Phys. Chem.* 98, 942.
- Skipper, N.T., Smalley, V.M., Williams, G.D., Soper, A., Thompson, C.H.J., 1995. Direct measurement of the electric double-layer structure in hydrated lithium vermiculite clays by neutron diffraction. *Phys. Chem.* 99, 14201–14204.
- Skipper, N.T., Williams, G.D., De Siqueira, A.V.C., Lobban, C., Soper, A.K., 2000. Time-of-flight neutron diffraction studies of clay–fluid interactions under basin conditions. *Clay Miner.* 35, 283–290.
- Skipper, N.T., Lock, P.A., Titiloye, J.O., Swenson, J., Mirza, Z.A., Howells, W.S., Fernandez-Alonso, F., 2006. The structure and dynamics of 2-dimensional fluids in swelling clays. *Chem. Geol.* 230, 182–196.
- Smith, D.E., Wang, Y., Chaturvedi, A., Whitley, H.D.J., 2006. Molecular simulations of the pressure, temperature, and chemical potential dependencies of clay swelling. *Phys. Chem. B* 110, 20046–20054.
- Sobolev, O., Cuello, G.J., Román-Ross, G., Skipper, N.T., Charlet, L., 2007. Hydration of Hg²⁺ in aqueous solution studied by neutron diffraction with isotopic substitution. *J. Phys. Chem. A* 111, 5123–5125.
- Sobolev, O., Cuello, G.J., Scheinost, A.C., Johnson, M.R., Nikitenko, S., Le Forestier, L., Brendle, J., Charlet, L., 2011. The short-range order of ions in clay minerals: Sm³⁺ coordination. *Phys. Status Solidi (a)* 208, 2293–2298.
- Soboleva, O., Buivinh, F.F., Kemner, E., Russinac, M., Beuneud, B., Cuello, G.J., Charleta, L., 2010. Water–clay surface interaction: a neutron scattering study. *Chem. Phys.* 374, 55–61.
- Squires, G.L., 1978. Introduction to the Theory of Thermal Neutron Scattering. Cambridge University Press, New York.
- Sterpone, F., Stirnemann, G., Hynes, J.T., Laage, D., 2010. Water hydrogen-bond dynamics around amino acids: the key role of hydrophilic hydrogen-bond acceptor groups. *J. Phys. Chem. B* 114, 2083–2089.
- Sutton, R., Sposito, G., 2001. Molecular simulation of interlayer structure and dynamics in 12.4 Å Cs-smectite hydrates. *J. Colloid Interface Sci.* 237, 174–184.
- Swenson, J., Bergman, R., Howells, W.S.J., 2000. Quasielastic neutron scattering of two-dimensional water in a vermiculite clay. *J. Chem. Phys.* 113, 2873–2879.
- Swenson, J., Bergman, R., Longeville, S., 2001a. A neutron spin echo study of confined water. *J. Chem. Phys.* 115, 11299.
- Swenson, J., Smalley, M.V., Hatharasinghe, H.L.M., Fragneto, G., 2001b. Interlayer structure of a clay–polymer–salt–water system. *Langmuir* 17, 3813–3818.
- Tuck, J.J., Hall, P.L., Hayes, M.H.B., Ross, D.K., Poinsignon, C., 1984. Quasi-elastic neutron-scattering studies of the dynamics of intercalated molecules in charge-deficient layer silicates. 1. Temperature-dependence of the scattering from water in Ca²⁺-exchanged montmorillonite. *J. Chem. Soc. Faraday Trans.* 80, 309–324.
- Tuck, J.J., Hall, P.L., Hayes, M.H.B., Ross, D.K., Hayter, J.B., 1985. Quasi-elastic neutron-scattering studies of intercalated molecules in charge-deficient layer silicates. 2. High-resolution measurements of the diffusion of water in montmorillonite and vermiculite. *J. Chem. Soc. Faraday Trans.* 81, 833–846.
- Wang, J.W., Kailinichev, A.G., Kirkpatrick, R.J., 2004. Molecular modeling of the 10-Å phase at subduction zone conditions. *Earth Planet. Sci. Lett.* 222, 517–527.
- Wang, J.W., Kailinichev, A.G., Kirkpatrick, R.J., 2006. Effects of substrate structure and composition on the structure, dynamics and energetics of water at mineral surfaces: a molecular dynamics modeling study. *Geochim. Cosmochim. Acta* 70, 562–582.
- Williams, G.D., Soper, A.K., Skipper, N.T., Smalley, V.M., 1998. High-resolution structural study of an electrical double layer by neutron diffraction. *J. Phys. Chem. B* 102, 8945–8949.

Publication II

Martins, M. L.; Saeki, M. J.; Telling, M. T. F.; Parra, J. P. R. L. L.; Landsgesell, S.; Smith, R. I.; Bordallo, H. N. **Development and characterization of a new bio-nanocomposite (bio-NCP) for diagnosis and treatment of breast cancer.** J. alloys compd, 584, 514–519, 2014.

Encapsulation of paclitaxel into a bio-nanocomposite. A study combining Inelastic Neutron Scattering to Thermal Analysis and Infrared Spectroscopy

Murillo L. Martins^{1,2,a}, Andrea Orecchini^{3,4}, Luis Aguilera⁵, Juergen Eckert⁶, Jan Embs⁷, Aleksander Matic⁵, Margarida J. Saeki², Heloisa N. Bordallo^{1,b}

¹Niels Bohr Institute, University of Copenhagen, DK-2100 Copenhagen, Denmark

²Instituto de Biociências - Universidade Estadual Paulista – CP 510, 18618-970 Botucatu – SP, Brazil

³Institut Laue-Langevin, BP 156, 38042 Grenoble, France

⁴Dipartimento di Fisica, Università di Perugia, I-06123 Perugia, Italy

⁵Department of Applied Physics, Chalmers University of Technology, SE-41296 Göteborg, Sweden

⁶Department of Chemistry, University of South Florida, 4202 E. Fowler Ave., Tampa, Florida 33620, United States

⁷Laboratory for Neutron Scattering, Paul Scherrer Institute, CH-5232 Villigen, Switzerland

Abstract. The anticancer drug paclitaxel was encapsulated into a bio-nanocomposite formed by magnetic nanoparticles, chitosan and apatite. The aim of this drug carrier is to provide a new perspective against breast cancer. The dynamics of the pure and encapsulated drug were investigated in order to verify possible molecular changes caused by the encapsulation, as well as to follow which interactions may occur between paclitaxel and the composite. Fourier transformed infrared spectroscopy, thermal analysis, inelastic and quasi-elastic neutron scattering experiments were performed. These very preliminary results suggest the successful encapsulation of the drug.

1 Introduction

Paclitaxel ($C_{47}H_{51}NO_{14}$, hereafter PTX) is an anticancer drug whose effectiveness has been shown against different kinds of tumors [1,2], including breast cancer [3], Fig.1. However, low water solubility and the fact that the drug damages healthy cells still limit its clinical application [4]. These issues can be minimized by encapsulating PTX into a bio-nanocomposite formed by a chitosan capsule modified by apatite crystals. The latter shows great affinity for breast cancer cells [5]. Additionally, by placing magnetic nanoparticles in the core of this bio-nanocomposite (hereafter bio-NCP) can allow for several further applications [6-9].

The synthesis of the bio-NCP itself has been recently reported [11]. Nevertheless, concerning the encapsulation, a number of questions remain open. For instance, it is well known that the PTX's anti-cancer activity is driven by its flexible structure [12-14], but the encapsulation can induce severe dynamical changes and interactions between the drug and the bio-NCP that may affect the releasing

process. This work is the very first attempt to shed light into this particular problem.

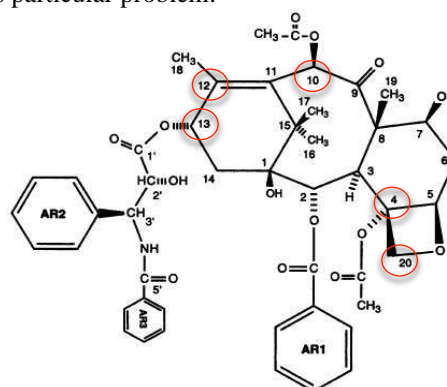


Fig.1. Schematic of the PTX molecule adapted from [10]. Circles highlight C-atoms cited along the text.

To better understand the dynamics of pure and encapsulated PTX, Fourier transformed infrared spectroscopy (FTIR), thermal analysis, as well as inelastic

^a e-mail: murillolongo@gmail.com

^b e-mail: bordallo@nbi.ku

(INS) and quasi-elastic neutron scattering (QENS) measurements were carried out [15]. Our results suggest that the drug can be successfully encapsulated. It seems however that the vibrations from the phenyl and acetyl groups are constrained. The in-vivo implications of this observation to the efficacy of this proposed drug carrier are out of the scope of this paper.

2 Experimental section

2.1. Samples preparation

All chemicals used for the preparation of the samples were purchased from Sigma-Aldrich.

The bio-NCP was prepared following the steps described in [11], with magnetic nanoparticles presenting the nominal formula $Mn_{0.75}Zn_{0.25}Fe_{1.70}O_4$, synthesized in a 0.1M NaOH boiling solution, after a 120 min reaction. In order to modify the chitosan surface with apatite the mimetization process was used [11].

The encapsulation of PTX into the bio-NCP was performed by the double emulsion method, which allows for the inclusion of hydrophobic molecules into hydrophilic systems, i.e. PTX into a chitosan capsule [4]. Hereafter, the sample containing the PTX encapsulated into the bio-NCP will be referred as bio-NCP + PTX.

2.2. Details on the experimental techniques

PTX and bio-NCP + PTX structure was investigated by X-ray powder diffraction (XPD) using the D10B-XPD beamline at the Brazilian Synchrotron Light Laboratory (LNLS, Brazil) using $\lambda=1.24\text{\AA}$.

To evaluate the solid-state properties of PTX, bio-NCP, bio-NCP + PTX and of pure chitosan Thermal Gravimetric Analysis (TGA) and Differential Scanning Calorimetry (DSC) measurements were performed using a TG209 F1 Iris ASC, NETZSCH and a DSC (Q100)-TA instrument, respectively. The measurements were carried out between 120K and 473K.

The dynamics of PTX, bio-NCP + PTX and the bio-NCP were further studied using FTIR, INS and QENS. FTIR measurements were carried out at room temperature between 400 and 4000cm^{-1} using an ATR Crystal (Bruker). INS data were collected at IN4 (ILL-France) at 10K with incident neutrons of about 17meV ($\lambda=2.2\text{\AA}$) and 68meV (1.1\AA). QENS and INS data were obtained with an incident wavelength $\lambda=5\text{\AA}$ (3meV, $\Delta E=100\mu\text{eV}$) using the FOCUS spectrometer (PSI-Switzerland). At FOCUS, PTX was measured at 100K, 150K, 200K, 250K and 300K, while the bio-NCP and bio-NCP + PTX at 100K, 200K and 300K. The analysis of the temperature dependence of the elastic intensity of the PTX data allows for identifying relevant dynamical transitions. For the neutron experiments, the samples were mounted using the slab geometry inside of aluminum containers with a calculated normal beam transmission 0.75. Vanadium runs were used to determine the resolution function and to calibrate the detectors efficiency. To analyze the data, the Bragg reflections were removed, the QENS spectra were fitted using the 1D PAN:Peak Analysis software [16] and the INS data were transformed into the generalized density of vibrational states using LAMP [17].

3 Results and discussion

3.1. Structural characterization

XPD pattern of PTX, Fig.2(a), shows two distinct crystalline phases attributed to a dehydrated and a hydrated form of the drug [19] with space groups P21212 and P1211, respectively. After the encapsulation, due to the loss of translation symmetry, only the ferrite and chitosan reflections can be observed in the bio-NCP + PTX pattern, Fig.2(b).

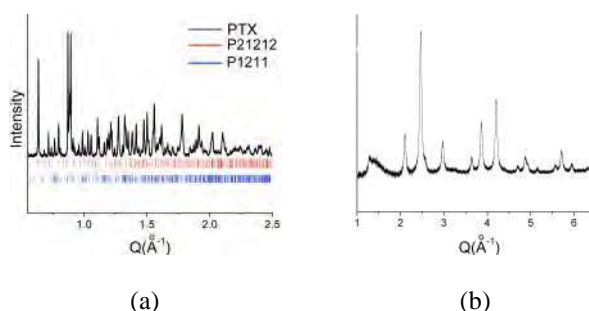


Fig.2. XPD of PTX (a) and bio-NCP + PTX (b) obtained at the LNLS using $\lambda=1.24\text{\AA}$. The PTX pattern shows the presence of both hydrated and dehydrated semicrystalline forms, while in the the bio-NCP patterns only the reflections associated to the ferrite and chitosan are seen.

3.2. Thermal Analysis

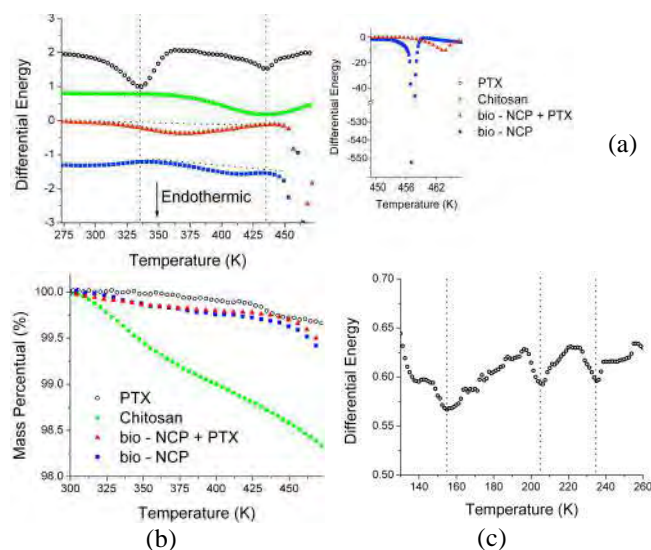


Fig.3. DSC analysis of PTX, bio-NCP, bio-NCP + PTX and pure chitosan between room temperature and 470K (a). The inset shows a comparison between the events in bio-NCP and bio-NCP + PTX above 450K. In (b), TGA shows the water loss in the samples and (c) depicts the DSC analysis for PTX between 120K and 300K.

The DSC and TGA results between 300 and 473K are shown in Figs.3 (a) and (b). An extended phase transition is noted for PTX between 287 and 367K accompanied by a tiny mass loss, while a second endothermic phenomenon is seen at 433K. The first phase transition refers to a partial dehydration of the compound inducing a structural rearrangement, while the second refers to a solid-solid transition [18]. These observations confirm that the analyzed PTX sample is a mixture of hydrated and

dehydrated forms. For pure chitosan, Fig. 3(a), an extended phase transition observed between 370 and 470K is related to a water loss of about 3% [19], while in the bio-NCP and bio-NCP + PTX this same transition is shifted to lower temperatures, i.e. between 340 and 435K and 310K and 430K, respectively. Due to confinement, the water loss in these samples occurs in two steps. As shown in the inset of Fig. 3(a), in the bio-NCP the higher temperature step involves more energy than observed in the bio-NCP + PTX. We can hypothesize that this is caused by a competition between the drug and the water molecules for interacting with the chitosan's NH and OH groups, thus reducing the material's hydration. To confirm this idea the samples were investigated by FTIR, as described below.

In the DSC data collected at lower temperatures, Fig. 3(c), three subtle phase transitions centered at about 155, 205 and 235K are noted for the PTX, while no significant changes are observed for the other samples (data are not presented). Although such changes are very small in the DSC experiment, they might manifest themselves in the neutron scattering experiments [20].

3.2. FTIR data analysis

Regarding the FTIR data, Fig.4, all the PTX vibrational peaks (black line) can be seen in the physical mixture (green line), while in the bio-NCP + PTX (red line) a considerable change in the spectra is noted. Furthermore, as shown in the inset of Fig.4, the PTX bands at 1703 cm^{-1} from the C=O ester stretching and at 1317 cm^{-1} , assigned to the COO stretching [21] present in bio-NCP + PTX confirm the presence of PTX in the composite. Moreover, bending vibrations of NH groups of chitosan, around 1563 cm^{-1} , as well as the vibrations of OH bonds in the primary groups of the polymer around 1414 cm^{-1} , [22] give rise to clear bands in the bio-NCP + PTX. Both observations corroborate with the DSC data, confirming the competition for interactions between PTX and the chitosan's NH and OH groups. Additionally, the prominent peak at 1650 cm^{-1} related to the C-N bonds, [23] is reduced in the bio-NCP + PTX. Since such bonds are formed during the cross-linking reaction and the formation of Schiff bases, which involve the NH groups, the reduction of this peak further reinforces the interaction of the drug with the chitosan.

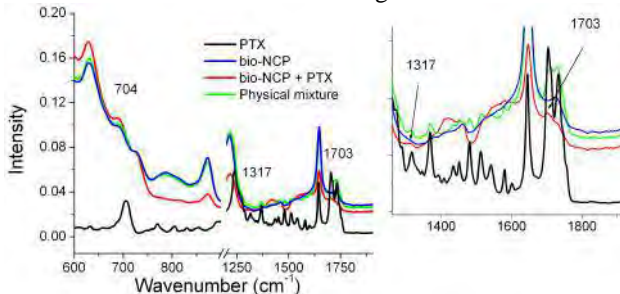


Fig.4. FTIR spectra for PTX (black), bio-NCP (blue), bio-NCP + PTX (red) and physical mixture of bio-NCP and PTX (green). The inset highlights the presence of PTX peaks in the bio-NCP + PTX at 1317 cm^{-1} and 1703 cm^{-1} .

3.2. Neutron Scattering: QENS and Vibrational Spectroscopy Results

Now we turn to the analysis of the temperature dependence of the low frequency spectra of pure PTX obtained on FOCUS, Fig.5(a). In the INS data four main broad bands centered at 80, 150, 103 and 250 cm^{-1} (the latter almost out of the instrument limit) can be observed below 200K. Moreover, a clear change in the vibrational spectra is seen in the same temperature region where the first phase transition was observed in the DSC analysis. This change is also accompanied by the observation of a quasi-elastic (QE) signal. To get insight on the activation energy of the processes related to the QE signal the data was fitted using a Dirac function and a sum of Lorentzians:

$$S_m(Q, \omega) = [A_0(Q)\delta(\omega) + A_1(Q)\sum_i L_i(\Gamma_i, \omega)] \otimes R(\omega) + B \quad (1)$$

where A_i gives the structure factors, A_0 is the elastic incoherent structure factor, $L_i(\Gamma_i, \omega)$ are the Lorentzian functions (QE components), with a half-width at half-maximum (HWHM) Γ . $R(\omega)$ represents the experimental resolution function (vanadium run) and B the background.

In order to get a better statistics the signal was summed over the total Q-range. The data collected at 100K could then be fitted using a single Lorentzian, while for all other temperatures an additional Lorentzian function was necessary to correctly describe the data, see Fig. 5.

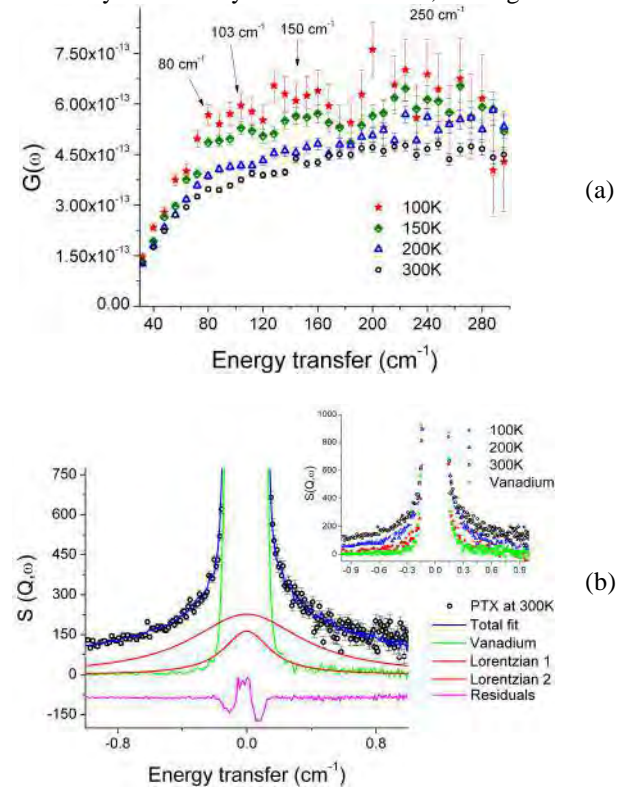


Fig.5. INS (a) and QENS data (b) obtained at 300K for the pure PTX using FOCUS at the PSI. Above 100K the data for PTX was fitted with two Lorentzian functions and one flat background. The inset depicts the QENS data obtained at selected temperatures, where a QE signal is visible.

Fig. 6(a) shows that the temperature dependence of the integrated intensity under the elastic line for pure PTX

reduces ~19% (see the inset) between 100 and 300K, corresponding to the activation of ~10 H in the PTX molecule, or at least three CH₃ groups. In addition, the changes in the slope of the curve at 150 and 200K corroborate well with the phase transitions revealed by the DSC data and the changes in the inelastic part of the spectra. Therefore one can argue that the PTX molecule indeed undergoes some dynamical transitions in this temperature range. Fig. 6(b) depicts the Arrhenius plot of the variation of the full width at half maximum (FWHM) for the drug molecule.

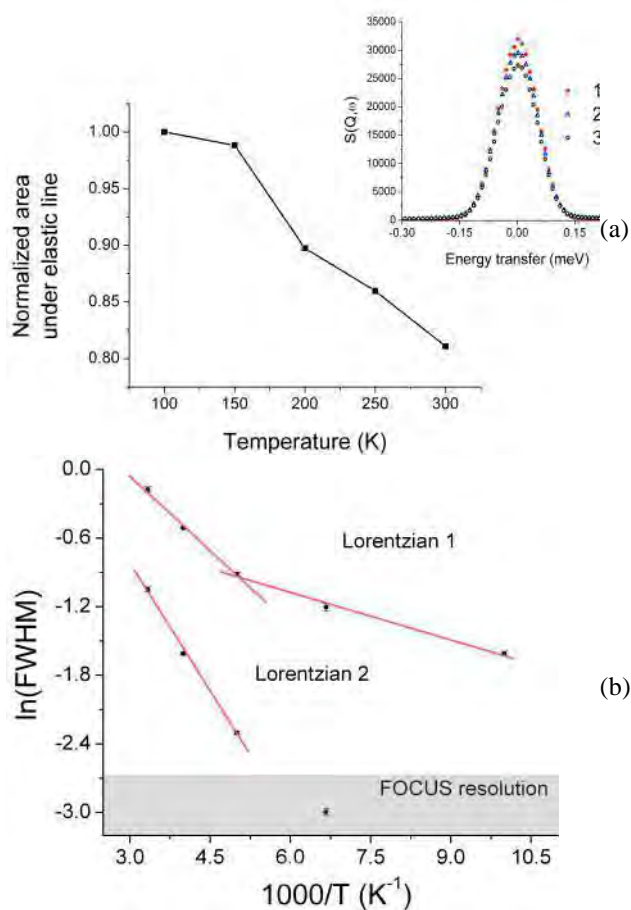


Fig.6. (a) Temperature dependence of the elastic line for pure PTX, shown in the inset for selected temperatures, integrated over the energy resolution interval. (b) Temperature dependence of the Full Width at Half Maximum (FWHM) of the QE signal observed for pure PTX obtained using the fitting procedure described in the text. The red lines indicate the Arrhenius model approximations. The error bars in (a) are smaller than the experimental points.

The relatively different values of the FWHM imply that in the PTX molecules re-orientational motions occur at a broad time scale. Using the Arrhenius law, activation energies of 1.16 and 3.6 kJ/mol were obtained for the first Lorentzian, and 6.11 kJ/mol, for the second one. Assuming that the time scale of our QENS experiments probes mainly the dynamics of methyl groups contained in a harmonic potential with three-fold symmetry, it is possible to crudely estimate the V_3 potential barrier as well as the first librational sub-state from the activation energy of these re-orientational motions using simplified numerical

relations E_{0-1} (meV) = $0.47[V_3(K)]^{0.548}$ and $E_{act}(K) = 0.598[V_3(K)]^{1.05}$ [20]. If this assumption is suitable, one would expect librational peaks around 64, 96 and 144 cm^{-1} . Based on our ongoing DFT calculations (private communication) [24], the two lower vibrations are mainly attributed to the acetyl groups bonded to C4 and C10 and the methyl group in C12, respectively (Fig.1), calculated at 66 and 96 cm^{-1} . Differences between the theoretical and experimental values as well as the broadening in the observed peaks in Fig.5 (a) denote that the methyl groups are not in a pure C_3 symmetry. For the lowest energy the side chain in C13 also plays an important role. Considering the higher energy vibration, calculated at 143 cm^{-1} , a contribution from C20 in the oxetane ring explains the broadening in the observed data.

Regarding the QENS spectra of the bio-NCP and bio-NCP + PTX the data collected at 100K and 200K could be described using a single Lorentzian and a flat background function, while for fitting the bio-NCP + PTX data collected at 300K an additional Lorentzian was necessary. No differences in the QE broadening could be noted at 100K and 200K, suggesting the strong confinement of the PTX inside the bio-NCP. However, as in seen Fig. 7, a slight difference between the bio-NCP and bio-NCP + PTX can be observed at 300K, thus allowing insight into the contribution from the drug itself. A different background offset was needed due to the increasing contribution of the Debye-Waller factor, and for the additional Lorentzian a FWHM value of 0.72meV was obtained. Considering that this value is close to the one found for the first Lorentzian used to fit the PTX data, 0.84meV, we suggest that the extra QE signal observed in the bio-NCP + PTX spectrum at 300K might be assigned to the drug. However, the validation of this idea needs further studies.

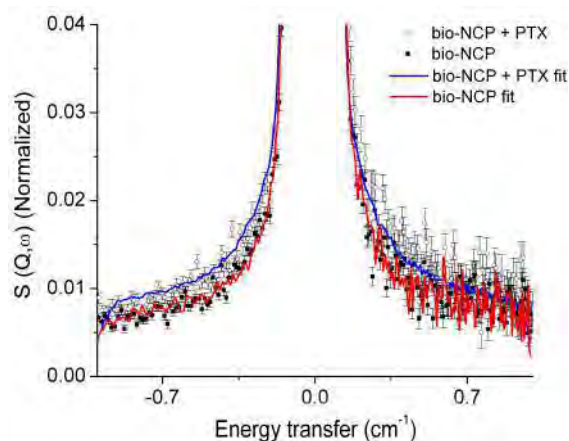


Figure 7. Normalized $S(Q,\omega)$ spectra of the bio-NCP and bio-NCP+PTX at 300K. The results for the fits of the QE signal are also shown.

Insight in the dynamics between 20 and 480 cm^{-1} was by analyzing the IN4 data. As shown in Fig.8, the band centered at 48 cm^{-1} in the PTX spectrum is damped in the bio-NCP + PTX. In this region, the DFT calculations show a great contribution from the PTX phenyl rings and acetyl groups, which therefore seem to be constrained by

encapsulation. In addition, small contributions around 110 cm^{-1} are noted in the difference curve obtained by subtracting the bio-NCP + PTX signal from that collected for the bio-NCP (green curve). Small contributions in the difference curve are further noted in the data collected using incident neutrons with 67.6meV energy around 280 cm^{-1} , 330 cm^{-1} and above 400 cm^{-1} . Such contributions indicate that the encapsulated drug preserves some of its vibrations.

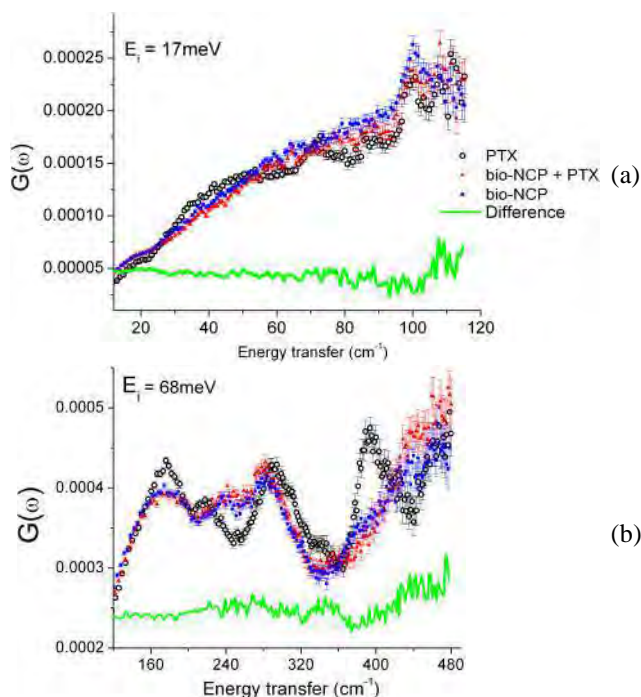


Fig.8. INS spectra collected using IN4 at 10K for PTX (black circles), bio-NCP + PTX (red triangles) and bio-NCP (blue squares). The green curve shows a difference between bio-NCP + PTX and bio-NCP using incident energies of 17 (a) and 68meV (b).

Conclusions and Discussion

Typically thermal analysis methods are considered to be the most suitable approaches for determination of a successful encapsulation process. Normally, these techniques are supplemented by FTIR to show that the loss of the melting peak of the pure drug is due to its complexation rather than thermal degradation or a loss of crystallinity. Generally, the bands due to the complexed part of the drug are shifted or have their intensities altered. However as the mass of the encapsulated drug does not exceed 5–15% of the complex, these alterations are usually hidden, and only in some cases spectroscopic changes indicating complex formation can be observed. In addition, in the case of crystalline drugs such as PTX studied in this paper, encapsulation leads to a disruption of the intermolecular hydrogen bonding of the pure drug. Consequently the Bragg reflections characteristic of the isolated molecules are absent in the XPD patterns of the encapsulated molecule, and only the Bragg reflections characteristics of the encapsulation itself can be observed. Owing to the same reason, intermolecular vibrations

cannot be observed in the complexed system, and no useful information is acquired in the far IR region.

Here we put forward a new idea that by using INS further insight on the local dynamics of the pure drug molecule and how its dynamics is affected by the encapsulation can be obtained. Since neutron scattering is not a surface technique and the sample does not need to be manipulated in order to obtain the data, this probe is extremely suitable for confinement studies. Additionally, we presented results following the classical approach to confirm that PTX was encapsulated into the bio-NCP.

Our results, even if in a very early stage, are encouraging. Using neutron scattering we show that a number of vibrational modes are damped indicating that the PTX molecule is constrained by the encapsulation. Moreover from the analysis of the QENS data we were able to obtain valuable information on the flexibility of the PTX molecular groups, and how this flexibility might be modified by encapsulation in the drug carrier bio-NCP + PTX. Further analyses are under way and will be discussed in a future publication.

MLM work was financed by the Brazilian Science without borders program. Measurements at the Swiss spallation neutron source SINQ has received funding under the NMI3-II Grant number 283883 (MLM), while the Danscatt program financed the experiments carried out at the ILL (MLM and HNB).

References

1. C. Wang, et al., *Int. J Pharm*, **400**, 201(2010).
2. X. Yu, M.V. Pishko. *Biomacromol*, **12**, 3205 (2011).
3. A. Camirand, et al. *Am J Cancer Res.*, **3**, 500 (2013).
4. P. Lv, et al., *Biomacromol*, **12**, 4230 (2011).
5. R. Meena, et al., *J. Nano. Res.* **14**, 712 (2012).
6. C. Alexiou et al., *Eur Biophys J*, **35**, 446 (2006).
7. A.I. Hilger et al., *J Magn.Magn.Mater*, **293**, 314 (2005).
8. T.Moraes et al., *Physiol. Meas.*, **24**, 337 (2003).
9. P.M. Ferguson. *Plos one*, **8**, 2 (2013).
10. D. Mastropaolo et al. *P.N.A.Sci.* **92**, p. 6920 (1995).
11. M.L. Martins et al. *J Alloys Compd*, **584**, 514 (2014).
12. Y.Li et al., *Biochemistry*, **39**, 281 (2000).
13. H.J.Williams, et al., *Tetrahedron*, **49**, 30, 6545 (1993).
14. J.K.Harper et al., *Cryst Growth Des*, **5**, 1737 (2005).
15. M.L. Martins et al., *Appl. Clay Sci.* **96**, 22 (2014).
16. R.T. Azuah, et al., *J. Res. NIST.* **114**, 341 (2009).
17. D. Richard, et al., *J. Neutron Research* **4**, 33 (1996).
18. R.T.Liggins et al. *J Pharm Sci*, **86**, 1458 (1997).
19. C.G.T.Neto et al., *Carb. Polymers*, **62**, 97 (2005).
20. H.N. Bordallo et al., *Biophys Chem*, **148**, 34 (2010).
21. S.Alipour et al., *Colloids Surf B*, **81**, 521 (2010).
22. A.Sionkowska et al., *Biomaterials*, **25**, 795 (2004).
23. J. Klinkaewnarong et al. *App. Phys.* **10**, 521 (2010).
24. M.L. Martins and J. Eckert, private communication.

Publication III

Murillo L. Martins, Andrea Orecchini, Luis Aguilera, Juergen Eckert, Jan Embs, Aleksander Matic, Margarida J. Saeki, Heloisa N. Bordallo. **Encapsulation of paclitaxel into a bio-nanocomposite. A study combining Inelastic Neutron Scattering to Thermal Analysis and Infrared Spectroscopy.** Accepted by European Physical Journal Web of Conferences.



Development and characterization of a new bio-nanocomposite (bio-NCP) for diagnosis and treatment of breast cancer



Murillo L. Martins^{a,b,*}, Margarida Juri Saeki^b, Mark T.F. Telling^{c,d}, Joao P.R.L.L. Parra^b, Sven Landsgesell^e, Ron I. Smith^c, Heloisa N. Bordallo^a

^aNiels Bohr Institute, University of Copenhagen, DK-2100 Copenhagen, Denmark

^bInstituto de Biociências – Universidade Estadual Paulista – CP 510, 18618-970 Botucatu, SP, Brazil

^cISIS, Rutherford Appleton Laboratory, Chilton, Didcot OX11 0QX, UK

^dDepartment of Materials, University of Oxford, Parks Road, Oxford, UK

^eHelmholtz-Zentrum Berlin für Materialien und Energie, Hahn-Meitner Platz 1, D-14109 Berlin, Germany

ARTICLE INFO

Article history:

Received 13 August 2013

Received in revised form 17 September 2013

Accepted 18 September 2013

Available online 27 September 2013

Keywords:

Composites
Nanostructures materials
Chemical synthesis
Synchrotron radiation
Neutron diffraction

ABSTRACT

Breast cancer is a public health problem throughout the world. Moreover, breast cancer cells have a great affinity for hydroxyapatite, leading to a high occurrence of bone metastasis. In this work we developed a bio-nanocomposite (bio-NCP) in order to use such affinity in the diagnosis and treatment of breast cancer. The bio-NCP consists of magnetic nanoparticles of Mn and Zn ferrite inside a polymeric coating (chitosan) modified with nanocrystals of apatite. The materials were characterized with synchrotron X-ray Powder Diffraction (XPD), Time-of-Flight Neutron Powder Diffraction (NPD), Fourier Transformed Infra-red Spectroscopy (FTIR), Scanning Electron Microscopy (SEM) and magnetic measurement with a Physical Property Measurement System (PPMS). We obtained ferrite nanoparticles with a high inversion degree of the spinel structure regarding the Fe and Mn, but with all the Zn in the A site. The coating of such nanoparticles with chitosan had no notable effects to the ferrite microstructure. In addition, the polymeric surface can be easily modified with apatite nanocrystals since the hydration of the bio-NCP during synthesis can be controlled. The resulting bio-NCP presents a spherical shape with a narrow size distribution and high magnetic response at room temperature and is a very promising material for early diagnosis of breast cancer and its treatment.

© 2013 Elsevier B.V. All rights reserved.

1. Introduction

Breast cancer is the most common type of cancer in women throughout the world and its incidence is independent of a country's level of development [1] or on its geographic position [2,3]. Therefore, breast cancer is a worldwide public health problem.

In addition, a high percentage of breast cancer cases lead to metastasis generating secondary tumours, mainly in the bone tissue [4,5]. Such tendency of breast cancer cells to migrate to the bones is most likely due to their affinity to hydroxyapatite $[\text{Ca}_{10}(\text{PO}_4)_6(\text{OH})_2]$ [6]. To date, mammography is the most common technique to diagnose breast cancer, since it is a cheap and accessible approach [7]. However, this technique detects only 65% to 90% of breast cancer cells and such sensitivity can be even lower in patients with dense breast tissue [8] or breast implants [9]. As a result, in certain cases, such as monitoring women with a high risk of breast cancer or scanning patients in search of foci of the

disease, the mammography technique needs to be replaced or used together with more sensitive methods.

In such cases, the use of Magnetic Resonance Imaging (MRI) has increased over the last several years since its sensitivity ranges from 80% to 95% [10]. On the other hand, MRI does report a high rate of false-positive diagnoses (from 20% to 80%) [11]; although such indices could be reduced by using contrast agents capable of targeting breast cancer cells specifically to highlight them during diagnosis procedures. For example, biomarkers such as Oestrogen receptor alpha (ER) and others could be used to target the breast cancer cells [12] as well as to carry a contrast agent. However, despite their efficiency in finding the tumour cells, the markers have no inhibitory action against the metastatic activity of malignant tumours. However it has been shown that crystals of apatite have inhibitory action against different metastatic cells [13–15], including the breast cancer ones [16].

Could breast cancer's affinity for apatite be harnessed to diagnose and treat this disease? If so, the biological properties of hydroxyapatite would require combination with physically and chemically different compounds within a single material. Following this idea, we have developed an innovative and versatile

* Corresponding author. Address: Niels Bohr Institute, Universitetsparken 5, bygn. D, 2100 København Ø, Denmark. Tel.: +45 21 30 88 29.

E-mail address: murillolongo@gmail.com (M.L. Martins).

bio-nanocomposite (bio-NCP), which could possibly be used for both diagnosis and treatment of breast cancer. Such bio-NCP consists of magnetic nanoparticles encapsulated into a polymeric nanosphere whose surface is modified with tiny crystals of apatite.

With regard its application for breast cancer diagnosis, our bio-NCP should be preferentially absorbed by the tumour cells, due to the presence of apatite on the polymer surface. In addition, the presence of magnetic nanoparticles in this material will allow the generation of a high T2 contrast in MRI [17–20], which will highlight the occurrence of abnormal cell activity even if the tumour is in a very early stage. Additionally, the magnetic properties of the bio-NCP could be guided to the breast region with an external magnetic field, thus accelerating the diagnosis process.

Regarding the treatment of breast cancer itself, the use of the same bio-NCP provides a first step in treatment by potentially reducing the formation of metastatic cells or even by using the approach of treating tumours with magnetic hyperthermia, a promising idea in which the first trials for the treatment of brain tumours in human patients have encouraging results [21,22]. More importantly, the configuration of our proposed bio-NCP (i.e. a polymeric nanocapsule) allows for the encapsulation of an anti-tumour drug, thus enabling further functionality as a magnetic drug delivery system.

Regarding the magnetic nanoparticles in this bio-NCP, Mn and Zn ferrite is used instead of γ -Fe₂O₃ (maghemite) or Fe₃O₄ (magnetite) so often used in medical applications [23–26]. Considering that all these compounds have a spinel structure, the presence of two crystallographic sites, A and B, gives rise to a ferrimagnetic arrangement where the magnetic moment on the A site will align antiparallel to any external magnetic field [27]. As a result, the overall magnetic properties of the nanoparticles are related not only to morphological features (i.e. particle size), but also to the ionic distribution within the crystalline structure. In this sense, Mn and Zn ferrites (Mn_(1+y)–_xZn_xFe_(2–y)O₄) provide the opportunity to tuning a wider range of magnetic properties, since molar ratio between Mn, Zn and Fe as well as their distribution within the spinel structure of the ferrite can be changed depending on different application requirements, such as MRI and drug delivering purposes. Moreover, these metals, in low quantities, are non-toxic to humans [28]. The polymeric coating for the bio-NCP is made with chitosan (poly-D-glucosamine), a non-toxic and biocompatible polymer widely used in biological applications [29–32] as well as a support for apatite growth [33].

Here we present all the development steps; from synthesis of the magnetic nanoparticles to the modification of the polymeric surface with apatite nanocrystals. A full characterization of the resulting material, from the microstructure of the magnetic nanoparticles to the properties of the whole assembly, is also reported. Our results provide original and important information about the future development and utilization of this approach against breast cancer. Using this approach, we hope to be able to diagnose as well as to reduce metastatic activity while delivering anti-tumour agents.

2. Materials and methods

2.1. Step 1: synthesis of the magnetic ferrite nanoparticles

Mn and Zn ferrites, Mn_(1+y)–_xZn_xFe_(2–y)O₄, were prepared by the co-precipitation method [34] with $y = 0.30$ and $x = 0.15, 0.20, 0.25$ and 0.30 , using Mn(NO₂)₂, Zn(NO₂)₂ and FeCl₃ (Sigma–Aldrich) as starting salts. To evaluate the influence of Zn composition on the synthesis, the salts were diluted in water, dropped into boiling 0.1 M NaOH solutions, allowed to react for 120 min and the resulting precipitates were collected using a magnet and washed with distilled water. To evaluate the influence of the NaOH concentration, nanoparticles with $x = 0.25$ were also precipitated into 0.5 M and 1 M NaOH solutions. To evaluate the influence of the precipitation time, nanoparticles with $x = 0.25$ were reacted for 0 and 30 min

in 0.1 M NaOH solutions. As will be shown below, it was observed that the nanoparticles with $x = 0.25$ precipitated using a 0.1 M NaOH solution for 120 min have the most useful properties for this study.

2.2. Step 2: coating with chitosan and surface modification with apatite

The optimised magnetic sample was coated with chitosan (Sigma–Aldrich) using the emulsion technique [35] as follows. 20 mg of chitosan were dissolved in 2 mL of acetic solution (4%), and to this solution, 1 mL of 40 mg/mL ferrite suspension was added and stirred for 30 min. The suspension was then added to 100 mL of paraffin oil containing 6.25 mL of oleic acid and vigorously stirred to complete the emulsion formation. To crosslinking, 0.1 mL of a 25% glutaraldehyde solution was added to the emulsion and stirred for 2 h. The resulting coated nanoparticles were washed with diethylether and acetone and dried at room temperature for 48 h.

The nanoparticles samples were dispersed in a 100 mL solution of CaCl₂ (Sigma–Aldrich) to allow the adsorption of Ca²⁺ ions onto the chitosan's surface. This process is called here the "aging" time. Phosphoric acid (H₃PO₄) was then added and the pH was adjusted to 7.4 via addition of NaOH, under stirring to facilitate the reaction of the ions with the polymeric surface. These stirring periods are called here "mimetization" times.

To ensure that only the apatite on the composite's surface was analysed, the nanoparticles covered with modified chitosan were separated using a magnet, washed with distilled water and dried at room temperature under vacuum. The influence of both aging and mimetization times were studied for both 1.50 and 1.67 Ca/P mol ratios using a fixed value of chitosan:apatite mass ratio = 2. After aging time periods of 1 h, 2 h, 4 h, 12 h and 24 h, H₃PO₄ was added to the reaction and stirred for 4 h in all experiments. To study mimetization time, the nanoparticles were allowed to react with CaCl₂ for 1 h and after the addition of H₃PO₄ were stirred for 1 h, 2 h, 4 h, 12 h and 24 h respectively. Finally, the influence of chitosan:apatite mass ratio was also studied for aging and mimetization of 1 h and 4 h and chitosan:apatite mass ratios of 1, 2 and 4.

2.3. Step 4: materials characterization

The crystalline phases formation were investigated by powder diffraction (XPD) using 10 KeV ($\lambda = 1.24$ Å) synchrotron radiation on the D10B-XPD beamline at the Brazilian Synchrotron Light Laboratory (LNLS, Brazil). Neutron powder diffraction (NPD) was obtained using the time-of-flight diffractometer POLARIS (ISIS, UK) [36] to investigate the ionic distribution in the ferrite's spinel structure. All structure refinements were performed using the software package GSAS [37] and input parameter data from the Inorganic Crystal Structure Database (ICSD). The presence of organic groups in the bio-NCP, as well as their hydration level, were further characterized by Fourier Transformed Infrared Spectroscopy (FTIR) using a Nicolet spectrometer, Nexus 670. In addition, morphologic analysis was performed by Scanning Electron Microscopy (SEM) using a FEI microscope, Quanta 200. In this characterization 10 images were obtained for each sample and the mean particle sizes were determined using the software ImagePro. Magnetic response of the selected nanocomposite was studied using a Quantum Design Magnetometer (VSM).

3. Results and discussion

3.1. Synthesis of magnetic ferrite nanoparticles

XPD patterns for the ferrite samples with $x = 0.15, 0.20$ and 0.25 are shown in Fig. 1(a) agree well with the spinel ferrite structure (ICSD 170911). The reduction of cell parameters (see Table 1) with increasing "x" denotes substitution of Mn by Zn into the ferrite. The crystallite sizes [38] also slightly decrease with the addition of Zn and reach the minimum value of 10.07 nm for $x = 0.25$. This composition was considered standard for further evaluation of the synthesis route.

The second stage of the magnetic nanoparticles production the influence of the alkaline solution upon synthesis was verified at $x = 0.25$. Fig. 1(b) highlights the molar dependence of the (311) spinel plane for each sample. The increase of NaOH concentration to 1 M leads to an inhomogeneous crystalline structure and a decrease of the cell parameter. As depicted by the calculated patterns in Fig. 1(b) and by the data presented in Table 1, such sample shows the formation of two distinct spinel phases – one of them with a very small crystallite size (~3 nm) (see the blue fit in Fig. 1(b)) – indicating a delay in crystallization in most part of the sample. Considering that variation in NaOH concentration used in this work does not cause considerable changes to the pH of the

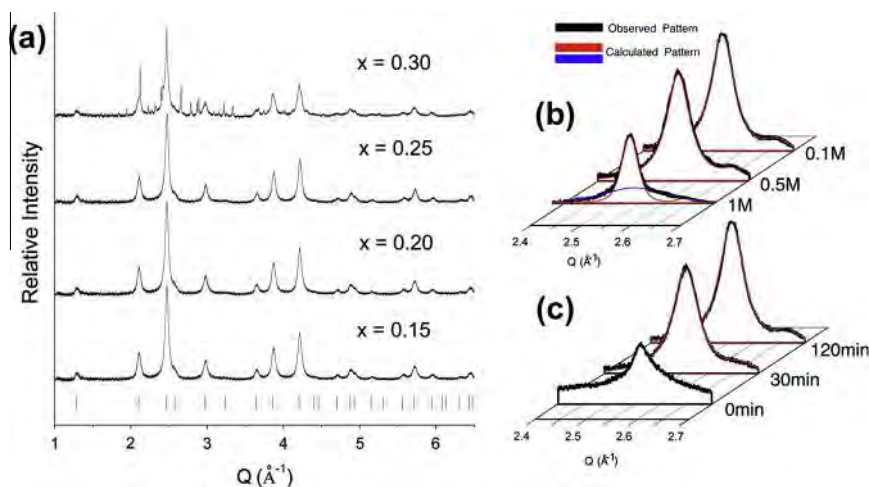


Fig. 1. (a) XPD patterns collected using 10 KeV radiation of $Mn_{(1.30-x)}Zn_xFe_{1.70}O_4$ precipitated with a 0.1 M NaOH solution for 2 h with $x = 0.15, 0.20, 0.25$ and 0.30 . The tick marks indicate the structural peaks of spinel ferrite with space group $Fd-3mZ$ (ICSD 170911). The observed and calculated Bragg peaks associated with the (3 1 1) spinel plane for $x = 0.25$ is depicted for different NaOH solutions (b) and different times (c). Samples with $x = 0.30$ and time = 0 min were not considered to structure refinement. The red lines in (a) and (b) are associated with the main ferrite phase and the blue line in (a) with the delayed spinel phase. (For interpretation of the references to colour in this figure legend, the reader is referred to the web version of this article.)

Table 1
Structural refinement parameters of ferrites nanoparticles with the general formula $Mn_{(1.30-x)}Zn_xFe_{1.70}O_4$ obtained from XPD data collected using 10 KeV synchrotron radiation. The results show the influence of x value, NaOH concentration and precipitation time on the lattice parameters and crystallite sizes. The sample with $x = 0.30$, precipitated in 0.1 M NaOH solution for 2 h, and the sample with the $x = 0.25$, precipitated in 0.1 M NaOH solution for 0 h, were not considered to the structure refinement analysis. The sample marked with bold letters was the one chosen as the ideal synthesis conditions.

x value	[NaOH] (mol/L)	Precipitation time (min)	a (Å)	Crystallite size (nm) ^a	wt%	χ^2 ^b	$R(F2)$ ^c
0.15	0.1	120	8.4479(1)	11.4(4)	–	2.392	0.0354
0.20			8.4326(2)	10.8(3)	–	2.257	0.0345
0.25	1		8.3989(14)	2.4(6)	74	2.354	0.029
			8.4413(2)	15.1(2)	26	–	–
	0.5		8.4300(2)	9.9(2)	–	2.751	0.046
	0.1	30	8.4273(1)	10.1(2)	–	2.515	0.039
			8.4231(2)	9.7(4)	–	2.751	0.046

^a Calculated with the Scherrer's formula.

^b Goodness of fit for Rietveld refinement.

^c Quality of structural refined model.

solutions, the delay in ferrite formation is mostly likely due to the increasing ionic strength into the solution. The reduced cell parameter given in Table 1 for the sample prepared with a 0.1 M solution indicates that this concentration guarantees the desired stoichiometry.

As a next step, the reaction time at $x = 0.25$ in a 0.1 M NaOH solution was evaluated. This sample was allowed to react for 0, 30 and 120 min, and the resulting diffractograms in the region related to the (3 1 1) spinel plane shown in Fig. 1(c) reveal that the crystallite size and cell parameter increases with time, indicating that time for the reaction and “Ostwald Ripening” process is crucial [39]. Indeed, the synthesis process is still incomplete after 30 min. As the ferrite composition with $x = 0.25$ precipitated in 0.1 M NaOH solution for 120 min has a notable structural homogeneity together with reduced crystallite size (Table 1), this sample was therefore considered to be the ideal starting material for the proposed bio-NCP.

To evaluate the ionic distribution in the spinel structure of the chosen ferrite ($Mn_{(1.05)}Zn_{0.25}Fe_{1.70}O_4$) the sample was also analysed by NPD. Fig. 2 shows the collected and calculated neutron diffractograms. A simplified spinel structure is also shown in the inset highlighting the A and B sites and the refinement parameters are shown in Table 2. We identified three distinct spinel phases. Two co-dominant phases (with 47 wt% and 32 wt%) present compositions close to the nominal chemical formula and the best fit was obtained by considering all Zn ions are positioned at the A site.

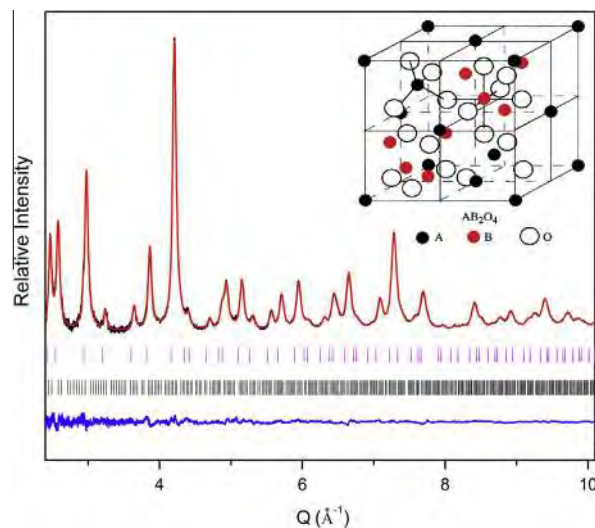


Fig. 2. Observed (black) and calculated (red) neutron diffraction pattern for ferrite nanoparticles with nominal composition $Mn_{(1.05)}Zn_{0.25}Fe_{1.70}O_4$. The blue curve shows the difference between the observed and the calculated patterns. The data was collected using the POLARIS diffractometer (ISIS, UK). The upper tick marks indicate the expected structural peaks of spinel ferrite with (ICSD 170911) and the lower tick marks indicate the expected structural peaks for the FeO (ICSD 40089) (space group $Pm-3m$). In the inset we show a simplified spinel structure adapted from Zhang et al. [24]. (For interpretation of the references to colour in this figure legend, the reader is referred to the web version of this article.)

Table 2

Refinement parameters and the final ionic distribution along the spinel structure obtained from ferrite nanoparticles with the nominal composition $Mn_{(1.05)}Zn_{0.25}Fe_{1.70}O_4$ as determined using NPD. A small amount of FeO (8 wt%) was also detected, but not enough to alter the nanoparticles' magnetic response.

Spinel Phase 1 $Mn_{1.08}Zn_{0.25}Fe_{1.67}O_4$			Spinel Phase 2 $Mn_{0.96}Zn_{0.25}Fe_{1.79}O_4$			Spinel Phase 3 $Mn_1Zn_{0.5}Fe_{0.5}O_4$		
Occupancy	A site	B site	Occupancy	A site	B site	Occupancy	A site	B site
Zn	0.25	–	Zn	0.25	–	Zn	0.5	–
Mn	0.23	0.85	Mn	0.22	0.74	Mn	0.5	1
Fe	0.52	1.15	Fe	0.53	1.26	Fe	–	–
wt% = 47% $a(\text{Å}) = 8.4161(6)$			wt% = 32% $a(\text{Å}) = 8.4422(3)$			wt% = 13% $a(\text{Å}) = 8.4355(20)$		

Refinement indices: $\chi^2 = 1.439$; $R(F2) = 0.0108$.

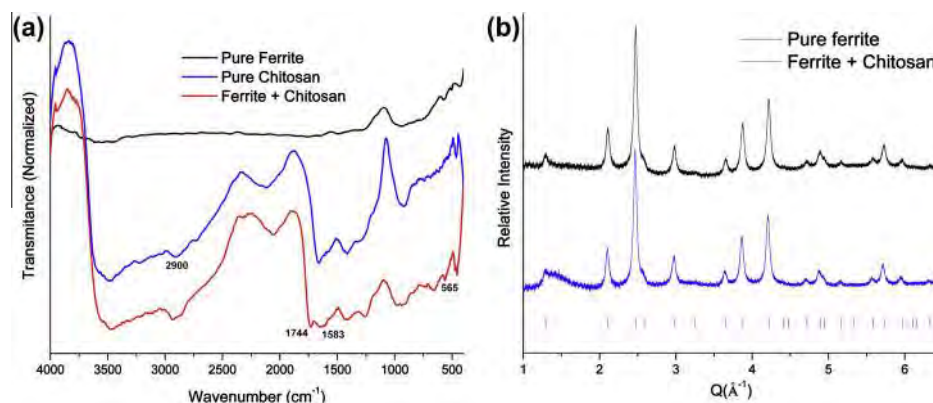


Fig. 3. (a) FTIR spectra of pure nanoparticles, pure chitosan and chitosan coated nanoparticles and (b) XPD patterns of pure nanoparticles and chitosan coated nanoparticles. The tick marks indicate the expected structural peaks of spinel ferrite.

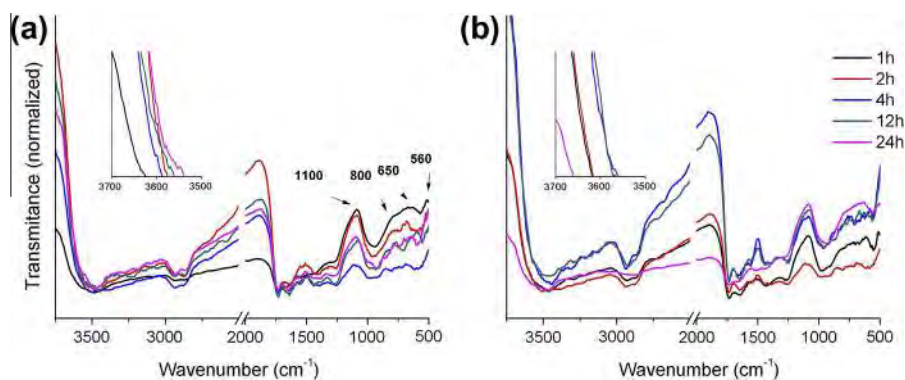


Fig. 4. FTIR spectra for bio-NCPs modified with apatite with $Ca/P = 1.50$. The effects of aging (a) and mimetization time (b) are presented. The insets show the OH bands shift.

Interestingly, both phases also have a very similar distribution of Mn and Fe ions. In the third spinel phase (with 13 wt%) one half of A site is occupied by Zn and the other half is occupied by Fe while the B site is occupied only by Mn. The presence of Zn ions only at the A sites of the spinels is an important result, since the presence of such metal in the B site would reduce the overall magnetization of the ferrimagnetic arrangement.

3.2. Coating the ferrite nanoparticles and apatite deposition

Fig. 3(a) shows FTIR spectra for pure ferrite, chitosan and ferrite coated with chitosan. The arrows indicate a blue shift of the C–H bonds band at 2900 cm^{-1} , as well as in the amide radicals' bands at 1744 cm^{-1} and 1583 cm^{-1} in the coated material. The latter is due to Schiff base formation on the cross-linking process [40]. The weak band at 565 cm^{-1} assigned to the Fe–O bond is notable on the coated ferrite spectra. Interestingly, the XPD patterns

(**Fig. 3(b)**) do not show changes to the ferrite structure, indicative of the formation of a secondary phase, which would jeopardize the magnetic response. The broad peak in the diffraction pattern between 1.5 Å^{-1} and 1.75 Å^{-1} is due to chitosan [33].

Fig. 4 shows the FTIR spectra of the aged (a) and mimetized (b) chitosan coated ferrite modified with apatite for $Ca/P = 1.50$. Analysis of the PO_4^{3-} bands between 1100 and 800 cm^{-1} , formed by the ν_1 , ν_3 and ν_4 vibrations [40] gives insight into the growth of apatite onto the bio-NCP surface, while the OH stretch bands between 3750 and 3250 cm^{-1} refer to the hydration of the material. For the apatite growth, the OH and NH_2 groups of the polymer should not be associated with water molecules, since their free electrons are preferential sites for Ca^{2+} adsorption. Thus, the nanoparticles must be dehydrated to increase the apatite formation, and a red shift in the OH bands would indicate an increase in the amount of water [41]. As **Fig. 4(a)** and (b) illustrate, $Ca/P = 1.50$ is too low to create an ionic strength in the solution capable of

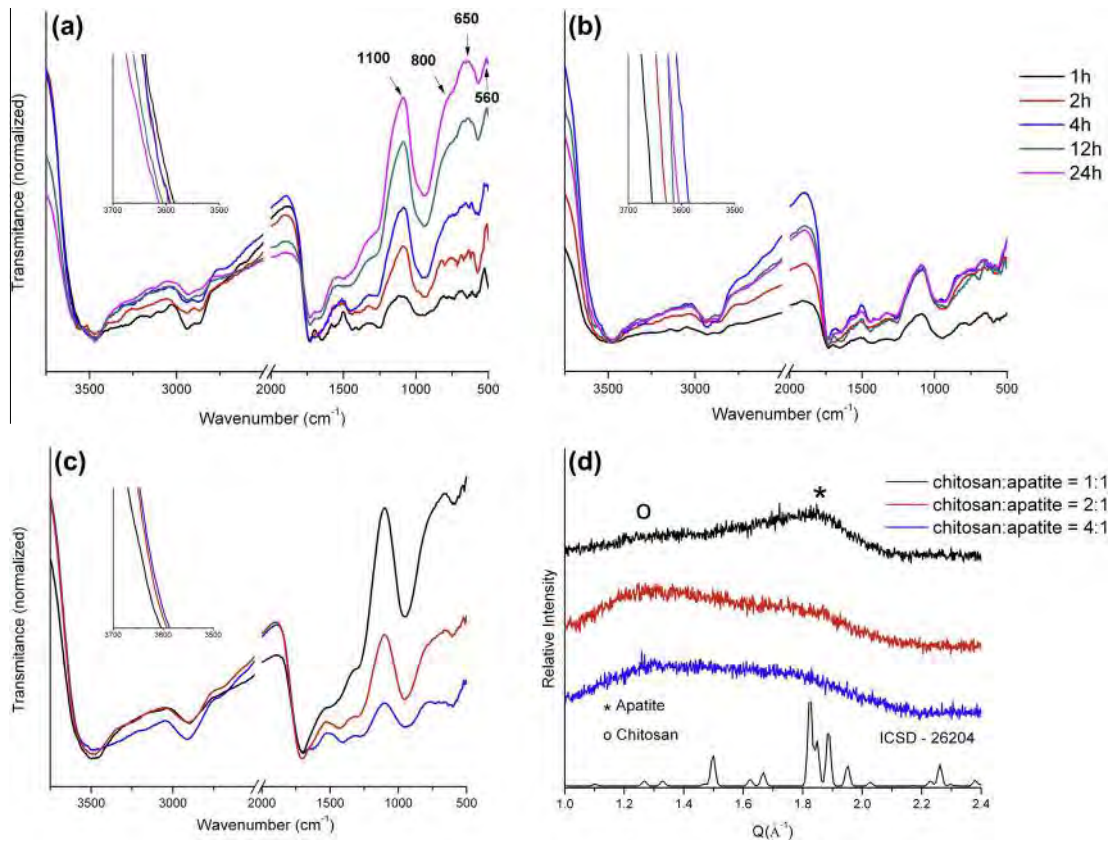


Fig. 5. FTIR spectra for bio-NCPs modified with apatite with Ca/P = 1.67. The effects of aging time (a), mimetization time (b) and chitosan:apatite mass ratio (c) are shown. The insets show the OH bands shift. (d) XPD patterns of bio-NCPs modified with different chitosan:apatite (Ca/P = 1.67) mass ratio. An ICSD profile for apatite is shown.

keeping the water molecules diffusing from the particles to the solution during long reaction times. Thus, an oscillation between the (de)hydration processes in the particles occurs and is reflected by changes in the position of OH bands with time shown in the insets of Fig. 4(a) and (b). As a consequence, the apatite growth is inhibited and no systematic increase of the PO_4^{3-} bands is noted with time. Using a Ca/P ratio of 1.67 the ionic strength was enhanced favouring dehydration of the nanoparticles surface. As the inset of Fig. 5(a) shows, even after 24 h aging time, the OH bands have a blue shift indicating dehydration of the bio-NCP. More relevant, however, is the increase in the intensity of the PO_4^{3-} bands with the reaction time. Fig. 5(b) shows that different mimetization times have little effect on the apatite formation. Finally, Fig. 5(c) depicts the spectra obtained from samples with different amounts of apatite and indicates an increase in the PO_4^{3-} bands together with blue shifts on OH bands as the amount of apatite increases. We argue that the ratio Ca/P = 1.67 allows controlling the (de)hydration processes, leading to stable samples.

To confirm that the increase in the PO_4^{3-} bands is truly related to an increase in the amount of apatite on the bio-NCP surface, one should be able to “see” the apatite structure formation by powder diffraction analysis. Aside from the fact that this compound has a very low scattering signal and tiny crystallite sizes, it adopts a hexagonal structure, whose strongest peaks overlap with the (3 1 1) Bragg peak of the ferrites. In order to get around this issue, we obtained XPD of composites containing (i) only chitosan and (ii) apatite with different chitosan:apatite mass ratios. In Fig. 5(d) we note that the broad apatite peak becomes greater for the chitosan:apatite = 1 sample suggesting the formation of a hexagonal apatite structure, reinforcing the idea that the FTIR signal of the PO_4^{3-} bands is due to the formation of apatite on the surface.

Fig. 6 presents typical SEM images revealing that for a chitosan:apatite mass ratio of 1:1 bio-NCPs of a mean size 200 nm are synthesized, while for a mass ratio of 4:1, particles with a mean size 100 nm and a narrow size distribution are obtained. For applications involving the transit of the bio-NCP inside the body, i.e.

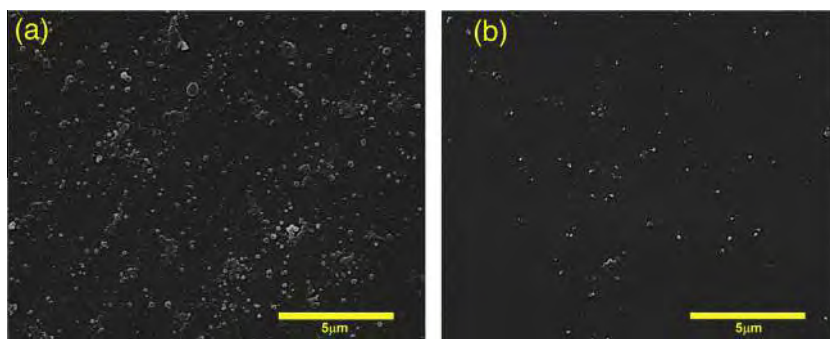


Fig. 6. SEM images for bio-NCPs with chitosan:apatite mass ratio of (a) 1:1 and (b) 4:1.

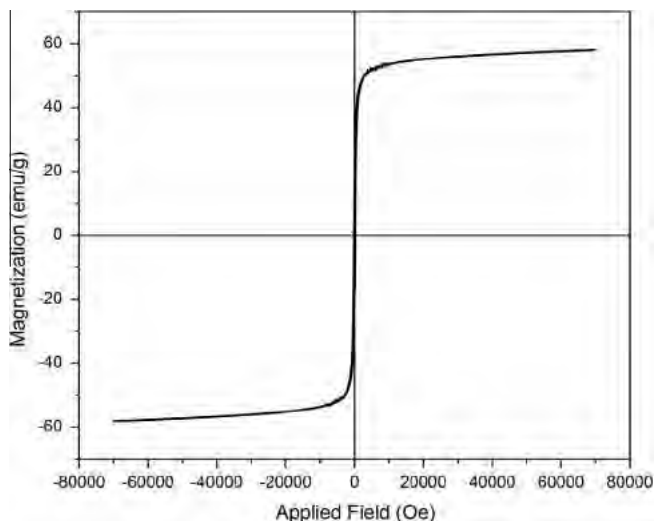


Fig. 7. Hysteresis loop at room temperature for a nanocomposite containing a Mn and Zn ferrite core, covered with chitosan and modified with apatite nanocrystals.

diagnosis and treatment of breast cancer, the narrow size distribution is more desirable, thus the magnetic response of this sample was evaluated. As presented on Fig. 7, a high saturation magnetization equals to 58 emu/g with a reduced hysteresis loss was observed, complying with the required properties for the applications of the bio-NCP as a drug delivery system as well as an MRI contrast agent.

4. Conclusions

The synthesis of a magnetic bio-NCP to be used in early stage breast cancer diagnosis and target treatment is reported. This bio-NCP is based on Mn and Zn ferrite nanoparticles, coated with a biocompatible polymer and modified with apatite nanocrystals. The structural properties of the magnetic nanoparticle itself are easily controlled through synthesis parameters and Mn/Zn ratio. Using the synthesis conditions considered to be the most ideal for this work, we obtained ferrite nanoparticles with a high inversion degree in the spinel structure regarding Fe and Mn, but with all the Zn in A site, contributing to a high magnetic saturation of the material. The coating with chitosan does not cause changes to the particle microstructure and can be easily modified with apatite. The hydration of the bio-NCP during synthesis plays an important role and can be controlled by varying the Ca/P ratio. The final bio-NCP presents a spherical shape, a narrow size distribution and magnetic properties ideal for transiting along the body for medical purposes. To conclude, the bio-NCP developed in this work has the desired physical properties and is a promising material for early diagnosis of breast cancer and its treatment.

Acknowledgments

CAPES, FAPESP, DanScatt and the Science Without Borders Program are thanked for financial support. LaMMB – MagLab, LNLS and ISIS are also acknowledged.

References

- [1] C. Allemani et al., *Int. J. Cancer* 132 (2013) 1170–1181.
- [2] F. Kamangar, G.M. Dores, W.F. Anderson, *J. Clin. Oncol.* 24 (2006) 2137–2150.
- [3] N. Bhoo-Pathy et al., *Eur. J. Cancer* 49 (2013) 703–709.
- [4] A.T. Berman, A.D. Thukral, W. Hwang, L.J. Solin, N. Vapiwala, *Clin. Breast Cancer* 13 (2) (2013) 88–94.
- [5] K.W. Hagberg, A. Taylor, R.K. Hernandez, S. Jick, *Cancer Epidemiol.* 37 (3) (2013) 240–246.
- [6] S.P. Pathi, D.D.W. Lin, J.R. Dorvee, L.A. Estroff, C. Fischbach, *Biomaterials* 32 (2011) 5112–5122.
- [7] D. Shopper, C. De Wolf, *Eur. J. Cancer* 45 (2011) 11.
- [8] F. Sardaneli et al., *Am. J. Roentg.* 183 (2004) 4.
- [9] T.R.C. Johnson et al., *Eur. Radiol.* 23 (2013) 991–996.
- [10] S.J. Lord et al., *Eur. J. Cancer* 43 (2007) 1905–1917.
- [11] N.H.G.M. Peters, I.H.M.B. Rinkes, N.P.A. Zuithoff, W.P.T.M. Mali, K.G.M. Moons, P.H.M. Peeters, *Radiology* 246 (2008) 116–124.
- [12] N. Patani, L. Martin, M. Dowsett, *Int. J. Cancer* 133 (2013) 1–13.
- [13] J. Li, Y. Yin, F. Yao, L. Zhang, K. Yao, *Mater. Lett.* 62 (2008) 3220–3223.
- [14] Y. Yuan, C. Liu, J. Qian, J. Wang, Y. Zhang, *Biomaterials* 31 (2010) 730–740.
- [15] P. Venkatesan et al., *Biomaterials* 32 (2011) 3794–3806.
- [16] R. Meena, K.K. Kesari, M. Rani, R. Paulraj, *J. Nano. Res.* 14 (2012) 712.
- [17] H. Choi, S.R. Choi, R. Zhou, H.J. Kung, I. Chen, *Academ. Radiol.* 11 (9) (2004) 996–1004.
- [18] C. Sun, J.S.H. Lee, M. Zhang, *Adv. Drug. Del. Rev.* 60 (2008) 1252–1265.
- [19] Z.R. Stephen, F.M. Kievit, M. Zhang, *Mater. Today* 14 (2011) 7–8.
- [20] P.M. Ferguson, K.W. Feindel, A. Slocombe, M. MacKay, T. Wignall, B. Delahunt, R.D. Tilley, I.F. Hermans, *P. One.* 8 (2) (2013) 565–572.
- [21] K. Maier-Hauff et al., *J. Neurooncol.* 81 (2007) 53–60.
- [22] K. Maier-Hauff et al., *J. Neurooncol.* 103 (2011) 317–324.
- [23] S. Nigam, K.C. Barick, D. Bahadur, *J. Magn. Mater.* 323 (2011) 237–243.
- [24] V. Chandolu, C.R. Dass, *Curr. Drug. Discov. Tech.* 10 (2) (2013) 170–176.
- [25] D. Kim, S. Lee, K. Im, K. Kim, K. Kim, H. Park, I. Shim, Y. Lee, *IEEE. Trans. Mag.* 41 (2005) 10.
- [26] D.H. Kim et al., *Curr. Appl. Phys.* 6S (2006) e242–246.
- [27] Z.J. Zhang, Z.L. Wang, B.C. Chakoumakos, J.S. Yin, *J. Am. Chem. Soc.* 120 (1998) 1800–1804.
- [28] M. Forsman, *Med. Biol. Eng. Comp.* 38 (2000) 169–174.
- [29] L. Kong, Y. Gao, G. Lu, Y. Gong, N. Zhao, X. Zhang, *Eur. Pol. J.* 42 (2006) 3171–3179.
- [30] S.A. Agnihotri, N.N. Mallikarjuna, T.M. Aminabhavi, *J. Controll. Rel.* 100 (2004) 5–28.
- [31] L. Li et al., *Nanotechnology* 18 (2007) 40.
- [32] S. Shanmuganathan, N. Shanmugasundaram, N. Adhirajan, T.S. Ramyaa Lakshmi, M. Babu, *Carbohydr. Polym.* 73 (2008) 201–211.
- [33] Y. Zhang, J.R. Venugopal, A. El-Turki, S. Ramakrishna, B. Su, C.T. Lim, *Biomaterials* 29 (2008) 4314–4322.
- [34] D. Zhao, X. Wang, X. Zeng, Q. Xia, J. Tang, *J. Alloys Comp.* 477 (2009) 739–743.
- [35] A.N. Maitra, P.K. Ghosh, T.K. De, S.K. Sahoo, Process for the preparation of highly monodispersed hydrophilic polymeric nanoparticles of size less than 100 nm, US Patent, 5,874,111, 1999.
- [36] R.I. Smith, S. Hull, A.R. Armstrong, *Mater. Sci. Forum.* 166–9 (1994) (1993) 251–256.
- [37] A.C. Larson, R.B. Von Dreele, General structure analysis system (GSAS), Los Alamos National Laboratory Report, 86 (2004) 748.
- [38] A.L. Patterson, *Phys. Rev.* 56 (1939) 978–982.
- [39] G.Y. Li, Y.R. Jiang, K.L. Huang, P. Ding, J. Chen, *J. Alloys Comp.* 466 (2008) 451–456.
- [40] J. Klinkaewnarong, E. Swatsitang, C. Masingboon, S. Seraphin, S. Maensiri, *Curr. App. Phys.* 10 (2010) 521–525.
- [41] J. Madejová, *Vib. Spectrosc.* 31 (2003) 1–10.

Publication IV

Murillo L. Martins, Rosanna Ignazzi, Juergen Eckert, Benjamin Watts, Ramon Kaneno, Margarida J. Saeki and Heloisa N. Bordallo. **Study on the antitumor drug paclitaxel encapsulated into a magnetic chitosan/hydroxyapatite bio-nanocomposite and first insights on the released drug.** In elaboration.

Study on the antitumor drug paclitaxel encapsulated into a magnetic chitosan/hydroxyapatite bio-nanocomposite and first insights on the released drug

Murillo L. Martins^{1,2}, Rosanna Ignazzi¹, Juergen Eckert³, Benjamin Watts⁴, Ramon Kaneno², Margarida J. Saeki² and Heloisa N. Bordallo¹*

¹Niels Bohr Institute, University of Copenhagen, DK-2100 Copenhagen, Denmark.

²Instituto de Biociências - Universidade Estadual Paulista – CP 510, 18618-970 Botucatu – SP, Brazil.

³Department of Chemistry, University of South Florida, 4202 E. Fowler Ave., Tampa, Florida 33620, United States.

⁴Swiss Light Source, Paul Scherrer Institute, CH-5232 Villigen, Switzerland.

Abstract

Cancer is the second most common cause of death in the US and in Europe. In principle, anyone can develop cancer, with a higher chance to happen in adults who are middle aged or older. In most part of cases cancer is treated with surgery, radiation and/or chemotherapy. Regarding the latter, Paclitaxel (PTX) is one of the most effective anti-cancer drugs currently available, however it instigates a number of undesirable side effects, which can be reduced by encapsulating the drug. The aim of this work was to study the dynamics of PTX encapsulated into a bio-nanocomposite (bio-NCP) that combines the magnetic properties of Mn-Zn ferrite nanoparticles to the biocompatibility of chitosan and hydroxyapatite. The study on the encapsulated drug dynamics was performed by means of state-of-the-art solid-state techniques, such as Near Edge X-Ray Absorption Fine Structure (NEXAFS), neutron scattering and infrared spectroscopies combined to DFT calculations and Scanning Transmission X-ray Microscopy (STXM). Our results show that the drug carrier has a core-shell like structure with the PTX distributed along the polymeric part. This

conformation leads to the containment of many of the active parts of the molecule, which seem to be recovered after the release. Initial, in-vitro testes showed the non-toxicity of the bio-NCP in macrophages. However considerable morphological changes were noted in colon (HCT116) and lung (3LL) cancer cells after being in contact with the composite. Further studies are necessary in order to understand the toxicity of the bio-NCP in cancer cells.

1. Introduction

Cancer is one of the biggest worldwide public health concerns. Specifically in Europe, the incidence of this disease has increased from 3.2 million new cases in 2008 to 3.45 million in 2012, with a death rate around 50% [1,2]. Certainly, new approaches for early diagnosis and treatment are still an arduous challenge, which calls for interactions between scientists from different areas, such as medicine, biology, chemistry, physics and mathematics.

Currently, the most common cancer treatment approaches are radio and chemotherapy, or a combination of both. The latter has, in fact, provided the best results in most types of cancer [3]. Radiotherapy is based on the application of a well-calculated radiation dose into the tumor tissue, while chemotherapy is based on drugs that are able to disrupt or interrupt the cancer cell life cycle. However, both techniques present drawbacks, for example the low efficiency of radiotherapy in multiple metastasis cases and the serious damage to life quality caused by chemotherapy [4,5].

Paclitaxel (PTX) is one of the most effective currently available anti-cancer drugs in the treatment of breast, lung and ovarian cancer treatments [6-9]. Its peculiar mechanism of action, based on the stabilization of cell microtubules, explains such a success. However, considerable limitations still exist, especially PTX low water

solubility ($\sim 0.4 \mu\text{g/mL}$) and its toxicity in healthy cells. To increase solubility, a drug is often formulated in organic solvents, such as dehydrated ethanol and polyoxyethylated castor oil. However, this approach causes many side effects, such as hypersensitivity reactions and hyperlipidaemia [10]. As an alternative, a promising approach is the development of new encapsulation systems for drug delivery. A common methodology is the use of soluble polymeric nano-carriers that allows for controlling the pharmacokinetic and biodistribution of the drug. Under these lines, the biopolymer chitosan has attracted great interest in biomedical applications due to its biocompatibility and biodegradability. This path has also been used as a PTX encapsulation matrix with satisfactory results [11,12].

On the other hand, toxicity of a drug to healthy cells can be attenuated by encapsulating the substance into a nanocomposite with the surface modified by compounds with low toxicity. Additionally, this procedure may further improve the drug adhesion to the cancer cells [13]. In this case, hydroxyapatite [$\text{Ca}_{10}(\text{PO}_4)_6(\text{OH})_2$] (HAP), which is the main inorganic constituent of human bones and teeth, is the candidate of choice. In the nano-scale, HAP presents special biocompatibility, non-immunogenicity, non-inflammatory behavior and high osteoconductivity and, most importantly, good adhesion to cancer cells, for example, from the breast [13,14]. Nanocomposites loaded with HAP nanoparticles have already shown anti-tumor properties in colon, prostate, liver, breast and other cancers [15-20].

Additionally to the features provided by the polymer and HAP modification, the inclusion of a drug into nano-carriers with magnetic properties, provided for example by Mn-Zn ferrites nanoparticles, offers remarkable possibilities. For instance, by using an external magnetic field it is possible to guide the drug along the body and attach it in the tissue of interest [21]. Moreover, the position of the material can be

easily monitored by either low cost gradiometric systems or by magnetic resonance imaging apparatus. Finally, an additional cancer treatment approach is possible by magnetic hyperthermia, which represents a cheap and promising technique to be used in combination to radio and chemotherapy [22-24].

The synthesis procedure of a bio-nanocomposite (bio-NCP) formed by Mn-Zn ferrites nanoparticles encapsulated with chitosan having the surface modified with HAP nanocrystals was recently described [25]. Here we describe the encapsulation of PTX into this bio-NCP and discuss how the drug interacts with such a complex encapsulation matrix. The main question to be answered is how and if the molecular dynamics of the drug, which is closely related to its anti-tumor activity is modified. This query is important because the encapsulation media may drastically change the drug conformation, which will not be necessarily recovered after the releasing process [26].

Comparing the dynamics of the encapsulated drug to that of the pure form is a key step to understand the polymer/drug interactions that might occur. However, the investigation of encapsulated drugs is rather challenging given the limitations of conventional techniques, especially considering the composition of the proposed bio-NCP and the complex PTX diterpene molecule, shown in Figure 1.

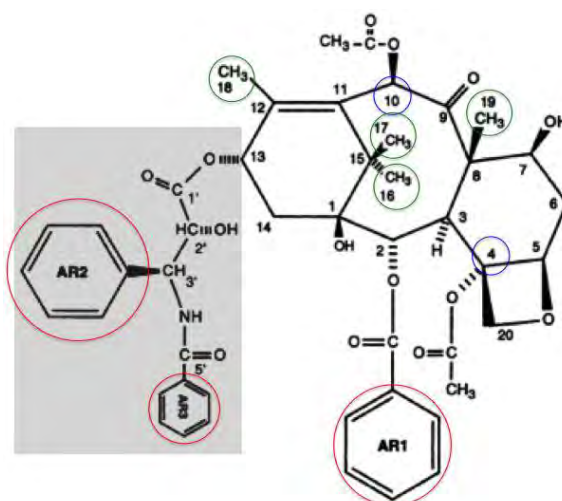


Figure 1. Schematic of the PTX molecule adapted from [27]. Circles highlight C-atoms cited along the text. Phenyl (AR1, A2 and AR3) are highlighted in red, methyl groups in green and carbons bonded to acetyl groups in blue.

In the present study, the presence of magnetic nanoparticles limits the use of Raman spectroscopy as well as NMR. On the other hand, although infrared spectroscopy can provide invaluable information about the encapsulation itself, it cannot give clear insight on the dynamics of the drug, unless it is in the bio-NCP surface [28]. Consequently, new approaches must be considered to perform such an investigation. For example, the application of the Near edge X-ray absorption fine structure (NEXAFS) allows for the characterization of different organic groups due to the interaction of X-rays with the K shell of the carbon atoms and, most importantly, the magnetic nanoparticles do not interfere in the result [29]. Additionally, by combining the NEXAFS spectra with the Scanning Transmission X-ray Microscopy (STXM) technique where several X-rays transmission images can be obtained at energies corresponding to an absorption line in the NEXAFS spectra compositional maps can be obtained and a visual analysis of the PTX distribution along the encapsulation system can be achieved.

Another virtuous approach, still not fully exploited in the characterization of encapsulated drugs is inelastic neutron scattering (INS) [30]. The relative simplicity of the neutron–nucleus interaction implies that, in contrast to Raman and infrared spectroscopy, no selection rules exist in neutron scattering and, in principle, all modes can be observed. Moreover, due to the exceptionally high incoherent scattering cross-section of hydrogen compared to any other elements, displacements involving hydrogen atoms dominate the vibrational density of available neutron states [31].

Additional features, especially in the INS data interpretation, can be obtained by combining such experimental results with theoretical data obtained by molecular dynamics simulations (MD). MD subject atoms to Newton's equation of motion and their interactions are obtained from a force field, which is a parameterization of the potential energy surface of the system [32]. Neutron scattering methods are the most relevant experimental reference for MD since both methods cover the same time and space domains (from 0.1 fs to 10 ns, and 1 – 100 Å), and neutrons probe the atomic nuclei, which are the basic objects in MD simulations.

In this work, by combining these state-of-the-art techniques (NEXAFS, STXM, INS and DFT) the characterization of PTX encapsulated into a bio-NCP formed by magnetic nanoparticles, chitosan and hydroxyapatite nanocrystals was possible. Our results show that the drug is distributed along the polymeric part of the bio-NCP and some vibrations, mainly from phenyl and acetyl groups are constrained by the encapsulation but they are most likely recovered after the PTX release. Moreover, we present extremely encouraging in-vitro toxicity tests for the drug-free bio-NCP performed in macrophages as well as preliminary assays with cancer cells.

2. Experimental

2.1. Sample preparation

Mn-Zn ferrites with nominal formula $\text{Mn}_{0.75}\text{Zn}_{0.25}\text{Fe}_{1.70}\text{O}_4$ were prepared by the co-precipitation method as described in [33], using $\text{Mn}(\text{NO}_2)_2$, $\text{Zn}(\text{NO}_2)_2$ and FeCl_3 as starting salts. The salts were diluted in water, dripped into boiling 0.1M NaOH solution, allowed to react for 120 min and the resulting precipitate was collected using

a magnet and washed with distilled water. The resulting particles were then dispersed in water and a 40 mg/mL ferrite suspension was obtained. Then, the encapsulation of the magnetic nanoparticles together with the PTX was performed by a double emulsion method [34]. To do so, 20 mg of chitosan were dissolved in 2 mL of 4% acetic solution. 1 ml of the Mn-Zn ferrite nanoparticles dispersion was added to the chitosan solution together with 0.25mL of the surfactant Tween 80. The resulting ferrite + chitosan dispersion was vigorously stirred for 30 min. Meanwhile, 25mg of paclitaxel was dissolved in 0.5mL of dicloromethane. After 30 min, the paclitaxel solution was added to the Mn-Zn ferrite + chitosan dispersion and stirred for 120 min. The resulting suspension of Mn-Zn ferrite + chitosan + paclitaxel was added to an organic solution prepared with 50mL of paraffin and 3.17mL of oleic acid and stirred for 120 min. At this moment, 0.1 mL of glutaraldehyde (25%) was dripped into the solution to perform the cross-linking reaction of chitosan. The reaction was stirred for 120 min at room temperature and then remained at 70⁰C for 12h. The resulting material was carefully washed with ethanol, ether and acetone to ensure that the sample contained no paraffin and surfactants and re-suspended in 100mL of 0.5M CaCl₂ solution and allowed to stir for 120 min in order to perform the surface modification with apatite by the mimetization method [25]. Then, 20 mL of H₃PO₄ 0.1% were added to the solution and the pH was adjusted to 7.4 with NaOH. Additional 60 min of stirring were conducted. Finally the sample was separated with a magnet and dried at 60⁰C for 72h. From now on, the sample containing the PTX encapsulated into the bio-NCP will be called as bio-NCP + PTX. A sample without PTX was also prepared by following all the steps above and is simply called as bio-NCP. All the reagents used in the procedures described above were purchased by Sigma-Aldrich.

2.2. *In vitro tests*

Human monocytes and HCT116 (colon cancer) and 3LL (lung cancer) culture

Human monocytes were isolated from 40 mL of peripheral blood of healthy donors collected with heparin. Blood sample was diluted with equal volume of phosphate buffered salt solution (PBS) and mononuclear cells were obtained by centrifugation on a gradient of Ficoll-Isopaque solution (d=1,077 g/mL) for 30 min at 900 x g. Mononuclear cell suspension was washed three times with fresh RPMI 1640 culture medium, and suspended with PBS containing 5% of fetal bovine serum (FBS) and centrifuged on a Percoll 51% gradient in order to separate most of monocyte (interface) from lymphocytes (pellet).

This monocyte-rich suspension as well as HCT116 3LL cells were washed three times with RPMI 1640, supplemented with 10% FBS, 1% nonessential aminoacids, 1% sodium pyruvate, 25 mM HEPES, 2mM L-glutamine, and 1% antibiotic/antimytotic solution (complete culture medium). Cells were set to 2×10^5 cells/mL and dispensed on a rounded glass slide (\varnothing 13 mm), previously coated with poly-L-lysine. Cultures were kept for 2h at 37°C under 5% CO₂, in order to promote cell attachment on slides.

In vitro challenge of monocytes with nanoparticles

Glass slides were washed three times with warm complete medium (1 mL each time) and challenged with 50 µg of different preparations of nanoparticles. Cell cultures were kept for 2 h at 37°C under 5% CO₂ to allow straight contact between cell surface and nanoparticles. Then, slides were washed with fresh PBS at room

temperature, cell monolayer were fixed with 2.5% glutaraldehyde and routinely processed.

Analysis by electronic microscopy

After fixation of monocyte monolayer on glass slides, cells were dehydrated with ethanol solutions at 7.5, 15, 30, 50, 70, 90 and 100% (2 times for 10 min each alcohol concentration), and submitted to supercritical drying (over the critical point) in a CO₂ atmosphere, for further metallization. Samples were then analyzed by electronic scanning microscopy (SEM) (FEI, Quanta 200) equipped with Oxford, Inca, 250P20 EDX to detect the internalization of the materials by mapping Fe over cells.

2.3. *Near Edge X-ray Absorption Fine Structure (NEXAFS) and Scanning Transmission X ray Microscopy (STXM)*

NEXAFS data were collected in the C K-edge energy range (250 to 350eV) for PTX, bio-NCP, bio-NCP + PTX and pure chitosan (commercial form). The samples were dispersed in ethanol and deposited on 5.0mm x 5.0mm silicon nitride membranes (Silson, England) and the experiments were performed at the PolLux beamline at the Swiss Light Source (SLS, PSI). Then, STXM images were collected using x-rays with selected energies where each of the bio-NCP + PTX components presented maximum absorption in the NEXAFS spectra as: 283eV, 286eV, 300eV, 320eV and 347eV. One image was also collected with X-rays with 275eV to be used as a background image, since no absorption is detected in this spectral region. The

images were uploaded together with the NEXAFS spectra to the software axis2000, aligned and superposed in order to create a composition map.

2.4. *Inelastic neutron scattering (INS), DFT calculations and infrared spectroscopy.*

The dynamics of PTX, bio-NCP and bio-NCP + PTX INS were investigated by means of INS using the FDS spectrometer at the Los Alamos Neutron Science Institute (USA). The samples were mounted using the slab geometry inside of aluminum containers with a calculated normal beam transmission 0.75 and analyzed at 10K. A vanadium run was used to calibrate the detectors efficiency.

DFT Calculations on gas-phase paclitaxel at 0 K were carried out at the B3LYP/6-31G level of theory with the GAMESS-UK package [35]. Periodic calculations on crystalline paclitaxel were performed with the VASP package [36] using the PBE functional along with Vanderbilt ultrasoft pseudopotentials [37].

Finally, 20mg of the bio-NCP+PTX sample was dispersed in aqueous media for 7 days to allow the PTX release and then analysed by infrared spectroscopy (FTIR) using a Nicolet spectrometer, Nexus 670. The peaks in the spectrum were indexed based on the DFT calculations.

3. Results

3.1. *In vitro tests*

The toxicity of pure ferrite nanoparticles as well as the bio-NCP were evaluated by the immunologic response generated in macrophages, which are defense cells of

the human body and tend to phagocytose foreign particles or molecules that may be a threat to the individual health, avoiding those to reach organs and tissues [38]. Figure 2 shows the behavior of the macrophages in the control group (a) as well as after being in contact for 2h with the pure ferrite nanoparticles (c) and the bio-NCP (d). The cells marked as green, as indicated by arrows in selected positions, present high Fe concentrations inside them, as determined by EDS. Regarding the assay with the pure ferrite, Figure 1(b), a considerable cellular uptake is noted, as depicted by the green spots. This observation indicates that the magnetic nanoparticles are recognized as foreign bodies leading to immune response by the defense cells. By coating the nanoparticles with the bio-NCP, Figure 1(c), the immune response is avoided and the EDS analysis does not detect high Fe concentration inside the macrophages, which are similar to the ones in the control group. Such a result highlights the potential of the bio-NCP as a PTX carrier not only in the sense of prolonging its circulation time, but also avoiding macrophages actions in the tumor sites that may jeopardize the action of the drug [39].

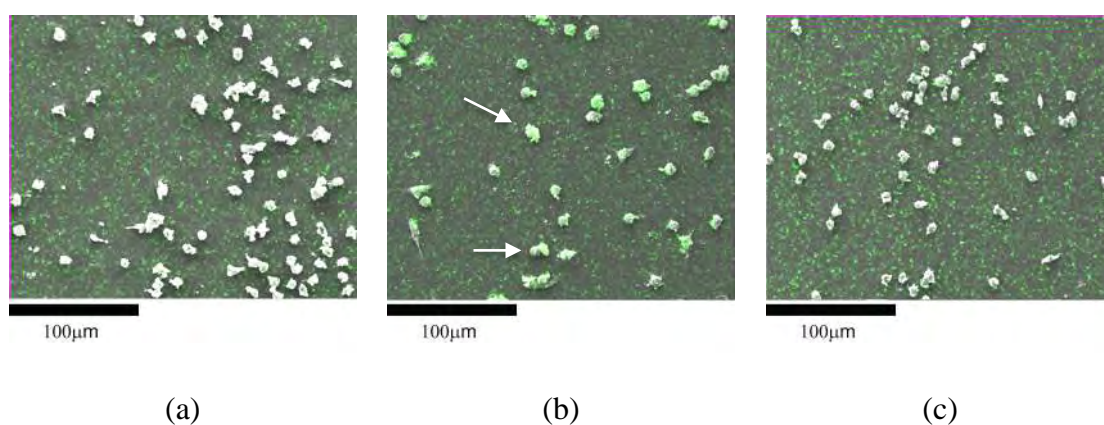


Figure 2. Immunologic response generated by macrophages in the control group (a) as well as after being in contact for 2h with pure Mn-Zn ferrite nanoparticles (b) and the bio-NCP. High Fe concentrations into the cells were determined by EDS and are depicted by the green color and highlighted by arrows in selected positions.

Initial in-vitro tests were performed with colon and lung cancer cells, as depicted in Figure 3. After being in contact with pure ferrite nanoparticles and the bio-NCP for 2h, the tumor cells present great morphological changes suggesting the adhesion of the nanoparticles. The highest Fe concentrations were detected in the regions where the morphological changes in the cells are more notorious, specially in the colon cells (Figure 3(a)).

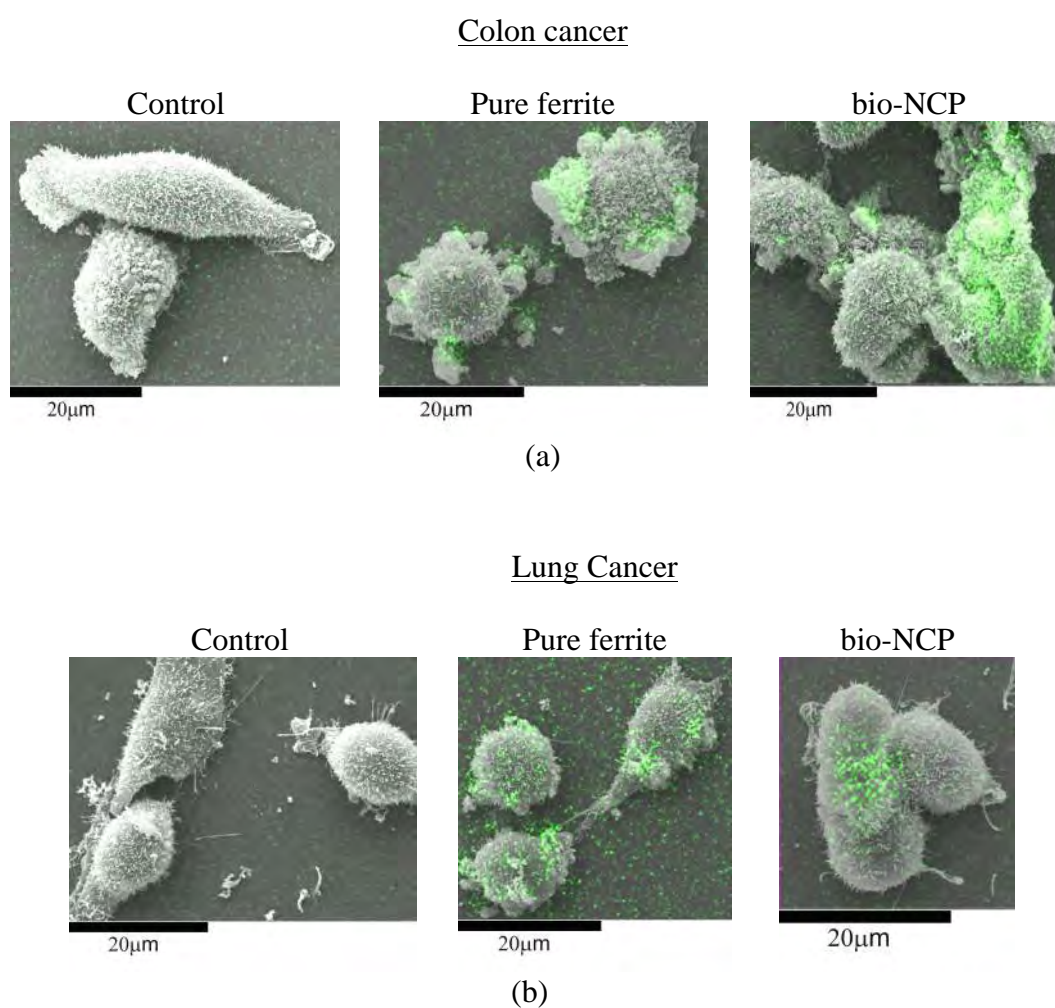


Figure 3. Initial in-vitro tests with colon (a) and lung cancer cells (b). The cells were allowed to be contact with pure ferrite nanoparticles and the bio-NCP for 2h, and present great morphological changes with great Fe concentrations mainly in the regions where such changes are more notorious.

Given the results from the initial in-vitro tests, the bio-NCP can be considered as a potential PTX carrier. However, considering the complex composition of the composite, understanding the drug/encapsulation interactions as well as the dynamical behavior of the encapsulated drug is a relevant step before further applications of this system. The obtained insights in this regard are presented as follows.

3.2. NEXAFS and STXM

Figure 4 presents the NEXAFS spectra for PTX, bio-NCP, bio-NCP + PTX and also for pure chitosan (as purchased). The PTX spectrum shows a convolution of excitations due to the considerable flexibility of the carbon bonds, leading to a smeared spectrum. Even though, the PTX fingerprint at 283.3eV is detected and can be related to a π^* bond, characteristic of aromatic rings. In the spectrum of bio-NCP, the broad at 291eV is then attributed to excitation of C and H bonds or C, H and N bonds from the crosslinked chitosan [40]. The remarkable peak in the bio-NCP spectrum at 347eV, which is close to the Ca L_{3,2}-edge, can be assigned to the apatite modification onto the chitosan surface [41]. Differently from the other samples the bio-NCP + PTX spectrum shows more defined peaks due to the confinement of the flexible PTX molecule that has now some excitations hidden in the NEXAFS experiment. This is an additional indicative that the encapsulation process succeeded. Moreover, the most interesting feature in the bio-NCP + PTX spectrum is the prominent peak at 286.9eV, which has the typical shape for the π^* ¹ bond excitation and might correspond to a C double bond found in a phenyl group present in the PTX

molecule. Finally, the peak at 288.7eV detected in the bio-NCP + PTX spectrum can be correlated to the π^* orbital excitation of a C=O bonds [40].

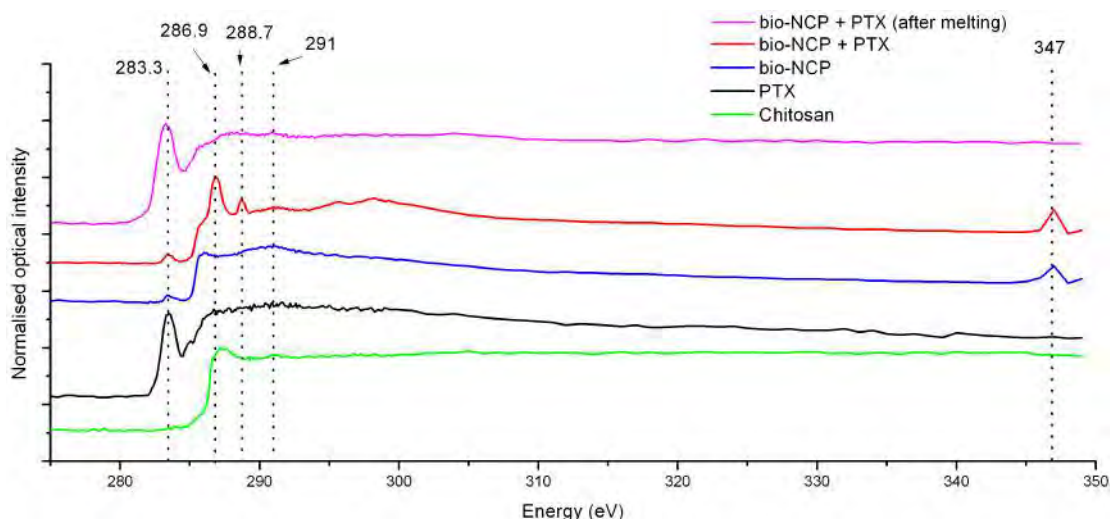


Figure 4. NEXAFS spectra for PTX, bio-NCP, bio-NCP + PTX and pure chitosan (as purchased). The PTX spectrum shows a characteristic peak at 283.3eV related to a π^* bond of aromatic rings. The bio-NCP spectrum shows a broad peak at 291eV from the crosslinked chitosan and an additional signal at 347eV from the apatite modification. For the bio-NCP + PTX, some excitations from the encapsulated drug are hidden and the spectrum shows peak at 286.9eV from double bond of phenyl group present and a peak at 288.7eV correlated to C=O bonds. The pink curve in the top represents the recovered PTX after melting the bio-NCP+PTX sample.

By using the information obtained by the NEXAFS spectra, one can have insight on the distribution of PTX into bio-NCP particles by means of STXM. Transmission images of such particles were collected using X-rays with maximum absorption by the nanocomposite components, as follows: 275eV, 283eV, 286eV, 300eV, 320eV and 347eV. The first one is used as a background image, since no peaks are detected in this region for all samples, while the image at 283eV can be

used as a fingerprint for the PTX. The images at 286eV and at 347eV were used to detect the bio-NCP and the images at 300eV, and 320eV have been taken to detect carbons in both the PTX and bio-NCP as well as to improve quality of the compositional, shown in Figure 5. The PTX is represented by yellow spots and the bio-NCP by the red ones. The background is shown in blue as well as the magnetic nanoparticles that are not detected in this energy range. The green spots denote regions with low PTX concentration, which leads to a mixture between yellow and blue. The images show that the drug is distributed along the polymeric shell with the magnetic nanoparticles forming the core of the composite.

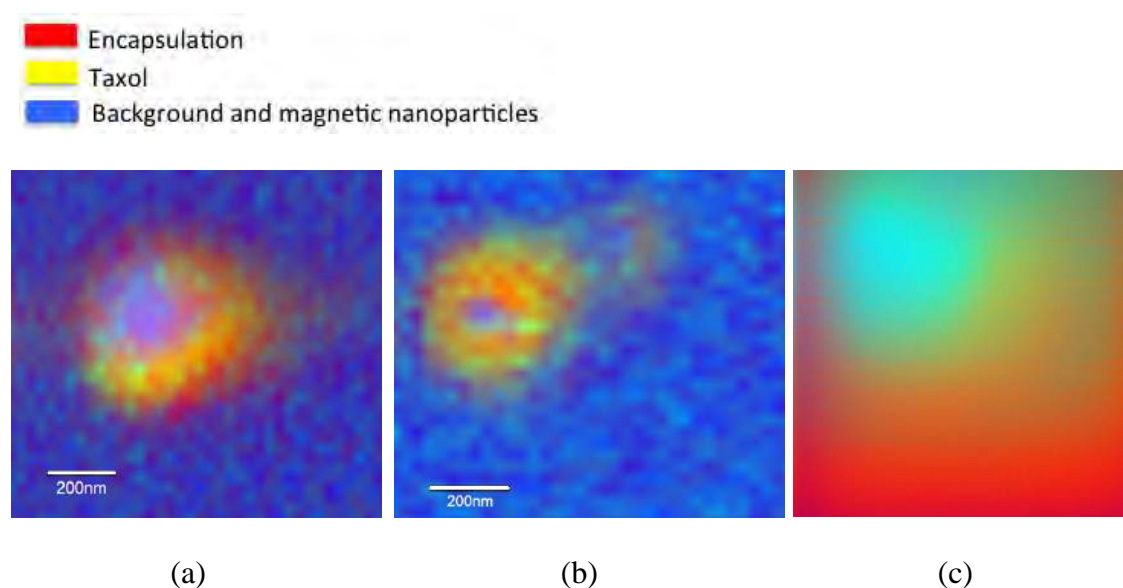


Figure 5. STXM images obtained after superposing images collected using X-rays with following energies: 275eV, 283eV, 286eV, 300eV, 320eV and 347eV. Figures (a) and (b) show the bio-NCP with a core-shell like conformation and (c) presents the nanocomposite after being irradiated.

At this point, the possibility of recovering the original PTX conformation after the release was investigated. To answer this question, the bio-NCP was irradiated so that the encapsulation media was melted and the drug was released. The resulting

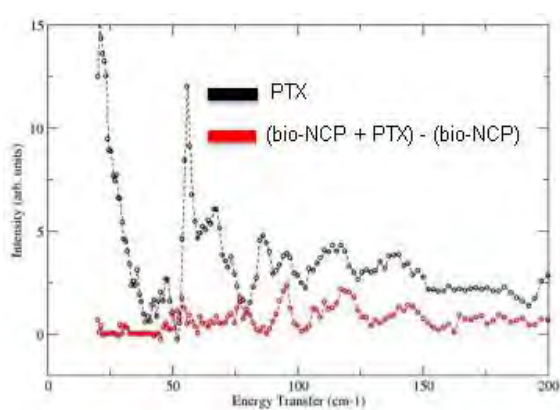
image is shown in Figure 5(c) where we clearly see that the polymer (red) spread through the image while a mixture of magnetic particles and PTX is seen in the middle (blue + green). A new NEXAFS spectrum of the melted sample was obtained as presented in the pink curve of Figure 4. The spectrum of the recovered PTX shows that the drug fingerprint was restored. One can then conclude that after being released (even in an extreme condition) the drug is recovered.

To conclude, the NEXAFS and STXM techniques provided us with valuable insight on the drug distribution within the encapsulation. However, the analysis of the encapsulation/drug interactions needs further assessment, which was provided by a combination of INS data and DFT calculations.

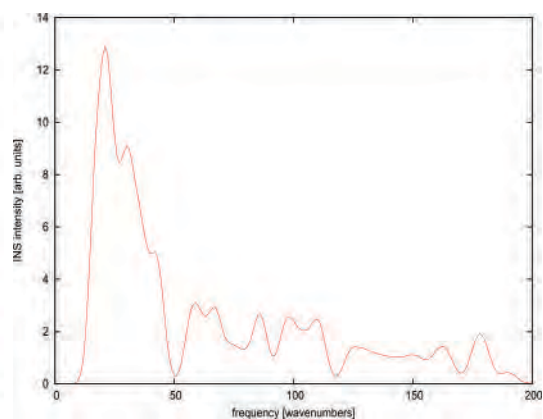
3.3. *Inelastic neutron scattering (INS), density functional theory (DFT) and infrared spectroscopy (FTIR)*

Inelastic neutron scattering (INS) data at low (a) and high (b) frequencies for the pure PTX (black) and the difference between the bio-NCP + PTX and bio-NCP (red) are presented in Figure 6. The respective results obtained by DFT calculations are shown in Figure 6(c) and (d). Differently from the NEXAFS spectra, the INS data offer good definition in the peaks and allows for observing the constrained vibrations in the encapsulated drug. It is clear that vibrations with frequencies below 90 cm^{-1} are frozen after encapsulating PTX into the bio-NCP. With the support of the DFT calculations, it is possible to identify the molecular groups in the drug that contribute to the most relevant vibrations, as listed in Table 1, presented as a supplementary information. By a comparing Table 1 and Figure 1, it is clear that the phenyl groups (aromatic rings - AR) as well as the acetyl groups 1 and 2, bonded to C10 and C4

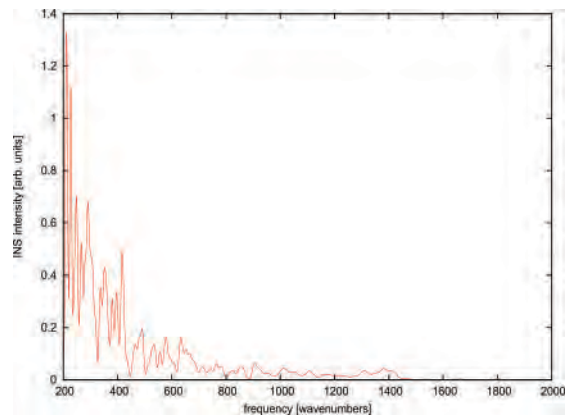
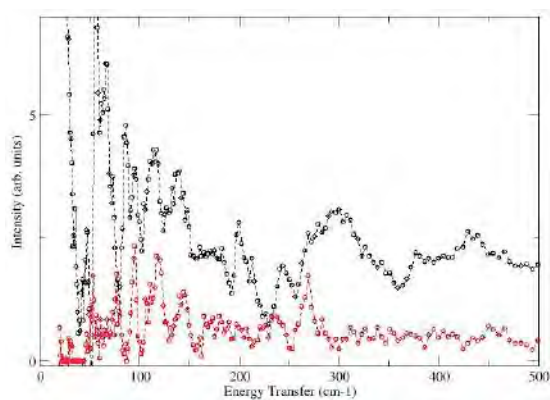
respectively are the most important contributions to the low frequencies vibrations in the PTX spectrum. Interestingly, in frequencies between 90 cm^{-1} and 150 cm^{-1} , where one can still see vibrations in the bio-NCP + PTX, the main contributions come from the terpene structure itself (C6, C7 and C14). This feature indicates that the rigid structure and the lattice vibrations of PTX are maintained. Meanwhile, the frequencies attributed to the methyl groups in C16 and C19 located at 212 cm^{-1} and in C17 at 250 cm^{-1} , seem to be damped when the drug is constrained while a remaining vibration in is detected around 270 cm^{-1} , most likely originated by the side chain bonded to C13. Finally, the modes attributed to the methyl group in C19 above 300 cm^{-1} are extremely attenuated when the drug is inside the bio-NCP, which is in agreement to our previous findings [28].



(a)



(b)



(c)

(d)

Figure 6. INS data collected at FDS for low (a) and high (b) frequencies. The black curve shows the PTX data while the red curve shows a difference between bio-NCP + PTX and bio-NCP, depicting only the contribution from the encapsulated drug. The respective results obtained by DFT calculations are presented in (c) and (d).

Therefore, the INS data lead us to conclude that the encapsulated drug presents the vibrations from the methyl, acetyl and phenyl groups highly constrained by the encapsulation into the bio-NCP, while the internal lattice vibrations remain unaltered. That could correspond to an inactive form of the drug, since the most relevant groups in the biological activity are inactive in the encapsulated PTX. After allowing the drug to be released in water dispersion, the FTIR data in Figure 7 shows the appearance of two additional peaks, in comparison to the original bio-NCP+PTX sample. The first peak, at 1390 cm^{-1} can be attributed to hydrophilic NH groups vibrations from the encapsulation itself, which are expected to be more evident after being dispersed in water. The second peak complies a region between 1443 and 1493 cm^{-1} , where, according to the DFT calculations, both methyl and phenyl groups play a role, as well as the C7 from the terpene ring. Therefore, this result indicates the reactivation of PTX after the release, even after being under strong confinement into the bio-NCP.

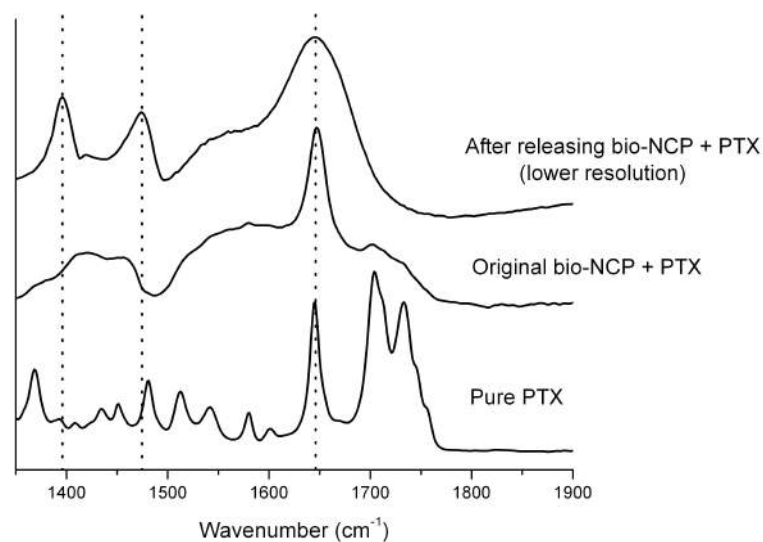


Figure 7. FTIR spectra of PTX, bio-NCP+PTX and the latter after being dispersed in water for 7 days. The additional peaks in the spectrum indicate the reactivation of PTX after the release. The spectra from pure PTX and bio-NCP+PTX were taken from [28].

4. Conclusions

We have studied the PTX encapsulated into a bio-NCP, whose low toxicity was confirmed by in-vitro assays and is certainly a potential carrier for this drug. Then, the dynamics of the encapsulated drug was investigated by combining experimental and theoretical results. A compositional map obtained by NEXAFS + STX confirmed that the drug is distributed along the polymeric shell, possibly in an inactive form, since the INS + DFT results show a great constraining in the molecule vibrations, especially on its methyl, acetyl and phenyl groups. Most importantly, we have strong indicatives that some of those vibrations can be recovered after the release. Finally, this work represents also the development of a methodology to study encapsulated drugs, based on state-of-the-art techniques.

5. References

- [1] Ferlay, J; Parkin, D. M. and Steliarova-Foucher, E. Estimates of cancer incidence and mortality in Europe in 2008. *Eur. J. Cancer*, 46, 4, 764-781, 2010.
- [2] Ferlay, J.; Steliarova-Foucher, E.; Lortet-Tieulent, J.; Rosso, S.; Coebergh, J.W.W.; Comber, H.; Forman, D. and Bray, F. Cancer incidence and mortality patterns in Europe: Estimates for 40 countries in 2012. *Eur. J. Cancer*, 49, 6, 1374-1403, 2013.
- [3] Beijer, Y. J.; Koopman, M.; Terhaard, C. H. J.; Braunius, W. W.; van Es R. J. J. and de Graeff A. Outcome and toxicity of radiotherapy combined with chemotherapy or cetuximab for head and neck cancer: Our experience in one hundred and twenty-five patients. *Clin. Otolaryngology*, 38, 1, 69-74, 2013.
- [4] Nakazaki, K.; Higuchi, Y.; Nagano, O. and Serizawa, T. Efficacy and limitations of salvage gamma knife radiosurgery for brain metastases of small-cell lung cancer after whole-brain radiotherapy. *Acta Neurochir.* 155, 107–114, 2013.
- [5] Monsuez, J.; Charniot, J.; Vignat, N. and Artigou, J. Cardiac side-effects of cancer chemotherapy. *Intern. J. Cardiol.*, 144, 1, 3-15, 2010.
- [6] Haldar, S.; Chintapalli, J. and Croce, C. M. Taxol Induces *bcl-2* Phosphorylation and Death of Prostate Cancer Cells. *Cancer res.*, 56, 1253, 1996.
- [7] Miller, K.; Wang, M.; Gralow, J.; Dickler, M.; Cobleigh, M.; Perez, E. A.; Shenkier, T.; Cella, D. and Davidson, N. E. Paclitaxel plus Bevacizumab versus Paclitaxel Alone for Metastatic Breast Cancer. *NEJM*, 357, 2666 – 2676, 2007.
- [8] Zhou, J.; Zhao, W.; Ma, X.; Ju, R.; Li, X.; Li, N.; Sun, M.; Shi, J.; Zhang, C. and Lu, W. The anticancer efficacy of paclitaxel liposomes modified with mitochondrial targeting conjugate in resistant lung cancer. *Biomaterials*, 34, 14, 3626 - 3638, 2013.
- [9] Vilos, C.; Morales, F. A.; Solar, P. A.; Herrera, N. S.; Gonzalez-Nilo, F. D.; Aguayo, D. A., Mendoza, H. L.; Comer, J.; Bravo, M. L.; Gonzalez, P. A.; Kato, S.; Cuello, M. A.; Alonso, C.; Bravo, E. J.; Bustamante, E. I.; Owen, G. I. and

Velasquez, L. A. Paclitaxel-PHBV nanoparticles and their toxicity to endometrial and primary ovarian cancer cells. *Biomater*, 34, 15, 4098 - 4108, 2013.

[10] Ma, P. and Mumper, R. J. Paclitaxel Nano-Delivery Systems: A Comprehensive Review. *J Nanomed Nanotechnol*. 4, 2, 1000164, 2013.

[11] Yu, X. and Pishko, M. V. Nanoparticle-Based Biocompatible and Targeted Drug Delivery: Characterization and in Vitro Studies. *Biomacromol.*, 12, 3205–3212, 2010

[12] Lv, P.; Wei, W.; Yue, H.; Yang, T.; Wang, L. and Ma G. Porous Quaternized Chitosan Nanoparticles Containing Paclitaxel Nanocrystals Improved Therapeutic Efficacy in Non-Small-Cell Lung Cancer after Oral Administration. *Biomacromol.*, 12, 4230 – 4239, 2011.

[13] Pathi, S. P.; Lin, D. D. W.; Dorvee, J. R.; Estroff, L. A. and Fischbach C. Hydroxyapatite nanoparticle-containing scaffolds for the study of breast cancer bone metastasis. *Biomater.*, 32, 5112–5122, 2011.

[14] Huang, J.; Lin, Y. W.; Fu, X. W.; Best, S. M.; Brooks, R. A.; Rushton, N.; Bonfield, W. Development of nano-sized hydroxyapatite reinforced composites for tissue engineering scaffolds. *J. Mater. Sci.: Materials in Medicine*, 18, 11, 2151-2157, 2007.

[15] Andronescu, E.; Fikai, M.; Voicu, G.; Fikai, D.; Maganu, M. and Fikai, A. Synthesis and characterization of collagen/hydroxyapatite: magnetite composite material for bone cancer treatment. *J. Mater. Sci. Materials in Medicine*, 21, 7, 2237-2242, 2010.

[16] Yuan, Y.; Liu, C.; Qian, J.; Wang, J. and Zhang, Y. Size-mediated cytotoxicity and apoptosis of hydroxyapatite nanoparticles in human hepatoma HepG2 cells. *Biomater*. 31, 730 – 740, 2011.

[17] Liang, Z.; Guo B.; Li, Y.; Li, X.; Li, X.; Zhao, L.; Gao, L.; Yu, H.; Zhao, X.; Zhang L. and Yang, B. Plasmid-based Stat3 siRNA delivered by hydroxyapatite nanoparticles suppresses mouse prostate tumour growth in vivo. *Asian J. Andrology*, 13, 481 – 486, 2011.

[18] Venkatesan, P.; Puvvada, N.; Dash, R.; Kumar, B. N. P.; Sarkar, D.; Azab, B.; Pathak, A.; Kundu, S. C.; Fisher, P. B. and Mandal, M. The potential of celecoxib-

loaded hydroxyapatite-chitosan nanocomposite for the treatment of colon cancer. *Biomater.*, 32, 3794 – 3806, 2011.

[19] Meena, R.; Kesari, K. K.; Rani, M. and Paulraj, R. Effects of hydroxyapatite nanoparticles on proliferation and apoptosis of human breast cancer cells (MCF-7). *J. Nanopart. Res.*, 14, 712, 2012.

[20] Jin, J.; Zuo, G.; Xiong, G.; Luo, H.; Li, Q.; Ma, C.; Li, D.; Gu, F.; Ma, Y. and Wan, Y. The inhibition of lamellar hydroxyapatite and lamellar magnetic hydroxyapatite on the migration and adhesion of breast cancer cells. *J Mater Sci: Mater Med.*, 25, 1025 – 1031, 2014.

[21] Alexiou, C.; Jurgons, R.; Seliger, C.; Brunke, O.; Irom, H. and Odenbach, S.. Delivery of Superparamagnetic Nanoparticles for Local Chemotherapy after Intraarterial Infusion and Magnetic Drug Targeting. *Anticancer Res.*, 27, 2019 - 2022, 2007.

[22] Americo, M. F.; Marques, R. G.; Randona, E. A.; Andreis, U. ; Stelzer, M. ; Cora, L. A.; Oliveira, R. B. and Miranda, J. R. A. Validation of ACB in vitro and in vivo as a biomagnetic method for measuring stomach contraction. *Neurogastroenterol Motil*, 22, 1340 – e374, 2010.

[23] Mikhaylov, G.; Mikac, U.; Magaeva, A. A.; Itin, V. I.; Naiden, E. P.; Psakhye, I.; Babes, L.; Reinheckel, T.; Peters, C.; Zeiser, R.; Bogyo, M.; Turk, V.; Psakhye, S. G.; Turk, B. and Vasiljeva, O. Ferri-liposomes as an MRI-visible drug-delivery system for targeting tumours and their microenvironment. *Nat. nanotech.*, 6, 2011.

[24] Di Corato, R.; Espinosa, A.; Lartigue, L.; Tharaud, M.; Chat, S.; Pellegrino, T.; Ménager, C.; Gazeau, F. and Wilhelm, C. Magnetic hyperthermia efficiency in the cellular environment for different nanoparticle designs. *Biomater.*, 35, 6400 – 6411, 2014.

[25] Martins, M. L.; Saeki, M. J.; Telling, M. T. F.; Parra, J. P. R. L. L.; Landsgesell, S.; Smith, R. I.; Bordallo, H. N. Development and characterization of a new bio-nanocomposite (bio-NCP) for diagnosis and treatment of breast cancer. *J. alloys compd*, 584, 514–519, 2014.

[26] Kuntz, I. Structure-Based Strategies for Drug Design and Discovery. *Science*, 257, 21, 1992.

- [27] Mastropaolo, D.; Camerman, A.; Luo, Y.; Brayer, G. D. and Camerman, N. Crystal and molecular structure of paclitaxel (taxol). *Proc. Natl. Acad. Sci. USA*, 92, 6920 - 6924, 1995.
- [28] Martins, M. L.; Orecchini, A.; Aguilera, L.; Eckert, J.; Embs, J.; Matic, A.; Saeki, M. J. and Bordallo, H. N. Encapsulation of paclitaxel into a bio-nanocomposite. A study combining Inelastic Neutron Scattering to Thermal Analysis and Infrared Spectroscopy. Accepted by *Eur. J. Phys.*
- [29] Watts, B.; Thomsen, L. and Dastoor, P. C. Methods in carbon K-edge NEXAFS: Experiment and analysis. *J. Electron Spectro. Relat. Phenom.*, 151, 105–120, 2006.
- [30] Bée, M. *Quasielastic Neutron Scattering, Principles and Applications in Solid State Chemistry, Biology and Materials Science*, CRC Press, 1988.
- [31] Martins, M. L.; Gates, W. P.; Michot, L.; Ferrage, E.; Marry, V.; Bordallo, H.N.. Neutron scattering, a powerful tool to study clay minerals. *Appl. Clay Sci.*, 96, 22-35, 2014.
- [32] Marry, V.; Dubois, E.; Malikova, N.; Durand-Vidal, S.; Longeville, S. and Brey, J. Water Dynamics in Hectorite Clays: Influence of Temperature Studied by Coupling Neutron Spin Echo and Molecular Dynamics. *Environ. Sci. Technol.*, 45, 7, 2850 – 2855, 2011.
- [33] Zhao D, Wang X, Zeng X, Xia Q, Tang J. Preparation and inductive heating property of Fe₃O₄-chitosan composite nanoparticles in an AC magnetic field for localized hyperthermia. *J. Alloys Compd*, 477, 739 – 743, 2009.
- [34] Maitra, A.N.; Ghosh, P.K.; De, T. K. and Sahoo, S.K. Process for the preparation of highly monodispersed hydrophilic polymeric nanoparticles of size less than 100 nm, US Patent. 5,874,111, 1999.
- [38] Guest, M. F.; Bush, I. J.; Van Dam, H. J. J.; Sherwood, P.; Thomas, J. M. H.; Van Lenthe, J. H.; Havenith, R. W. A.; Kendrick, J. The GAMESS-UK electronic structure package: Algorithms, developments and applications. *Mol. Phys*, 103, 719, 2005.
- [36] Kresse, G.; Furthmüller, J. Efficient iterative schemes for ab initio total-energy calculations using a plane-wave basis set. *Phys. Rev. B: Condens. Matter Mater. Phys.*, 54, 11169, 1996.

- [37] Vanderbilt, D. Soft self-consistent pseudopotentials in a generalized eigenvalue formalism. *Phys. Rev. B*, 41, 7892, 1990.
- [38] Nathan, C. Secretory products of macrophages: twenty-five years on. *J. Clin. Invest.* 122, 4, 1189–1190, 2012.
- [39] Shree, T.; Olson, O. C., Elie, B. T.; Kester, J. C., Garfall, A. L.; Simpson, K.; Bell-McGuinn, K. M.; Zabor, E. C.; Brogi, E. and Joyce, J. A. Macrophages and cathepsin proteases blunt chemotherapeutic response in breast cancer. *Genes Dev.* 25, 2465-2479, 2011.
- [40] Stöhr, J. NEXAFS Spectroscopy, Second Printing Springer, 2003
- [41] Benzerara, K.; Yoon, T. H., Tyliczszak, T., Constantz, B.; Spormann, A. M. and Brown Jr, V. Scanning Transmission X-Ray Microscopy Study of Microbial Calcification. *Geobiol.*, 2, 249-259, 2004.

Supplementary information

Table 1. Most relevant contributions from the PTX molecule in the INS vibrations obtained by DFT calculations. AR denotes the Aromatic Rings,

Vibration (cm⁻¹)	Main contributions
6.45	AR1, AR2, AR3
10.81	AR1, AR3
17.05	AR1, AR2
21.85	AR1, AR3,
31.38	Acetyl 1, Acetyl 2, AR2
34.07	AR2, AR3
42.48	Oxetane ring, Acetyl 2
57.74	AR2, AR3
74.9	Acetyl 1, Acetyl 2, Methyl in C18
79.21	Acetyl 1, Acetyl 2
85.87	Methyl in C18
87.09	AR1
96.38	C6, C7
105.39	Acetyl 2
110.45	C14 and Methyl in C18
124.85	C6
130.42	C6
148.72	Oxetane ring

212.20	Methyl in C16 and Methyl in C19
214.84	C1', C14
227.08	C16, C17
240.81	C13, C14, Acetyl 1
247.81	Methyl in C17
269.05	C1', Methyl in C16 and Methyl in C17
305.39	Methyl in C19
335.76	Methyl in C19
401.20	Methyl in C17 and Methyl in C18

Publication V

Murillo L. Martins, Marcos F. Calabresi, Caio Quini, Juliana F. Matos, José R. A. Miranda, Margarida J. Saeki, Heloisa N. Bordallo. **Enhancing the versatility of Alternate Current Biosusceptometry (ACB) through the synthesis of a dextrose-modified tracer and a magnetic muco-adhesive cellulose gel.** Submitted to “Materials Science and Engineering C”.

Enhancing the versatility of Alternate Current Biosusceptometry (ACB) through the synthesis of a dextrose-modified tracer and a magnetic muco-adhesive cellulose gel

Murillo L. Martins^{a,b,*}, Marcos F. Calabresi^b, Caio Quini^b, Juliana F. Matos^b, José R. A. Miranda^b, Margarida J. Saeki^b, Heloisa N. Bordallo^a

^a Niels Bohr Institute, University of Copenhagen, DK-2100 Copenhagen, Denmark

^b Instituto de Biociências - Universidade Estadual Paulista – CP 510, 18618-970 Botucatu – SP, Brazil

*murillolongo@gmail.com

Corresponding author:

Murillo L. Martins

Niels Bohr Institute

Universitetsparken 5, bygn. D

2100 København Ø - Denmark

phone: +45 21 30 88 29

murillolongo@gmail.com

Abstract

Alternate Current Biosusceptometry (ACB) is a promising bio-magnetic method, radiation free and easily performed used for gastric emptying exams. Due to development on its sensitivity level, interesting nature, noninvasiveness and low cost it has attracted a lot of attention. In this work, magnetic nanoparticles of Mn-Zn ferrite as well as dextrose-modified nanoparticles were synthesized to be used as possible tracers in ACB gastric emptying exams. In addition, a magnetic muco-adhesive gel was obtained by modifying the ferrite nanoparticles with cellulose. Based on in-vivo tests in rats, we show that the pure ferrite nanoparticles, whose isoelectric point was found to be at $\text{pH} = 3.2$, present a great sensitivity to pH variations along the gastrointestinal tract, while the reduction of the isoelectric point by the dextrose modification leads to suitable nanoparticles for rapid gastric emptying examinations. On the other hand, the in-vivo tests show that the muco-adhesive cellulose gel presents substantial stomach adhesion and is a potential drug delivery system easily traceable by the ACB system.

Keywords: Alternate Current Biosusceptometry; gastric emptying; bio-magnetic materials; muco-adhesive gel; cellulose; dextrose.

1. Introduction

Nowadays, there is an increasingly perspective for magnetic nanoparticles application in medicine either in diagnosis and treatment of diseases [1-3]. Particularly, the Alternate current biosusceptometry (ACB) technique, in which the position of a given magnetic material can be investigated by a first order gradiometric system, has extended such a perspective to the gastrointestinal tract (GIT) [4]. Definitely diagnosis of diseases related to the GIT, such as Chagas Disease [5], Parkinson's [6] or Diabetes Mellitus [7] through imaging techniques are typically performed by gastric emptying (GE) scintigraphy, so far considered the gold standard technique [8-10]. However, despite its considerable accuracy, some aspects are still subject of discussion. For instance, the high cost involved in the production of radioisotopes is a barrier for the application of scintigraphy in underdeveloped countries. In addition, the patients are exposed to radioactive doses that, while low, still limit the performance of periodic investigations and requires expansive radiation protection policies [11]. The fascinating aspect of ACB is that new developments have allowed a signal-to-noise ratio similar to the one achieved by scintigraphy [12]. Moreover, as a magnetic tracer, normally ferrite particles [13-16], replaces the radioactive one, and a first order gradiometer replaces the scintigraphy apparatus, this imaging technique allows for cheaper and safer examinations. To demonstrate such potential, we have tuned the physical and chemical properties of Mn-Zn ferrite nanoparticles suspensions to show that ACB can be used as an accurate technique for rapid GE exams.

Regarding the application of ACB in the treatment of GIT diseases, such a technique can also allow tracking the position of muco-adhesive gels that have been used as an efficient way to delivery complex molecules while retaining a dosage form at the site of action [17]. To do so, magnetic nanoparticles can be incorporated to the gels and their retention time into the GIT can be evaluated in research laboratories without requiring the euthanasia of animals [18]. Additionally, by adding magnetic nanoparticles to the muco-adhesive gels one can provide additional possibilities to these materials such as magnetic hyperthermia applications as well as prolonged retention times by magnetic attraction with an external magnet [19]. To prove this prospective, we have prepared a magnetic cellulose based gel, considering the remarkable muco-

adhesive properties of this polymer [20], and were able to show that the presence of magnetic nanoparticles do not disrupt the adhesion capacity of the cellulose.

2. Materials and methods

2.1. *Synthesis of Mn-Zn ferrite nanoparticles by the co-precipitation method*

Manganese zinc ferrite of nominal composition $\text{Mn}_{0.75}\text{Zn}_{0.25}\text{Fe}_{1.70}\text{O}_4$ was synthesized by the co-precipitation method [21] using $\text{Mn}(\text{NO}_2)_2$ (Sigma-Aldrich), $\text{Zn}(\text{NO}_2)_2$ (Sigma-Aldrich) and FeCl_3 (Sigma-Aldrich) as starting salts, which were diluted in aqueous solution with the appropriate amounts. The mixture was then dripped onto NaOH (Sigma-Aldrich) solution (0.1M) under ebullition and vigorously stirred for 120 min. In a typical experiment, 0.4g of ferrite was prepared in 300mL of NaOH solution. This ratio of ferrite mass to NaOH solution allowed nanoparticles in the order of 100nm to be obtained, having a strong magnetic response and able to be suspended in water. The resulting black precipitate, after being removed with a magnet, was washed to achieve nanoparticles with neutral pH and dispersed in water in order to obtain a 20 mg/mL suspension.

2.2. *Modification of the ferrite nanoparticles with dextrose and synthesis of the magnetic muco-adhesive cellulose gel*

Following well-known procedures [22], the modification with dextrose was performed by peptizing 80mg of ferrite nanoparticles with HNO_3 (Sigma-Aldrich) 0.5%, while an aqueous solution of dextrose (Chemco) was prepared with the pH adjusted to 10. The ferrite was then added to the dextrose solution with a mass ratio of ferrite/dextrose = 1/12, and the resulting suspension stirred for 15 hours. Subsequently, the suspension was carefully washed to extract any excess of dextrose and adjusted to a concentration of 20 mg/mL.

For the synthesis of the magnetic muco-adhesive cellulose gel, 1g of crystalline cellulose (Blanner) were added to an aqueous solution containing 1g of urea (Sigma-Aldrich) and 1.5g of NaOH. The resulting solution was vigorously stirred for 15 min at 5°C leading to a viscous and transparent solution that was added to the ferrite suspension, in a mass ratio of ferrite/cellulose = 1.5/1, and stirred for 30 min. The

material was then added to an ammonium sulfate solution (8% w/v), for coagulation as well as cellulose recuperation and stirred for 30 minutes. Finally the reaction was subjected to slow stirring for a few minutes, the resulting material was removed with a magnet and washed to achieve neutral pH. The final suspension was adjusted to a concentration of 20mg/mL, resulting in a viscous black gel.

2.3. Materials characterization

X-ray powder diffraction (XPD) analysis performed using a Rigaku diffractometer (D/MAX-2100/PC, Cu-K α , 1.54Å (Ni filter) confirmed the spinel structure in the pure ferrite nanoparticles. Furthermore, based on these data no traces of secondary phases was observed. By means of a Nano ZS zetameter the zeta potential of the magnetic nanoparticles was evaluated as a function of pH by suspending the particles in 0,001mol/L KNO₃ solution. In addition, to verify the homogeneity and morphology of each synthesized nanoparticle Scanning Electron Microscopy (SEM) measurements were carried out with a FEI, Quanta 200. Finally, the presence of the organic groups in the modified ferrite nanoparticles was evaluated via Fourier Transformed Infra-Red (FTIR) using a Nicolet spectrometer, Nexus 670.

2.4. In-vivo gastric emptying exams

The in vivo exams were performed in 3-months-old male Wistar rats (200–250 g) purchased from the Animals Laboratory, ANILAB (Paulínia-SP, Brazil). The rats were housed in individual cages under controlled temperature (24 ± 2 °C), humidity, and lighting (12-h light/dark cycle) with ad libitum access to a commercial diet (Purina® rat chow Brazil) and tap water. The animals were fasted for 24h before the procedures, where 1 mL of each material was administered by gavage to different rats. As depicted in Fig. 1(a), two anatomic regions were marked in the rats: i) stomach and ii) cecum. Using the ACB gradiometric system, as shown in Fig. 1(b), we analyzed the tensions generated in these points due to the presence of the magnetic material at 15 minutes intervals for 240 minutes, so that a temporal distribution of the tracer along the animals' tract was obtained. After such a time the animals were euthanized and the amounts of

magnetic material retained in their stomachs could be analyzed. These procedures were approved by the CEEA – IBB (Protocol No. 410-CEUA).

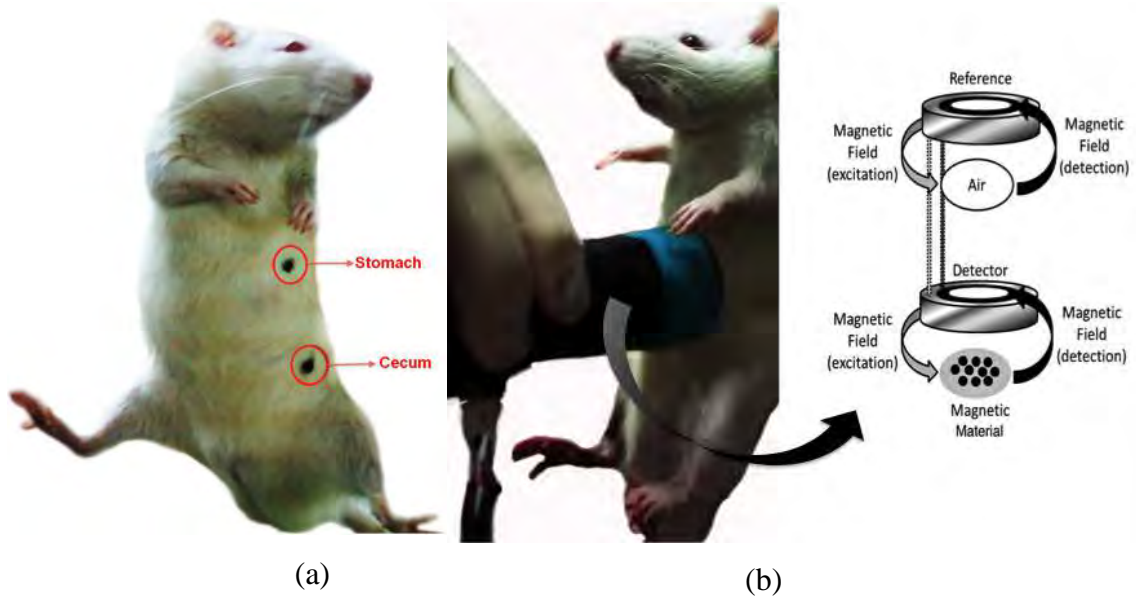


Figure 1. (a) Anatomic regions in the rat where the signal generated by the presence of the magnetic fluid was evaluated by ACB: stomach and cecum (beginning of the intestine). (b) During the gastric emptying exam using the ACB technique the gradiometer is positioned close to the stomach and to the intestine of the rat every 15 minutes for 240 minutes (adapted from [23]). The inset shows a schematic view of a first order gradiometer scheme used in ACB, adapted from [4].

3. Results and Discussion

Fig. 2(a) shows the SEM images of the pure ferrite nanoparticles, which exhibit agglomerates with mostly spherical shapes and a diameter around 100nm. The SEM results for the dextrose stabilized material, Fig. 2(b), shows the formation of polymeric structures with heterogeneous shapes with the magnetic nanoparticles incorporated into them, while the cellulose gel (Fig. 2(c)) is formed by spherical particles with a diameter around 100 nm. The latter indicates that the gel is formed by magnetic nanoparticles efficiently coated into cellulose capsules, into which drugs and biomolecules could be inserted for controlled release in the gastrointestinal tract (GIT).

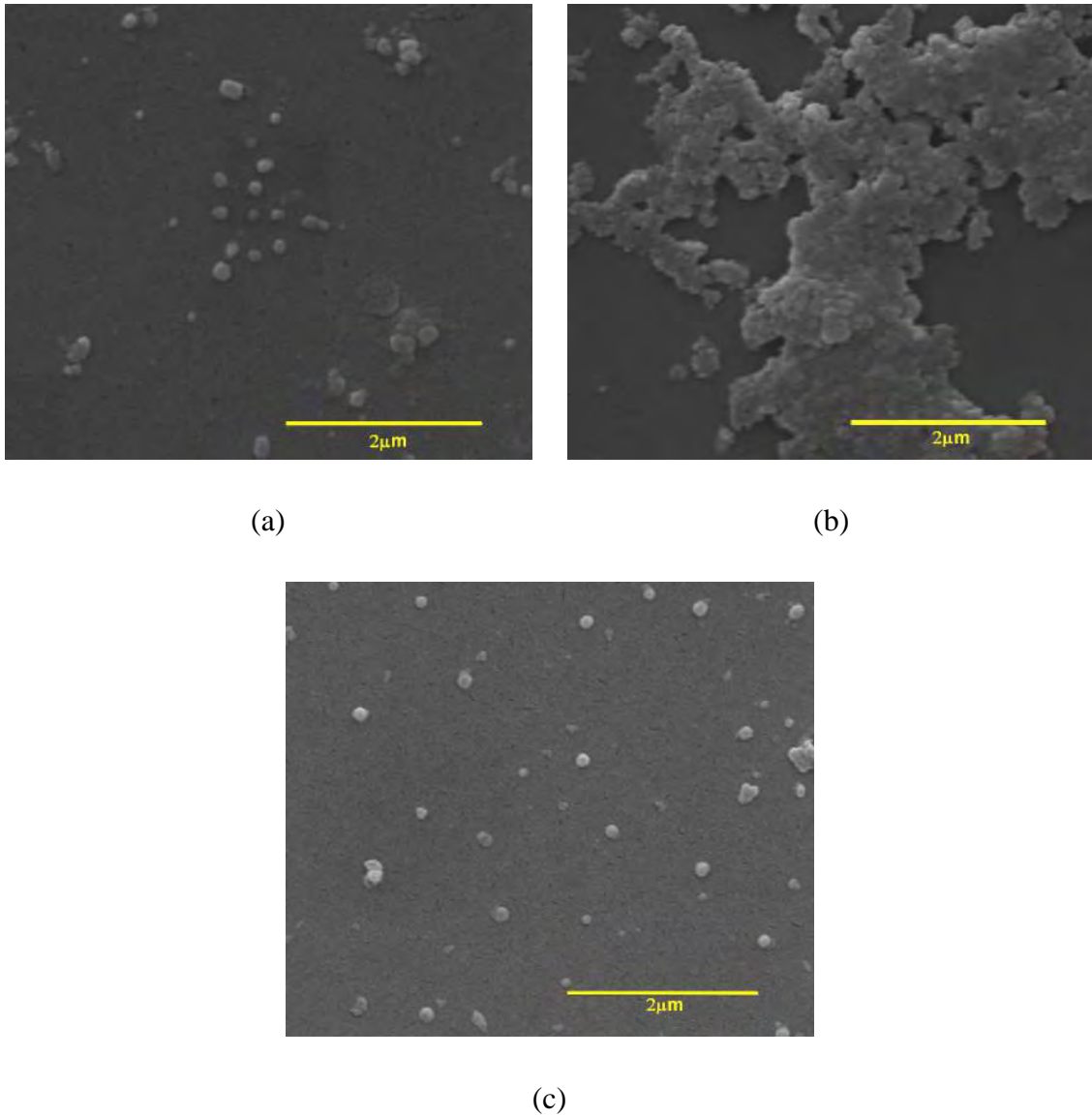


Figure 2. Scanning electron micrograph of representative samples of Mn-Zn ferrite nanoparticles (a), nanoparticles modified with dextrose (b) and nanoparticles modified with cellulose (cellulose gel) (c). The ferrite nanoparticles and the gel exhibit mostly spherical shapes, while after the modification with dextrose the formation of polymeric structures is clearly observed.

In order to further verify if the ferrite nanoparticles were successfully modified, all specimens were analyzed by FTIR, as depicted in Fig. 3. It is possible to see that the Fe-O characteristic bands at 428 and 571cm^{-1} [24] are present in the pure ferrite spectra, but hidden by the cellulose, Fig.3 (a), and the dextrose, Fig.3 (b), signals. In both modified materials, however, the presence of the ferrite nanoparticles is confirmed by the presence of the out of plane vibrations from the hydroxyl groups located at 937cm^{-1}

that characterize the nanoparticles surface [25], as well as by the slope in the spectra at low wavenumber values, caused by the nanoparticles scattering [26].

In the case of the gel, Fig. 3(a), a comparison to the spectrum obtained for pure cellulose shows a slight intensity reduction in the C-OH stretching as well as in the CH₂ stretching and symmetric bending modes, located around 1160, 1430 and 2920 cm⁻¹, respectively while, the C=O stretching mode at 1650 cm⁻¹ remains almost unchanged. The decrease in the CH₂ modes intensity indicates a reduction in the crystalline level of the cellulose present in the gel in comparison to the pure polymer [27], which can be related to the dissolution of the cellulose in the alkaline solution during the magnetic gel synthesis process described in Section 2.2. The reduction in crystallinity can be taken as a successful step in the synthesis process as it improves the ability of the cellulose to form hydrogen bonds with the GIT walls, which is one of the main features for prolonging the retention time of muco-adhesive materials [28,29].

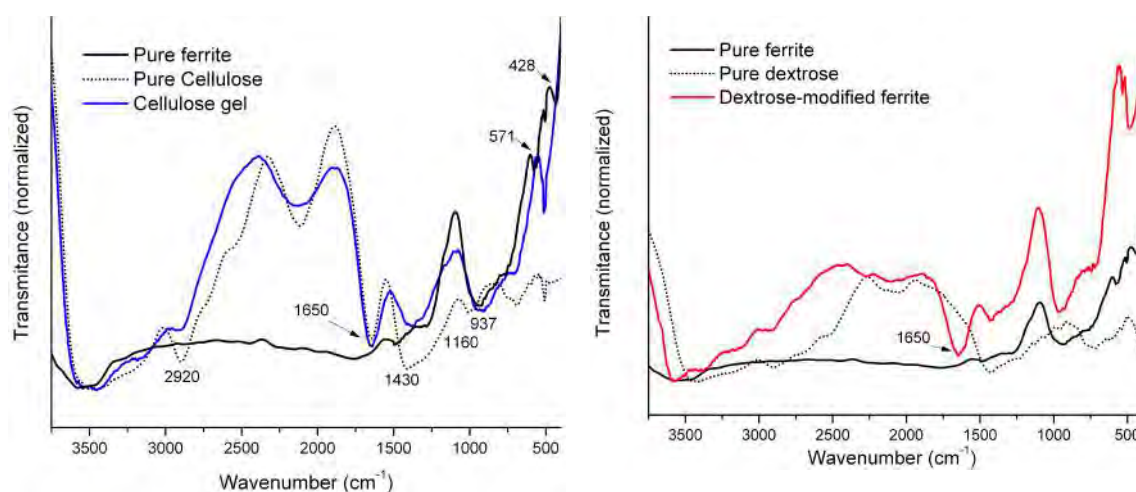


Figure 3. FTIR spectra of pure ferrite (black line), pure cellulose (dotted line) and magnetic cellulose gel (blue line) (a) and pure ferrite (black line), pure dextrose (dotted line) and dextrose-modified ferrite (red line) (b). The slight decrease in the intensity of the CH₂ stretching mode around 2920 cm⁻¹ observed for the gel indicates a reduction in the crystalline level of the polymer, while the observation of the C=O stretching at 1650 cm⁻¹ indicates the presence of dextrose with an open chain configuration in the dextrose-modified ferrite.

From the dextrose-modified ferrite spectrum, Fig. 3(b), it is clear that a new mode at 1650 cm⁻¹ is observed. This vibration was previously observed for dextrose with an open chain configuration instead of the dominant cyclic chain of the pure sugar [30] and

assigned to a C=O stretching mode. This large change in the molecular configuration can be attributed to the dissolution of the polymer in the nanoparticles during modification process as well.

4. In-vivo tests: Gastric emptying (GE) exams

4.1. GE using pure ferrite

Fig. 4(a) shows the GE profile (closed dots), as well as the signal in the animal's cecum (open dots) when pure ferrite was administered to the rats. A fast initial emptying is followed by retention of the tracer after 60 min. After 130 min the reduction in the signal in the stomach is once again resolved by the ACB apparatus and shows a slow-down when compared to the initial slope of the exam. Interestingly, these changes are also reflected in the signal detected at the intestine, which increases with time in three distinct steps.

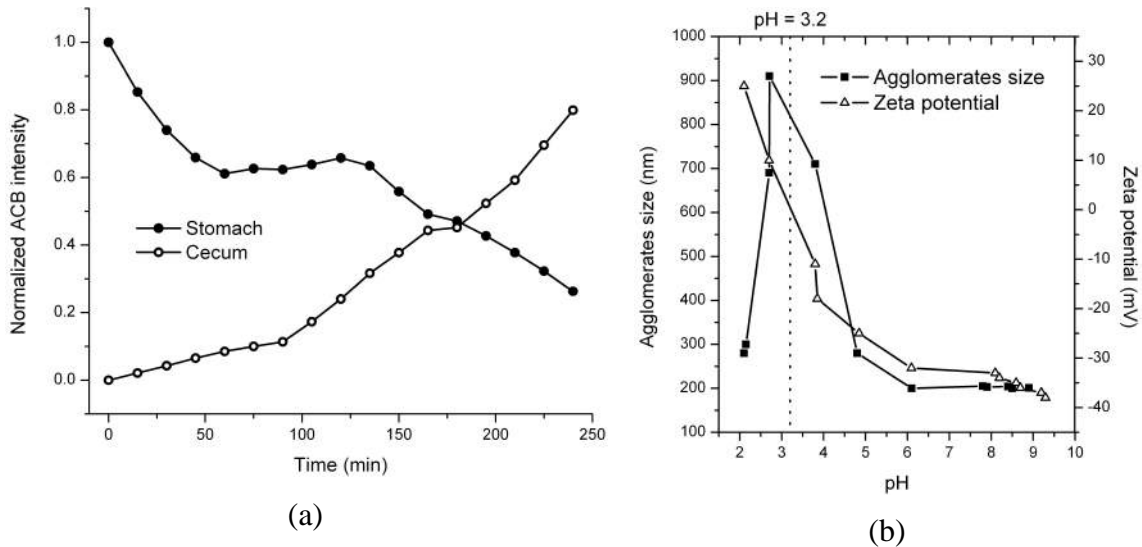


Figure. 4. Patterns of gastric emptying (GE) and arrival in the cecum of rats (Wistar) with pure ferrite nanoparticles (a). In (b), the agglomerates size (squares) and zeta potential (triangles) with the pH variation for the pure ferrite suspension are shown. The IEP of the suspension is found to be in pH = 3.2 (dotted line). The stomach gastric emptying pattern in (a) presents a fast initial emptying followed by a plateau after 60 min, and a new reduction in the signal after 130 min. These three distinct steps are also detected in the intestine arrival pattern, which increases with time.

These findings can be explained by the close relation between the viscosity of the nanoparticles suspension and the pH and Isoelectric Point (IEP). Considering that along the gastrointestinal tract the nanoparticles are exposed to different pH values (~1.2 in the stomach and ~6 in the intestine), changes in the suspension's viscosity are supposed to occur during the GE exams. Consequently, the same is expected in GE speeds, since the flow of highly viscous suspensions tends to be slower than for less viscous ones. To further corroborate this idea, the evolution of zeta potential (triangles) and agglomerates size (squares) with pH of the pure ferrite suspension, Fig. 4(b), were evaluated, as well as the IEP, depicted by the dot line and found to be in $\text{pH} = 3.2$. Therefore, in the beginning of the GE exam, the very low stomach pH leads to a low viscosity of the particles suspension, which explains the fast initial emptying. However, after 60 min, when the retention of the nanoparticles is detected, they are most likely subjected to a pH value close to the suspension's $\text{IEP} = 3.2$, corresponding to the transition between the stomach and intestinal environment. At this same time the viscosity (agglomerates size) reaches its maximum value. As the ACB does not resolve any reduction in the signal, thus generating a plateau in the curve, we can conclude that the pure ferrite nanoparticles provide for a very sharp sensitivity to the pH changes between the stomach and the intestine. Consequently, in clinical situations, such as gastritis or ulcers, where this physiological parameter changes dramatically, ACB can be used as a powerful diagnostic probe.

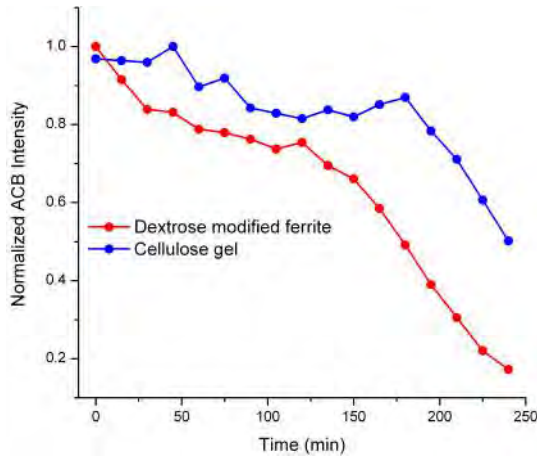
4.2. GE using the dextrose-modified ferrite and the magnetic cellulose gel

Based on the results presented above one would expect that

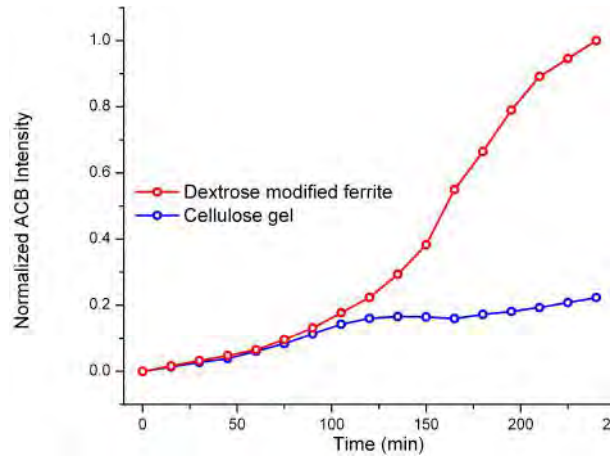
- i) since the increasing pH along the GIT will continuously decrease the viscosity of the tracer, rapid GE exams should be possible using the magnetic nanoparticles stabilized with dextrose, with a reduced IEP (around 2 [22]),.
- ii) for the cellulose gel, the IEP of the nanoparticles is kept almost the same as the one measured for the pure nanoparticles [31], however the swelling ability together with the possibility of hydrogen bonding with the GIT walls due to the polymer, should extend the retention time of the material. If

this assumption is correct this gel can be considered as a good candidate for developing a new muco-adhesive carrier.

Indeed as seen in Fig. 5(a) (red dots), by drastically decreasing the IEP of the nanoparticles through modification with dextrose the gastric emptying pattern becomes smoother. The initial emptying is not as fast as seen for the pure nanoparticles, and no plateau is noted in the stomach's signal curve. After 240 min, the signal decreases to 17% of the initial value, while for the pure ferrite the signal decreases to only 26%. The effectiveness of the suspension containing dextrose as a tracer agent for GIT exams is retrieved by the smooth pattern also obtained for the signal in the intestine; see Fig. 5(b). In comparison to the signal measured in the animal's cecum after the exam with pure ferrite, the dextrose-containing tracer shows a large increase of around 20%. Furthermore, and as anticipated for the magnetic cellulose gel, a very different emptying profile is observed (blue dots in the Fig. 5(a)). In this case, after 200 min, the initial signal decays only 30%, while after 240min the final signal corresponds to 50% of the initial value. These findings indicate that the presence of magnetic nanoparticles do not damage the muco-adhesive property of cellulose, and, most importantly, indeed provides the gel the ability of being traced by ACB. Moreover, the signal measured in the animal's cecum presents a reduction of more than 80%, in comparison to the dextrose-modified material highlighting the retention of the gel in the stomach.



(a)



(b)

Figure 5. Patterns of gastric emptying (a) and arrival in the cecum (b) of rats (Wistar) with dextrose-modified ferrite nanoparticles (red) and the magnetic cellulose gel (blue). The dextrose-modified nanoparticles show an efficient gastric emptying while the cellulose gel is well retained in the stomach, especially in the first 180 min.

Fig.6 shows the amount of remaining magnetic materials in the stomach of euthanized rats. It is clear that after the procedure with dextrose-modified ferrite (Fig. 6(b)) this amount is considerably smaller in comparison to the pure ferrite (Fig. 6(a)), thus highlighting the efficiency of the first as a magnetic tracer for rapid GIT exams. On the other hand, the dramatically higher amount of remaining material after the procedure with the magnetic cellulose gel (Fig. 6(c)) lead us to conclude its suitability as a traceable muco-adhesive drug delivery system for the GIT.

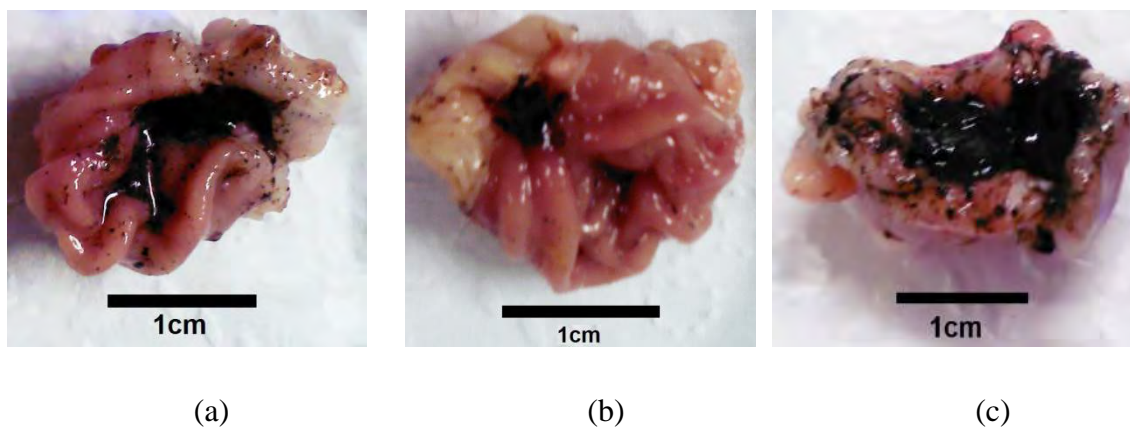


Figure 6. Stomachs of euthanized rats after gastric emptying using the magnetic materials described in the text. After the procedure with pure ferrite (a) a slight amount of material remained, which is drastically reduced by using the dextrose-modified material (b) but increased by using the magnetic cellulose gel (c). The results highlight the fast transit of the dextrose-modified nanoparticles through the gastrointestinal tract and the muco-adhesion of the cellulose gel.

5. Conclusions

This work validates the concept that by modifying the surface of magnetic nanoparticles the versatility of ACB can be enhanced, while its applications can be extended from diagnosis to treatment of gastric diseases. We have shown that pure nanoparticles, with an IEP = 3.2, are highly sensitive to pH variations along the gastrointestinal tract, and that this sensitivity is reduced by the particles modification with dextrose. Such modification provides for a faster and more efficient gastric emptying examination. In addition, we have developed a bio-magnetic cellulose gel composed by polymeric nanocapsules containing ferrite nanoparticles, which can be substantially retained in the stomach walls, and consequently presents the potential to be used as a traceable drug delivery system for gastric diseases.

Acknowledgments

MLM thanks CAPES, FAPESP and the Science Without Borders Program for financial support. The Multi-User Laboratory of “Faculdade de Ciências de Bauru” is also acknowledged for providing the X-ray diffractometer as well as for the thermal

analysis instrumentation. Dr. Walter Kalceff (UTS, Australia) is gratefully acknowledged by MLM and HNB for fruitful discussions.

References

- [1] D. Ling, T. Hyeon. *Small*, 9 (2013), pp. 1450–1466.
- [2] S. Amiri, H. Shokrollahi. *Materials Science and Engineering: C*, 33 (2013), pp. 1–8.
- [3] D. Ho, X. Sun, S. Sun. *Accounts of chemical research*, 44 (2011), pp. 875–882.
- [4] M. F. Américo,; R. G. Marques, E. A. Zandoná,; Andreis, U.; Stelzer, M.; L. A. Corá, R.B. Oliveira, J. R. A. Miranda. *Neurogastroenterol. Motil.*, 22 (2010), pp. 1340–1374.
- [5] R. B. Oliveira, L.E. Troncon, R.O. Dantas, U.G. Meneghelli. *Am. J. Gastroenterol.*, 93 (1998), pp. 884-889.
- [6] J. G. Greene, A. R. Noorian, S. Srinivasan. *Exp. Neurol.*, 218 (2009), pp. 154–161.
- [7] A. E. Bharucha, M. Camilleri, L. A. Forstrom, A. R. Zinsmeister. *Clin. Endocrinol.*, 70 (2009), pp. 415–420.
- [8] A. H. Maurer, *Semin. Nucl. Med.*, 42 (2012), pp. 101-112.
- [9] H. A. Ziessman, A. Chander, J. O. Clarke, A. Ramos, R. L. Wahl *J. Nucl. Med.*, 50 (2009), pp. 726-731.
- [10] P. Sachdeva, N. Malhotra, M. Pathikonda, U. Khayyam, R. S. Fisher, A. H. Maurer, H. P. Parkman. *Dig. Dis. Sci.*, 56 (2011), pp. 1138–1146.
- [11] P. Covens, D. Berus, V. Caveliers, L. Struelens, D. Verellen. *Rad. Meas.*, 46 (2011), pp. 1291-1294.
- [12] M. F. Américo, R. B. Oliveira, G. Romeiro, O. Baffa, L. A. Corá, J. R. A. Miranda, *Neurogastroenterol. Motil.*, 19 (2007), pp. 804–811.
- [13] C. C. Quini, M. F. Américo, L. A. Cora, M. F. F. Calabresi, M. Alvarez, R. B. Oliveira, J. R. A. Miranda. *Journal of Biological Engineering*, 6 (2012), n. 6.
- [14] M. C. B. Teixeira, I. Magalhães, P.V.M. Galvão, G.S. Souza, J.R.A. Miranda, R.B.

- Oliveira, L.A. Corá. *Transplantation Proceedings*, 44 (2012), pp. 2384 – 2387.
- [15] F. C. Paixao, C. C. Quini, L. A. Bradshaw, W. O. Richards, O. Baffa, J. R. A. Miranda. *IFMBE Proceedings*, 39 (2013), pp 1389-1392.
- [16] R. G. Marques, M. F. Americo, C. T. Spadella, L. A. Corá, R. B. Oliveira, J. R. A. Miranda. *Physiol. Meas.*, 35 (2014), pp. 69 – 81.
- [17] G. P. Andrews, T. P. Laverty, D. S. Jones. *European Journal of Pharmaceutics and Biopharmaceutics*, 71 (2009), pp. 505–518.
- [18] T. Ito, Y. Yeo, C. B. Highley, E. Bellas, C. A. Benitez, D. S. Kohane. *Biomaterials*, 28 (2007), pp. 975 – 983.
- [19] J. Dobson. *Drug development research*, 67 (2006), pp. 55–60.
- [20] Y. Miyazaki, K. Ogihara, S. Yakou, T. Nagai, K. Takayama. *International Journal of Pharmaceutics*, 258 (2003), pp. 21–29.
- [21] M. L. Martins, M. J. Saeki, M. T. F. Telling, J. P. R. L. L. Parra, S. Landsgesell, R. I. Smith, H. N. Bordallo. *J. Alloys Compd.*, 584 (2014), pp. 514–519.
- [22] M. Latorre-Esteves, A. Cortés, M. Torres-Lugo, C. Rinaldi. *J. Magn. Magn. Mater.*, 321 (2009), pp. 3061-3066.
- [23] M. L. Martins, H. N. Bordallo. *Magnetics Technology International*, 3 (2013), p. 42.
- [24] K. A. Mohammed, A. D. Al-Rawas, A. M. Gismelseed, A. Sellai, H. M. Widatallah, A. Yousif, M. E. Elzain, M. Shongwe. *Physica B*, 407 (2012), pp. 795 – 804.
- [25] G. Vaidyanathan, S. Sendhilnathan. *Physica B: Condensed Matter*, 403 (2008), pp. 2157 – 2167.
- [26] D. Tsankov, K. Hinrichs, A. Roseler, E. H. Korte. *Phys. stat. sol. (a)*, 188 (2001), pp. 1319–1329.

- [27] K. K. Pandey. *J. Appl. Polym. Sci.*, 71 (1999), pp. 1969-1975.
- [28] J.D. Smart. *Advanced Drug Delivery Reviews*, 57 (2005), pp. 1556–1568.
- [29] D. S. Jones, A. D. Woolfson, A. F. Brown. *International Journal of Pharmaceutics*, 151 (1997), pp. 223 – 233.
- [30] J. Wang, M. Hon. *Journal of Applied Polymer Science*, 96 (2005), pp. 1083 – 1094.
- [31] M. Elimelech, X. Zhu, A. E. Childress, S. Hong. *Journal of Membrane Science*, 127 (1997), pp. 101-109.

Publication VI

Murillo L. Martins, Ariovaldo O. Florentino, Alberto A. Cavaleiro, Rafael I.V. Silva, Dayse I. Dos Santos, Margarida J. Saeki. **Mechanisms of phase formation along the synthesis of Mn–Zn ferrites by the polymeric precursor method.** *Ceramics International* 40, 16023 – 16031, 2014.



Mechanisms of phase formation along the synthesis of Mn–Zn ferrites by the polymeric precursor method

Murillo L. Martins^{a,*}, Ariovaldo O. Florentino^a, Alberto A. Cavalheiro^b, Rafael I.V. Silva^a,
Dayse I. Dos Santos^c, Margarida J. Saeki^a

^aInstituto de Biociências, Universidade Estadual Paulista, CP 510, 18618-970 Botucatu, SP, Brazil

^bUniversidade Estadual de Mato Grosso do Sul, Unidade de Ensino de Naviraí, Rua Emilio Mascoli, 275, 79950-000 Naviraí, MS, Brazil

^cFaculdade de Ciências, Universidade Estadual Paulista, CP 473, 17015 970 Bauru, SP, Brazil

Received 11 April 2014; received in revised form 22 July 2014; accepted 25 July 2014

Available online 1 August 2014

Abstract

Considering the wide application of crystalline Mn–Zn ferrites microparticles, understanding synthesis routes that allow the achievement of such materials is a constant need. In this work, Mn–Zn ferrites, $\text{Mn}_{(1-x)}\text{Zn}_x\text{Fe}_2\text{O}_4$ ($0.15 \leq x \leq 0.30$), were synthesized by the polymeric precursor method in well-controlled steps and the mechanisms of phase formation under different thermal treatments were studied. Such investigation was performed by means of thermal analysis (TG/DTA), synchrotron X-ray powder diffraction (SXP) (including in-situ and anomalous scattering experiments) and scanning electron microscopy (SEM). The ferrite precursor powders present the spinel as single crystalline phases whose cell parameters increase as Mn is substituted by Zn, indicating possible Fe deficiencies into the structure. The crystallization degree of these samples is also affected by the Mn substitution and reaches a maximum for $x=0.25$. Further thermal treatments in air at 700 °C and 1100 °C lead to additional events also related to the Zn content, such as carbonates elimination and crystallization of the contaminant phase hematite. Thermal treatments under N_2 atmosphere at 700 °C allow the achievement of powders with only the spinel phase, especially for $x=0.25$ for which highly crystalline and homogeneous ferrite is obtained despite the Fe deficiency determined by anomalous scattering SXP. Finally, thermal treatments at 1100 °C under N_2 atmosphere jeopardize the stability of the spinel structure and lead to hematite precipitation.

© 2014 Elsevier Ltd and Techna Group S.r.l. All rights reserved.

Keywords: Mn–Zn ferrites; Polymeric precursor method; X-ray diffraction; Thermal analysis

1. Introduction

Mn–Zn ferrites are one of the most widely used magnetic materials due to their low hysteresis loss and high magnetic saturation. The applications of these versatile ceramic compounds range from transformers [1] and transmission devices [2] to biomedical applications [3–5]. Most importantly, despite the great amount of studies regarding their applications found in literature from the past three decades [6–8] as well as their new applications as nanoparticles [9], an increase in the demand for the development of Mn–Zn ferrite micro-particles, especially for microwave absorption purposes still exists [10–12]. Therefore,

the improvement and understanding of various synthesis routes that allow the achievement of highly crystalline materials is a constant need.

Traditionally, these materials can be synthesized by solid-state reactions that involve very high-energy procedures [13] leading to the achievement of particles in the micro scale without any preliminary step, but basically no control over the mechanism of particle formation. On the other hand, by means of chemical (wet) routes the initially smaller Mn–Zn ferrite particles can be further subjected to thermal treatments resulting in highly crystalline microparticles through very well controlled steps.

As examples of chemical routes that allow the synthesis of Mn–Zn ferrites we can cite the co-precipitation [14] and hydrothermal [15] methods that lead to very fine and homogeneous powders.

*Corresponding author. Tel.: +55 14 3880 0573.

E-mail address: murillolongo@gmail.com (M.L. Martins).

However, the very low amount of the yield material in the end of such processes can be considered a drawback. Instead, these chemical routes are better suited for the synthesis of materials for biomedical applications, as the amount of required material is in the order of milligrams. As an alternative, the polymeric precursor method (PPM) [16] ought to be considered, since it can result in an amount of homogeneous material in the order of grams, which can be further subjected to well controlled thermal treatments and sintering processes for the achievement of highly crystalline microparticles [17]. The PPM is based on the formation of metal complexes with organic chelating agents, such as the citric acid. Then, a polyalcohol, such as glycerol, is added to the reaction in order to promote the synthesis of polyester where the metals are homogeneously distributed. Such polymer is obtained as a so-called precursor resin or gel and is subjected to a first thermal treatment leading to its decomposition and formation of a precursor powder. Finally, the precursor powder can be further subjected to new thermal treatments and sintered materials can be obtained.

It is well known that Mn–Zn ferrites crystallize as a spinel structure, which presents two characteristic crystallographic sites: a tetrahedral site (A), normally occupied by divalent ions, and an octahedral site (B), normally occupied by trivalent ions. Variations in this “normal” arrangement might occur, giving rise to an inverted spinel structure, with trivalent ions in A and divalent ions in B. Moreover, the spinel structure presents a ferrimagnetic arrangement where the magnetic moment in the A site will align antiparallel to any external magnetic field [18]. Consequently, the overall magnetic properties of Mn–Zn ferrites are related not only to morphological features (i.e. particle size), but also to the ionic distribution within the crystalline structure, which highlights the importance of elucidating the mechanism involved in the spinel phase formation.

In this work Mn–Zn ferrites with the chemical formula $Mn_{(1-x)}Zn_xFe_2O_4$ were synthesized by the PPM with different values of Zn concentration ($0.15 \leq x \leq 0.30$) and the mechanism of the spinel phase formation and the origin of undesirable secondary phases have been studied in the precursor powders as well as in the ceramic materials obtained through different thermal treatments. In addition, to elucidate the highly relevant role played by the Zn concentration in this spinel family, we also discuss the influence of the different atmospheres used during distinct thermal treatments.

2. Materials and methods

2.1. Synthesis of Mn–Zn ferrite by the PPM

Mn–Zn ferrites, $Mn_{(1-x)}Zn_xFe_2O_4$, were prepared by the polymeric precursor method (PPM) with $x=0.15$, 0.20, 0.25 and 0.30 using $Zn(NO_3)_2$ (Sigma-Aldrich, 99%), $Mn(NO_3)_2$ (Sigma, 97%) and $Fe(NO_3)_3 \cdot 9H_2O$ (Aldrich, 98%) as starting salts. The salts were diluted in water and added to aqueous solutions of citric acid with molar ratio metals:citrate = 1:4 for the metals chelation. Then, glycerol ($(CH_2)_2CH(OH)_3$, Chemco, 95%) was added to the solutions in a molar ratio glycerol:citrate = 2:1. At this point, urea was added to the reaction in a

molar ratio urea:manganese = 6:1. Since urea is a strong reducing agent, its addition tends to retard the oxidation of the Mn^{+2} ions during the synthesis process. The resulting solutions were then stirred and heated up to 60 °C to obtain the precursor resins, which were treated at 400 °C for 2 h to eliminate the excess of organic compounds. Therefore, precursor powders having a complete range in Mn and Zn concentrations were obtained.

The resulting precursor powders were further subjected to thermal treatments at 700 °C for 2 h under air and under N_2 atmosphere and at 1100 °C for 2 h under N_2 atmosphere for the formation of ceramic microparticles. The precursor powders with $x=0.25$ and 0.30 were also subjected to thermal treatments at 1100 °C for 2 h in air and under N_2 atmosphere. A thermal treatment at 1100 °C for 24 h under N_2 atmosphere was also performed for $x=0.25$.

2.2. Materials characterization

2.2.1. Precursor powders characterization

The precursor powders were studied through thermal analysis (TGA/DTA) using a Netzsch, STA 409. First, all samples were analysed under 40 mL/min air flow (White Martins, 4.7) between room temperature and 1200 °C using the heating rate of 10 °C/min. The precursor powder with $x=0.25$ was also studied under a 40 mL/min N_2 flow (White Martins, 4.7) in the same temperature range. The initial mass was kept approximately constant for all samples.

The crystalline phases were investigated by means of synchrotron X-ray powder diffraction (SXPDP) using 10 keV ($\lambda=1.24 \text{ \AA}$) synchrotron radiation at the D10B-XPD beamline at the Brazilian Synchrotron Light Laboratory (LNLS, Brazil) in a Q -range of $1.5 \text{ \AA}^{-1} < Q < 6 \text{ \AA}^{-1}$. The precursor powder with $x=0.25$, which was found to present the most crystalline spinel structure between all compositions, was also subjected to an in situ experiment by using an ARARA furnace. In such experiment, the sample was heated up to 400 °C and a SXPDP pattern was collected in the region of the (311) Bragg reflection of the spinel phase. The same procedure was repeated at 450 °C, 600 °C and 750 °C.

Morphologic analyses were also performed in all samples by means of scanning electron microscopy (SEM) using a FEI microscope, Quanta 200. To these analyses, the powders were dispersed in isopropanol by means of ultrasound bath for 15 min.

2.2.2. Characterization of the ceramic microparticles

The crystalline phases of all the ceramic samples were investigated by powder diffraction (SXPDP) using the same experimental setup described in Section 2.2.1. The ceramic sample prepared with $x=0.25$ and treated at 700 °C for 2 h under N_2 atmosphere was then found to be the most crystalline sample and was further analysed by using 7 keV ($\lambda=1.77 \text{ \AA}$), which is close to the Fe K -edge absorption, and 9.5 keV ($\lambda=1.30 \text{ \AA}$) radiation, which is close to the Zn K -edge absorption. By using the anomalous scattering properties of such metals, the composition of the crystalline ferrite could be determined. Morphological

analysis in this sample was also performed using SEM as described in Section 2.2.1.

All structure refinements were performed using the software package GSAS [19] and input parameters data from the Inorganic Crystal Structure Database (ICSD).

3. Results and discussion

First, a morphological characterization of the precursor powders of Mn–Zn ferrite with chemical formula $Mn_{(1-x)}Zn_xFe_2O_4$ ($x=0.15, 0.20, 0.25$ and 0.30), obtained after treating the precursor resins at $400\text{ }^\circ\text{C}$ for 2 h was performed by SEM. From the images, depicted in Fig. 1, we note that as the amount of Zn increases, the particles seem to be immersed into bigger and inhomogeneous structures, most likely formed by remaining organic compounds and carbonates, originated during the synthesis process.

Therefore, to evaluate the influence of such compounds in the samples and also to elucidate the thermal behaviour of the precursor powders, thermal analyses (TGA/DTA) were conducted

in air atmosphere. In Fig. 2(a) the TGA analyses are presented, while Fig. 2(b) depicts the DTA analyses. The observed curves can be divided into 4 distinct temperature ranges: (I) from $50\text{ }^\circ\text{C}$ to $300\text{ }^\circ\text{C}$, (II) from $300\text{ }^\circ\text{C}$ to $450\text{ }^\circ\text{C}$, (III) from $450\text{ }^\circ\text{C}$ to $750\text{ }^\circ\text{C}$ and (IV) from $750\text{ }^\circ\text{C}$ to $1200\text{ }^\circ\text{C}$. In the temperature range (I) all powders present mass losses due to the elimination of water and organic compounds adsorbed onto the materials surface. Subsequent mass losses take place along the temperature range (II), while the well-defined exothermic processes shown in the DTA curve suggest the elimination of the remaining organic compounds in the materials. The formation of the ferrite phase can also be part of such exothermic process, which is less prominent for $x=0.25$ and 0.30 , since the thermal treatment performed to obtain the precursor powders is certainly not enough to crystallize the whole material.

At the temperature range (III) all samples present sequences of exothermic processes, which are also likely related to elimination of organic compounds and crystalline phases formation and take longer for $x=0.25$ and 0.30 . The samples with $x=0.15$ (red curve) and 0.20 (blue curve) present very slight mass gains, which can be caused by metals oxidation.

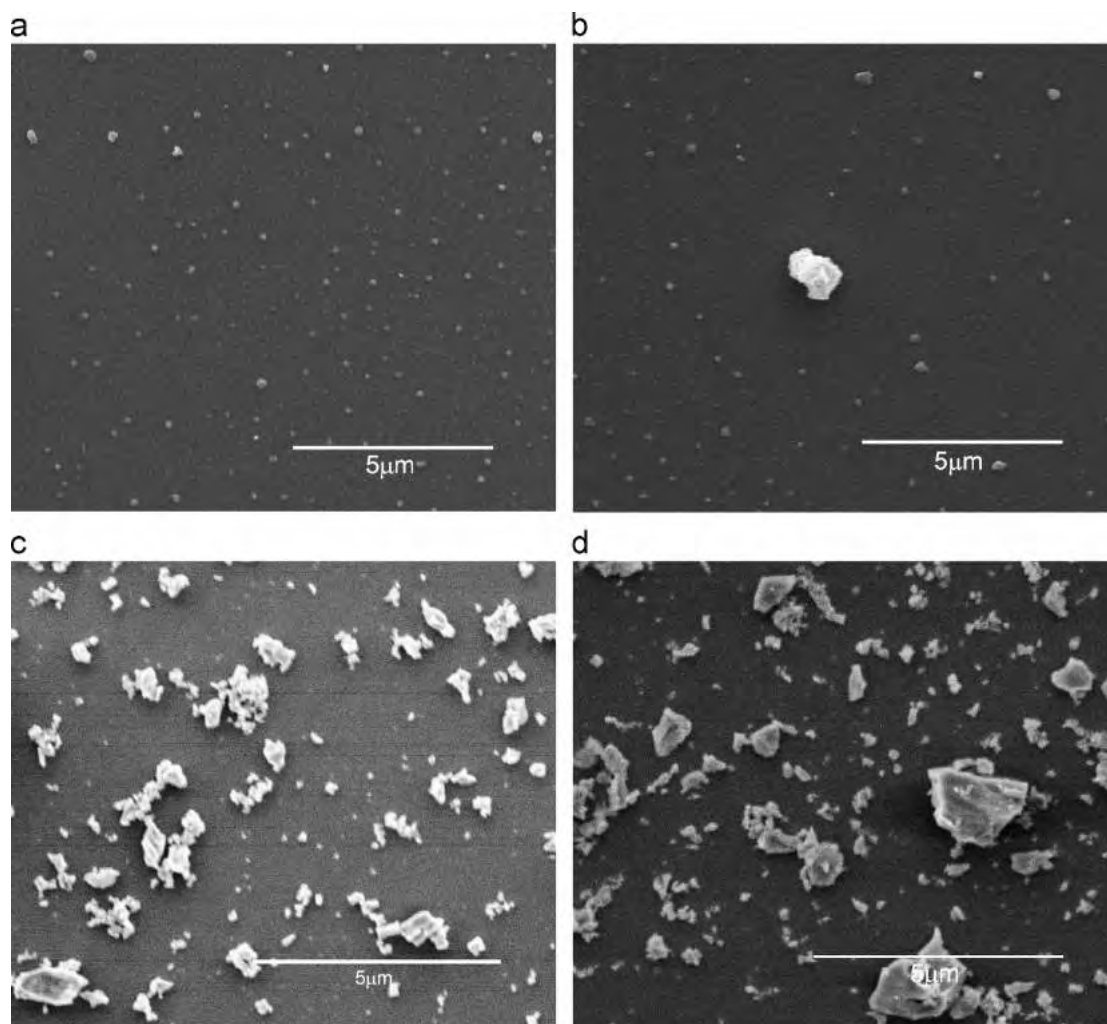


Fig. 1. SEM images of the precursor powders of Mn–Zn ferrite with chemical formula $Mn_{(1-x)}Zn_xFe_2O_4$ where, $x=0.15$ (a), 0.20 (b), 0.25 (c) and 0.30 (d). As x increases, the dispersion of the particles is prejudiced.

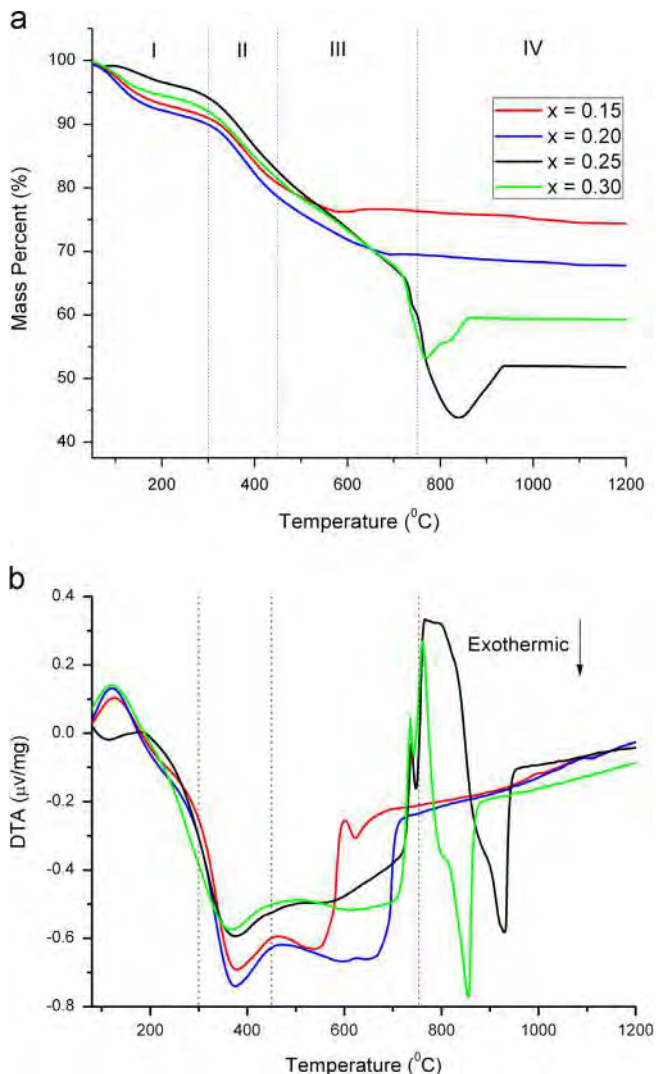


Fig. 2. Thermal analyses, TGA (a) and DTA (b) in air atmosphere of the precursor powders of Mn–Zn ferrite. The analyses are divided in 4 temperature ranges: (I) from 50 °C to 300 °C; (II) from 300 °C to 450 °C and (III) from 450 °C to 750 °C and (IV) from 750 °C to 1200 °C.

At the beginning of the temperature range (IV) great mass losses are noted in the samples with $x=0.25$ and 0.30 together with endothermic events and followed by mass gains and exothermic processes, while for $x=0.15$ and 0.20 the TGA and DTA curves are stabilized. The mass losses concomitantly with the endothermic events indicate a possible elimination of the carbonates [20] whose presence was speculated based on SEM images, while the mass gains and exothermic events are likely related to metals oxidation and crystalline phases formation.

To better understand the phase transitions observed in the thermal analysis, the precursor powders were subjected to thermal treatments in air atmosphere at different temperatures and further studied by SXP. The structure refinement results are shown in Table 1.

First, the SXP patterns obtained for the precursor powders are presented in Fig. 3. In these samples, all compositions

present the spinel structure as a single crystalline phase and the crystallite size increases as the amount of Zn increases from 0.15 to 0.25 and drastically decreases for $x=0.30$ (see Table 1). This result is in contradiction with the results found in the literature to Mn–Zn ferrites synthesized by other chemical routes, for example the co-precipitation method, where the increase of Zn continuously decreases the crystallite size [21]. Regarding the cell parameters (Table 1), there is also an increase with the insertion of Zn into the material, which is, once again, not in agreement with the results presented in the literature for Mn–Zn ferrite synthesized by other chemical routes. In attempt to understand this contradiction, we may consider the ionic radii values, obtained from [22,23], presented in Table 2. A possible explanation for the observed increase in cell parameter is the substitution of Fe^{+3} by Zn^{+2} in the A site where the latter is naturally more likely to be placed [24] and is not the more stable site for the Fe^{+3} ions [25]. Therefore, such a substitution tends to favour the crystallization process and increase the crystallite size. For $x=0.30$, the crystallization and coalescence of the particles is prejudiced and the crystallite size is reduced. So, in one hand, controlled amounts of Zn (from $x=0.15$ to 0.25) favor the ferrite crystallization by possibly substituting unstable Fe^{+3} ions into the spinel's A site. On the other hand, the continuous increase in the Zn content in substitution to Mn in the material stoichiometry (x value), lead to a reduction in the crystalline spinel formation, which is somehow expected and in agreement with the literature since the nucleation of crystallites are influenced by the probability of site occupancy by the cations. With three sites available for each unit cell (two octahedral, one tetrahedral), Mn^{+2} ions present a higher chance of getting absorbed by a nucleus unlike the Zn^{+2} that only occupies the tetrahedral sites. In this way, the excessive substitution of Mn^{+2} by Zn^{+2} jeopardizes the nucleation process and growth of particles [25]. If the assumption that Fe^{+3} is substituted by Zn^{+2} in the A site with the increasing x (from 0.15 to 0.25), is right, part of the Fe ions might remain attached to organic compounds or to the amorphous carbonates present in the sample and only eliminated around 750 °C according to the thermal analysis.

To elucidate the exothermic process noted at the temperature range II the most crystalline precursor powder (with $x=0.25$) was heated to 400 °C and subjected to an in situ SXP experiment, whose result is shown in Fig. 4(a). An increase in the cell parameter is depicted by the shift in the (311) Bragg reflection to low Q values. Such a result suggests a continuous substitution of Fe^{+3} ions by Zn^{+2} in the A site and confirms that the formation of the ferrite phase is also part of the exothermic process at the temperature range II of the DTA analysis. It is clear, however, that the energies involved in the processes of the powders with $x=0.25$ and 0.30 are lower than for the other samples despite of the observed similar mass losses in all compositions. For $x=0.25$ such a difference can be explained by the higher crystallinity already present in the precursor powder that leads to a lower contribution from the crystallization process in the exothermic peak. Regarding the sample with $x=0.30$, the lower amount of energy involved

Table 1

Structural refinement parameters of Mn–Zn ferrites with the general formula $Mn_{(1-x)}Zn_xFe_2O_4$ ($0.15 \leq x \leq 0.30$) obtained from SXPd data collected using 10 keV synchrotron radiation. The results show the influence of x value (Zn content), and thermal treatments parameters such as temperature and atmosphere, in the spinel structure formation. All the thermal treatments presented in this table were performed for 2 h and only the samples with spinel as a major phase are presented.

x	Temperature (°C)	Atmosphere	Spinel phase weight fraction (%)		a (Å) ^a	d (nm) ^b	R_{Bragg} ^c
0.15	Precursor (400)	air	100		8.3994(05)	6	0.0560
		N ₂	100	10	8.4184(00)	74	0.0514
	1100	N ₂	44		8.4769(00)	24	
			46		8.4716(02)	8	
			44	90	8.4924(00)	16	0.0819
			46		8.4044(00)	25	
0.20	Precursor (400)	air	100		8.4119(02)	7	0.0512
		N ₂	100	47	8.4316(00)	67	0.0601
	1100	N ₂	53		8.4446(01)	38	
			45	100	8.4047(00)	39	0.0539
			55		8.4498(01)	18	
					8.4167(01)	10	0.0539
0.25	Precursor (400)	air	100		8.4362(00)	85	0.0698
		N ₂	100		8.3956(00)	60	0.0565
	1100	N ₂	97	34	8.4281(01)	27	
				63	8.4248(07)	5	0.0393
					8.4460(00)	43	0.0529
					8.3909(00)	48	0.0563
0.30	Precursor (400)	air	100		8.4507(01)	14	
		N ₂	100				
	1100	N ₂	95	43			
				52			

^aCell parameter values. The numbers in parenthesis indicate the standard deviations.

^bCrystallite size calculated by means of the Scherrer equation and using the width of the (311) Bragg reflection of the spinel phase centred around 2.5 \AA^{-1} .

^cQuality of the structural refinement model.

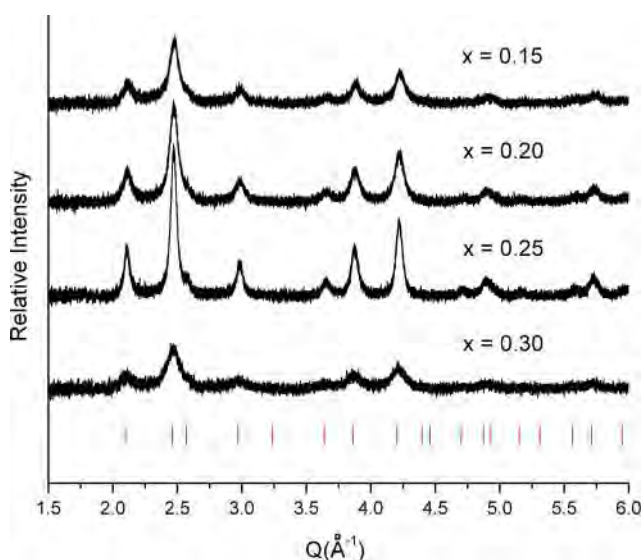


Fig. 3. SXPd patterns of the precursor powders of Mn–Zn ferrite with chemical formula $Mn_{(1-x)}Zn_xFe_2O_4$ ($x=0.15, 0.20, 0.25$ and 0.30). The tick marks indicate the expected structural peaks of spinel ferrite with space group $Fd-3mZ$ (ICSD 170911). All compositions present the spinel structure as a single phase.

in the process might reflect the slower crystallization process of the spinel structure caused by the excess of Zn.

A second in situ SXPd experiment was performed in order to elucidate the thermic events at the temperature range III of the DTA analysis. In this experiment, the precursor powder with $x=0.25$ was heated between $450 \text{ }^\circ\text{C}$ and $750 \text{ }^\circ\text{C}$, and, as indicated

by arrows in Fig. 4(b), the sample presents the crystallization of a secondary phase indexed as hematite (Fe_2O_3 —space group $R-3cH$, ICSD 15840) as part of the remaining organic compounds are decomposed and Fe ions are released. Such a phase can be formed simply by the reaction between Fe^{+3} and the interstitial or environmental oxygen and its crystallization together with the metals oxidation and the elimination of the remaining organic compounds lead exothermic processes in the DTA curves (temperature range III). Since these processes take longer as the amount of Zn in the samples increases from $x=0.15$ to $x=0.25$, one should expect an increase in the hematite content in powders obtained after treating the precursor powders with the same values of x (0.15 to 0.25) at $700 \text{ }^\circ\text{C}$. This hypothesis is confirmed by the SXPd data presented in Fig. 5(a) and the structure refinement results presented in Table 1, which show that the hematite mass content changes from 22 wt% to 63 wt% when x increases from 0.15 to 0.25. For $x=0.30$ the hematite content is reduced to 33 wt%.

A possible explanation for the increase in the hematite content from $x=0.15$ to $x=0.25$ lies on the hypothesis, previously discussed in the precursor powders SXPd analysis, that by increasing the Zn content in the samples the Fe concentration into the spinel is reduced. Consequently, the Fe concentration outside the spinel becomes higher and the hematite formation might be favoured. Regarding the sample with $x=0.30$, where the hematite precipitation is reduced, we can hypothesize that the exceeding Zn outside the spinel can also combine to the Fe ions retarding their reaction with oxygen. The slight metals oxidation observed when $x=0.15$ and 0.20 is than reasonable since the crystallization of hematite can take some amount of Fe^{+3}

from the spinel leading to changes in the Mn ions valence for charge balancing inside the structure.

Then, the precursor powders with $x=0.25$ and 0.30 were subjected to thermal treatments for 2 h in air at $1100\text{ }^{\circ}\text{C}$, where, according to the TGA and DTA curves, these samples are stable after the carbonates elimination. From Fig. 5(b), we note that the exothermic events between $800\text{ }^{\circ}\text{C}$ and $1000\text{ }^{\circ}\text{C}$ (previously shown in the Fig. 3(b)) are mainly due to the formation of additional hematite, likely due to the incorporation of Fe ions released from the carbonates.

To better understand the influence of the atmosphere of the thermal treatments in the spinel phase crystallization, the precursor powder with $x=0.25$ was submitted to a TGA/DTA analysis under N_2 atmosphere (Fig. 6(a)). The curves also present the carbonates elimination, characterized by a great mass loss and an endothermic process around $690\text{ }^{\circ}\text{C}$. After such elimination, a new exothermic process indicating the formation of crystalline phases is observed. Curiously, by keeping the temperature increase in the thermal analysis under N_2 , the sample presents a mass gain around $1100\text{ }^{\circ}\text{C}$ (similarly to the analysis in air atmosphere around $800\text{ }^{\circ}\text{C}$) accompanied by exothermic events, suggesting, despite of the N_2 atmosphere, the oxidation of metals and formation of new crystalline phases.

Table 2
Effective ionic radii of ions in a spinel structure [22,23].

Ion	Tetrahedral site (A site)	Octahedral site (B site)
Fe^{+2}	0.615	0.74
Fe^{+3}	0.485	0.645
Mn^{+2}	0.655	0.80
Mn^{+3*}	0.58	0.72
Zn^{+2}	0.58	0.73

As shown in Fig. 6(b), thermal treatment at $700\text{ }^{\circ}\text{C}$ under N_2 atmosphere in the precursor powders only induces the formation of spinel phases. Most likely, after the carbonates elimination, the released Fe ions could not react with the environmental oxygen due to the N_2 atmosphere facilitating their incorporation to the spinel structure.

Some particular features can be noted in the structural refinement data of the samples treated at $700\text{ }^{\circ}\text{C}$ under N_2 , presented in Table 1. First, for $x=0.15$ the formation of three distinct spinel phases are noted, which can be related to the low stability of the precursor powder caused by the likely high concentration of Fe^{+3} in the A site. For this sample, the major phases present considerable larger cell parameters in comparison to the precursor powder, and, according to the values given in Table 2, it is most likely basically formed by Mn and Fe. In fact, all compositions present increases in cell parameters in comparison to the respective precursor powders, which can be attributed to the reduction of Fe^{+3} to Fe^{+2} , and the massive incorporation of the last into the spinel structures. The sample with 0.20 does not present a single spinel phase as well. However, in this case, two spinel phases are detected but with a considerable lower discrepancy in cell parameter values.

The sample with $x=0.25$ whose precursor powder was the most crystalline, as expected, also possesses the most crystalline spinel phase after the thermal treatment in N_2 atmosphere. Most importantly, such sample presents a single spinel phase, highlighting the importance of the correct Zn amount in the ferrite crystallization process. The progress of the sintering process in such sample can be well seen, as indicated by the arrow in the SEM image shown presented in Fig. 7.

Additionally, by means of anomalous scattering the composition of this crystalline structure was determined as: $[\text{Mn}_{0.29}\text{Zn}_{0.33}\text{Fe}_{0.38}]_{\text{A site}}[\text{Mn}_{0.52}\text{Fe}_{1.48}]_{\text{B site}}\text{O}_4$; note that there is still a deficiency of Fe into the structure in comparison to the nominal composition, even after all the thermal treatments.

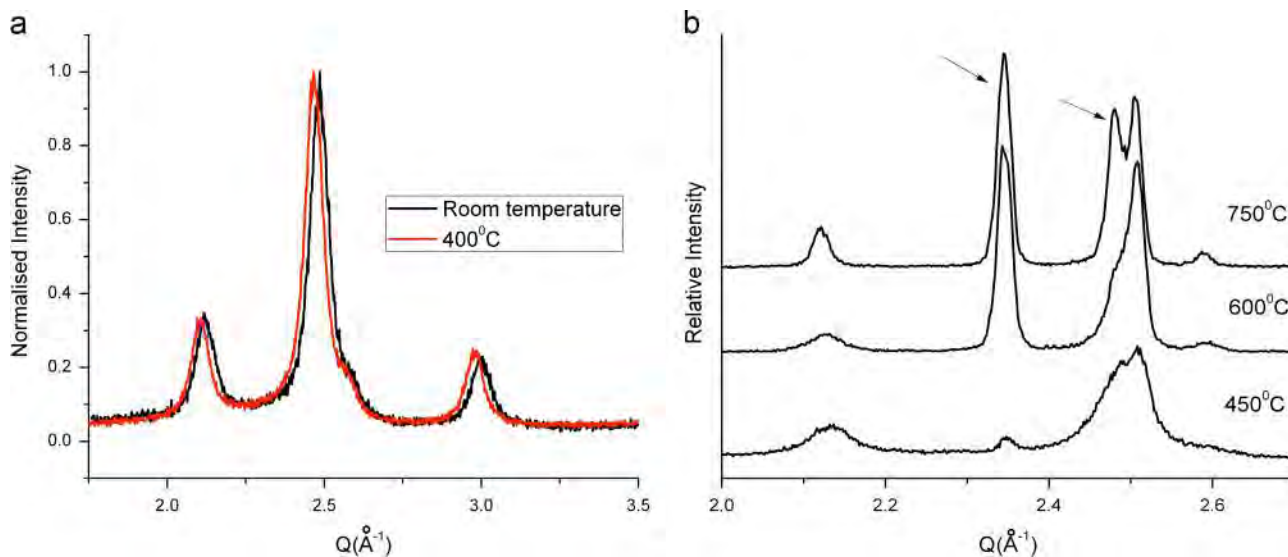


Fig. 4. In situ SXP patterns collected at $400\text{ }^{\circ}\text{C}$ (a) and in the temperature range between $450\text{ }^{\circ}\text{C}$ and $750\text{ }^{\circ}\text{C}$ (b) for the precursor powder with $x=0.25$. In (a) the continuous increase in the cell parameter, depicted by the shift in the peaks to the low Q values, can be noted in the sample, while in (b) the arrows indicate the formation of the secondary phase hematite.

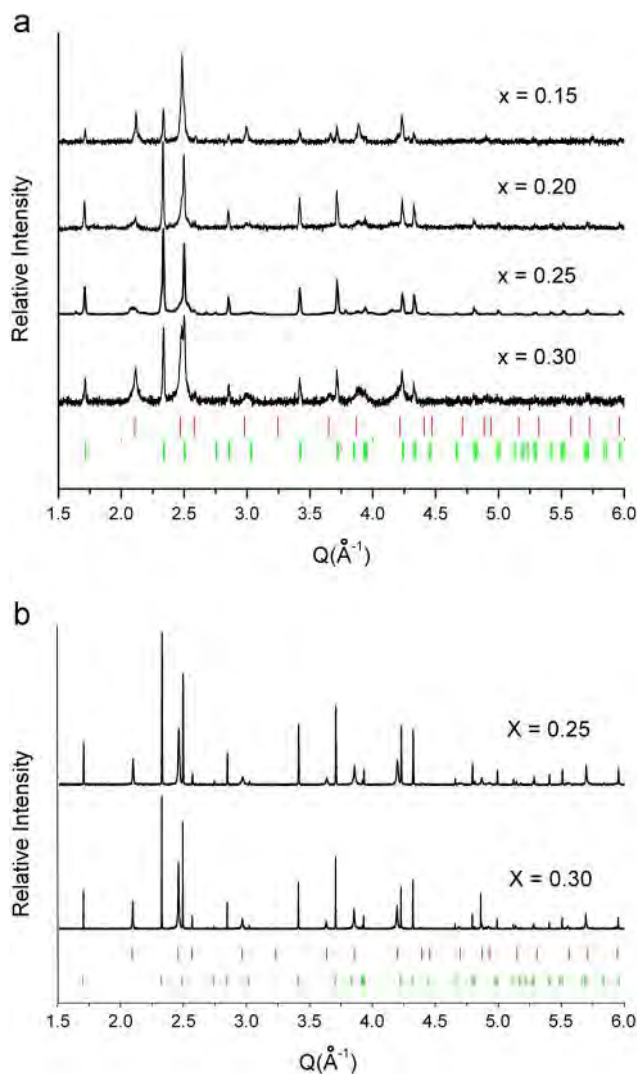


Fig. 5. (a) XSPD patterns of all the precursor powders after thermal treatment at 700 °C in air (b) and the precursor powders with $x=0.25$ and 0.30 after thermal treatment at 1100 °C in air. All samples present considerable amounts of the secondary phase crystallization of the secondary phase hematite (Fe_2O_3).

To further investigate samples behaviour at 1100 °C, the precursor powders were subjected to thermal treatments at this temperature for 2 h in N_2 atmosphere. As depicted in Fig. 8 all the samples present spinel ferrites and traces of hematite. Regarding the spinel phases, in all compositions it was possible to detect two distinct structures: one with a considerable lower crystallization degree and cell parameter closer to the ones obtained in the samples treated at 700 °C in N_2 atmosphere, and a second spinel structure with a higher crystallization degree and reduced cell parameter (see Table 1). The only exception is for $x=0.15$ where the less crystalline spinel phase presents a reduced cell parameter.

The reduced unit cells in one of the spinel phases is most likely due to the metals oxidation previously hypothesized on TGA analysis. Such great oxidation, together with the disorder found in the other spinel phase and the hematite traces in the samples are indicative of low stability of the ferrite at 1100 °C even under N_2 atmosphere. Such instability can be confirmed

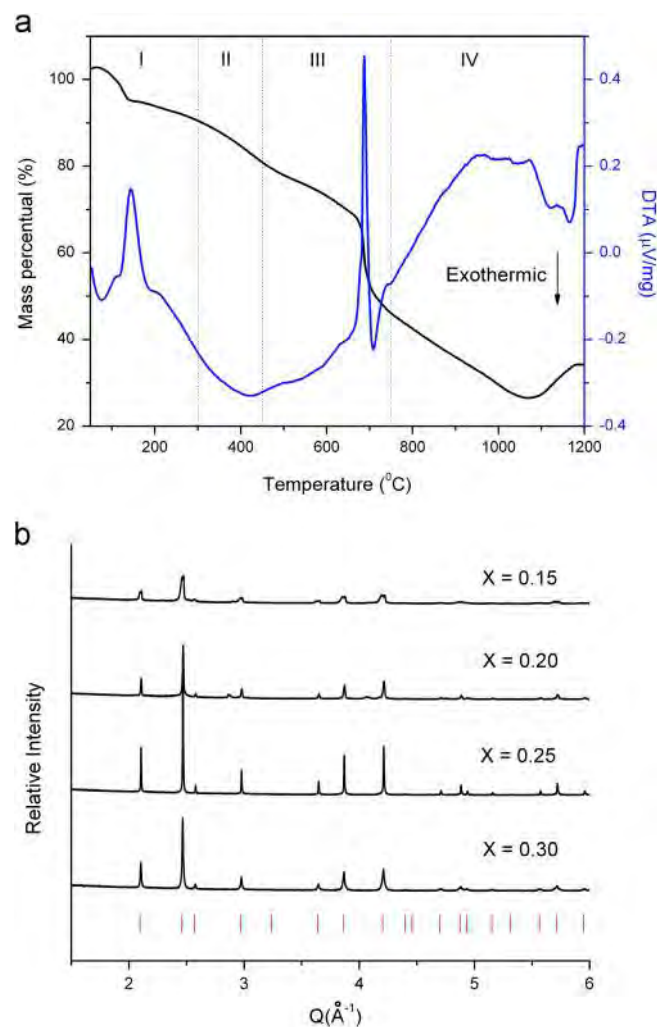


Fig. 6. Thermal analysis (TGA/DTA) of the precursor powder with $x=0.25$ in N_2 atmosphere (a) indicate a possible phase formation around 700 °C and the XSPD patterns of all the precursor powders after thermal treatment at 700 °C in N_2 atmosphere for 2 h (b) show that such thermal treatment allows the achievement of crystalline spinel phase.

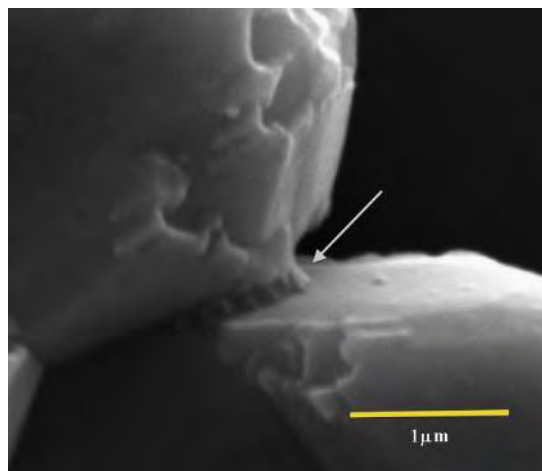


Fig. 7. SEM image of the sample with $x=0.25$ after thermal treatment at 700 °C for 2 h under N_2 atmosphere. The arrow indicates the sintering process in the material.

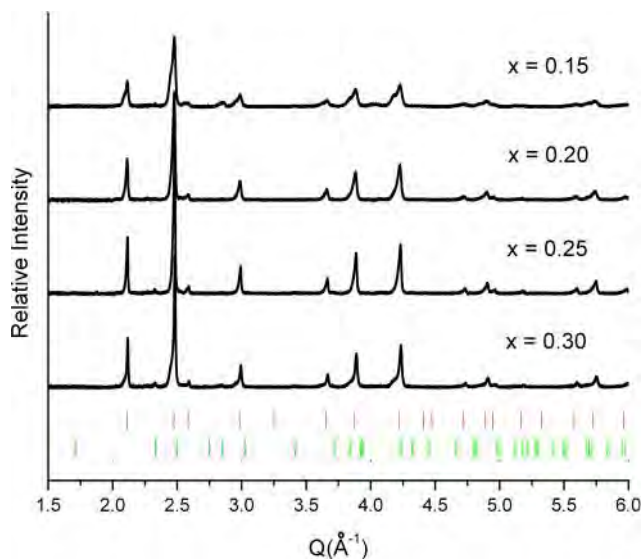


Fig. 8. SXPD patterns of all the precursor powders after thermal treatment at 1100 °C in N₂ atmosphere for 2 h. The samples present the spinel ferrite (red marks) with traces of hematite (green marks). (For interpretation of the references to color in this figure legend, the reader is referred to the web version of this article.)

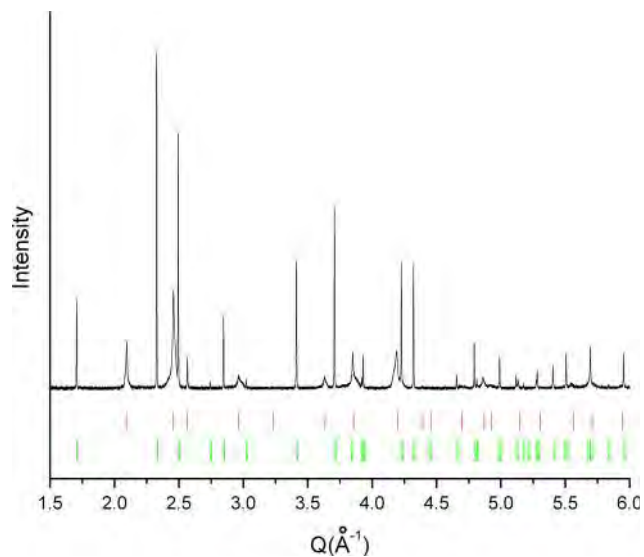


Fig. 9. SXPD pattern of the precursor powder with $x=0.25$ after thermal treatment at 1100 °C in N₂ atmosphere for 24 h. The samples present the spinel ferrite (red marks) and a great amount of hematite (green marks). (For interpretation of the references to color in this figure legend, the reader is referred to the web version of this article.)

by exposing, for example, the precursor powder with $x=0.25$ to a long thermal treatment at 1100 °C under N₂ atmosphere for 24 h. The SXPD pattern of the resulting sample is depicted in Fig. 9 and a great amount of hematite can be once again noted.

4. Conclusions

In this work we report a structural study on the mechanisms of phases formation during the synthesis of Mn–Zn ferrite by the polymeric precursor method. Materials with the

composition Mn_(1-x)Zn_xFe₂O₄, where $0.15 \leq x \leq 0.30$, were synthesized and the precursor powders obtained after a thermal treatment on the precursor resins at 400 °C for 2 h in air present the spinel ferrite as a single crystalline phase. However, such structures present a Fe deficiency closely related to the amount of Zn. After thermal treatments of the precursor powders at 700 °C and 1100 °C in air, the samples present great amounts of the undesirable secondary phase hematite (Fe₂O₃), which also show strong relation with the Zn concentration. On the other hand, thermal treatments on the precursor powders at 700 °C for 2 h under N₂ atmosphere lead to powders with only the spinel structure phase. In this case, $x=0.25$ is the optimum Zn content and highly crystalline and homogeneous samples are obtained. Finally, thermal treatments at higher temperatures jeopardize the stability of the spinel phases even under N₂ atmosphere.

Acknowledgments

The authors thank CAPES and FAPESP for the financial support. LNLS is also acknowledged for the beamtime for the diffraction experiments.

References

- [1] P. Hu, D. Pan, S. Zhang, J. Tian, A.A. Volinsky., Mn–Zn soft magnetic ferrite nanoparticles synthesized from spent alkaline Zn–Mn batteries, *J. Alloys Compd* 509 (2011) 3991–3994.
- [2] H. Waqas, A.H. Qureshi, K. Subhan, M. Shahzad., Nanograin Mn–Zn ferrite smart cores to miniaturize electronic devices, *Ceram. Int.* 38 (2012) 1235–1240.
- [3] Q. Tang, D. Zhang, X. Cong, M. Wan, L. Jin, Using thermal energy produced by irradiation of MnZn ferrite magnetic nanoparticles (MZF-NPs) for heat-inducible gene expression, *Biomaterials* 29 (2008) 2673–2679.
- [4] M. Lin, D. Zhang, J. Huang, J. Zhang, W. Xiao, H. Yu, L. Zhang, J. Ye, The anti-hepatoma effect of nanosized Mn–Zn ferrite magnetic fluid hyperthermia associated with radiation in vitro and in vivo, *Nanotechnology* 24 (2013) 255101–255109.
- [5] M.L. Martins, M.J. Saeki, M.T.F. Telling, J.P.R.L.L. Parra, S. Landsgesell, R.I. Smith, H.N. Bordallo, Development and characterization of a new bio-nanocomposite (bio-NCP) for diagnosis and treatment of breast cancer, *J. Alloys Compd.* 584 (2014) 514–519.
- [6] E. Hirota, T. Mihara, A. Ikeda, H. Chiba., Hot-pressed Mn–Zn ferrite for magnetic recording heads, *IEEE Trans. Magn.* 7 (1971) 337–341.
- [7] Y. Sakaki, T. Matsuoka, Hysteresis losses in Mn–Zn ferrite cores, *IEEE Trans. Magn.* 22 (1986) 623–625.
- [8] H. Saotome, Y. Sakaki, Iron loss analysis of Mn–Zn ferrite cores, *IEEE Trans. Magn.* 33 (1997) 728–734.
- [9] J. Xie, C. Yan, Y. Zhang, N. Gu, Shape evolution of multibranched Mn–Zn ferrite nanostructures with high performance: a transformation of nanocrystals into nanoclusters, *Chem. Mater.* 25 (2013) 3702–3709.
- [10] X. Zhang, W. Sun, Microwave absorbing properties of double-layer cementitious composites containing Mn–Zn ferrite, *Cem. Concr. Compos.* 32 (2010) 726–730.
- [11] W. Wen-Jie, Z. Chong-Guang, J. Qing-Jie, Fabrication and performance optimization of Mn–Zn ferrite/EP composites as microwave absorbing materials, *Chin. Phys. B* 22 (2013) 128101–128105.
- [12] A.M. Gama, M.C. Rezende, C.C. Dantas, Dependence of microwave absorption properties on ferrite volume fraction in MnZn ferrite/rubber radar absorbing materials, *J Magn. Magn. Mater.* 323 (2011) 2782–2785.

- [13] A. Zapata, G. Herrera, Effect of zinc concentration on the microstructure and relaxation frequency of Mn–Zn ferrites synthesized by solid state reaction, *Ceram. Int.* 39 (2013) 7853–7860.
- [14] R. Arulmurugan, G. Vaidyanathan, S. Sendhilnathan, B. Jeyadevan, Mn–Zn ferrite nanoparticles for ferrofluid preparation: Study on thermal-magnetic properties, *J. Magn. Magn. Mater.* 298 (2006) 83–94.
- [15] L. Nalbandian, A. Delimitis, V.T. Zaspalis, E.A. Deliyanni, D. N. Bakoyannakis, E.N. Peleka, Hydrothermally prepared nanocrystalline Mn–Zn ferrites: synthesis and characterization, *Microporous Mesoporous Mater.* 114 (2008) 465–473.
- [16] Pechini M.P.. U.S. Patent 3.438.723, 1969.
- [17] J. Hou, R.V. Kumar, Y. Qu, D. Krsmanovic, Controlled synthesis of photoluminescent $\text{Bi}_4\text{Ti}_3\text{O}_{12}$ nanoparticles from metal–organic polymeric precursor, *J. Nanopart. Res.* 12 (2010) 563–571.
- [18] Z.J. Zhang, Z.L. Wang, B.C. Chakoumakos, J.S. Yin, Temperature dependence of cation distribution and oxidation state in magnetic Mn–Fe ferrite nanocrystals, *J. Am. Chem. Soc.* 120 (1998) 1800–1804.
- [19] A.C. Larson, R.B. Von Dreele, General structure analysis system (GSAS), Los Alamos Nat. Lab. Rep. 86 (2004) 748.
- [20] Y. Liu, J. Zhao, H. Zhang, Y. Zhu, Z. Wang, Thermal decomposition of basic zinc carbonate in nitrogen atmosphere, *Thermochim. Acta* 414 (2004) 121–123.
- [21] R. Arulmurugan, B. Jeyadevan, G. Vaidyanathan, S. Sendhilnathan, Effect of zinc substitution on Co–Zn and Mn–Zn ferrite nanoparticles prepared by co-precipitation, *J. Magn. Magn. Mater.* 288 (2005) 470–477.
- [22] R.D. Shannon, C.T. Prewitt, Effective ionic radii in oxides and fluorides, *Acta Cryst* 25 (1969) 925–946.
- [23] H. St., C. O’Neil, A. Navrotsky, Simple spinels: crystallographic parameters, cation radii, lattice energies, and cation distribution, *Am. Mineral.* 68 (1983) 181–194.
- [24] P.V. Kovtunencko, Defect formation in spinels in oxygen nonstoichiometry, *Glass Ceram.* 54 (1997) 143–148.
- [25] R. Gimenes, M.R. Baldissera, M.R.A. da Silva, C.A. da Silveira, D.A. W. Soares, L.A. Perazolli, M.R. da Silva, M.A. Zaghete, Structural and magnetic characterization of $\text{Mn}_x\text{Zn}_{1-x}\text{Fe}_2\text{O}_4$ ($x=0.2; 0.35; 0.65; 0.8; 1.0$) ferrites obtained by the citrate precursor method, *Ceram. Int.* 38 (2012) 741–746.